The cosmic ray induced muon spectrum measured with the L3 detector

To
Tanja,
my parents,
Edel Juul Eriksen,
and the memory of Kirsten Beirholm,
who believed in me when times were tough.

The cosmic ray induced muon spectrum measured with the L$_3$ detector

Een wetenschappelijke proeve op het gebied
van de Natuurwetenschappen, Wiskunde en Informatica.

Proefschrift

ter verkrijging van de graad van doctor
aan de Katholieke Universiteit Nijmegen,
op gezag van de Rector Magnificus
prof. dr. C. W. P. M. Blom,
volgens besluit van het College van Decanen
in het openbaar te verdedigen op
maandag 4 November 2002,
des namiddags om 1.30 uur precies,
door

Bert Gøtterup Petersen

geboren op 2 februari 1970 te Kolding, Denemarken.

Promotor:	**Prof. Dr. M. Pohl**
Copromotor:	**Dr. C. Timmermans**

Manuscriptcommissie:	**Prof. Dr. J. Kuijpers**	
	Prof. Dr. T. Hebbeker	RWTH Aachen
	Dr. P. LeCoultre	ETH Zürich

Typeset using LaTeX2ε

Contents

Introduction

The Earth is constantly being bombarded with cosmic rays, most of these are protons believed to originate from within our galaxy. The magnetic field of the Earth acts as a shield against the low energy particles. When a high energy cosmic ray enters the atmosphere it collides with the nucleus of one of the atoms in the upper atmosphere. The amount of energy available in this collision results in the creation of a large number of particles, creating a large cascade of particles. Charged pions are created in the initial and secondary collisions, as well as decay products of heavier particles. In more than 99.9% of the cases the decay of a charged pion results in the creation of a muon and a muon neutrino. The "long" live-time (about 2.2 µs) of muons along with their high Lorentz factor, and low cross-section for hard processes allow a large fraction of them to reach sea-level. On the way to the surface a muon only looses about 1.8 GeV on average due to soft processes such as ionization.

This thesis presents a measurement of the muon spectrum and the charge ratio in the momentum range $40 < p < 1000$ GeV at sea level. The zenith angle dependence is measured in the range $0.6 < \cos\theta < 1.0$, i.e. from about 53° to vertical. The measurement is done with the L3+Cosmics detector at CERN, Geneva (6° of longitude East and 46° of latitude North). It is based on the data collected in 1999.

The outline of this thesis is as follows.

Chapter 1 presents a brief overview of experimental cosmic ray physics. It contains a short historical introduction to the field, highlighting the close connection between cosmic ray physics and particle physics. The discussion is continued with an overview of observational methods in astroparticle physics. Finally the muon spectrum itself is discussed, and the scientific interest of an accurate measurement.

Chapter 2 contains a detailed description of the experimental set-up. This includes a discussion of the relevant parts of the L3 muon chamber system. Then follows a detailed description of the modifications which were made to enable the accurate measurement of cosmic ray muons. The independent data acquisition software is also discussed in some detail.

Chapter 3 discusses the reconstruction of cosmic ray muons. The focus is placed on the author's original contributions. Finally, a short description of the detector simulation is given, including a discussion of the overburden.

Chapter 4 describes the event selection. The events are logically grouped in so-called "runs". For a precise measurement with large statistics, it is an advantage that the events entering the analysis have been taken under the same experimental conditions. The criteria for a full run to be used in the analysis is described as well as the criteria for the individual

events.

Chapter 5 evaluates the performance of the experimental set-up. The most important efficiencies are discussed. In addition, the critical importance of the experimental live-time calls for a dedicated validation study, which is also described. Finally, the resolution of the momentum measurement is discussed along with a check of the absolute momentum scale.

Chapter 6 provides a detailed account of the analysis resulting in the measurement of the cosmic ray induced muon spectrum. A large effort has gone into the evaluation of the potential sources of systematic uncertainties. A detailed account of these sources and their influence is presented as well. Finally, the zenith angle dependence of the flux and charge ratio as obtained in this study are discussed.

Throughout this thesis $\hbar = c = 1$ is used in all calculations, unless specifically stated otherwise.

Chapter 1

Cosmic rays

The study of cosmic rays belongs to the field of astroparticle physics, which is a strongly interdisciplinary and fast evolving area of research[*]. This chapter pictures the perspective in which this research must be viewed. After a short historical introduction, a summary of astroparticle physics is given, followed by an overview of the experimental situation regarding the cosmic ray induced muon spectrum. Finally, a brief discussion of the theoretical models predicting the muon flux and charge ratio is given.

1.1   Historical introduction

The study of cosmic rays has a long and exciting history (Longair 1992). The story begins in the revolutionary era at the turn of the twentieth century. In 1879 Crookes discovered the "cathode rays" using a vacuum tube. These were later shown to have a mass of only 1‰ of that of the hydrogen atom in the classical series of experiments by J. J. Thomson. This marked the discovery of the first sub-atomic particle: the electron. In 1895 W. C. Röntgen discovered that Crookes' tube also emits a second type of radiation, which he named X-rays. About ten years later, C. G. Barkla showed that X-rays are polarized, and thus associated them with electromagnetic radiation. In 1896 A. H. Becquerel discovered that his photographic plates darken when exposed to uranium, thus discovering natural radiation. In 1898 E. Rutherford used the penetrative power of radiation to establish that there are at least two separate components: α- and β-rays. It takes about ten years before it is shown that α-rays consist of what we today know as the nucleus of a helium atom. On the other hand is was quickly shown that β-rays consist of electrons. In 1900 P. Villard added γ-rays to the list, as the most penetrating radiation known.

Cosmic rays enter the stage at about 1900 when it was observed that electroscopes[†] dis-

---

[*]The interested reader is referred to the following excellent books: "High Energy Astrophysics" (Longair 1992). "Cosmic Rays and Particle Physics" (Gaisser 1990) and "Gauge Theories in Particle Physics" (Aitchison & Hey 1989).

[†]The electroscope plays an important role at the time. It is a closed vessel in which two gold leaves, connected at one end and left loose at the other, are located in the middle. The leaves are electrically insulated from the vessel. When they are electrically charged they repel each other, and move apart. When ionizing

charge even when kept away from known sources. On the bases of these measurements, C. T. R. Wilson in 1900 proclaimed the existence of an extraterrestrial radiation. Observations made to confirm this hypothesis proved inconclusive, and the hypothesis was dropped for the following ten years. It was later shown by Rutherford that many of the initial results were in fact caused by naturally occurring radiation either in the form of contamination of the vessel, or the radiation from the rock of railway tunnels. In 1910 the Dutch high-school teacher T. Wulf used his sophisticated electroscope to measure the ionization at the foot and at the top of the Eiffel Tower. To his big surprise, the ionization was only reduced by a factor of two at the top, whereas it was known that the intensity of γ-rays (the most penetrating radiation known at the time) would drop by a factor two through about 80 m of air. At the top of the Eiffel Tower he thus expected a negligible intensity of radiation originating from the Earth surface, 330 m below. In 1910 and 1911 A. Gockel made balloon flights up to a height of about 4 km, he found that the ionization did not decrease with height. His results were, however, uncertain due to different experimental problems.

During 1912 and 1913, in what is normally considered as the discovery of cosmic rays, V. F. Hess and then W. Kolhörster made manned balloon flights to measure the ionization at increasing altitudes. By 1914, these flights had taken Kolhörster to the impressive altitude of 9 km. It was however Hess who observed the first definite increase of ionization at higher altitudes. He was quick to conclude that the source of the radiation was extraterrestrial:

> *The result of the present observations seems to be most readily explained by the assumption that a radiation of very high penetrating power enters our atmosphere from above, and still produces in the lower layers a part of the ionisation observed in closed vessels.* (Hess 1912)

It was R. A. Millikan who in 1925 introduced the term "cosmic rays", which is still used today. In 1929 D. V. Skobeltsyn recorded the first cloud chamber pictures of cosmic rays. He observed charged tracks which hardly bend in a magnetic field, and identified them as being high energy Compton electrons produced by high energy gamma rays. He believed the cosmic rays to be "ultra gamma radiation", thus the term cosmic rays. Today, we consider this as a misidentification, but one must keep in mind that this experiment was performed seven years before the discovery of the muon. A year later, however, Millikan and C. D. Anderson discovered the positive electrically charged electron-like particle, known as positron. The experiment was a refined version of Skobeltsyn's. The discovery of the positron coincided with P. A. M. Dirac's formulation of relativistic quantum mechanics, in which he also obtained "negative energy" solutions, known as anti-particles. It was concluded that the positron is the anti-particle of the electron.

In addition to positively charged tracks, Anderson also observed the same effect as Skobeltsyn, i.e. tracks which bend much less than electrons or positrons. In 1936 Anderson and S. Neddermeyer are sufficiently confident of the results to announce the discovery of "mesotrons" with a mass about 200 times that of the electron. Today we call these particles

---

particles move through the vessel they ionize the gas, and cause a small leakage current, which discharges the leaves. This causes them to move back towards the rest position. The speed with which this happens is a measure of the amount of ionizing particles.

Generation	1	2	3	Electric charge [e]
Quarks	u (up)	c (charm)	t (top)	+2/3
	d (down)	s (strange)	b (bottom)	-1/3
Leptons	e	μ	τ	-1
	ν_e	ν_μ	ν_τ	0

Table 1.1: *Overview of the three so-called generations of fermions along with their electric charge. It is worth noting that all naturally occurring material on Earth is made out of particles from the first generation.*

muons (μ). This discovery also coincided with a theoretical landmark. Namely H. Yukawa's theory of the strong force*, i.e. the force which holds the protons and neutrons together to form a nucleus. In his theory Yukawa introduces a particle to mediate the force. This particle should have a mass of about 250 times the mass of the electron. The mass of Yukawa's mediator and the mesotron was similar, and it was, therefore, natural to suppose that they were one and the same particle. However, the observed probability of mesotron nucleus interaction are much lower than expected from Yukawa's theory. In fact Yukawa's mediator(s) are the pions ($\pi^\pm$, π^0) and not the muon, but the pion was only discovered in 1947.

After the Second World War cosmic rays continued to play an essential role in the shaping of particle physics. In 1947 G. Rochester and C. Butler observed the first "V" tracks in their cloud chamber. They correctly suggested these events to be caused by the spontaneous decay of an unknown particle. These particles became known as strange† particles. Most of these new particles had a mass of about half that of the proton, and are known today as kaons ($K^\pm$, K^0). One particle, however, had a mass larger than that of the proton, the lambda particle (Λ). Around the same time a new experimental technique was being developed by C. F. Powell, namely photographic emulsion chambers. These photos, when developed, provide a three-dimensional image with unprecedented accuracy of charged particles passing through the emulsion. The pion was the first particle to be discovered with this new technique. Refined versions of emulsion chambers still today produce the most accurate tracking available.

Two further particles were discovered in cosmic rays, namely the Ξ^- and Σ^+ in 1952 and 1953, respectively. By 1953 the accelerator technology was so advanced, that cosmic rays no longer were at the forefront of particle physics. Accelerators have the obvious advantage that one knows the energy of the primary particle(s), and they can be directed into the heart of the detectors. 1953 also marks the year of the discovery of the neutrino (Reines & Cowan 1953). Both during the birth of neutrino physics in the 1980s and the discovery of neutrino oscillations (Fukuda *et al.* 1998) cosmic rays again played an prominent role.

For completeness, it should be noted that many more particles were discovered with the first generation of accelerator experiments before particle physics in the mid 1960s got a firm

---

*Yukawa's theory of the strong force is a good phenomenological model of the force between protons and neutrons. Today however, we know that both protons and neutrons consist of three quarks. We consider the force between quarks as fundamental and it is this force we mean when today we speak of the strong force. The modern theory of the strong force is known as quantum chromodynamics (QCD), but it was formulated only in the late 1960s.

†Later the name strange was given to the quark, which in fact had been discovered here.

theoretical ground to stand on. The quark model reduced the large number of baryons and mesons to only 6 quarks[*]. With the current knowledge, all matter can be decomposed into the quarks and leptons shown in table 1.1. The interactions between the particles were soon formulated within the framework of gauge theory. Many people contributed to the creation of what is now know as "The Standard Model" which, in spite of vigorous experimental tests, still stands as the theory of the propagation and interaction of the fundamental particles. It is important to notice that the gravitational force is not part of the standard model. Within the framework of A. Einstein's general theory of relativity, gravitation is considered as a deformation of space-time.

Recently the last elementary fermion, the tau neutrino ν_τ, may have been directly observed (DONUT Collaboration 2001). Thus the so-called Higgs boson, which is held responsible for endowing mass to the particles, is the last ingredient of the Standard Model still undiscovered.

1.2   Astroparticle physics

Astroparticle physics addresses the study of high energy particles originating from outer space. A broad range of areas are involved in these types of studies:

Cosmology: e.g. the inferred non-baryonic dark matter component, dark energy, and the observed baryon asymmetry. *Dark matter* is a term used to describe the missing mass, the discrepancy between the inferred gravitating mass density of the universe (about 30% of the critical density[†]) and the observed luminous matter density (only about 3% of the critical density). It thus represents the matter which has not been seen. *Non-baryonic dark matter* has to be the dominant component of the dark matter, and it may consist of massive neutrinos and non-standard model particles surviving since the Big Bang. Einstein's cosmological constant is a possible explanation of the *dark energy* (about 70% of the critical density).

Baryon asymmetry is the observation that the material around us is made of matter rather than anti-matter, whereas matter and anti-matter were created in equal amounts according to the standard Big Bang model.

Astrophysics: tests of solar and star models, sources and transport of cosmic rays, point-like and diffuse sources of photons. The measurement of low-energy solar neutrinos will further constrain the *models of the sun*. Almost a century after the discovery of *cosmic rays*, the issue of their origin is still not fully settled. The status of cosmic ray physics is discussed further below.

High-energy photons have been the source of much excitement over the last years, most prominently so the discovery of gamma ray bursts.

---

[*]The first quark (bottom) of the third generation was in fact only discovered in 1970s and the second (top) in the 1990s.

[†]The critical density defined as $\rho_{crit} = \frac{3H_0^2}{8\pi G}$ is the density resulting in a flat universe. H_0 is the Hubble constant at present and G is Newton's gravitational constant. Recent measurement (BOOMERanG Collaboration 2002) indicate that the universe is flat.

Particle physics: neutrino oscillations, Big Bang relics, non-standard components of the Universe, deviations from microscopic symmetries etc. The discovery of *neutrino oscillations* is discussed further below. The importance of *Big Bang relics* and *non-standard components of the Universe* is not limited to cosmology, but would also show the way to physics beyond the standard model.

From the experimental front a broad range of techniques are used in order measure these particles and determine their origin. The experiments may be grouped in three classes:

Experiments aiming to measure the incoming primary: These are exclusively balloon or satellite born detectors aiming at measuring the primary photons and/or hadrons. Two good examples of this type of detectors are AMS (AMS Collaboration 1994) and BESS (BESS Collaboration 2000b).

Experiments measuring the air shower: These are typically mountain top, ground level or underground detectors measuring parts of the air shower caused by the interaction of the primary particle with the Earth's atmosphere. Most cosmic ray experiments fall in this category, as does L3+Cosmics.

Experiments measuring neutrino interactions: These are a relatively new type of experiments. They are huge[*] underwater or under-ice detectors aiming at measuring the interaction of neutrinos inside the volume. The existing experiments (e.g. Super-Kamiokande (Fukuda *et al.* 1998)) are measuring the atmospheric or solar neutrinos, but the future experiments (Halzen *et al.* 1999) aim at measuring high energy neutrinos from astronomical sources. This type of experiment thus contains features of both of the above mentioned types.

In the following, the discussion is limited to the area of classical cosmic ray physics, i.e. the hadronic component of cosmic rays. The electromagnetic (electron and photon) components of cosmic rays are negligible above 1 GeV as far as flux is concerned. First, a short discussion of the primary spectrum and its composition are presented. Then the properties of the muon spectrum are discussed.

Figure 1.1 shows the all particle (hadron) cosmic ray spectrum. It is essentially a featureless power law spectrum, but the values of the spectra index and the few features which are present hold clues as to the origin of the cosmic rays:

- The spectrum below 10 GeV is affected by solar modulation. The sun emits a supersonic plasma wind with an embedded magnetic field, which deflects the low energy cosmic rays from outer space. The solar wind intensity varies with the 11 year solar cycle, and the observed flux is found to be anti-correlated with the solar activity.

- The so-called "Knee" in the cosmic ray spectrum is located between 10^{15} and 10^{16} eV, it is characterized by a steepening of the spectrum from $E^{-2.7}$ to about $E^{-3.2}$. The cosmic rays below the knee are believed to be accelerated by diffusive shock acceleration[†],

---

[*]To enable neutrino telescopes to make astronomical observations from active galactic nuclei they must have an active volume of about 1 km^3. This is due to the low cross section for neutrino interactions with matter.

[†]For a detailed discussion of the acceleration mechanisms see (Gaisser 1990).
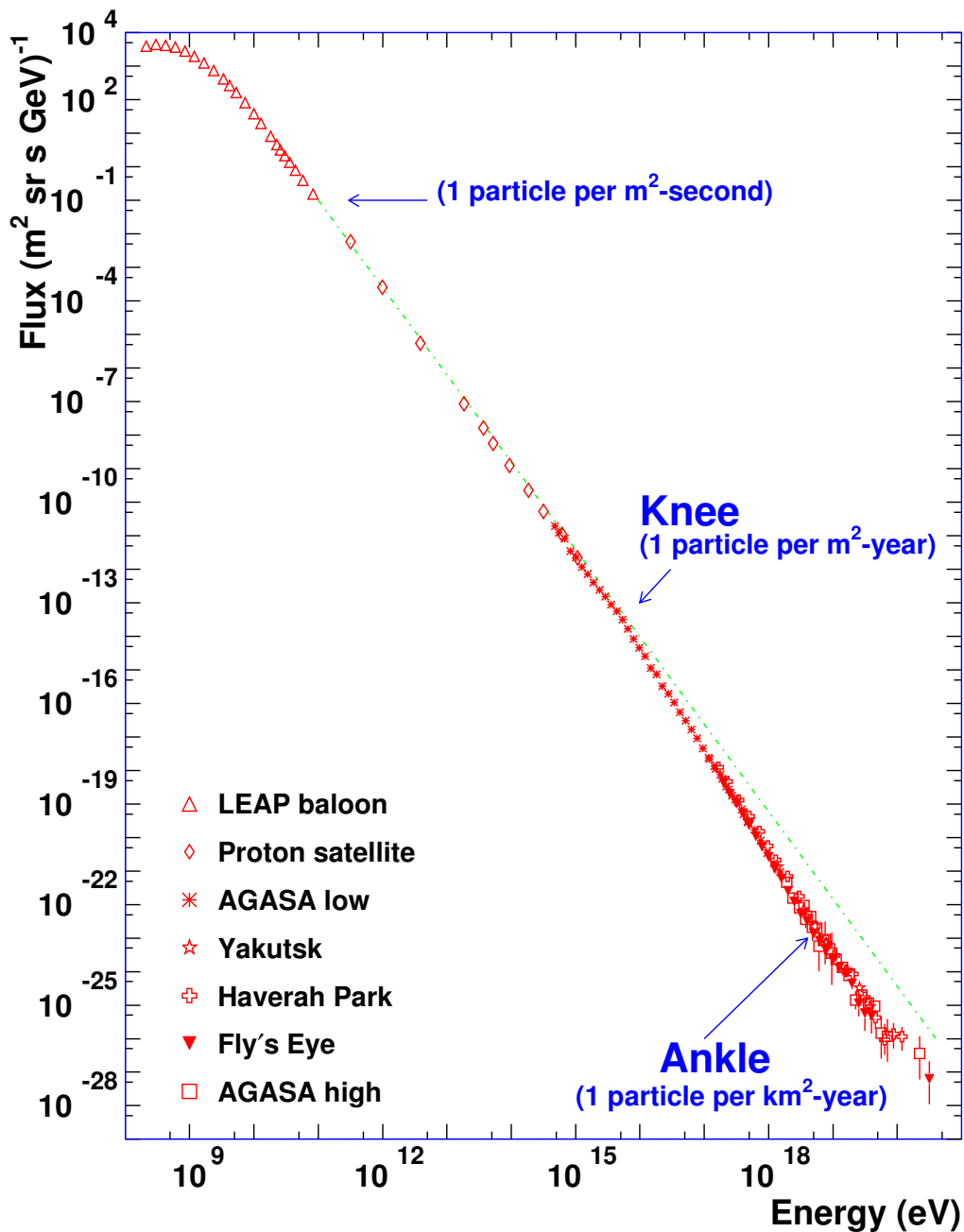
Figure 1.1: *The all particle spectrum of cosmic rays. To fully appreciate this spectrum it is important to notice that it spans over more than 12 orders of magnitude in energy and over more than 30 orders of magnitude in flux. From the large number of data sets a small group has been selected (Sea et al. 1991, Grigorov et al. 1971, AGASA Collaboration 1992, Afanasiev et al. 1996, Lawrence et al. 1991, Flye's Eye Collaboration 1994). The plot is a modified version of the one available at:* `http://astroparticle.uchicago.edu/cosmic_ray_spectrum_picture.htm`*.*

with supernova explosions within our galaxy as the most likely candidates. However, no source has convincingly been identified so far, but this situation may be changing (Butt, Torres, Combi, Dame & Romero 2001).

The origin of the kink in the spectrum is not fully understood, several scenarios have been proposed:

- The acceleration in supernova remnants reaches its rigidity cut-off.

- A change in the propagation of the galactic cosmic rays, perhaps corresponding to a more rapid escape from the galaxy (Ptuskin, Völk, Zirakashvili & Breitschwerdt 1997).

- Only one or maybe a few "nearby" sources are responsible for this part of the spectrum (Erlykin, Lipski & Wolfendale 1998).

The two first scenarios involve a rigidity cut-off: $p_{max}/Z = eVBL$, which increases for particles with a larger electric charge (Z). The third scenario predicts the onset of a new proton source in this energy range. This has inspired a large set of measurements of the chemical composition in this energy range. However, the results presented so far are contradictory (Swordy *et al.* 2002).

- The ankle at 10^{18} eV is characterized by a hardening of the spectrum. Around this energy the confinement of the galactic cosmic rays is expected to end. The gyroradius in the 3 µGauss galactic field becomes comparable to the size of the galaxy. The hardening of the spectrum is thus expected to be due to extragalactic sources.

- The third structure, the so-called GZK[*] cut-off (Greisen 1966, Zatsepin & Kuzmin 1966), is one which should be observed, but is not! Very soon after the discovery of the 2.7 K cosmic black-body radiation it was noticed that these photons impose a problem for very high energy protons. At a proton energy of about $6 \cdot 10^{19}$ eV the reaction with a microwave photon passes the threshold for pion creation:

$$p + \gamma_{2.7 \text{ K}} \rightarrow p + \pi^0 \qquad (1.1)$$
$$\rightarrow n + \pi^+$$

Just above the threshold the cross section increases further due to the Δ resonance. Below the GZK cut-off the attenuation length exceeds 1000 Mpc, while above it reduces to about 20 Mpc. For heavy nuclei, photodisintegration plays a similar role, but at slightly higher energies (Nagano & Watson 2000).

By now AGASA has observed a significant number of events above the GZK cut-off, which has resulted in a large number of papers proposing their origin. The proposals vary from sources "close by" such as nearby active galactic nuclei, nearby gamma ray bursts, jets of large radio galaxies, and intergalactic shocks to exotic production

---

[*]For a thorough discussion of the highest energy cosmic ray events and their implications see (Nagano & Watson 2000).

methods such as the decay of topological defects. However, it is worth noticing that the recent measurements from HiRes (Bergman 2002), in contrast to the AGASA results, confirm the GZK cut-off.

The low energy part ($E < 10^{11}$ eV/nucleon) of the spectrum has recently been measured with an overall uncertainty of about 5% by both AMS and BESS (AMS Collaboration 2000a, AMS Collaboration 2000b, BESS Collaboration 2000a). It is important to note that the proton spectrum from these two experiments actually agree within the quoted uncertainty. This is also the case for the helium fluxes, where the disagreement of about 10%, is covered by the larger uncertainties on the helium fluxes. Both experiments are limited by exposure time rather than resolution, and both are planning upgrades to enable them to extend their measurements. Direct measurements are extended up to about 10^{15} eV/nucleon with balloon born experiments which use either tracking calorimeters (Ivanenko *et al.* 1993, Ryan, Ormes & Balasubrahmanyan 1972) or emulsion chambers (JACEE Collaboration 1998, RUNJOB Collaboration 2001). The measurements between 10^{14} eV/nucleon and 10^{15} eV/nucleon have large uncertainties, dominated by low statistics. The low statistics is caused by the modest size of these experiments along with the limited exposure time. At the low end, between 10^{11} eV/nucleon and 10^{12} eV/nucleon the only measurement (Ryan *et al.* 1972) fails to overlap with the precise measurements below 10^{11} eV/nucleon. Recently, it has been suggested (Gaisser, Honda, Lipari & Stanev 2001) that the normalization of this measurement should be lowered by 25%.

Above about 10^{15} eV/nucleon the spectrum is measured indirectly by air shower detectors. Figure 1.2 schematically shows the different detector types used in measuring cosmic ray induced air showers. Below the different techniques are briefly described:

Čerenkov telescopes: Many of the particles in an air shower travel faster than the speed of light in the atmosphere, and are thus sources of Čerenkov radiation. The half opening angle of the Čerenkov light is given by $\cos\theta_c = 1/n\beta$ for a medium with an index of refraction n. The emitted light is well collimated, since this angle in air has a maximum of about $1.3°$, which is small compared to the dispersion of electrons around the shower axis. Most of the electrons in an atmospheric shower emit Čerenkov radiation and since the photons are not absorbed in the atmosphere, Čerenkov light constitutes an almost calorimetric measure of the shower. This technique also allows for the determination of the direction of the primary particle and development[*] of the shower, thus making it a very powerful tool. The basic Čerenkov telescope includes parabolic reflectors for the light collection with phototubes in the focal plane and fast electronics for resolving individual photoelectrons. Its ability to distinguish primary photons from protons along with its excellent angular resolution has made this technique very favorable for TeV γ-ray astronomy. The small opening angle on the other hand makes this technique less favorable for very high energy cosmic rays. Furthermore, the telescopes can only be operated at night. The HEGRA Imaging Atmospheric Čerenkov Telescope (HEGRA Collaboration 1999) is a good example of this technique.

---

[*]The shower profile is very sensitive to the type of primary. Photon induced showers are typically smaller and more elliptical than their hadronic counterparts.
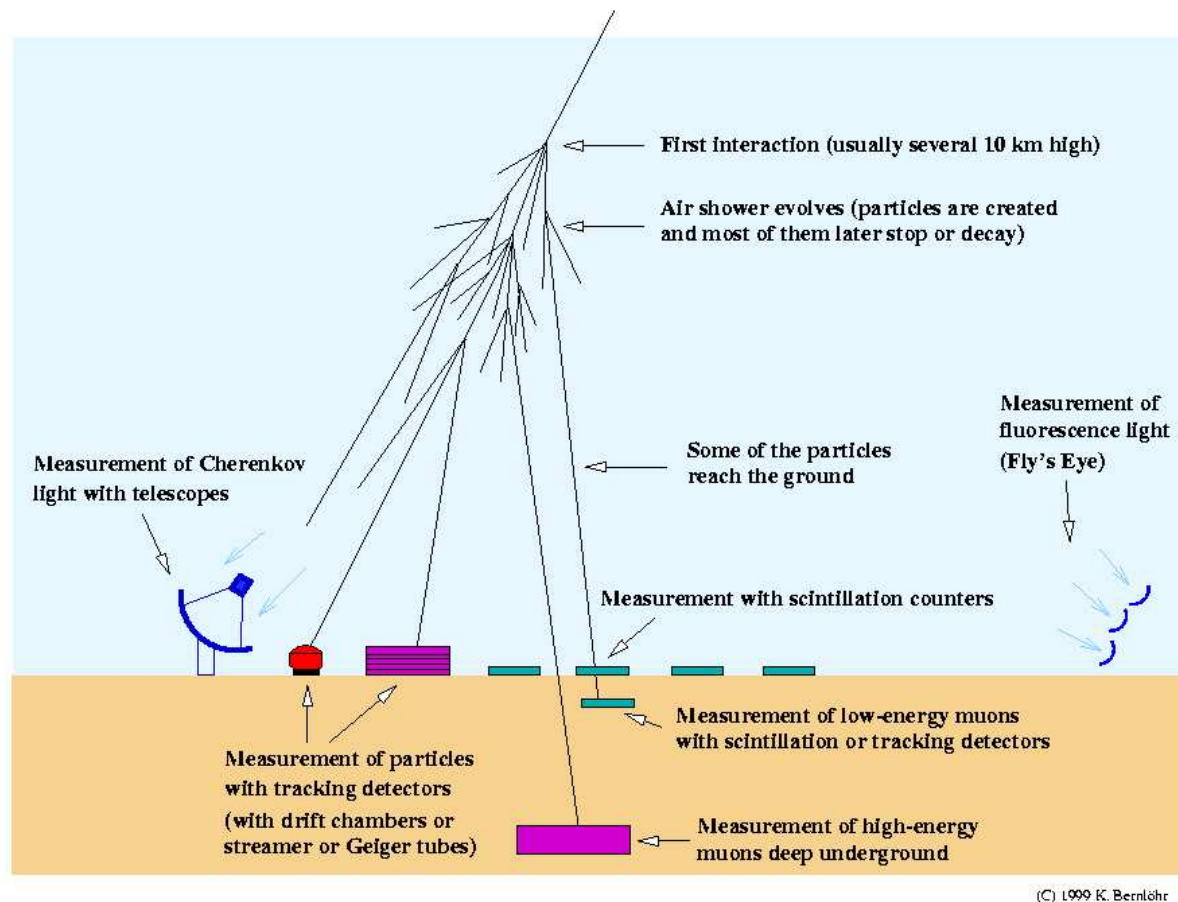
Measuring cosmic-ray and gamma-ray air showers

First interaction (usually several 10 km high)

Air shower evolves (particles are created and most of them later stop or decay)

Measurement of fluorescence light (Fly's Eye)

Measurement of Cherenkov light with telescopes

Some of the particles reach the ground

Measurement with scintillation counters

Measurement of low-energy muons with scintillation or tracking detectors

Measurement of particles with tracking detectors (with drift chambers or streamer or Geiger tubes)

Measurement of high-energy muons deep underground

(C) 1999 K. Bernlöhr

Figure 1.2: *Schematic view of an air-shower, showing the different types of detectors used to measure atmospheric showers. Notice that the drawing is not to scale.*

Fluorescence telescopes: An atmospheric shower loses much of its energy in ionizing and exciting air molecules. Part of this energy is then emitted by the molecules in form of fluorescence light. Even though the air is a very inefficient scintillator, the signal due to fluorescence light can be detected during the night from showers generated by very high energy primaries. Fluorescence telescopes are also constructed of focusing mirrors and photomultipliers (PMTs). Both the Fly's Eye (Flye's Eye Collaboration 1985) detector and its successor HiRes (Abu-Zayyad *et al.* 2000) are good examples of a fluorescence telescope.

The main difference between fluorescence and Čerenkov light is the angular distribution. The Čerenkov light is emitted in a narrow cone along the main axis of the shower, while the fluorescence photons are emitted isotropically. In the Fly's Eye experiment the first autonomous detector obtained an almost 2π coverage of the sky by combining 67 detectors each with 12-16 PMTs at the focal plane of each mirror. For both fluorescence and Čerenkov telescopes the resolution is improved by deploying more than one

telescope. In contrast to the Čerenkov telescopes, the fluorescence telescopes are only really applicable for showers caused by primaries with an energy above 10^{17} eV. This is caused by the poor scintillation efficiency of air.

Recently it has been proposed (Streitmatter 1998, Catalano 2001) to measure the fluorescence light produced by the air from a satellite. If realized, these experiments will achieve a much larger acceptance than their ground based counter parts.

Extensive Air Shower arrays: When an air shower reaches the surface its geometry is a particle disk (mainly electrons and photons), one or two meters thick, with a radius of hundreds of meters. Even for showers generated by hadrons the electromagnetic component carries a large part of the primary energy. This is mainly due to π^0 decay into photons. A basic air shower array consists of a number of small detectors (1-10 m^2), distributed over a large area ($\approx 10^4 - 10^6$ m^2). Typically the individual detectors are scintillators with photomultipliers. The direction of the shower can be estimated by comparing the arrival times of the shower at the different detectors. The total number of particles in the shower is obtained by fitting the sampled particle densities to a lateral distribution function*. Many modern arrays also include muon detectors, which are often simply shielded scintillator towers. The largest array constructed so far, covering an area of 100 km^2, is the Akeno Giant Air Shower Array (AGASA Collaboration 1992) in Japan.

Underground muon-detectors: Muons are created in the decay of the charged pions and kaons, of which both are very common in hadronic showers. Muons are also created in the decay of hadrons containing heavier quarks, e.g. charm, which are commonly known as "prompt" muons. Due to the large mass and very short live-time of these hadrons, the spectrum of these muons is harder than that from the conventional decay of pions and kaons. For the momentum range relevant for this study, the prompt muons play no significant role (Costa 2001).

The muon detectors vary significantly in their design, since they (almost without exception) are designed for different purposes. The MACRO detector (MACRO Collaboration 1993) which was located in the Gran Sasso tunnel in Italy is a good example of such a detector, its primary goal was the search for monopoles. L3+Cosmics also falls in this category of detectors. It will be described extensively in chapter 2. The interest in the measurement of muons underground will be discussed in section 1.3, but it is important to notice that these measurements do not provide any event by event information about the primary.

The large modern experiments (e.g. Kaskade, AGASA and Auger) combine several of the above techniques in order to obtain a larger number of observables per shower. In the winter shutdown between 1999 and 2000 a small air shower array was added to L3+Cosmics (Wilkens 2003) to accompany the measurement of the muon component.

---

*The lateral distribution of electrons in a shower was first calculated numerically by Nishimura and Kramata. Some years later, Greisen represented their results by a formula (Greisen 1956) which now is known as the NKG formula. Variations of the original formula are still used today.

1.3 Features of the muon spectrum

Measurements of the cosmic ray induced muon spectrum have been performed since the earliest days of cosmic ray physics. The large penetrative power of muons along with their electric charge makes them relatively easy to detect. A large volume of data thus already exists, but mainly at energies below 100 GeV. It is common in a thesis like this to summarize the existing measurements, but the large number of measurements along with their varying quality make this a large-sized task. The reader is referred to two recent compilation of the existing data (Hebbeker & Timmermans 2002, Naumov 2001), here the compilation from Naumov is reproduced in figure 1.3 and figure 1.4. Notice that these plots also include the data sets which are disregarded by (Hebbeker & Timmermans 2002). Furthermore, (Hebbeker & Timmermans 2002) contains a fit of the available data for the vertical flux as well as an estimate of the uncertainty on the shape and the normalization. The uncertainty on the shape is less than 2% below 100 GeV, whereas it rises to 15% at 1 TeV. The quoted uncertainty on normalization is 7%. The uncertainty on the normalization is dominated by the fact that the normalization of the data sets fall in two incompatible categories: the measurement with solid iron magnets (high) and the measurements using the same superconducting magnet (low). Therefore, in this study the focus is on producing a precise measurement of the vertical flux for energies as high as possible, as well as extending the flux measurement to larger zenith angles.

The interest in the muon spectrum got a boost in the mid 1980s when IMB observed fewer neutrino interactions with stopping muons than expected (IMB Collaboration 1986). Other experiments confirmed the lack of muon neutrinos, but the uncertainty was large due to the uncertainty on the absolute flux of atmospheric neutrinos[*]. This became known as the *atmospheric neutrino anomaly*. The creation of muons and muon neutrinos are intimately related via the weak charge current interaction, they are created together in the decay of pions and kaons, and an additional muon neutrino is created in the decay of a muon. Below the decay chain of a π^+ is shown:

$$\pi^+ \rightarrow \mu^+ + \nu_\mu$$
$$\mu^+ \rightarrow e^+ + \nu_e + \overline{\nu}_\mu \tag{1.2}$$

This means that a precise measurement of the muon spectrum indirectly constrains the flux of muon neutrinos. The atmospheric neutrino anomaly has played an important role in establishing the existence of neutrino oscillations. Neutrino oscillations are caused by a difference in the mass- and weak eigenstates, similar to the one observed in the quark sector. For the quarks the oscillation between K_L^0 and K_S^0 is well-known. In 1964 it lead to the discovery of CP violation (Cronin 1981). If neutrino oscillations occur the neutrinos must have a mass, though not necessarily large. In the classical formulation of the standard model the neutrinos are assumed to have zero mass. In the case of mixing between two flavors of neutrinos[†] the

---

[*]Part of this uncertainty has been removed (Gaisser 2002) by the precise measurements of the primary proton and helium flux by AMS and BESS mentioned above.

[†]The current data strongly suggest an oscillation between ν_μ and ν_τ.

Figure 1.3: *Near-vertical differential muon spectrum at ground level. Notice that the error band from (Hebbeker & Timmermans 2002) includes both the uncertainty of the shape and the normalization. The theoretical prediction from the CORT code (Fiorentini et al. 2001) is also indicated. From (Naumov 2001).*
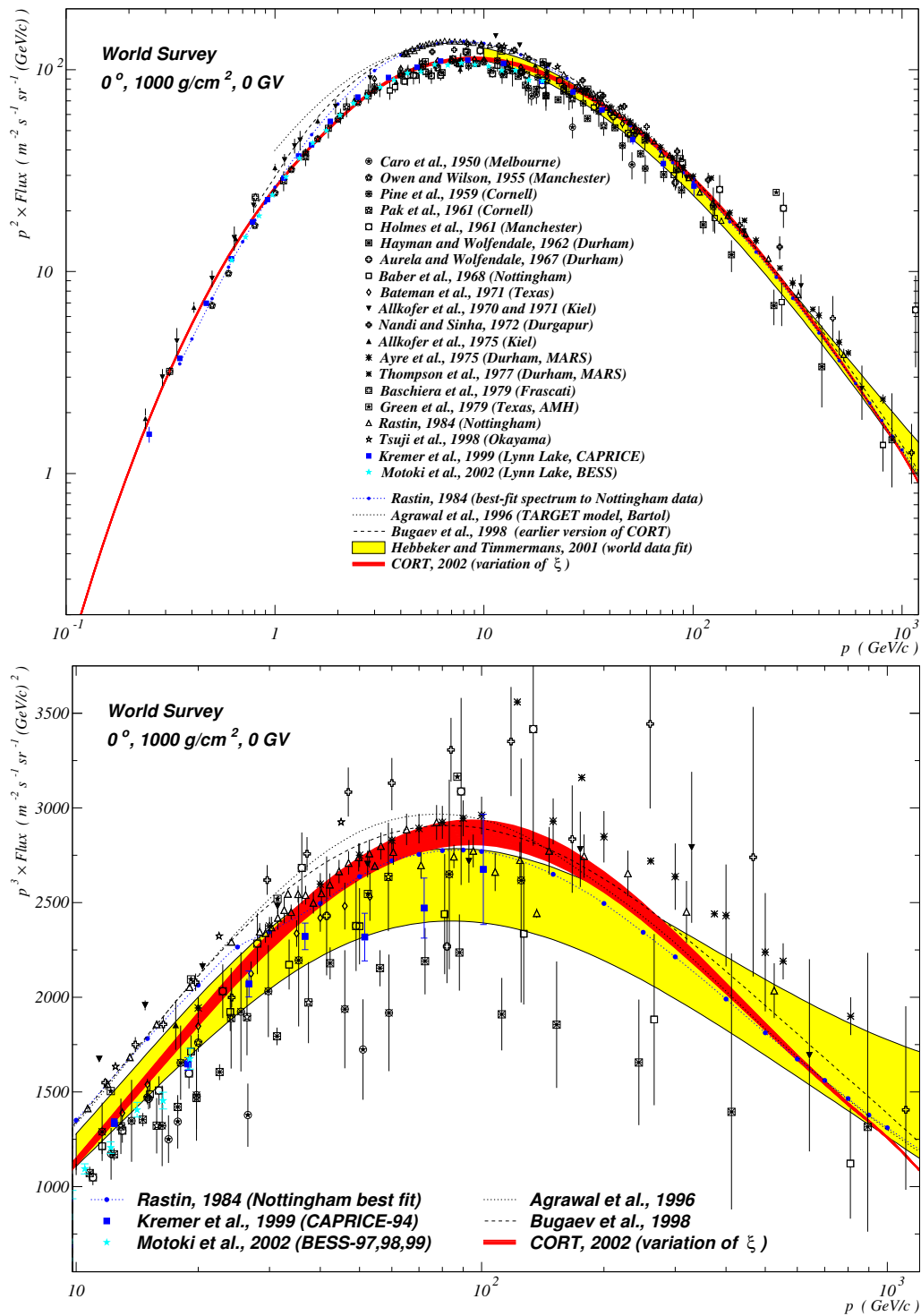
Figure 1.4: *Near-vertical muon charge ratio at ground level. Notice that the error band from (Hebbeker & Timmermans 2002) includes both the uncertainty of the shape and the normalization. The theoretical prediction from the CORT code (Fiorentini et al. 2001) is also indicated. From (Naumov 2001).*
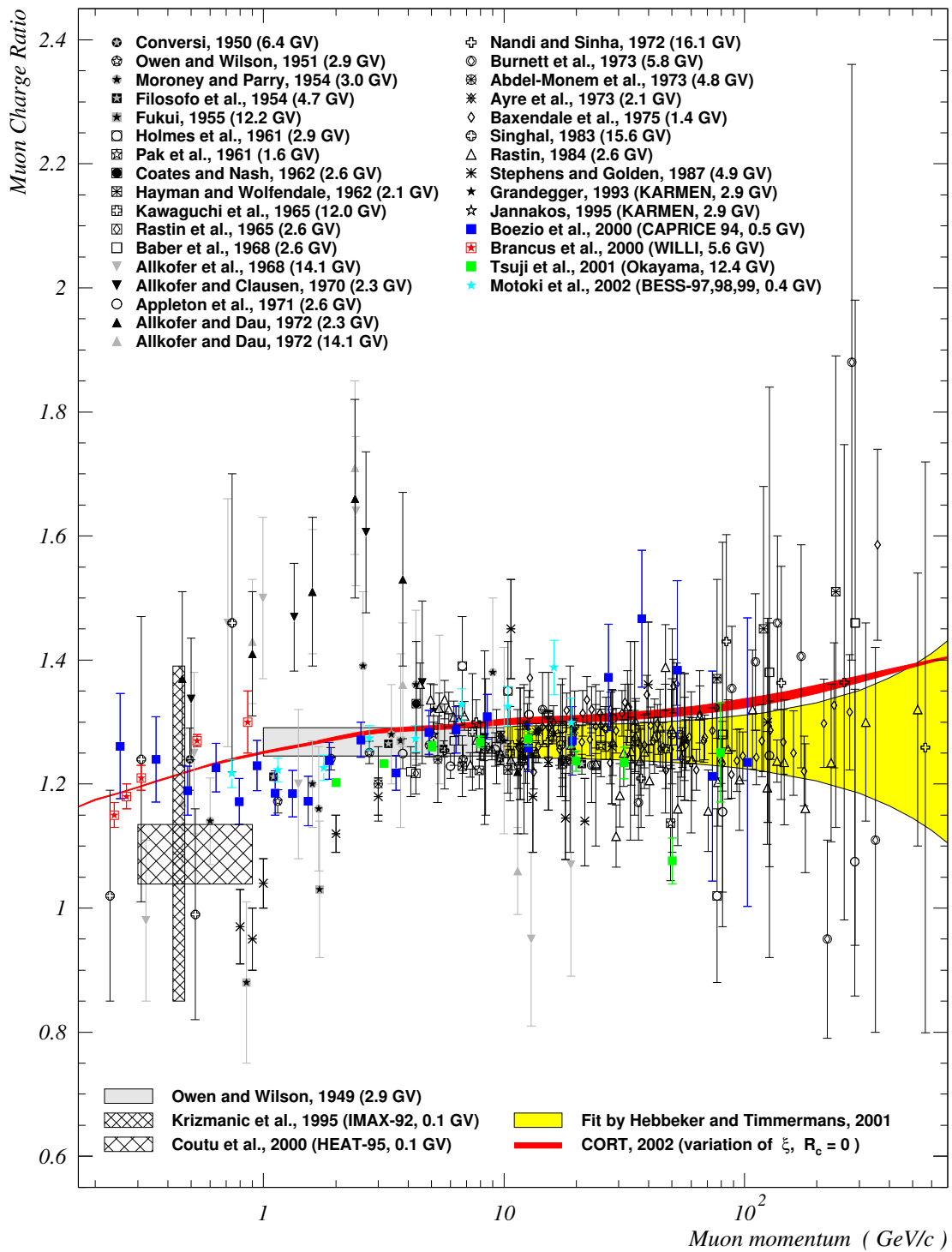
probability of observing a ν_μ, which also was created as a ν_μ of energy E, after it has traveled a distance L is given by (Gaisser & Honda 2002):

$$\mathcal{P}_{\nu_\mu \to \nu_\mu} = 1 - \sin^2(2\theta_m)\sin^2\left[1.27\,\delta\text{m}^2\frac{L\,[\text{km}]}{E\,[\text{GeV}]}\right] \tag{1.3}$$

where $\delta\text{m}^2 = \text{m}_\tau^2 - \text{m}_\mu^2$ is the difference of the squared masses of the two mass eigenstates and θ_m is the angle that characterizes the mixing between the two states. From equation (1.3) it is clear, that a way to avoid the problem of knowing the absolute initial flux is to measure the neutrinos at different distances from their creation point. This was realized by the Super-Kamiokande experiment in the measurement of the flux of low energy muon neutrinos interacting inside the detector as a function of the zenith angle (Fukuda *et al.* 1998). In practice this means that the flux of muon neutrinos is measured from just above the detector up to the ones created in the atmosphere on the other side of the Earth. The best fit to the Super-Kamiokande data results is: $\delta\text{m}^2 \approx 3.2 \cdot 10^{-3}$ eV with full mixing, i.e. $\theta_m \approx \pi/4$. For a thorough discussion of the experimental evidence on neutrino oscillations the reader is referred to (Jung, McGrew, Kajita & Mann 2001, Kajita & Totsuka 2001).

In light of the discovery of neutrino oscillations the interest in a precise measurement of the muon flux has shifted. One may summarize the situation as follows:

- The absolute neutrino flux is still important to check the consistency of the measurements and calculations used to infer the existence of neutrino oscillations.

- The absolute flux of atmospheric neutrinos is important for the upcoming neutrino telescope(s) in several ways; for calibrating the detector as well as checking its performance and more importantly the atmospheric neutrinos constitute the main background for the measurement of extraterrestrial neutrinos.

- Air showers cannot really be calculated ab initio. Measuring the zenith dependence, the muonic component at different atmospheric depth is sampled and give important constraints to model builders. The uncertainties due to the intra- and extrapolations of the hadronic cross sections used in the air shower models contribute largely to the uncertainty on the measurement of neutrino oscillation (Gaisser & Honda 2002). This is also the case for the air shower measurements in the region around the knee (Swordy *et al.* 2002).

Furthermore, as can be seen in figure 1.3 and figure 1.4 the available data above 100 GeV is scarce and has large uncertainties. In addition, the zenith angle dependence of the flux as well as the charge ratio effectively probes the air showers at different atmospheric depth.

1.4   The CORT code

This section provides a short description of the CORT (Cosmic-Origin Radiation Transport) code (Fiorentini *et al.* 2001). The results obtained in this thesis will be compared to the

predictions of this model (see chapter 6). Many models have been developed to simulate air shower cascades, most of these, including CORSIKA (Heck, Knapp, Capdevielle, Schatz & Thouw 1998), use the Monte Carlo method to evaluate the large complicated set of equations describing the production and transport of hadrons in an air shower. This means that they generate individual cascades in a stochastic fashion. When properly normalized, a combined sample of cascades provides a prediction of a large variety of observables. Furthermore, these simulated showers can be entered into detector simulation packages one by one, allowing low level comparisons with the data. This approach, however, has one big disadvantage, it requires a lot of computation power.

The CORT code on the other hand implements a numerical integration of the kinematic equations describing the propagation of nuclei, light mesons, muons and neutrinos. The model is 1-dimensional in the sense that all secondaries are assumed to follow the direction of the primary particle, but 3-dimensional in the sense that the direction of the primary is varied. The model is developed for the prediction of the flux of low and intermediate energy atmospheric neutrinos relevant for neutrino oscillations. The geomagnetic effects are implemented as maps of effective vertical cut-off rigidities, compatible with the recent AMS proton flux measurements (AMS Collaboration 2000c). At the energies relevant for this work the geomagnetic effects can be neglected. The atmosphere is modeled with an isothermal stratosphere and a constant[*] gradient of the temperature below the tropopause.

The components of the primary cosmic rays are separated in five groups: H, He, CNO, Ne-S, and Fe. The energy spectra of H and He measured by BESS98 and JACEE are fitted by a 7 parameter function[†]. The spectra of the three heavier groups are assumed to follow the spectrum of helium, but with a lower normalization. This means that all nuclei are assumed to have the same origin, e.g. galactic supernova remnants. Since the BESS measurement took place during a solar minimum and the solar modulation is neglected in the model, the flux from CORT must be seen as a maximum at low energies. This effect, however, can also be neglected for the energies relevant for this measurement.

CORT uses a semi-empirical model for inclusive nucleon and light meson production in collisions of nucleons with nuclei. The model is tuned to the available accelerator data. In contrast to most other models CORT does not use a simple superposition model. The superposition model treats the collision of two nuclei as A_{pro} (the number of nucleons in the projectile) independent collisions with the target nucleus, where each nucleon has an equal fraction of the total projectile energy. Unable to model a full nucleus-nucleus collision, the model used by CORT includes a term for the spectator part of projectile into the superposition model. It thus describes the part of the projectile which remains unchanged by the collisions. In (Naumov 2001) a large range of CORT predictions are compared to existing measurements.

---

[*]As a function of the atmospheric depth.
[†]For the technical details see (Fiorentini *et al.* 2001).

Chapter 2

The L_3+Cosmics experiment

The main aim of the L_3+Cosmics experiment is to measure the absolute flux of cosmic ray induced muons at sea level. This is done using the unique barrel muon chambers of L_3. To be able to take data independently of the "normal" running of the L_3 experiment, the development of a dedicated readout and DAQ system was required, as well as the installation of additional scintillators.

In this chapter the L_3+Cosmics experimental set-up is described. First a brief introduction to LEP and the L_3 detector is given. This is followed by a description of the main principles and features of the barrel muon chambers. Afterwards a description of the additionally installed hardware is given. At the end of the chapter an overview of the dedicated DAQ system is presented.

2.1   LEP and L_3

Situated underneath the French-Swiss border at CERN, Geneva, the Large Electron Positron collider (LEP) was the world's largest e^+e^- collider. In the first half of the 1990s it provided collisions with a center of mass energy around the Z-boson mass. In the second half of the 1990s the energy was gradually increased, first enabling the pair production of the $W^\pm$-bosons, later also double Z production and eventually ending up at the impressive center of mass energy of more than 208 GeV. The increased energy opened a new window for the search for the Higgs boson, as well as searches for physics beyond the standard model.

Four big particle detectors, symmetrically located around the 26.7 km long LEP ring, were used to detect a variety of particles produced in the e^+e^- collisions. Each of the four detectors, called ALEPH, DELPHI, L_3 and OPAL (ALEPH Collaboration 1990, DELPHI Collaboration 1991, L3 Collaboration 1990, OPAL Collaboration 1991), were designed emphasising rather different aspects of particle detection. The L_3 detector was designed to make a very precise measurement of leptons as well as photons, hoping that this would optimise the discovery potential. A striking feature, which all four detectors had in common, is that their sub-detectors were built around each other like the layers of a Russian doll. For L_3 (see figure 2.1) the layers from the inside out are organised as follows:
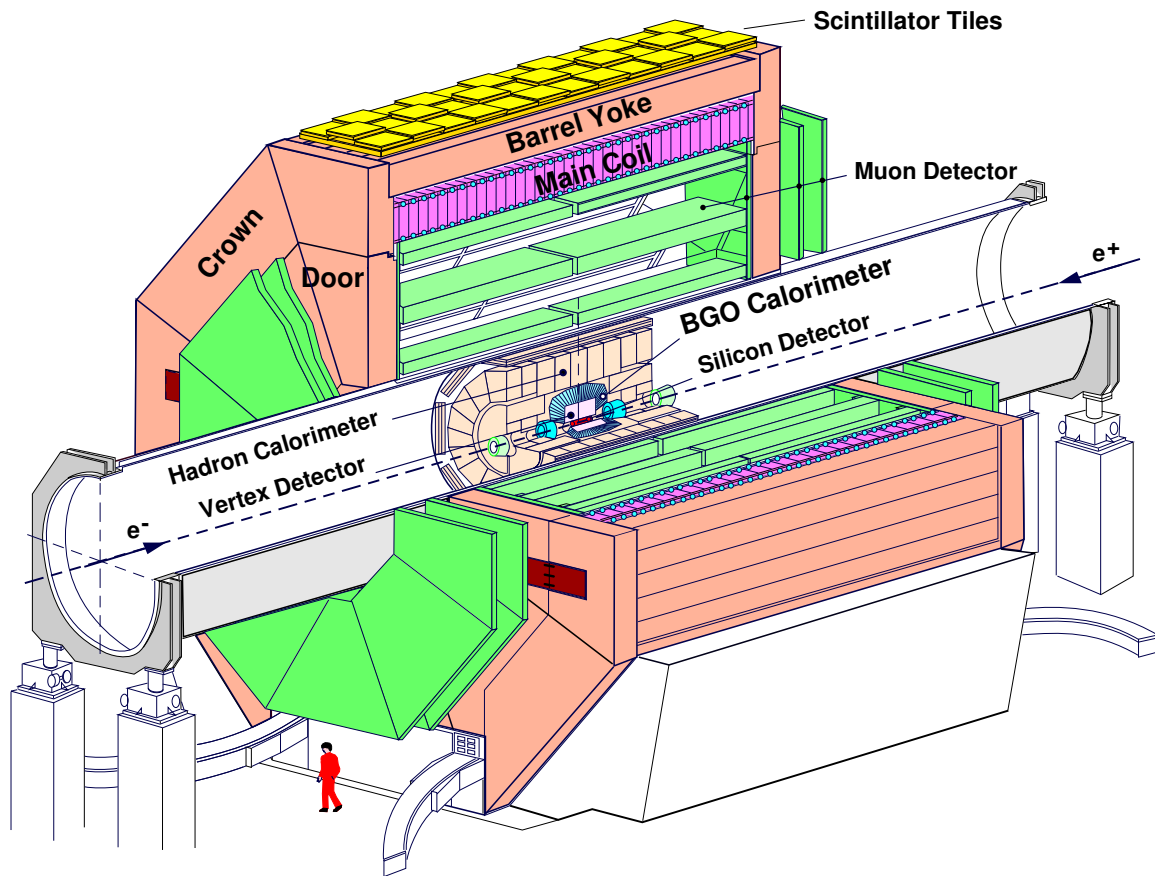
Figure 2.1: *Schematic view of the L$_3$ detector.*

SMD Silicon Microvertex Detector.

The vertex detector (L3 Collaboration 1994) consists of two concentric cylinders of silicon strip detectors, the inner one has a radius of 6.0 cm and the outer one has a radius of 7.7 cm. The SMD allows the measurement of two to three 3d points on the trajectory track, with a resolution of 7.5 μm in *xy* and 14 μm in *z* for non-inclined tracks (Adam *et al.* 1994), which makes it particularly useful for secondary vertex identification.

TEC Time Expansion Chamber.

The central tracking detector is made out of two concentric cylindrical segmented drift chambers (measuring in the *xy* plane) surrounded by two thin cylindrical proportional chambers measuring the *z* coordinate. The radius of the inner and outermost sense wire in TEC is 10.98 cm and 42.5 cm respectively.

ECAL Electromagnetic calorimeter.

This detector consists of 10734 Bismuth-Germanium-Oxide (BGO) crystals, organised with 7662 in the barrel part and 1536 in each of the two endcaps. The crystals are

about 24 cm long, shaped as truncated pyramids pointing to the vertex, with an offset of 10 mrad. An electron, positron or photon entering a crystal will induce an electro-magnetic shower (i.e. a cloud of secondary photons and $e^{\pm}$), which spreads out over several crystals. Essentially all of the energy deposited by a particle will be converted into low energy photons, which are detected by photodiodes located at the end of the crystals. Not only the deposited energy, but also the location is measured.

SCNT Scintillator counters.

A set of long scintillators (read out at both ends) with a good time resolution are arranged outside ECAL. They are used to distinguish $Z/\gamma \rightarrow \mu^{+}\mu^{-}$ events from cosmic muons, as well as to perform the so-called bunch tagging, identifying from which bunchlet[*] the event originated. Bunch tagging is of vital importance for interpreting the time measured in the drift chambers, thus the location of the tracks in the chambers.

ALR Active lead rings.

A small forward sampling[†] calorimeter made of layers of lead and scintillators. At a distance of 1.04 m from the vertex, it forms a small ring around the beam-pipe. In addition to closing part of the gap between ECAL and LUMI, it also protects TEC from beam induced background.

LUMI Luminosity monitor.

A ring of 304 BGO crystals is located close to the beam-pipe on both sides of the vertex. The distance to the vertex is 2.65 m. They are used to measure small angle Bhabha scattering events. From this well-known process the luminosity of the colliding beams can be calculated.

In 1993 silicon micro-strip detectors (Koffeman 1996) were installed in front of LUMI to improve the spatial resolution on the impact point.

VSAT Very small angle tagger.

In two-photon physics it is important to detect the scattered electron and positron. VSAT (van Rhee 2000) was installed in 1996 to serve this purpose. VSAT consists of 24 small BGO crystals on each side of the beam-pipe, which are located at a distance of 8.05 m from the vertex behind the LEP quadrupoles.

HCAL Hadronic calorimeter.

The hadronic calorimeter is a sampling calorimeter (like most other hadronic calorimeters), where plates of depleted uranium act as absorber. The active medium is composed of layers of proportional chambers. Uranium is chosen because of its large nuclear cross section ($\propto A^{2/3}$). Its natural radiation of α-particles provides an internal calibration source. The proportional chambers measure a signal proportional to the

---

[*]When LEP is operating in the so-called 4×2 mode, it means that there are 4 bunches of electrons and 4 bunches of positrons circulating in the ring (with a distance of 22.23 µs). Each of them contains 2 separate bunchlets of particles separated by 320 ns.

[†]In contrast to ECAL which is a homogeneous calorimeter, since its absorber material is also the active/scintillating medium.

number of charged particles in the hadronic shower, which in turn is proportional to the total energy of the shower.

HCAL also serves as a filter, which prevents other particles than muons and neutrinos (which escape detection altogether) from reaching the muon chambers. As the LEP energy increased, the energy and thereby the depth of the hadronic showers of, for instance, $Z/\gamma \to q\bar{q}$ events increased, whereby the probability of a shower not being contained in HCAL became non-negligible.

MUFI Muon filter.
> The muon filter is located between the barrel part of HCAL and the support tube. It increases the absorption power for pions by about one absorption length. The muon filter is also a sampling calorimeter with proportional chambers, but the absorber is brass and not uranium.

MUCH Muon Chambers.
> The outermost detector, intended to measure the track of through-going muons, is by far the largest of the L₃ sub-detectors. It is the only sub-detector outside the stainless steel support tube. The muon detector is divided into two parts:

> **Barrel:** The original L₃ muon spectrometer (Peng 1988, L3 Collaboration 1990, Fabre 1992) is a large and modular structure consisting of two octagonally shaped rings each with eight "octants" (see figure 2.2). The entire spectrometer is located in the 1000 m³ magnetic volume created by the 7800 ton octagonally shaped solenoid. The 168 turns of the water cooled aluminum coil carry a current of 30338 A. This results in a magnetic field of 0.51 T.
>> The barrel detector was designed to measure the muon momentum with an accuracy of about 2.0% at 45 GeV. In practice a resolution of 2.5% was achieved (L3 Collaboration 1993). In section 2.2 this sub-detector will be described in greater detail.

> **Forward-Backward:** In 1995 the angular acceptance (L3 F/B Muon Group 1996) of the L₃ muon spectrometer was increased by the addition of muon chambers on both sides of the doors of the L₃ magnet (See figure 2.1). Bending power in the forward direction was achieved by introducing a 1.24 T toroidal magnetic field in the doors. This was instrumented as 36 turns of a water cooled aluminum coil with a current of 6300 A.

For this study, only the barrel muon chambers are used, the other detectors only represent dead material.

L₃ is located below 30 m of molasse, its the chemical composition was thoroughly studied before the construction of the LEP tunnel. This knowledge is important in calculating the energy loss of muons between the surface and the detector. This location has an advantage over other cosmic ray experiments like MACRO in that the surface above the experiment is flat. The shallow depth results in a muon momentum threshold of about 20 GeV. The molasse is thick enough to absorb the hadronic and electro-magnetic component of the air showers.
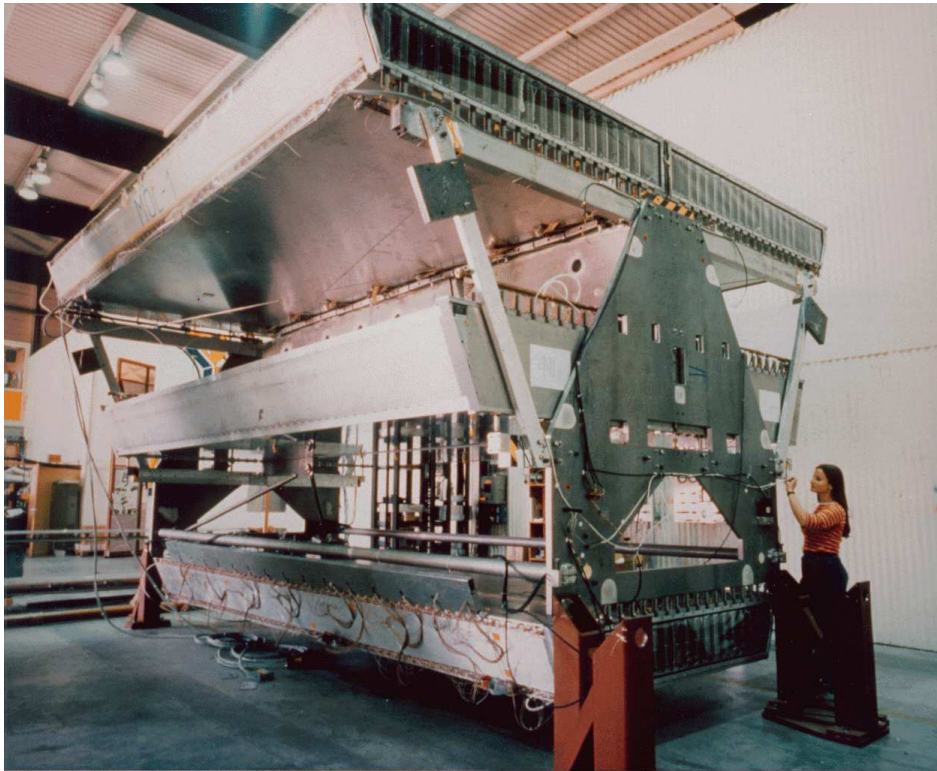
Figure 2.2: *A muon chamber octant, before installation. The octant is shown from the side which eventually ends up in the middle of the detector. The signal cables of the P-chambers are not yet installed. The large feet located in all four lower corners are not part of the octant, but they mimic the Ferris wheel. A Ferris wheel is the mechanical structure where 8 octants are attached to constitute a ring.*

2.2 The L$_3$ muon chambers

The 16 octants of the L$_3$ barrel muon spectrometer are fixed eight by eight on two torque tubes creating two so-called Ferris wheels, which can slide along the axis of the support tube on dedicated rails. Each octant consists of five precision chambers (P chambers) organised in three layers. There are two chambers in the outer layer (`MO`), two in the middle layer (`MM`) and one in the inner layer (`MI`). These P-chambers measure the projection of the muon trajectory onto the bending plane (*xy*). The projection along the direction of the magnetic field (*z*) is measured by the so-called Z chambers, which are organised in four layers: two on the in- and outside of the `MO` layer (known as `MOI` and `MOO`, respectively) and two on the in- and outside of the `MI` layer (known as `MII` and `MIO`, respectively). The distance between `MO` and `MI` is about 2.9 m, which defines the smallest lever arm of a muon track contained in one octant*.

The underlying principle in the design of the L$_3$ muon spectrometer can be expressed as

---

*Notice that for a muon with an energy of 30 GeV originating from the vertex, the requirement that it is confined to one octant only causes a loss of 4%. For muons originating in the atmosphere, the loss is larger.
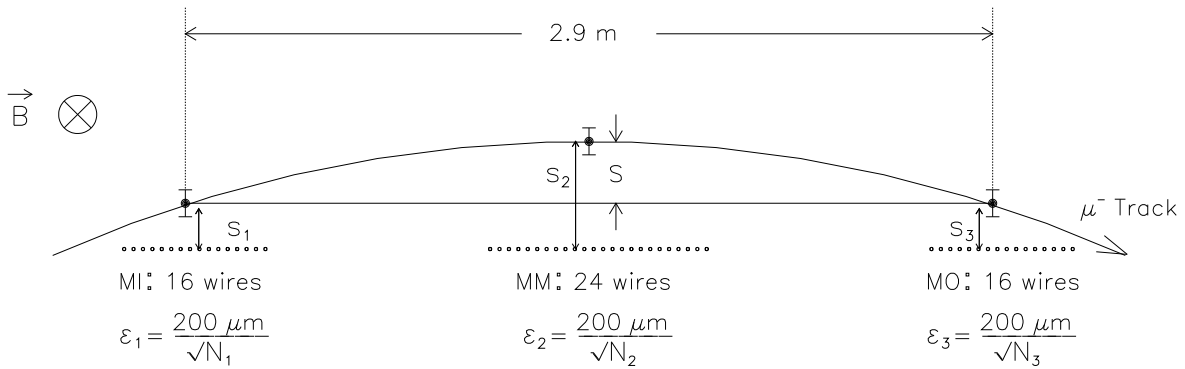
Figure 2.3: *Schematic view of the sagitta measurement.*

the relation between sagitta (*s*) and the transverse momentum (p_t). The sagitta is defined as the maximum deviation of a curve from a straight line (of length *L*) spanned out by two points on the curve (see figure 2.3). In equation (2.1) the relation is given for the ideal situation[*] of a particle moving in a homogeneous magnetic dipole field (assuming $s^2 \ll L^2$):

$$s = \frac{L^2 B \cdot c}{8 \cdot p_t} \tag{2.1}$$

with p_t in [eV/*c*], *B* in [T], *s*, *L* in [m] and where *c* is the speed of light in [m/s]. The sagitta depends quadratically on the lever arm and only linearly on the strength of the magnetic field. This favours a large spectrometer at the expense of a more modest magnetic field.

The remaining part of this section is dedicated to an overview of the technical aspects of the muon spectrometer vital to the momentum measurement of both beam induced and cosmic ray induced muons.

2.2.1   P-chambers

The P chambers are the drift chambers (Sauli 1977, Knoll 1989) which measure the *x* and *y* coordinates of a number of points or hits along the trajectory of a track. From these hits the sagitta can be calculated (see figure 2.3):

$$s = s_2 - \left(\frac{s_1 + s_3}{2}\right) \tag{2.2}$$

This formula shows that the measurement in MM weighs twice that of MI and MO. Along with the well-known fact (Duinker *et al.* 1982) that the resolution improves by *N* independent measurements along the track as $1/\sqrt{N}$, it is clear that one should use more sense wires in MM than in the two other layers. A configuration of 16-24-16 sense wires was chosen as a compromise between resolution and the price of the detector. The anode/sense wires are made of gold plated tungsten and have a diameter of 30 μm. They are positioned in 9 mm

---

[*]In the real situation a numerical approach is needed to account for the inhomogeneous magnetic field and multiple scattering in the material of the muon detector.

intervals with a field shaping wire (75 µm CuBe) in between. Each drift cell is bounded by cathode mesh planes, and is 101.5 mm wide. The mesh wires are 30 µm W-Au wires, with a spacing of 2.25 mm (see figure 2.4). The sense plane is extended with two additional sets of inactive sense and field wires at both sides to ensure the continuity of the electrostatic field and thereby minimize edge effects. Each MO, MM and MI chamber contains 21, 15 and 19 cells respectively corresponding to 336, 360 and 304 sense wires and in total about 3000 wires per chamber.

All wires of a chamber are glued to a Pyrex plate which in turn is glued on a carbon fiber bridge, forming a kind of ladder structure at each end of the 5.6 m long chambers. To reduce the gravitational sag on the sense wires (with a tension of 1.25 N) from 380 µm to 90 µm, a third bridge was introduced to support the wires at the middle. The support bridge causes a 9 mm region along the wires to be inefficient and affects the accuracy of the measurement up to a distance of ±15 mm in z (L3 Muon Group 1990).

Figure 2.4: *Schematic view of a drift cell of the P chambers.*

The 250 m³ volume of the P-chambers is filled with a mixture of 61.5% Argon and 38.5% Ethane at 3 mbar overpressure. To reduce aging effects 0.2% of water is added to the gas mixture. With this gas mixture and the nominal HV settings the parallel drift velocity $\left(\frac{dx}{dt}\right)$ is about 48.5 µm/ns and the Lorentz angle is about 18.5°. These two parameters along with an overall time offset are calibrated by the L3 muon group each year using a sample of $Z/\gamma \rightarrow \mu^+\mu^-$ events (Fabre 1992). For L3+Cosmics a different approach was chosen (Ma 2002). With the correct calibration a single wire resolution of better than 200 µm is achieved (see section 3.1.1).

A muon track recorded in all three P layers of an octant (see figure 2.3) is known as a "triplet". A track only recorded in two of the three layers is know as a "doublet". With the numerical approach used in the reconstruction program it is also possible to determine the momentum of doublet tracks, from angular bending in the magnetic field, but the resolution is much worse.

2.2.2 Z-chambers

The projection of the track along the direction of the magnetic field is measured by the 96 Z chambers (Cerrada, Durán, González, Martínes, Olmos, Salicio & Willmott 1988, Zhang 1994). A chamber consists of two superposed layers of drift cells. Each cell (see figure 2.5) consists of two parallel aluminum I-beams connected to a negative HV and a 50 µm gold-plated molybdenum anode wire in the center of the cell. Each cell is 27 mm high, 91.8 mm wide and 1880 mm long. It is closed by two 1 mm thick aluminum plates,
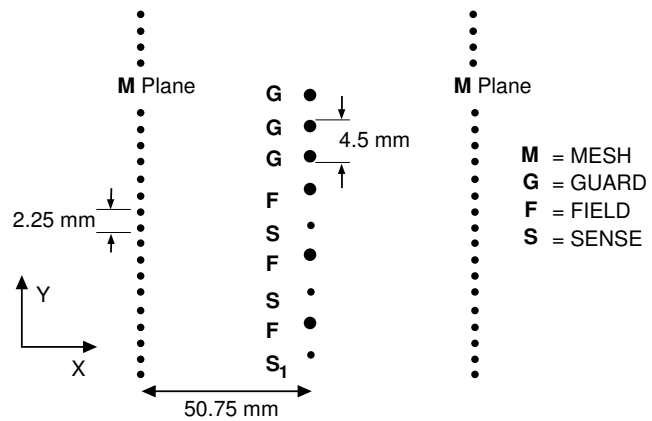
(a) A detailed view of a Z-chamber cell, where the electric field lines are shown.

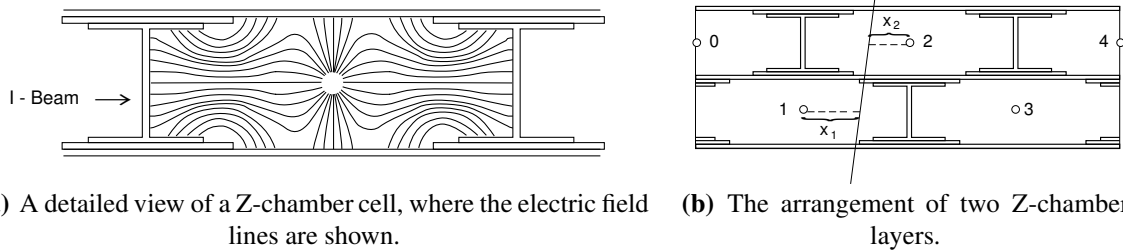**(b)** The arrangement of two Z-chamber layers.

Figure 2.5: *A detailed view of a Z cell, and the principle of the measurement of a track through two layers of Z-chambers.*

which are insulated from the I-beams by a 1 mm high and 43 mm wide fiber-glass strip. The two layers of a Z-chamber are shifted with respect to each other by half the width of a cell, thus reducing the left-right ambiguity problem. Each chamber consists of about 116 cells. The drift gas used consists of a mixture of 91.5% Argon and 8.5% Methane. A single wire resolution of 500 μm and a maximum drift-time of 1.5 μs are achieved at the nominal HV settings of cathode, -2500 V, and the anode wire, 2150 V.

2.2.3 T$_0$ calibration

To obtain a good spatial resolution in the drift chambers, a good time resolution is required. Signals, induced on sense wires by a charged particle passing through the gas, are passed via a printed circuit board out of the gas volume. They then propagate along a few meters of cable before they enter[*] the amplifiers (Rewiersma 1986). From the amplifiers the signals are propagated along an about 25 m long cable before entering the discriminators (Rewiersma 1987). Finally, they are transmitted over about 40 m of cable before reaching the TDCs. In order to understand the relative propagation time of any two signals through this complicated path, a dedicated time calibration, known as T0Cal (Duinker *et al.* 1988, Rewiersma 1992), was established.

Ideally, one would pulse each sense wire individually to check the propagation time, but with about 33500 sense wires, this scheme is not feasible. Instead the sense wires of the P chambers are pulsed using the capacitive coupling to the field wires, whereby pulsing all field wires of a cell at the same time causes a signal on all the sense wires of the cell. For the Z chambers the 16 channel amplifier cards are pulsed. Thus the propagation of the signal from sense wire to amplifier is not calibrated by the T0Cal system. However, care is taken that these cables have the same length. Each of the 16 octants have eight T0Cal drivers (six for the P chambers and two for the Z chambers). Each T0Cal driver has 15 or 16 output signals going to a single P cell or Z amplifier board. To avoid cross-talk between the cells connected to the same driver, each driver is connected to cells in all three layers of an octant and with a spacing of at least 3 cells between two cells connected to the same driver. The sense wire signals are measured relative to an additional output signal of the T0Cal driver

---

[*]The signals from the P chambers of a SLAVE octant pass via jumper cables to the corresponding MASTER octant, where they are ORed with their corresponding signals from the MASTER octant at the input of the amplifier.

called the "return pulse". The eight return-pulse signals per octant are ORed, so that each of the 16 octants only has one cable carrying the critical reference timing signal. The 16 return-pulse signals are ORed in the so-called SUPER-OR, which is located close to the TDCs. The output of the SUPER-OR is delayed and then used as a common-stop signal for the LeCroy TDCs.

2.2.4 The alignment system

Intrinsic to the measurement of the momentum of a muon with the sagitta method as described in section 2.2.1 is the need for accurate knowledge of the location of the wires with which the measurement is performed. The design requirement of a 2% momentum resolution at 45 GeV means that the error on the sagitta due to a misalignment of the wires must be less than 37 μm. As a result a high precision mechanical support structure was designed (Peng 1988, Fabre 1992), as well as an opto-mechanical system which continuously monitors the alignment (Leijtens 1993). Below, a brief description of the alignment system will be given.

The alignment system known as RASNIK consists of a LED, a lens and a four quadrant light sensitive photo-diode (4QD). The LED emits a homogeneous square beam of light, which the lens focuses onto the 4QD. The system is applied to cases where the locations of both the LED and the 4QD are known. A difference in intensity between the four quadrants reveals a displacement of the lens in the plane perpendicular to the light beam. The dynamic range of the system is ±450 μm, and an accuracy of better than 20 μm is achieved over the full range, which mainly is caused by the non-linear behaviour of the system for large displacements. In practice the system is used within a range of ±50 μm, where an accuracy of the order of 5 μm is obtained (Fabre 1992). To achieve this accuracy each system was calibrated on an optical bench before installation. The system comes in two variants, known as the horizontal and the vertical alignment system.

Figure 2.6: *Schematic view of the RASNIK system.*

The horizontal alignment system measures the location of the support bridge inside a P chamber. This measurement could be done with two sets of RASNIK systems, but to ensure redundancy a third system was installed. The LEDs are mounted on the Pyrex plate at one end of the chamber, the lenses are mounted on the middle bridge and the 4QD are mounted on the Pyrex plate at the other end of the chamber.

The vertical alignment system measures the displacement of the MM chamber with respect to the MI and MO chambers, in the direction perpendicular to the wire planes. Each octant has four systems installed; two at each end, again to create a redundancy in the measurement.

Figure 2.7: *Schematic view of the L3+Cosmics readout.*

The LEDs are mounted on the outside of the MI chamber. Here an insulated brass pin, mechanically connected to the LED, touches one of the wires of the middle sense plane. The lenses are mounted on the gauge block which defines the distance between the two chambers of MM. The 4QDs are mounted on the gauge block which defines the distance between the two chambers of MO. A gauge block is equipped with two brass pins which barely touch a sense wire in each of the chambers. The distance between the tip of the two pins is exactly two times the cell width. The *x* coordinate of the pair of the MO chamber is mechanically fixed.

To achieve the desired alignment the location of the chambers were adjusted after the actual installation to remove any misalignment and torsion. The regular measurements from the RASNIK systems are written to the L3 muon database, and the appropriate corrections can be applied during the reconstruction of the events.

2.3 The additional hardware

The goals of the L3+Cosmics experiment requires to measure cosmic muons in parallel with L3's exploration of the physics at LEP. To achieve this goal two fundamental problems had

Figure 2.8: *Schematic view of a scintillator tile. The splitting of the eight files in two bundles can be seen.*

to be solved:

- In order to measure the drift-time, one must know when the charged particle traversed the drift chamber. In L3 this is done by measuring when the beams collided, but for cosmic rays a direct measurement must be made.

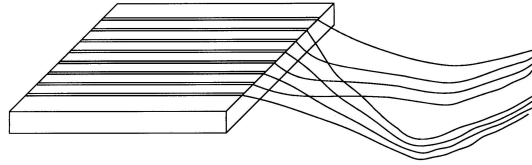- The about 20000 signals coming from the chambers must be split in a way which is transparent to L3 and whereby no deterioration of the signal quality is introduced in any of the two branches.

In this section the solutions to these two problems will be discussed in detail. In addition, the trigger and readout scheme will be discussed (see figure 2.7 for an overview).

2.3.1   The scintillator system

The measurement of the reference time, needed to reconstruct the drift-chamber signals, calls for the introduction of a new detector. Covering the outside of the three top faces of the magnet with scintillators enables a measurement of the time when a muon enters the detector. The scintillators cannot be placed inside an octant, since the additional matter increases the multiple scattering, and thus reduces the momentum resolution. There is not room enough to place the scintillators between MO and the coil of the magnet, therefore a location outside the magnet is the only option. However the existing infrastructure on the outside of the magnet creates a lot of boundary conditions causing a rather different design on the three different sides.

The mere size of the area which needs to be covered requires a modular design where the number of readout channels is kept at a reasonable level. The smallest units are the $25 \times 25 \times 2$ cm^3 scintillator tiles (see figure 2.8), which are read out using eight wavelength shifting fibers. The fibers are connected to clear fibers, which guide the light to the photomultiplier tubes (PMTs). The fibers of a tile are grouped in two bundles, each going to a PMT. Requiring a coincidence between the two PMTs removes the uncorrelated thermal noise of the PMTs. This improves the signal to noise ratio by about two orders of magnitude. A cassette is formed by 16 tiles in a 4×4 configuration housed in an aluminum box. This is the basic mechanical structure. The fibers of 6 cassettes are connected to two PMTs making a 2×3 m^2 unit known as a scintillator module*. Great effort has been made to ensure that all

---

*Octant 3 module 9 only has four cassettes, since it was not possible to mechanically place two of the six.

fibers have the same length. This ensures a good time resolution of the system independent of where the particle passes. The time resolution has been determined to be 1.5±0.1 ns (Bähr, Grabosch, Kantserov, Leich, Leiste & Nahnhauer 1997).

On octants one and two 12 modules were placed while on octant three only 10 modules could be installed due to the many pipes. In total 202 m^2 of scintillators are installed.

Scintillator electronics

Cables of about 50 m length connect the 68 PMTs with the discriminator units known as L3CD (Leich 1998b). The L3CD cards are housed in a VME crate located in the main block-house. These eight channel units combine several functions: Amplification, discrimination, twofold coincidence and monitoring. When the two analog signals, coming from the two PMTs looking at the same module, arrive at the L3CD unit they are first amplified individually. Afterwards they pass a programmable time-over-threshold discriminator, where the first level of noise reduction is performed. The next step is the twofold coincidence, which is critical, since it is of vital importance that the timing of both signals remains undistorted. The reason for wanting the timing of both signals is that one can choose the earliest signal. When choosing the first signal one will normally also choose the largest signal. This is the one where the rise-time of the signal is the fastest, therefore the discriminator introduces the smallest time slewing. This trick is needed to obtain a 1.5 ns resolution. Both timing signals at the output of the coincidence unit are split in two, where one is stretched and converted to ECL. The signals are fed into a dedicated TDC (see section 2.3.3). The second signal goes to a FIFO* from which the coincidence rate can be monitored via the VME-bus.

The HV supply for the PMTs is manufactured by CAEN and located in the main block-house. It is controlled and monitored with a VME module which is located in the same crate as the L3CDs. The controller of this VME crate is using the VxWorks operating system.

2.3.2 The CPC card

The signals from the muon chambers are fed into the 96 channel LeCroy FASTBUS TDCs. On the LeCroy TDC the signal is split into two. One signal is used for the L3 time measurement, and the second is sent to an auxiliary connector on the reverse of the large module. Before L3+Cosmics the so-called "Muon Personality Card" MPC (Groenstege 1989) was connected to the auxiliary connector. It makes a logical OR of two neighbouring wire signals, which is then sent to the so-called "Personality Card Controller" (PCC). The PCC performs the task of road-finding. Its output is used by the first and second level trigger.

It was possible to replace 224 MPC cards with the new "Cosmic Personality Cards" CPC (Groenstege, Wijnen, Rewiersma & Stolte 1999b). The additional 10 years of technological development made it possible to fit the redesigned MPC functionality along with the signal splitting as well as the new functionality into two MACH 466 devices without introducing any effect on the L3 electronics (Groenstege & Boerkamp 1998). Left with a vir-
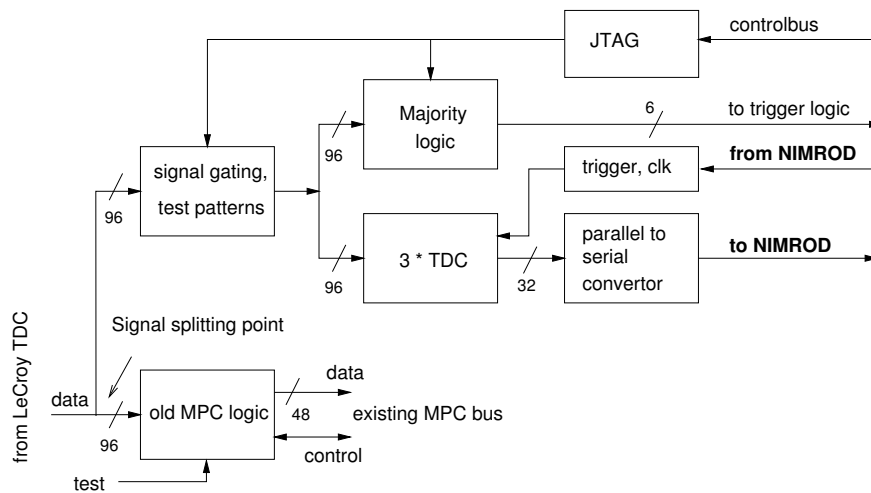
---

*First In First Out.

Figure 2.9: *Schematic view of the CPC card.*

tually empty board, the CPC card could in addition host: the majority logic, the new TDCs and a readout controller (see figure 2.9).

The majority logic

The majority logic provides input to the L$_3$+Cosmics trigger. It is used to give information of the type "Octant 2 MI, MM and MO are hit". The decision if a layer is hit depends on the number of channels hit in each CPC. This is compared to a programmable threshold value. The Z-chambers are not used in the trigger decision, since the information contains a sizeable noise level.

The layout of the FASTBUS crates are such that the 18 P chamber TDCs of one octant are located in the same crate, and that the 2×10 Z chamber TDCs from 2 octants occupy a full crate. A P chamber CPC card is connected either to 6 MI or MO cells or to 4 MM cells. In each P crate there is one exception, which is connected to one MI cell and two MM cells.

The majority logic stretches all wire signals longer than 15 ns to about 1.2 μs. This overcomes the problem of the large drift-time of the electrons in the gas of the chambers. The determination if the cells of a CPC card have been hit, simply means counting the number of stretched wire signals at any given time. Every 200 ns, this number is compared to a programmable threshold. When the threshold level is exceeded the majority logic sends out a 1.5 μs long "majority" signal to the trigger. A programmable register on the CPC card is used to activate the correct majority line. A small flat cable runs along the row of CPC cards in a crate. It essentially implements a wired-OR, in which all CPC cards connected to the same layer will activate the same line. Each P crate has such a cable which runs via the auxiliary crate (see section 2.3.3) to the trigger. The 96 input channels of the CPC cards connected to both MI and MM are split in two halfs, each with its own programmable threshold and layer information.

The low noise level in the P chambers allows the use of a low majority threshold. This in turn removed the potential problem at the border between two CPC cards. For the 1999 data
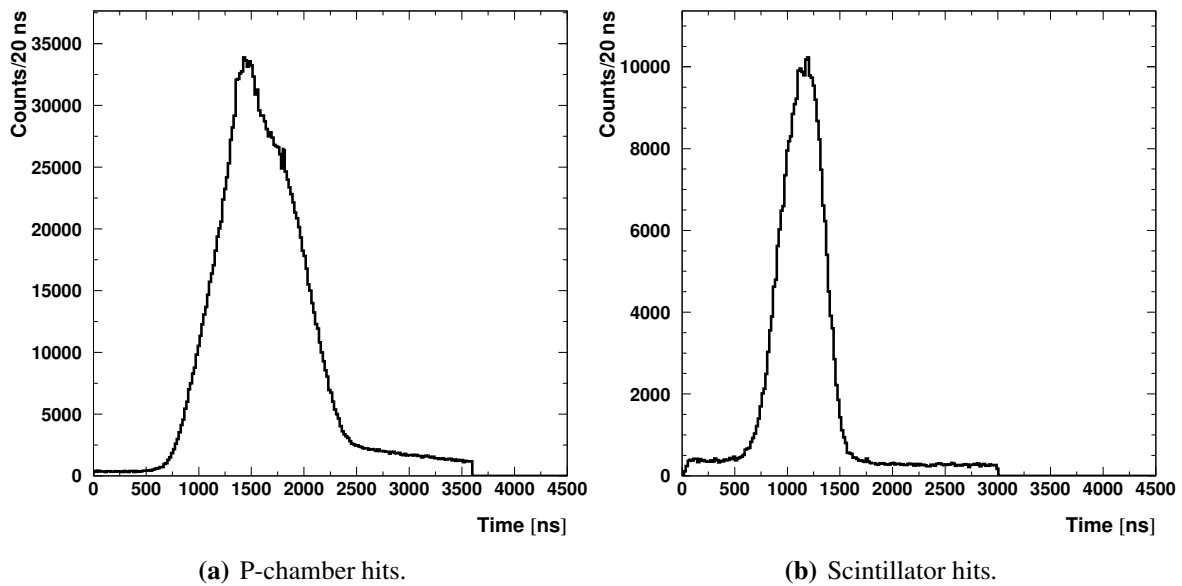
(a) P-chamber hits.

(b) Scintillator hits.

Figure 2.10: *The raw time distribution of hits within the search window. The start of the window is for all TDC set to be 4.2 μs earlier then the trigger time.*

taking a threshold of 8 wires per CPC was chosen.

The TDCs

The 32 channel TDC chip (Christiansen 1997), developed at CERN, was chosen. It is a prototype for the coming LHC experiments. Being a general purpose TDC, it has an impressive amount of features which can be selected and tuned according to the needs of the application. Here a short description of the main features used on the CPC card is presented.

A bin size of $\frac{25}{32}$ ns is obtained by running the chip with a 40 MHz clock frequency. This precision is sufficient for measuring the chamber and scintillator signals. Internally, this precision is achieved using a course counter following the clock. A fine time-scale is made by a 32 element delay locked loop (DLL). When a channel is hit the content of the course counter and the state of the DLL are stored in one of the two available time registers, before it can be decoded and copied to the event buffer. The circular event buffer is common to all channels, it has a depth of 256 words. The dual input register allows to record double hits with intervals as short as 15 ns. The trigger signal gets a time stamp in a similar manner. This is temporarily stored in an eight words deep FIFO. When a trigger is received, a trigger matching algorithm starts selecting hits from the event buffer using a programmable time window relative to the trigger time. Before a selected hit reaches the 32 word deep output FIFO, the trigger time plus a programmable offset is subtracted. In figure 2.10 the raw time distribution can be seen. The long tail of late P-chamber hits is caused by cells with a lower voltage. The lower voltage causes a lower drift velocity and thus a broader distribution. The real scintillator times are located on top of a flat background of noise hits. To reduce the data volume only leading edges are measured.

The readout controller

The main life-line for a CPC card is the so-called front end link (FELink), which is a standard FTP* ethernet cable. The external 40 MHz clock, trigger and reset signals are sent to the CPC on the cable. The CPC sends the data from the TDCs using the same cable. The distribution of these signals as well as the handling of the readout of the TDC is the job of the readout controller.

When a trigger reaches the CPC it is distributed to the three TDCs to initiate the local trigger matching. When the readout controller is ready it sends out a header word, in which the local event number and the unique CPC number can be found. Next the data (if any) from the three TDCs follow, the TDC data are adjusted to comply with the data-format of the experiment (Wijnen, Petersen & Timmermans 1999). At the end a trailer word is sent which marks the local end of the event. In this word the total number of words sent for this particular event can be found (minimum 2). All data is serialised, achieving a maximum data rate of about 1 Mwords/s.

2.3.3 The auxiliary crate

The auxiliary crate is a VME size crate with a customized backplane. It contains two CPC cards. One of these is used to measure the timing of the scintillator signals and the other is used for the majority signals as well as the external trigger signals. Some of the trigger classes require at least one scintillator hit. To simplify the cabling and the functionality of the trigger module (CTT) the 68 scintillator signals are ORed, stretched and delayed in the auxiliary crate†.

It is worth noticing that by using CPC cards for the scintillator signals as well as for the miscellaneous signals, the data streams of the two independent detectors are combined, avoiding the complexity of event building.

The 16 return pulses from the T_0 calibration system (see section 2.2.3) are connected to the CPC card containing the scintillator signals. A small modification to the SUPER-OR gives access to each of these 16 signals.

2.3.4 The NIMROD

The 226 CPC cards are read out using 17 VME modules known as NIMRODs‡ (Groenstege, Rewiersma, Wijnen & Zwart 1999a, Rewiersma 1998, Groenstege, König, Rewiersma & Wijnen 1996). Each NIMROD is capable of handling up to 16 FELinks (i.e. CPCs). The asynchronous data streams of the FELink are individually decoded. These blocks are combined in a fast RAM from which they can be read as soon as all the blocks of the event, including the NIMROD header, are completed. Before entering the readout buffer

---

*Foiled Twisted Pair cables, these cables are also used for fast-Ethernet.

†In fact the majority logic part of both the scintillator and trigger CPC card was reprogrammed to contain this functionality.

‡In principle the task could be done by 16 NIMRODs, but due to some problems with the 1999 version of the NIMROD it was decided to add an additional module to reduce the load.

Class	Description
1	Triplet in any octant **with** a scintillator hit.
2	Triplet in octant 0 or 4 **without** a scintillator hit.
3	Triplet in octant 1, 2 or 3 **without** a scintillator hit.
4	Triplet in octant 5, 6 or 7 **without** a scintillator hit.
5	Three singlets in adjacent octants **with** a scintillator hit.
6	Two doublets **with** a scintillator hit.
7	Doublet and two singlets **with** a scintillator hit.
8	Doublet and a singlet **with** a scintillator hit.
9	Doublet **with** a scintillator hit.
10	Triplet and at least one other chamber **without** a scintillator requirement.
11	5 chambers **without** a scintillator requirement.
12	6 or more chambers **without** a scintillator requirement.

Table 2.1: *The description of the 12 trigger classes used in the 1999 data taking.*

zero suppression is imposed. This means that the header and trailer words of CPCs without TDC data will be removed[*]. In this way the total data volume was reduced by more than 60% (Timmermans 1998). But even if none of the FELinks had any TDC data, the NIMROD will send out its own header and trailer words, these words can optionally be removed by the on-line software.

In addition to the event building the NIMROD has the important task of distributing the 40 MHz clock as well as the trigger and reset signals to the CPCs.

2.3.5 The trigger

The trigger module (CTT) (Verkooijen 1999) is a VME module. The trigger decision is based on the 24 majority signals from the P chambers and the `OR`ed scintillator signal. Since there is no beam crossing signal which defines the timing of a potential event, the experiment is self triggering. The different trigger classes listed in table 2.1 are suited for very different purposes:

1: The golden trigger. Events in which a good momentum measurement is possible.

2 & 4: Classes suited for the search for possible neutrino induced events, i.e. horizontal muons.

3: Along with class 1 it is used to determine the scintillator efficiency from the raw data set (see section 5.1).

---

[*]Every 1024 events the zero suppression is overruled, whereby a consistency check of the full event is possible.

5-8: Single muon events where the track crosses neighbouring octants. This is a topology which requires a special reconstruction algorithm. Due to the lacking monitoring of the inter-octant alignment the momentum resolution of these classes of events is expected to be significantly worse than that of class 1.

9: Intended for the determination of the trigger efficiency of class 1 (see section 5.3).

10-12: Classes intended for the search for exotic events (Chen *et al.* 1997) as well as multi-muons.

The formation of the octant coincidence is most important, but also the most difficult due to the lack of synchronisation of the layer signals. This is overcome by counting the number of majority signals which are in coincidence both per octant and in total. When one of the counters is decremented (i.e. when the first trailing edge is reached) the maximum coincidence has been reached. At this time the check for the scintillator coincidence is performed. Each class can be switched on or off as well as prescaled. When any of the class signals pass the prescalers, a "cosmic trigger" is said to have fired. During normal data taking the trigger rate was about 450 Hz. This was achieved by prescaling classes 3, 4 and 9 by a factor 20[*]. The cosmic trigger can, along with the external triggers be enabled or disabled. The most important external triggers are:

1 Hz clock: This trigger is in practice always enabled, since it provides an unbiased sample of events, which for instance can be used to determine the noise level in the chambers. It also defines a minimum event rate, which if not satisfied is an indication of a serious problem with the readout or the front-end electronics.

T0Cal return pulse: This trigger is only enabled during T0Cal runs (see section 2.2.3).

LED return pulse: This trigger is only enabled during the LED runs, in which a LED is activated in each of the scintillator modules one after the other.

The last obstacle, before a real trigger signal is generated, is the rate limiter. Here several external as well as internal conditions can disable the trigger:

- Any NIMROD can disable the triggers, this is done when its event buffer is more then 80% full.

- The GPSTIM module (see section 2.3.6) will disable the triggers in between runs. Therefore it is in actual control over the triggers. To prevent overlapping events each trigger will cause a dead-time of 2 µs, this is controlled by the CTT but imposed by the GPSTIM.

- To protect against overflow in the trigger buffer of the TDCs, which is 8 triggers deep, the CTT keeps track of the number of pending triggers. If this number exceeds 7 the triggers are disabled.

---

[*]The prescale factor was altered a few times, but for most of 1999 it was 20.

All in all the trigger latency is about 3 μs and has a spread of about 200 ns due to the spread in the drift-times from event to event (see figure 2.10b).

When a trigger is fired the CTT puts two words in its output buffer. The first contains a hit pattern telling which majority signals were present. The second word has the class and source information as well as the event number.

2.3.6   The GPSTIM

A very important quantity when measuring an absolute flux is the live-time of the experiment. This task, as well as the communication with the external GPS module, is dealt with by the GPSTIM module (Leich 1998a). When a run is started the GPS module is asked for the absolute time[*], which is propagated through to the run header. In addition a course (1 Hz) and a fine (10 MHz) counter are started. Their values are copied to the header of each event, whereby the exact time of each event is known. The precise absolute time is of no importance to the analysis presented here, but it is of vital importance when the data is used for astronomy. It is also the only way to correlate events from different detectors.

As explained above there are several conditions which can disable the triggers. This introduces a dead-time somewhere along the duration of a run. To keep track of the total effective running time the GPSTIM has a 10 MHz live-time counter which is started the moment the experiment is declared "alive" and the triggers enabled. Since the communication with the GPS module is rather slow this is typically 2 s after the "start of run". The internal signal in the CTT, which disables the triggers is passed to the GPSTIM and it will thus also stop the live-time counter. The value of the live-time (without the lower 23 bits) is copied to the event header, thus the value in the last event of a run represent the total effective live-time of the run.

2.4   The data acquisition software

In addition to the new hardware it was necessary to make a new and independent data acquisition system (DAQ). A high degree of automation was imposed on the design of the system, thus eliminating the need for a dedicated shift taker. The importance of knowing the exact conditions of each run requires the use of a database where a large set of vital information is stored (e.g. the trigger condition). The functionality of the system naturally divides it into two parts, namely the event stream and the slow control. These parts will be described separately below.

The design of the system is complicated by the fact that all the constituent computers use a different operating system (see figure 2.11a). In DELPHI a similar problem has led to the development of DIM (Gaspar & Dönszelmann 1993), which provides an easy access to the basic TCP/IP protocol and interrupt handling. This package was chosen for the inter-process communication. To avoid interrupts, the processes on the event pipe get their messages from

---

[*]Notice that the settings of the module were such that it was using the Central European summer time all year around.

(a) Layout of the L₃+Cosmics DAQ system.

(b) The event pipe.
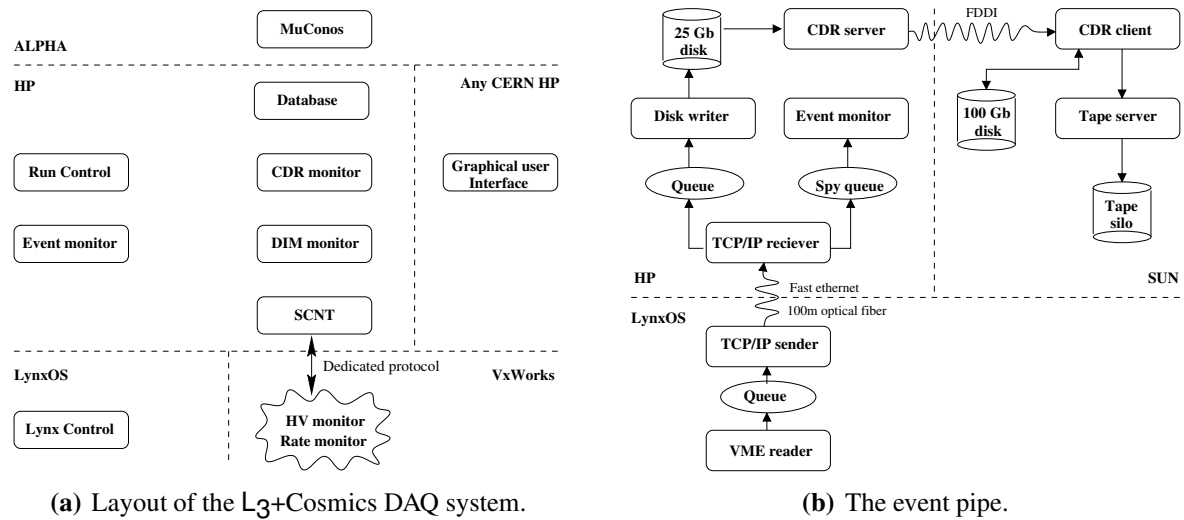
Figure 2.11: *Layout of the L₃+Cosmics DAQ system.*

Type	Pre-fix	Description
Physics	r	The data-taking mode with which the later data analysis is performed.
T0Cal	t	The run type for the T_0 calibration (see section 2.2.3 on page 26).
LED	l	The run type during the seldom check of the scintillator system using the LED system.
Test	g	The run type for tests of the system.

Table 2.2: *The four run types. The prefix is the first character in the name of the file where the data is stored.*

their parent process using shared memory. In total 231 DIM commands and services are used for the inter process communication.

2.4.1 Run Control

The run control process (RunCo) is running on the HP (see figure 2.11a) and is the master of the DAQ system. It is the parent process of the event pipe processes on the HP. On the VME crate controller[*] running LynxOS, a similar process (LynCo) is running, which in turn is the parent for the event pipe processes there.

Within the system four different types of data are defined (see table 2.2). The user has to specify the run type when starting a run. Knowing the run type RunCo will send to the database a request for the next new run number in the sequence. When the database is ready for a new run, RunCo will initiate the electronics by sending the appropriate command to

---

[*]The crate where the NIMRODs, the CTT and the GPSTIM are located.

the VME controllers (both LynxOS and VxWorks). When they return with an "OK", RunCo will start the run. The system typically runs in "automatic" mode. This means the system continuously tries to take physics data. A run is stopped by either the maximum output file size being reached or the report of a hardware error. To reduce the dead-time between runs only a minimum initialization* is performed in between two consecutive runs in automatic mode. However, if the database reports a user change in one or more of the vital parameters, a full initialisation is performed.

2.4.2 The event stream

As was mentioned in section 2.3.3 data from the two independent detectors is merged in the NIMRODs, thus freeing the DAQ from the task of event-building. As can be seen in figure 2.11b an event starts its path in the LynxOS controller. Here a process polls on a register in the GPSTIM module to check if its event block is present. After reading the information from the GPSTIM the information from the CTT will be read. Finally the data from the NIMRODs is read. If any of the modules fail to provide data within a fixed time, an error message will be send to RunCo, which in turn will stop the run. While reading the data from the NIMRODs an additional zero-suppression is imposed, whereby the header and trailer words of NIMRODs without data will be removed. At this stage the event conforms to the data format (Wijnen *et al.* 1999). The event then passes via a queue to a process, which sends it up to the HP via TCP/IP. Here the receiving process sends it via a queue to the process which will write it to the output file on the local disk. During normal data taking the data flow amounts to about 500 kB/s, but the system is capable of handling up to 1 MB/s.

The Central Data Recording system (Pantzer *et al.* 1998), provided and run by the CERN IT division, is used for the job of writing the data files to tape and afterwards removing them from the local disk. A file is first copied (using `rfcp`) to a SUN machine located at the computer center, from where it is written to a RedWood tape located in one of the big tape silos.

2.4.3 The slow control

As the L3 muon group takes care of the slow control of the muon chamber, our slow control tasks are limited to control and monitor the scintillator system, spy on the slow control information of the L3 slow control and monitor the data quality. The realisation of these tasks will be briefly described below.

Scintillator control

As described in section 2.3.1 the scintillator electronics consist of two basic parts, namely the HV supply and the discriminators (L3CD). The control and monitoring of these systems are done on the controller of the VME crate which houses the electronics modules.

---

*A big reduction in dead-time is achieved by skipping the initialization of the CPC cards via JTAG (Parker 1998).

The nominal values for the HV supplied are obtained channel by channel via DIM from the database and are loaded into the CAEN mainframe. From here on, the mainframe will autonomously maintain the desired voltage, unless a channel pulls a current which is beyond the limit, in which case the voltage will be lowered. The software monitors the actual voltage and status (e.g. over-current) of each channel.

In a similar way the threshold for the L3CDs is obtained from the database. However it is not possible to monitor the actual value. Instead, the raw coincidence rate of two PMTs connected to the same scintillator module can be monitored. This provides information not only about hardware problems, but also about changes in external factors such as the amount of synchrotron radiation produced by LEP.

Both the HV monitoring data and the coincidence rates are send via DIM to the database.

Interface to the L_3 DAQ

During the L_3 physics data taking the information obtained by the muon slow control is written to the muon database. To reduce the size of the muon database, this information is **not** written to the database in between the L_3 runs. To overcome this problem a special cluscom[*] file was made for us on the L_3 on-line VAX/Alpha cluster, where the essential muon slow control information is written irrespectively of the status of the L_3 DAQ. MuConos is the name of the dedicated program which is running on one of the Alphas, where it reads the content of the cluscom file and sends it to the L_3+Cosmics database server via DIM. The cluscom also contains information about the magnet current, the LEP status, the L_3 DAQ status and the outside temperature and pressure.

Once a day the muon shift taker performs a T_0 calibration (see section 2.2.3), when this happens the normal L_3+Cosmics data taking must stop and a T0Cal run must be started immediately[†]. The L_3 muon DAQ sends an interrupt to MuConos when it starts the initialisation for a T0Cal run. MuConos then sends a DIM command to RunCo to stop the current run and start a T0Cal run. At the end of the calibration run, the muon DAQ sends a second interrupt to MuConos which then sends a DIM command to RunCo to stop the T0Cal run. If the run mode before the T0Cal run was "automatic", RunCo will return to this mode.

Event monitor

The event monitor is a small program running on the HP which gets a copy of events in a special spy queue. Its main task is to thoroughly check the syntax on the event data as well as its consistency. All active elements of the readout chain maintain an event counter, which for each event is copied to the data stream. If a module misses a trigger or fails to sends its information for a given event, a mismatch between the elements of the event occurs. Such an error will not disappear by itself and it is very hard to correct for in the off-line software. The monitor has to spot this type of problems and send RunCo the command to stop the run.

---

[*]A cluscom is a memory block, which can be accessed by all processes on the same VMS cluster.

[†]Since L_3+Cosmics is not allowed to interfere with L_3, the muon DAQ does not wait for an acknowledgement from RunCo before it enables the pulsing of the wires.

In 1999 this type of problem occurred frequently due to a problem with the trigger token of
the CPC card and a problem on the NIMROD auxiliary card. In the winter shutdown these
problems were corrected, and the problem occurred only seldom in 2000.

In addition to the detection of direct errors in the data, the monitor also counts the occur-
rence of data from each NIMROD, CPC and TDC separately. This information is integrated
over 3 minutes and then stored as a set of histograms in a dedicated shared memory. The
occurrence rate per CPC is also sent to the database.

To prevent the monitor from using all the CPU power, it is running with a lower priority
than the rest of the DAQ processes.

2.4.4   The database server

The database server provides an interface to a dedicated database, which is made with the
ZEBRA (Brun, Goossens, Schaile, Shiers & Zoll 1995) based L$_3$DB package. The choice
for this database system is motivated by the fact that the database has to be accessible from
the off-line reconstruction and simulation programs. Internally the data is organised in a tree-
like structure similar to the directory structure on computers. Data is entered to a specific
directory with a start and an end of validity time. When retrieved, the most recent entry in
the specified directory which is valid at the time requested by the user will be returned. Fol-
lowing the strategy of the L$_3$ muon database, the directories are split in two: *constant* and
monitored. The *constant* directories contain information which rarely changes (e.g. the trig-
ger condition). The *monitored* directories contain the information which regularly changes
(e.g. the scintillator coincidence rates).

On the on-line side of the interface, the most recent entry from each *constant* directory
is provided as a DIM service. For most of these services the server also provides a DIM
command with which the data can be changed. Since it is vital that the conditions do not
change during a run, any change to a *constant* directory will be buffered. Only when RunCo
sends the database server the command to prepare for a new run, the change will be send to
the database and will be visible in the associated DIM service.

For the *monitored* directories the database server receives a DIM command from the
source process telling that a particular data block has changed. This data is then immediately
entered in the database.

Chapter 3

Cosmic muon reconstruction and simulation

In this chapter the reconstruction and simulation of cosmic ray muons are described. For each event, the DAQ records a set of times from the muon chambers and from the scintillators. The reconstruction program uses this information to estimate the properties of the muon(s), e.g. the momentum and direction. The simulation program on the other hand generates virtual muons with well defined properties, and sends them through a virtual version of the detector. The simulated detector response is sent through the reconstruction program, thus allowing for a comparison between the generated and reconstructed properties of the muons. Furthermore, the complexity of the set-up does not allow for an analytical calculation of the acceptance of the detector (see section 6.1.5), i.e. the effective surface and opening angle of the detector. Therefore it is estimated numerically using the so-called Monte Carlo method. Both reconstruction and detector simulation programs are written within the GEANT framework (Brun *et al.* 1994) (see table 3.1 for a description of the GEANT volumes commonly used in this thesis). They are both modified versions of the programs (Fabre 1992, Foreman 1993) used by L3 to simulate and reconstruct muons created in the annihilation of a high energy electron and positron. A priori it seemed like only minor changes would be needed, e.g. changing the time-of-flight calculation. However, in the pilot study for this experiment (van Mil 2001) it became clear that more changes were needed. Additionally, further changes were needed compared to the programs described in (van Mil 2001), mainly due to the modifications in the set-up (see chapter 2).

First a short description of the event reconstruction is given, the focus is put here on the parts in which the author has been directly involved. Finally, a brief description of the event simulation is given.

3.1 Event reconstruction

The event reconstruction starts out by initializing the GEANT description of the experimental set-up. Parts of the description can be altered via a set of data-cards, which are also used to specify the input and output files. Afterwards the decoding of the run-header of the data

Name	Description
MBAR	The MBAR volume contains the barrel part of the L3 muon chamber system. It is an octagonally shaped cylinder with a coaxial octagonally shaped hole, where the z-axis is the symmetry axis. The outside boundary is located between the MO chamber and the cooling circuit of the coil, while the inside boundary is between the MI chamber and the support tube. The two ends are flat and located between the chambers and the magnet doors.
LEP3	The LEP3 volume contains the entire detector. It is also an octagonally shaped cylinder. Its radius was increased to allow for the scintillator volumes on top of the magnet (Korn 1998).

Table 3.1: *The description of the two most commonly used GEANT volumes.*

format (Wijnen *et al.* 1999) follows. In here the starting time of the run is located. The starting time enables the retrieval of the run specific information from the database (see section 2.4.4), e.g. the location of the CPC cards. When the initialization phase is successfully completed the program is ready to read in the events. All events are treated in the same way. When the run-trailer or end-of-file is reached the program enters in the termination phase, in which the output files and databases are closed before the program terminates.

At the heart of the measurement of charged particles with drift chambers (see section 2.2) lies the measurement of the drift-time, i.e. the measurement of the time differences between when the particle went through the chamber and when the electron avalanche reaches the sense wire. Before any interpretation of the raw time measurement in the drift chambers is possible, one must thus provide a reasonable estimate of the starting time, i.e. when the particle went through the chamber. One of the major differences between the reconstruction of the LEP induced muons[*] and the cosmic ray induced muons lies in the determination of this starting time. For the LEP induced muons the starting time can be derived from the time of the primary interaction, which is obtained by a pick-up coil situated around the beam-pipe. For L3+Cosmics the scintillators on top of the magnet provide the reference time. If only one scintillator hit is present, it can easily be used. A problem, however, arises when several scintillator hits were recorded in the event. Namely, which one is the correct one? It turned out that using the most likely time according to the distribution of the scintillator hits (see figure 2.10b) is a good strategy. A further refinement of this approach was developed (Unger 2002), in which one uses the hit wire chamber cells to define a road towards the scintillator plane. If this road leads to a scintillator hit, then it is used; otherwise the one found by the original algorithm is used.

Following the strategy outlined by L3, the next part of the reconstruction is performed octant by octant. One thus aims at reconstructing a full sub-track within an octant, i.e. an object containing the best possible measurement of the trajectory within an octant. The sub-tracks are, if possible, at the end (see section 3.1.2) combined into a full track. In contrast to the

---

[*]During the data taking used by pilot study (van Mil 2001), the electronics were set up in such a way as to mimic the situation of the LEP induced muons.

original L₃ code, this algorithm does allow tracks to cross between the `MASTER` and `SLAVE` side of the same octant. By following the modularity of the detector, the tracks which cross neighboring octants are not completely reconstructed. For instance, a track which crosses `MO` and `MM` in octant 2 and `MI` in octant 3 would only be reconstructed as a doublet in octant 2, while the singlet in octant 3 would be disregarded. For muons originating from the center of the detector this constraint barely affects the acceptance, but for muons created above the detector this constraint reduces the acceptance significantly. There are, however, two strong reasons why the constraint is maintained for the reconstruction used in this thesis:

1. There is no sufficiently accurate measurement of the exact location of the octants. This is in sharp contrast to the large effort involved in the measurement of the inter-octant alignment (see section 2.2.4). If these tracks were to be reconstructed they would thus have an unacceptable large uncertainty on the estimated momentum.

2. Geometrically speaking combining P-segments, i.e. rows of hits within a P-chamber (see below), from chambers from different octants is a simple extension of the current algorithm, since it all takes place in the *xy*-plane. But for the Z-chamber hits, the story is much more complicated, since they require a three-dimensional approach from the very beginning.

For physics topics for which the acceptance is more important than the precision of the momentum measurement, one has tried to remove the inter-octant constraint. The technical difficulty in realizing this so-called cross-octant reconstruction has shown to be even bigger than initially feared.

When the starting time has been found, the pattern recognition in the chambers can start. To ensure that the pattern recognition of both the P- and Z-chambers can be performed in two-dimensions all coordinates are rotated to the so-called local-coordinate system. In this representation each octant is rotated to be in the position of octant 2, i.e. the upper most octant. To convert the measured time in the TDCs into a drift-time several correction must be applied. Below the corrections used for P-hits are presented:

$$T_{drift} = T_{TDC}^P - T_0^P + T_{corr}^P - T_{TOF}^P - T_{prop}^P - \left(T_{TDC}^{SCNT} - T_{corr}^{SCNT} - T_{LR}^{SCNT}\right) \qquad (3.1)$$

where T_{TDC}^P and T_{TDC}^{SCNT} are the measured time for the P- and SCNT-hit, respectively. T_0^P is the wire by wire correction obtained by the hardware T_0-calibration (see section 2.2.3). T_{corr}^P is the chamber dependent correction determined off-line (Ma 2002). T_{TOF}^P is the time-of-flight from the scintillator to the P-wire. T_{prop}^P is the time it takes for the signal to propagate along the P-wire, i.e. in the z direction. T_{corr}^{SCNT} is the scintillator module dependent time correction, which also is determined off-line (Ma 2002). T_{LR}^{SCNT} is the average time difference between the left and right PMTs looking at the same module. This correction is only applied to left PMT hit, and must thus be applied before the decision is made which of the two fired first. Several of these corrections require full knowledge of the trajectory, thus initially only a coarse correction can be applied. A so-called cell-map is used to convert the drift-time into a geometrical point (Onvlee 1989, Foreman 1993, Zhang 1994). Finally, before the pattern recognition can start, the so-called killing of "bad" cells is performed (Unger 2002). For a

period at the end of 1999 the efficiency of each cell was determined. Hits from cells with an efficiency below 80% are disabled[*].

The pattern recognition is performed for each P-layer individually. It has to group the hits together into so-called segments, i.e. the hits which constitute the arc of the muon trajectory in the chamber. During the pattern recognition, the arc is approximated by a straight line, which enables the use of a simple histogramming method. For every combination of two points a line is defined. With respect to a reference point close to the hits one calculates the distance of closest approach ($d_\perp$) and the polar angle (α) (see figure 3.1). For each line these two quantities are entered into a histogram. The algorithm is thus a relatively slow, O(N^2), but the efficiency is high. Histogram bins with more than 11 entries of at least 6 different hits are used to make the very first segments. A circle is then fitted (Karimäki 1991) to the hits constituting a segment. Using the fitted circle the residual of each individual hit can be calculated. This allows for the dropping of hits which in fact are too far away and picking of hits which were not included in the original set. This procedure is iterated a few times. In between each iteration new circle parameters are fitted. The final dropping of hits imposes a 2 mm cut, which is followed by the picking of hits within 3 mm. It was noticed that the histogramming method had problems when it had to find segments separated by a large distance. This can be understood with the correlation between $d_\perp$ and α which occur when the reference point is too far away from the hits. As a consequence of this, the peak in the histogram due to the far away segment gets spread out over too many bins and chances are it goes unnoticed. This problem was overcome by not performing the pattern recognition for all hits in a layer at the same time, but splitting it up in smaller pieces. If two groups of hits are separated by at least one empty cell, the pattern recognition is performed on the two groups separately.

Figure 3.1: *The line defined by two points. The distance of closest approach ($d_\perp$) and the polar angle (α) are indicated.*

A priori it is impossible to tell if the muon passed on the left or the right side of the sense wire plane (see figure 2.4). As a consequence of this, each TDC hit results in two spatial hits, one on each side of the sense wire plane. The pattern recognition is thus supposed to find the real segment and its ambiguous counter part. In most cases this ambiguity is resolved when the segments are combined into sub-tracks. However, when the muon passes almost parallel to the sense wire plane two ambiguous sub-tracks may emerge. This ambiguity must then be resolved when the sub-tracks are combined into a full track (see section 3.1.2).

Due to the low number of sense wires in the Z-chambers, the pattern recognition here combines the four layers around MI, the four layers around MO together. In cases where less
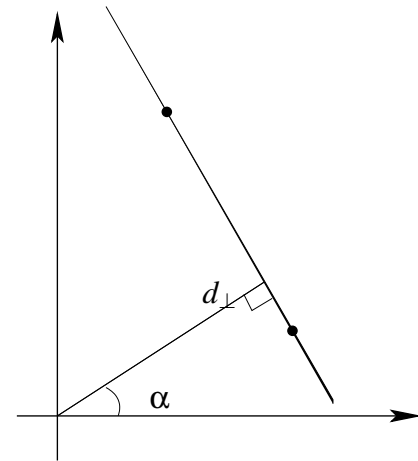
---

[*]With more statistics it was shown that not all "bad" cells had been removed. This may explain part of the discrepancy between data and Monte Carlo (see chapter 6).

than three layers are hit in both the upper and lower Z-chambers, the pattern recognition is performed on the full octant. Also for the pattern recognition in the Z-chambers a straight line approximation is used. In contrast to the P-chambers, brute force is used and all possible straight lines of three or four hits are tried, which results in a remarkably slow $O(N^4)$ algorithm. The χ^2 of the straight line fit is used to judge which combinations are meaningful and which are not. This is in fact the single most time consuming part of the full reconstruction program. Several attempts were made to improve on this, but the low redundancy in this measurement makes more elaborate algorithms inefficient. Also the Z-chambers have ambiguous hits, part of this problem is, however, removed by the geometrical layout of the rows of cells (see figure 2.5). If possible a segments from the upper Z-layers is matched by one from the lower Z-layers, resulting in a full trajectory in the yz-plane.

To obtain a full sub-track the P-segments are combined together to form a P-track, which is combined with a Z-track. The best combination is chosen on the basis of the χ^2 of circle fit to the full P-track. The correction for the propagation along the P-sense wire, T^P_{prop}, creates a correlation between the Z-track and the P-hits. This correlation allows for the usage of the circle fit χ^2 to distinguish the different combinations of P- and Z-tracks. The full sub-track then enters the so-called re-fit phase, where the final adjustment of the time corrections are applied along with the alignment corrections (see section 2.2.4). Finally a 3σ cut is imposed on the P-hits, using the measured resolution (see section 3.1.1). At this stage the so-called reference points are determined, which is a 3-dimensional point per segment. The last refinement of the sub-tracks is the so-called swim-fit. The swim-fit has to correct for the effect of the inhomogeneous magnetic field and the energy loss inside the octant. For this purpose GEANE (Innocente, Maire & Nagy 1991) is used to track the muon along its physical direction, i.e. for the upper octants from the reference point in the MO chamber to the reference point in the MI chamber and vice versa for the lower octants. The track is represented by a five-dimensional vector $(1/p, \frac{dx}{dy}, \frac{dz}{dy}, x, z)$, where p is the estimated momentum at the particular location[*]. The third spatial coordinate can be omitted since the vector is only used on planes defined by surfaces of GEANT volumes. The swim fit minimizes the distance between estimated and measured quantities. At the MI and MO chambers the following quantities are measured: x, z, $\frac{dx}{dy}$ and $\frac{dz}{dy}$. Since there is no Z-chamber around the MM chamber here only x and $\frac{dx}{dy}$ are measured. In contrast to the swim-fit used in the pilot study (van Mil 2001), which did not use the slopes, this fit has up to 5 degrees of freedom. The interested reader is referred to (Innocente *et al.* 1991) for the mathematical details of the fit. Due to the non-linearity of the problem, the solution must be found through a set of iterations. In most cases only a few iterations are necessary. As a result of the swim-fit, the five-dimensional vector is provided along with the associated covariance matrix, both of which are used in the track matching (see section 3.1.2).

---

[*]Notice that the coordinates x and y are swapped compared to the notation in (Innocente *et al.* 1991).
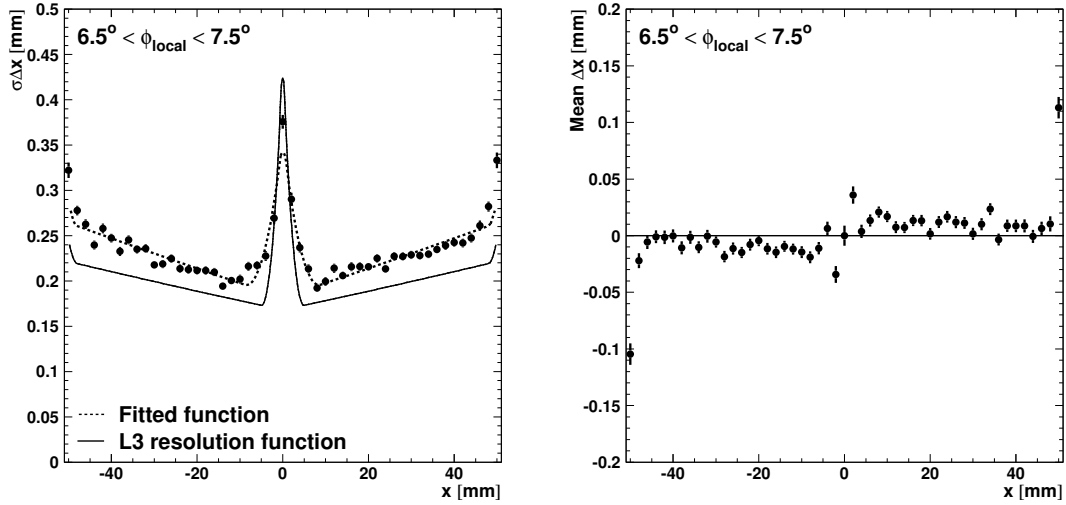
(a) The measured width of the Gaussian fit of the residual distribution as a function of the drift distance.

(b) The measured mean of the Gaussian fit of the residual distribution as a function of the drift distance.

Figure 3.2: *The measured single wire resolution for* $6.5° < \phi_{local} < 7.5°$.

3.1.1 Single wire resolution

One measure of the quality of the measurement of the P-hits is the single wire resolution. The single wire resolution also plays an important direct or indirect role in all the track fits mentioned above, since it is used to estimate the uncertainty of the measurement of the hit positions. This resolution can be written as (Onvlee 1989):

$$\sigma = \sqrt{\sigma_1^2 + 100^2} \qquad \text{(in μm)} \tag{3.2}$$

$$\sigma_1 = P_1 + P_2 \cdot |x| + \begin{cases} P_3 \cdot (P_4 - |x|)^2 & \text{if } |x| < P_4 \\ 0 & \text{if } P_4 < |x| < 48 \text{ mm} \\ 50 \cdot \left(\frac{|x|-48}{2.7}\right)^2 & \text{if } |x| > 48 \text{ mm} \end{cases} \tag{3.3}$$

where x is the distance to the sense-wire plane and $P_1 \dots P_4$ are the free parameters of the function. The 100 μm additional uncertainty in equation (3.2) has been added for compatibility with the original L3 function. The function shows a slow linear rise from the sense- to the mesh-plane, with an additional quadratic rise at both wire planes. The quadratic terms are caused by the non-linearity in the electric field close to the wires. One can use the width of the measured residual distributions to estimate the single wire resolution. In L3 one uses the residuals with respect to the segments, but here the residual with respect to the full circle fit is used. The residual distribution is fitted with a single Gaussian, in 50 bins of the distance to the sense-plane and in 62 bins of the angle with respect to the sense plane ϕ_{local}. Figure 3.2 shows an example of the fitted width and mean as a function of x for a particular ϕ_{local} bin. The figure also shows the fit of equation (3.2) to the distribution of the width along the original L3 function. The sensitivity is not good enough to fit the quadratic term at the

(a) P_1

(b) P_2

(c) P_3

(d) P_4
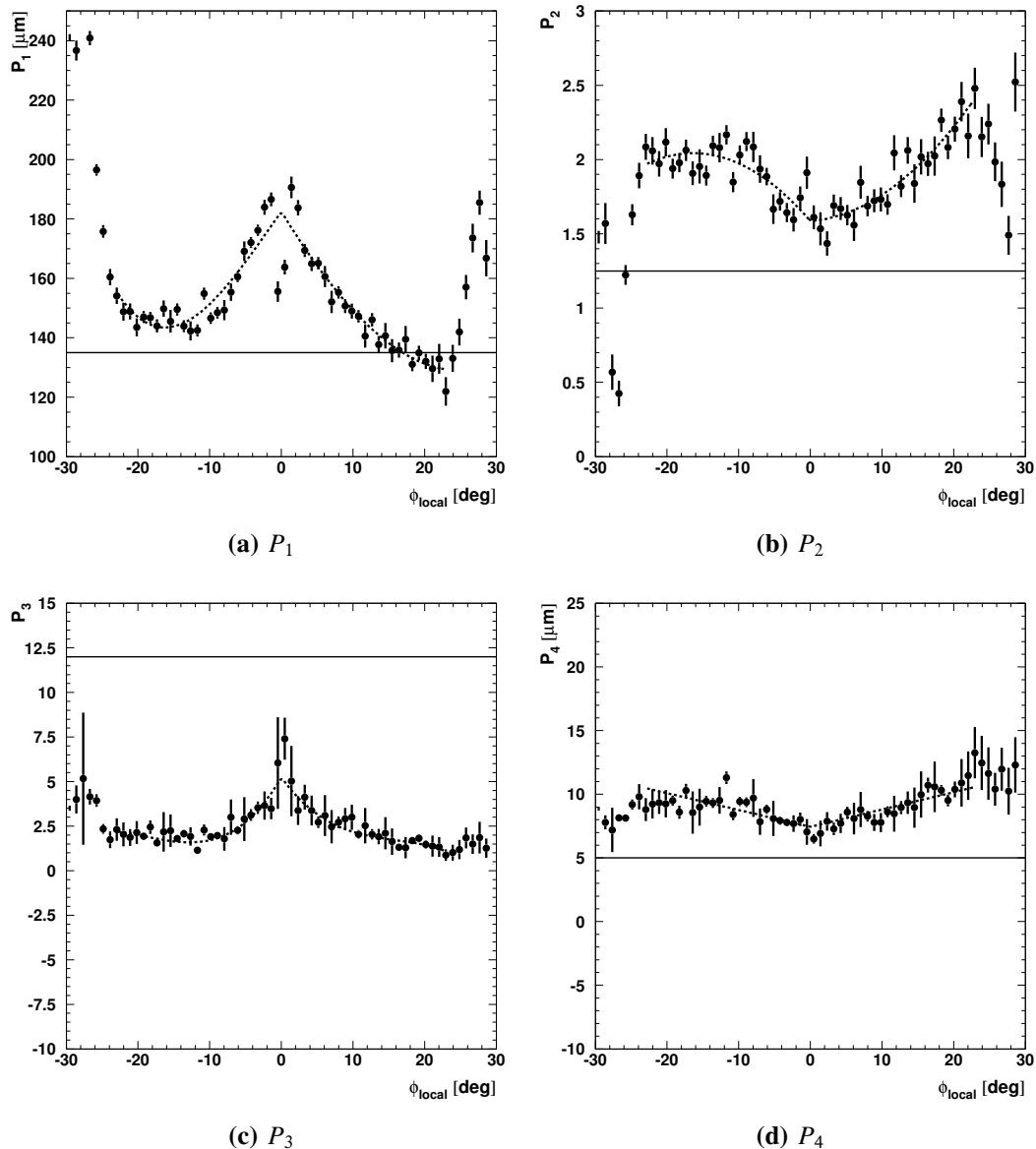
Figure 3.3: *The measured ϕ_{local} dependence of the four parameters of the resolution function (see equation (3.2)). The dotted lines represent the result of the polynomial fits, while the solid lines show the original ϕ_{local} independent values from L3.*

mesh-plane. It is clear that the obtained resolution is slightly worse than the one obtained by L3. Part of this is due to the fact that the residuals are determined with respect to the circle fit of the full track. Part of the uncertainty in the reference time, as measured by the scintillators, thus enter in the residual distribution. Furthermore it can be seen that the fitted mean is slightly different from zero. On the right side of the sense-wire plane ($x > 0$) the mean is systematically positive and on the left side it is slightly negative. This about 10 μm shift is disturbing, but its origin could not be determined.

Figure 3.3 shows the distribution of the four fitted parameters of equation (3.2) as a func-

tion of ϕ_{local}. Since the original $\mathsf{L_3}$ function was independent of ϕ_{local} the $\mathsf{L_3}$ values can be seen as constants. From figure 3.3a it can be seen that in particular for tracks parallel to the wire plane ($\phi_{local} = 0$) the resolution is worse than the one estimated by the $\mathsf{L_3}$ function. The fact that the resolution is better for positive angles can be understood when considering the Lorentz angle, i.e. the about 18° angle of the drift line with respect to the electric field lines caused by the magnetic field. For ϕ_{local} angles above about 22.5°, the maximum angle for muons originating from the center of the detector, the resolution quickly deteriorates. An attempt was made to improve this by creating a new cell-map (Zillig 1998). This cell-map not only solves the large angle problem, but it has a significantly better single wire resolution relative to the segments. Unfortunately, however, it causes a systematic tilt of the segments with respect to the tracks, so the original $\mathsf{L_3}$ cell-map is still used.

The linear increase (P_2) is somewhat worse than the value estimated by $\mathsf{L_3}$. On the other hand the quadratic term near the sense-wire plane (P_3) is significantly lower, but the region is a bit larger.

3.1.2   Track matching

The track matching has the task of finding and combining the sub-tracks from the upper and lower octants which belong together. For this purpose, the method described in (Innocente *et al.* 1991) is used. It is a statistical combination of the two five-dimensional vectors (ζ_i and ζ_j) representing the measurement of the sub-track in the upper and lower octant along with the associated covariance matrices (V_i and V_j). The following χ^2 is used to assess the quality of the combination:

$$\chi^2 = \left(\zeta_i - \zeta_j\right)^T \left(V_i + V_j\right)^{-1} \left(\zeta_i - \zeta_j\right) \tag{3.4}$$

Before the vectors of the two sub-tracks can be compared they must be determined at the same plane. To achieve this, all sub-tracks are tracked backwards, against their physical direction, using GEANE (Innocente *et al.* 1991) until they reach the outside of the `MBAR` volume. This means that the comparison is performed in the gap between the upper octants and the water cooling of the aluminum coil.

For each combination of an upper and lower sub-track[*] the χ^2 from equation (3.4) is calculated. The combinations are sorted by their χ^2 value, in such a way that the combination with the lowest χ^2 value can be determined easily. The two sub-tracks constituting the best combination are then combined to a full track:

$$\zeta = \left(V_i^{-1} + V_j^{-1}\right)^{-1} \left(V_i^{-1}\zeta_i - V_j^{-1}\zeta_j\right) \tag{3.5}$$

$$V = \left(V_i^{-1} + V_j^{-1}\right)^{-1} \tag{3.6}$$

The combinations containing at least one of these two sub-tracks are removed before the procedure is restarted in a recursive fashion. Only combinations with a χ^2/dof below 250 are considered as physical.

---

[*]This excludes the low energy muons which are bent so strongly in the magnetic field that they do not enter the lower octants, but instead leave the detector via a different upper octant. These events are few and uninteresting, due to their low momentum.

The sub-tracks which remain at the end of the recursive procedure are left as unmatched tracks. The sub-track parameters and covariance matrix are thus used for the full track.

The resolution of the combined track (see equation 3.6) is thus at most improved by $1/\sqrt{2}$ compared to the best of the constituent sub-tracks. This is a clear improvement compared to the procedure followed in (van Mil 2001), but in principle one could further improve the resolution. When treating the upper and lower octants as one instead of as two detectors, the total path length (L) in equation (2.1) would increase by about a factor four. If, and only if, the components of the resolution function (see section 5.5) would remain constant, the resolution would improve by about $3^2/12^2 = 1/16$. The missing alignment system between the octants does, however, mean that the contribution from the alignment error will increase. The potential gain encouraged the development of a method following the swim-fit procedure through the full detector (Unger 2002)[*].

Measurement of covariance matrix elements

Using GEANE for both the swim-fit and the backtracking to `MBAR`, it allows for the usage of the swim-fit covariance matrix as input for the backtracking. For this type of backtracking GEANE uses a slightly different representation of the five-dimensional vector: ($1/p$, λ, ϕ, $x_\perp$, $y_\perp$), where p is the estimated momentum, λ and ϕ are the dip and azimuth angles relating to the momentum components as:

$$\begin{pmatrix} p_x \\ p_y \\ p_z \end{pmatrix} = |p| \begin{pmatrix} \cos\lambda\cos\phi \\ \cos\lambda\sin\phi \\ \sin\lambda \end{pmatrix} \qquad (3.7)$$

The location is defined by the two coordinates ($x_\perp$, $y_\perp$) in the plane perpendicular to the direction defined by the muon. The GEANE package provides routines to convert the track parameters as well as the covariance matrix from one representation to the other.

The covariance matrix propagated by GEANE can thus directly be used in the statistical combination (see equation 3.4). In spite of the many improvements to GEANE (Lavrijsen 2002), this simple procedure results in a poor matching efficiency[†] especially for data. In particular at high momenta the efficiency is low, e.g. at 1 TeV the matching efficiency for the data is only 70%. Attempts to scale the elements of the covariance matrix were made, but without a satisfactory result. As a last resort the elements of the average covariance matrix are determined statistically with:

$$V_{lm} = \frac{1}{2} \begin{cases} \frac{1}{N(N-1)} \sum \left(X_l - \bar{X}_l\right)\left(X_m - \bar{X}_m\right) & \text{for } l \neq m \\ \frac{1}{N-1} \sum \left(X_l - \bar{X}_l\right)^2 & \text{for } l = m \end{cases} \qquad (3.8)$$

$$X_l = \left(\Delta\zeta\right)_l \qquad \text{e.g. } X_2 = \lambda_1 - \lambda_2$$

where the sum is over the N events used for the measurements. The factor $\frac{1}{2}$ is there to split the full covariance matrix at the matching plane into the one for the sub-tracks. This

---

[*]The obtained gain to the resolution function is at the moment of writing still unclear.
[†]Section 6.1.1 describes the method used to determine the matching efficiency.
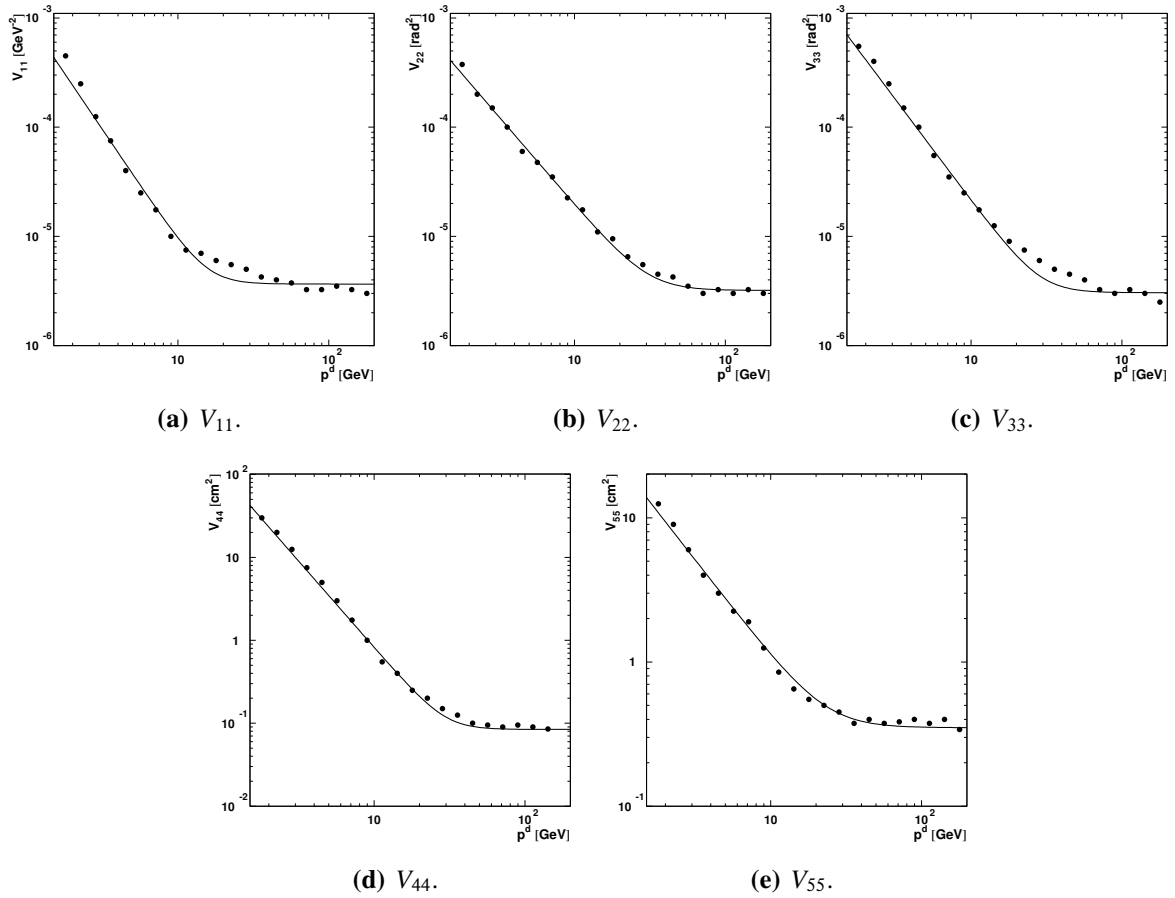
(a) V_{11}.   **(b)** V_{22}.   **(c)** V_{33}.

(d) V_{44}.   **(e)** V_{55}.

Figure 3.4: *The measured momentum dependence of the diagonal elements of the triplet covariance matrix. The fitted function is also shown.*

means that the covariance matrix determined event-by-event through GEANE is replaced by the *average* covariance matrix determined from the observed sample. The events used in this measurement do not go through HCAL. This requirement is imposed to restrict the covariance matrix to the measurement error only. The average covariance matrix is determined for triplets and doublets separately. Figure 3.4 shows the momentum dependence of the measured diagonal elements. The weighed average of the momenta at the matching plane is used as an estimator of the momentum. The measured values are fitted with:

$$V_{ii}(x) = \sqrt{\left(a \cdot e^{bx}\right)^2 + c^2} \qquad x \equiv \log_{10} p \qquad (3.9)$$

Figure 3.5 shows the measurement of the momentum dependence of the four non-zero correlation coefficients. It is important to notice that the elements which one would expect to be zero also are found to be zero. The fitted values for the covariance matrix are used as input to GEANE before the backtracking to the matching plane. In this way GEANE provides the additional contributions to the covariance matrix, due to the material of HCAL etc. In section 6.1.1 it can be seen that the obtained matching efficiency for all momenta is larger than 95%.

(a) $\rho\left(1/p, \phi\right)$.

(b) $\rho\left(1/p, y_\perp\right)$.

(c) $\rho\left(\phi, y_\perp\right)$.

(d) $\rho\left(\lambda, z_\perp\right)$.
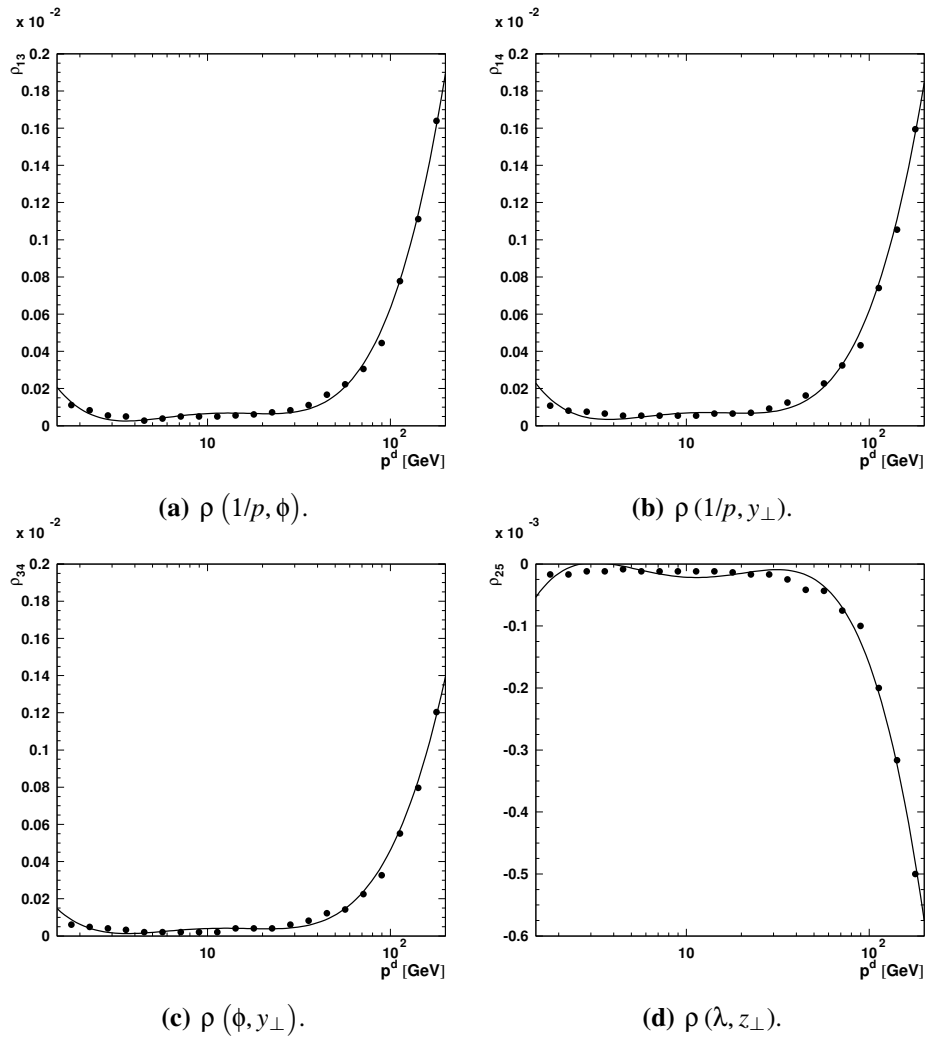
Figure 3.5: *The measured momentum dependence of the four non-zero correlation coefficients. The fitted fourth order polynomials are also shown.*

3.2 Event simulation

Estimating the acceptance of the detector is a very important part of the measurement of the muon spectrum. The complexity of the experimental set-up, however, prohibits an analytical calculation of the acceptance. Instead, as is common in almost all high energy physics experiments, the acceptance integral is evaluated with the so-called Monte Carlo method (Metzger 1992). This implies the creation of a computer model of the experimental set-up. In the computer model a virtual experiment can be performed. Comparing the outcome of this virtual experiment to the known input allows for an estimate of the acceptance (see section 6.1.5).

The computer model used here is created within the GEANT framework (Brun *et al.* 1994). The majority of the model is identical to the L3 simulation package. The differences in the experimental set-up, however, require a few modifications, for instance including the

Parameter	α_0	α_1	α_2	α_3	α_4	α_5	α_6	α_7	α_8
Value	-1.472	14.42	-47.92	80.94	-62.84	25.95	-6.014	0.7456	-0.0387

i	0	1	2
β_i	-1.903	0.1434	0.01450
x_i	21.258	-33.25	16.15
z_i	23.532	-27.212	10.521

Table 3.2: *The parameters used in L_3Cgen for the generation of the single muon events.*

additional scintillators on top of the magnet (Korn 1998), and the magnetic field in the coil and yoke of the magnet. The sections below provide a summary of the modifications.

3.2.1 L_3Cgen

An important element of the simulation is the generation of the muons participating in the virtual experiment. For this purpose a dedicated program, L_3Cgen, was written (Hebbeker & Korn 1998, Ramelli 2002). Instead of performing a full simulation of the air-shower cascade caused by the interaction of the primary cosmic ray with the atmosphere, L_3Cgen only generates muons. The muons are, however, generated according to the distribution obtained by a full air-shower simulation using CORSIKA 5.20 (Heck *et al.* 1998, Heck & Knapp 2001). One thus obtains a fast generation, while maintaining the best known angular and energy distributions. L_3Cgen generates single muon events, which makes it ideal for the acceptance estimates. The muons are generated with a fixed charge ratio of 1.3. The momentum distribution is generated according to:

$$\frac{dN}{dp} = \left(\alpha_0 + \alpha_1 L + \alpha_2 L^2 + \alpha_3 L^3 + \alpha_4 L^4 + \alpha_5 L^5 + \alpha_6 L^6 + \alpha_7 L^7 + \alpha_8 L^8 \right) / p^3 \tag{3.10}$$

where $L \equiv \log_{10} p$ and the nine[*] parameters can be found in table 3.2. The muons are generated homogeneously as a function of the azimuth angle, and with the following zenith angle dependence:

$$\frac{dN}{d\cos\theta} = 1 + \left(\beta_0 + \beta_1 l + \beta_2 l^2 \right) \left(1 - |\cos\theta| \right) \tag{3.11}$$

where $l \equiv \ln_e p$ and the three parameters can be found in table 3.2. The generation of the spatial coordinates is a bit more complicated. Points are generated homogeneously on a plane parallel to the surface, which contains the center of the detector. The boundaries of this rectangular plane are given by:

$$|x| < x_{max} = x_0 + x_1 \cos\theta + x_2 \cos^2\theta \tag{3.12}$$

$$|z| < z_{max} = z_0 + z_1 \cos\theta + z_2 \cos^2\theta \tag{3.13}$$

---

[*]Notice that the original parameterization (Hebbeker & Korn 1998) was modified (Ramelli 2002) to obtain a better description of the high energy part of the spectrum.

Type	Momentum interval [GeV]								Total
	5-20	20-50	50-200	200-500	500-10000	20-10000	50-100	100-200	
Real	1759985	989900	420480	668095	353155	620235	471090	840695	6123635
Ideal	179000	71600	100240	42540	7950	174000	-	-	575330

Table 3.3: *The number (in thousands) of generated events in the different momentum ranges. The numbers are provided for both the so-called "real" and "ideal" Monte Carlo production (see section 3.2.3) used in this thesis.*

where the values of the parameters can be found in table 3.2. This is done to minimize the number of tracks generated outside the sensitive volume of the detector. The generated point is propagated onto the surface plane along the line defined by the two angles.

When generating the muon momentum according to a steeply falling distribution, as is done here, only very few high energy events will participate in the virtual experiment. This results in large statistical errors on the high energy part of the quantities one wants to determine. This is not acceptable. To overcome this problem the full momentum range is divided into several smaller intervals (see table 3.3), within which the muons are generated according to equation (3.10).

3.2.2 Environmental description

The original GEANT description[*] from L3 only contained the detector, but for the measurement of muons originating in the atmosphere the overburden must be included. The energy loss of muons in the material combined with the steeply falling momentum spectrum makes this an important issue. The composition of the ground around the L3 site was studied prior to the construction of the LEP ring. In the area around the Jura mountains the ground consists almost entirely of molasse. The chemical composition and density of molasse was also studied and can be found in (van Mil 2001). The technical drawings of the cavern and access shafts were made available from CERN, which allowed for the correct addition of these structures to the GEANT description of the set-up (van Mil 2001).

To reduce the relative depth of the Aleph cavern the entire LEP tunnel is tilted by 1.39%. This means that the L3 experiment is slightly inclined compared to the surface. This feature is also included in the description. Figure 3.6 shows a schematic view of the surroundings of the L3 detector, as implemented in GEANT. Both the LEP- and side tunnels are omitted from the description, since they are below the line of sight for downward going muons. The main shaft contains several concrete structures, figure 3.6 shows that both the shielding of the elevator and stairway is included as well as the concrete beams[†] (half way up). The four so-called counting houses, located at the top of the shaft, are however not included. They contain part of the L3 electronics as well as the control room. It is estimated, however, that they only contain a rather modest amount of material, which can be neglected. The structures

---

[*]The GEANT description of the propagation of muons through matter has been updated according to (Bottai & Perrone 2001), which improves the cross-sections above 10 TeV.

[†]A row of concrete beams, known as the "plug", close off the hole during LEP running.
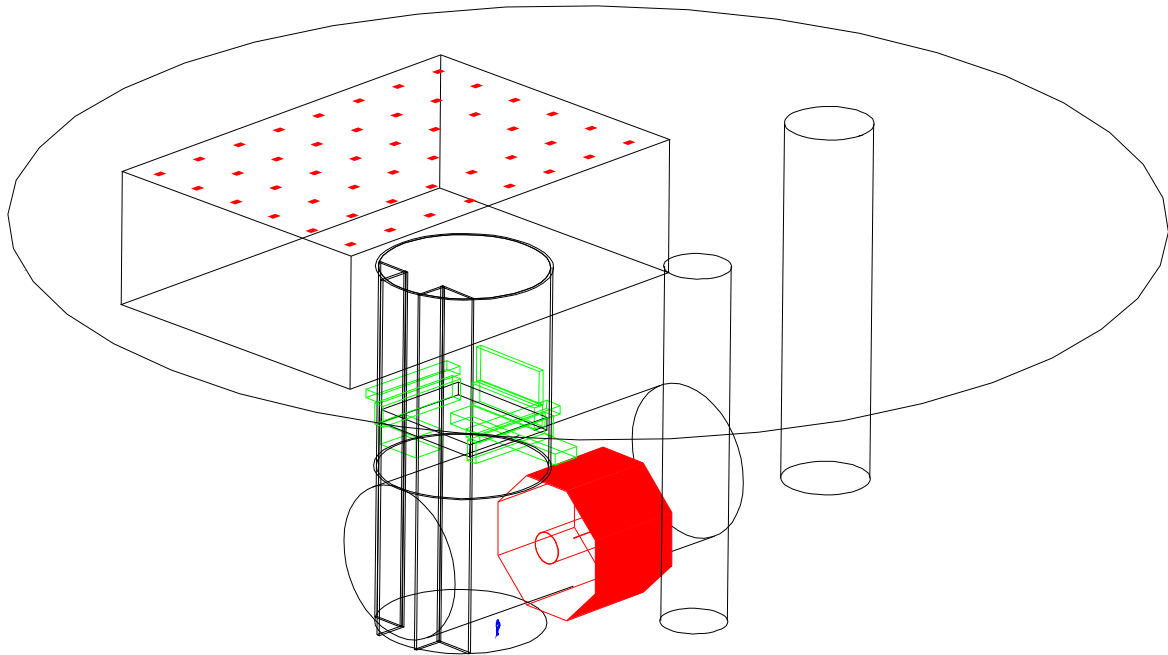
Figure 3.6: *A schematic view of the GEANT description of the surroundings of the L₃ detector. The main shaft can be seen in the foreground to the left, the side shaft is in the foreground in the center while the third shaft is visible further back to the right. The outline of L₃ detector can be seen shaded in the center. The large circle indicates the surface of the Earth. The large construction hall above the main shaft can also be seen.*

above the ground are also mostly neglected. There might be significant amounts of material placed at different locations in the area. But most of them are occasionally moved around, thus making it an impossible task to keep track of them. This adds an uncertainty to the low energy part of the spectrum, which must be estimated (see section 6.2.7). However, it is important to note that the surface as such is flat. The Jura mountains are only visible for zenith angles larger than about $70°$.

3.2.3 Detector simulation

The detector simulation has to predict the response of the detector due to the passage of particles through it. The vast majority of this complicated task was, however, already done by L₃. Only the scintillators on top of the magnet had to be added (Korn 1998, Yao 1999). The precise location of the modules, as measured by the CERN geometers, are used for the GEANT description. Also the fragmentation of the scintillators into tiles (see section 2.3.1) are implemented, thus correctly accounting for the small gaps between the tiles. Both the time slewing and time resolution are implemented according to the measurements performed in the laboratory. The simulation of the muon chambers has not changed much compared to the original L₃ code, although the P-hits are generated according to the measured single wire resolution (see section 3.1.1).

The simulation program can run in two different modes, known as the "real" and "ideal" Monte Carlo. As the word suggests, the ideal simulation produces the response of the perfect L3, i.e. a detector where all elements are operational and 100% efficient. The goal, however, is not to simulate what the ideal detector could do, but as accurately as possible to simulate the response of the physical detector. The real detector is not 100% efficient and does not have all elements operational. In the real simulation the measured scintillator efficiencies (see section 5.1) are applied. Furthermore, the hits from the dead cells (see section 5.2) are disregarded[*]. An additional problem with this type of imperfection is that they may vary with time. For the muon chambers for instance, an attempt is made each winter shutdown to repair inefficient P-cells, e.g. remove a broken wire or cleaning of the wires. At the beginning of the year these cells are put back on high voltage. After some time the problem may reoccur or a different wire might break, the voltage of the cell in question is then lowered or completely removed, thus making an efficient cell inefficient or completely dead. The overall efficiency of the detector thus generally deteriorates through the year, but it happens that a specialist during the year successfully gets the high voltage of a cell from its lowered state back to the nominal (Timmermans 1992). Ideally one would keep track of the changes to the set-up and simulate events for the different states of the detector. One then has to take care of generating an amount of events per state, which is proportional to the amount of integrated live-time the real detector was exposed to in this state[†]. For the muon chambers L3+Cosmics, however, chose a more simple approach. Hits from cells, which at the end of the year are found to be less efficient than 80%, are killed for both data and Monte Carlo events for the full year. It was estimated that this approach causes a loss of about 10% of the data. The scintillator efficiency on the other hand is stable apart from the first part of 1999, where several interventions were made to improve the magnetic shielding and thus the efficiency. The data from that part of 1999 is not used in the analysis presented here (see section 4.1), and thus no Monte Carlo production is needed for that period.

---

[*]In practice the killing of the hits from dead cells is performed in the early phase of the events reconstruction. This is identical to what happens in the reconstruction of the data events.

[†]This type of scheme is in fact applied for the L3 e^+e^- Monte Carlo production.

Chapter 4

Selections

This chapter describes the selections used for the analysis of the 1999 data. Firstly, the conditions for selecting a run, subsequently, the actual event selection is discussed.

4.1 Run selection

To achieve a precise measurement of the muon spectrum it is preferred to have very stable running conditions over a long period of time. Naturally, in real life the situation is more complicated. An experiment running 24 hours a day for several months in a row will encounter more or less serious hardware problems along the way. When a problem occurs one will typically stop the data taking while solving it. This procedure was not always followed in the L$_3$+Cosmics experiment, thus making an off-line run selection mandatory. The reason for not stopping the DAQ was twofold:

- The collaboration is also interested in rare events, such as muons from gamma ray burst photons and the decay of exotic particles (Chen *et al.* 1997). In fear of missing these spectacular events, it was standard procedure to keep the DAQ running whenever possible. Data taking thus continued through periods with smaller problems, or problems which were outside the control of the experiment (e.g. LEP induced background in the scintillators).

- Not having a dedicated shift-taker led to the fact that not all problems where noticed and tackled right away.

The large volume of monitoring data available in the on-line databases provide a good set of oberservables, which are used off-line, in order to perform the run selection. Below a description of the selection criteria is given. To ensure stable conditions the criteria used for this analysis are very strict. The criteria for accepting a run are:

DB info: The database must have valid monitoring information during the run regarding: the rate encountered in the scintillators, the magnetic field, the muon chamber high voltage and discriminator thresholds, and the scintillator high voltage. In this group the reading of the muon chamber discriminator thresholds is causing most problems.
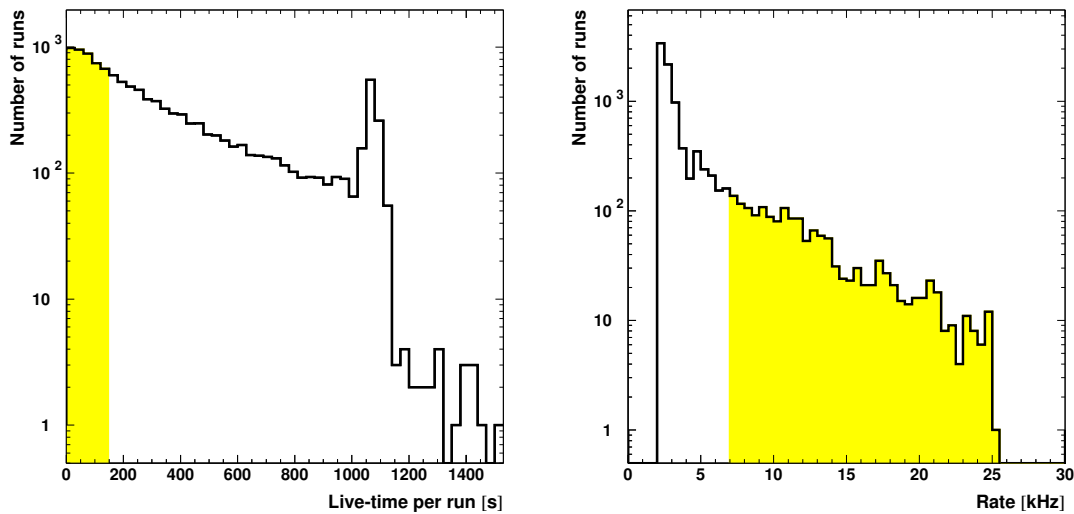
(a) Live-time distribution. The peak at about 1100 s corresponds to the limit on the file size, the runs beyond were taken with a different trigger setting.

(b) The distribution of the maximum scintillator rate per module during a run. The nominal background rate of about 2 kHz per module can be seen as the peak to the left.

Figure 4.1: *The distribution of two of the most important criteria in the run selection. The plots only show the runs which satisfy all but the criteria in question. The shaded area indicate the runs removed by the cut.*

Run status: The average trigger rate during the run must not exceed 600 Hz. This cut serves as an additional security to avoid runs where the magnet was off*. The number of events must exceed 1000, and the live-time must exceed 120 s (see figure 4.1a). Very short runs are indicative of hardware problems. Among these cuts the cut on the live-time removes the largest fraction of live-time.

SCNT rate: The largest absolute scintillator rate (see section 2.4.3) per module during the run must not exceed 7.0 kHz (see figure 4.1b). Large rates are caused by LEP synchrotron radiation. Situations with a large amount of LEP induced noise in the scintillators have two negative effects:

- The reconstruction efficiency goes down. This is caused by the increased chance of picking the wrong scintillator hit as starting time. A bad starting time will reduce the probability of the pattern recognition finding the track. Without a track the correct scintillator hit cannot be determined.

- The scintillator efficiency goes down. This is caused by the 300 ns dead time of the L3CD. A larger rate thus increases the probability of a real hit falling within the dead-time of a noise hit. At a noise rate of 16.7 kHz this probability is 0.5%.

---

*When the magnet is on, low energy muons and electrons are bend so hard that they do not intercept enough P-chambers to cause a trigger. This is not the case when the magnet is off. The particles only occupy a small energy interval, but due to the steeply falling spectrum this interval contains a relatively large number of particles

Criteria	Fraction of	
	runs [%]	live-time [%]
DB info	2.9	3.6
Run status	27.8	4.2
SCNT rate	15.1	19.5
Basic	14.0	17.1
Occupancy	2.6	2.0
Manual	8.1	6.4
Total	55.4	42.5

Table 4.1: *The fraction of runs and integrated live-time which was removed by each of these criteria. The numbers are obtained for the period after July 15th.*

A cut of 7.0 kHz is used instead of 16.7 kHz, since a study of the scintillator efficiency as a function of the noise rate (Unger 2002) has indicated an additional loss of scintillator hits. It is not clear if this loss occurs in the L3CD or in the CPC card.

Basic: The current in both the barrel and toroid magnet must be nominal. The MUCH and scintillator HV must be at nominal. The MUCH discriminator thresholds must be at their nominal values. This information is obtained from the L_3 database, which is only available when L_3 is taking data. Among these criteria the P-chamber HV is the most common source of problems.

Occupancy: Every three minutes the on-line monitor (see section 2.4.3) measures the rate of occupancies per FELink (i.e. how frequently a FELink submitted data). This information can be used to ensure that the read-out chain was operational, and that HV and discriminator thresholds where nominal. It turned out that the fraction of FELinks which gave data in this interval (denoted *occupancy*) was a good way to condense the large data volume. A run is selected if the lowest *occupancy* is larger than 99.9%.

For the *occupancy* to be statistically significant it is important that the on-line monitor actually has 3 minutes of data to integrate over. Occasionally the DAQ has a long deadtime between two runs, which reduces the effective integration time of the intervals at the boundaries of runs. To overcome this problem the first and last database entry per run is discarded if its *occupancy* is less than 99.9%. This on the other hand created a set of short runs without a valid *occupancy*, for these runs the last valid *occupancy* reading is used.

Manual: A small set of runs are manually excluded, these runs typically have severe hardware problems. Most of these cases where understood when reading the logbook.

For a more thorough discussion of the criteria see (Ladron 2000)[*]. In the first month of running it was noticed that the scintillator efficiency was lower than what had been measured

---

[*]The actual criteria as described above differ slightly from the ones described in (Ladron 2000).

during the installation. This was traced back to problems in the magnetic shielding of the PMTs. This finding initiated a series of interventions, in order to improve the shielding. The last intervention took place on July 15th, 1999. To avoid these problems only data taken after this date will be used in the analysis[*]. The total and individual contributions to the reduction in the data volume due to the run selection can be found in table 4.1. To ensure that the run selection achieved its goal of establishing stable running conditions, a study of the rate of selected events (see section 4.2 for the description of the event selection) was performed. Figure 4.2 shows the rate of selected events above 50 GeV as a function of the run number. In general the rate is very stable, but around run 55000 some fluctuations can be seen. Overall the rate is slightly lower at the end of the data taking compared to the beginning. Figure 4.2 indicates that these effects are correlated with the changes in the atmosphere. The effective atmospheric temperature (T_{eff} see figure 4.2 bottom) is defined as the average temperature in the atmosphere weighed by the pion density[†] as a function of the column depth. T_{eff} is calculated (Hebbeker 2000) using the balloon data acquired at Payerne, which is about 100 km from CERN.

Figure 4.3a shows the distribution of the rate of selected events with a momentum at the surface larger than 50 GeV for runs with more than 3200 selected events. Both the measured relative width (σ_m) and the expected relative width (σ_t) are shown, where the expected relative width is estimated as $1/\sqrt{<N>}$. These two value do not agree for the full sample but do when the atmospheric conditions are stable (see figure 4.3c). This shows that the run selection ensures stable conditions, but that the atmospheric variations cause a significant effect. The discrepancy can be used as an estimator of the influence of atmospheric conditions on the measured rate and thus also on the flux:

$$\Delta_{atm} = \sqrt{\sigma_m^2 - \sigma_t^2} = 2.5 \ \% \tag{4.1}$$

This estimate must be considered as a conservative estimate since the used rate has not been subject to all the corrections which are applied in the flux analysis (see chapter 6).

Out of the 3127162206 events recorded after July 15th 1778360039 events were selected. The integrated live-time of the selected runs corresponds to 4057152.4 s. The average pressure and effective temperature weighed by the live-time of the selected runs is 963.1 mbar and 224.7 K, respectively.

4.2 Event selection

The measurement of the shape of the muon momentum spectrum ($\approx p^{-3}$) induced by cosmic rays requires a good momentum resolution. With the large data set available it is possible to enforce strict cuts to improve the resolution. The details of the study of the momentum resolution along with the obtained resolution are discussed further is section 5.5 on page 76. Cuts applied to obtain a high quality event sample are described below in some detail. Table 4.2 shows the loss of events for each of the cuts applied.

---

[*]The first run used in the analysis is number 34351.
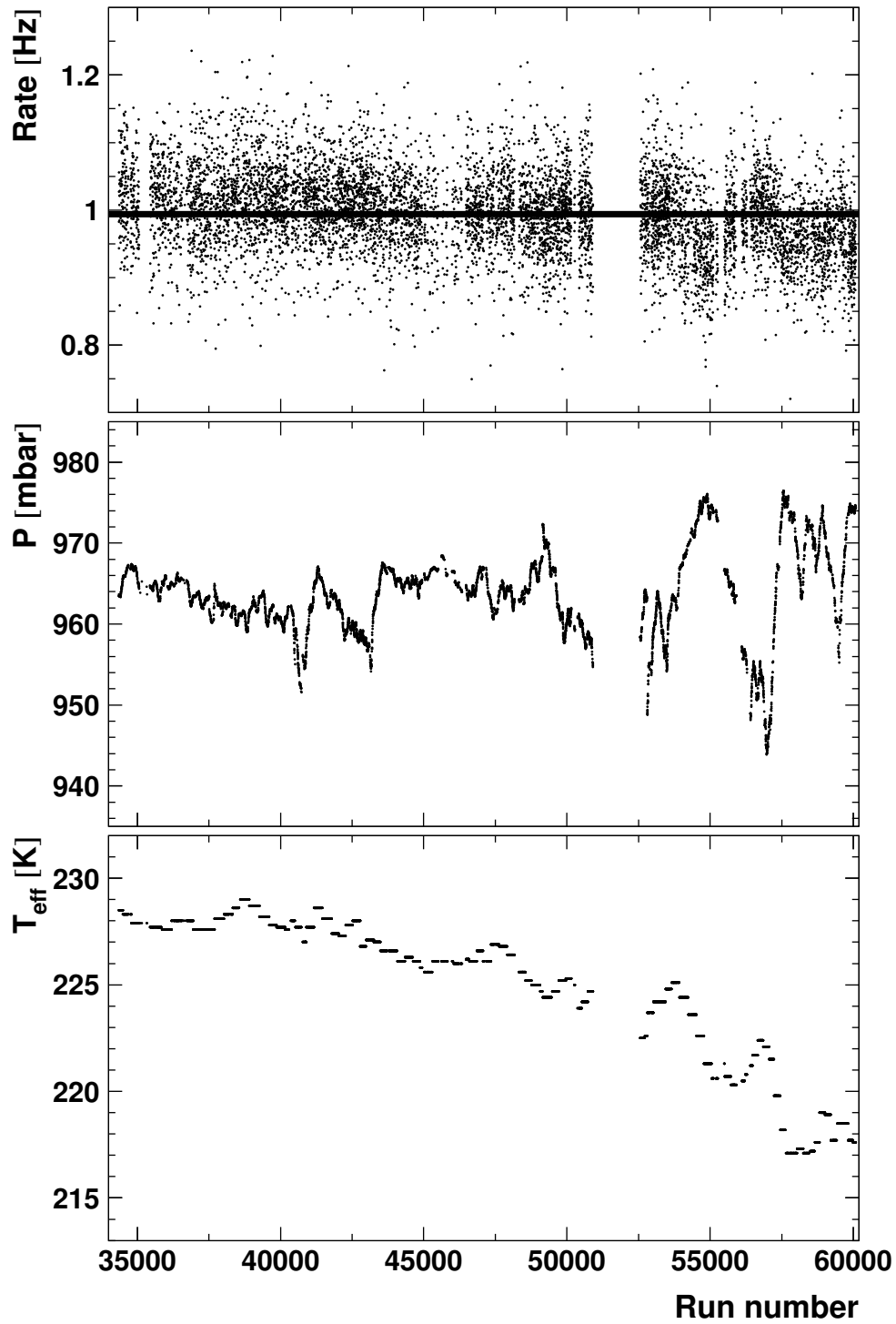[†]The kaon contribution is thus neglected.

Figure 4.2: *The rate ($p^s > 50$ GeV), pressure and effective temperature as a function of the run number. The average rate is indicated by a line in the upper plot.*
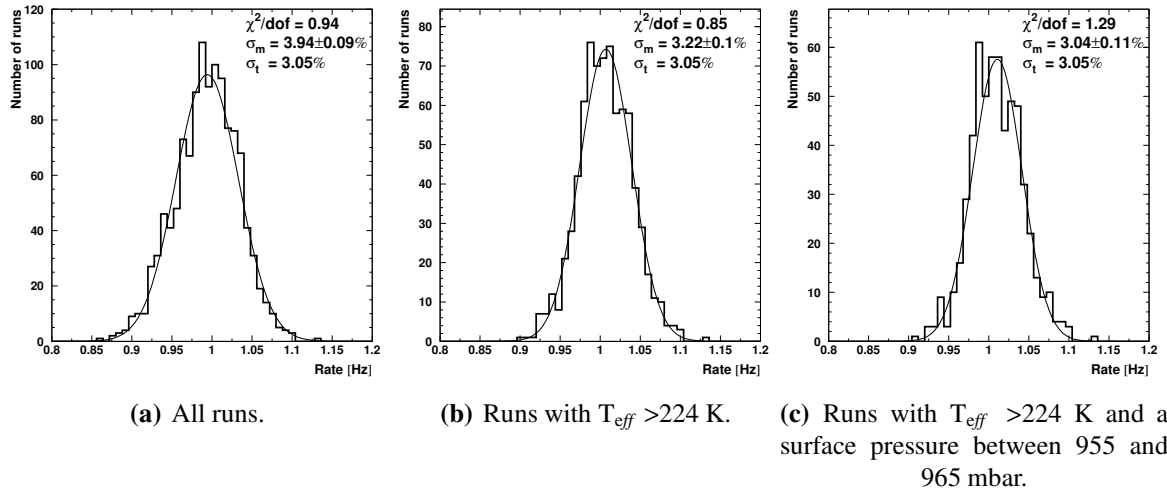
(a) All runs.

(b) Runs with T_{eff} >224 K.

(c) Runs with T_{eff} >224 K and a surface pressure between 955 and 965 mbar.

Figure 4.3: *The distribution of the rate of selected events with a minimal momentum at the surface of 50 GeV. Only runs with more than 3200 selected events are used, this is done to reduce the statistical error on the rate estimate. The distribution is shown for the set of runs without any additional criteria, as well as for two cases where the atmospheric conditions are stable (see figure 4.2). First limiting the effective temperature and then also the pressure. σ_m is the measured width and the σ_t is the expected width.*

Criteria	Loss [%]	
	Data	**Monte Carlo**
Class 1	26.94	–
Reconstruction	9.64	68.74
Topology	33.84	36.25
`MASTER/SLAVE`	9.61	8.21
Two sub-tracks	59.42	71.08
Coincidence gate	6.45	–
P-triplet	65.30	75.41
Z-layers	8.47	2.94
Scintillator match	9.29	4.88
P-hits	33.87	20.89
Local ϕ	11.86	11.38
Circle fit χ^2/dof	32.78	28.17
Total	98.31	99.40

Table 4.2: *The loss due to each cut. The cuts are imposed one after the other. For each cut the loss of events is taken relative to the number of events satisfying all previous criteria. **Total** corresponds to the full loss of the selection.*

Trigger class: Only events of trigger class 1 are used. As described in section 2.3.5 on page 34, trigger class 1 is the P triplet class for events with a scintillator hit. Doublets have a significantly worse resolution and are of no interest for this analysis. The same is true for the so-called cross-octant tracks, where a doublet in one octant and a singlet in the neighboring octant constitute a triplet. Without a proper inter-octant alignment system these tracks have a poor intrinsic momentum resolution. This cut is only applied to data.

Due to the loose trigger requirement, requiring a class 1 trigger removes a large fraction of the data. For Monte Carlo no trigger requirement is imposed to avoid having to correct for the efficiency of the trigger simulation.

Reconstruction: An event must obviously have been reconstructed to assess if it was caused by a muon, and if so, to estimate its momentum and direction. The loss due to this requirement is large for Monte Carlo, not because the reconstruction efficiency is so low, but because most low energy muons are stopped in the molasse and because the generator surface is significantly larger than the active area of the detector.

Topology: Tracks found in the horizontal octants are neglected. There are very few tracks in the horizontal octants, which makes the time calibration of these octants difficult (Ma 2002) and thus less reliable. In addition tracks in octant 11 are rejected due to a problem with one of the drivers of the t0-calibration system. The last cell on both sides of a P-chamber has, due to the geometrical constraints, an electrostatic configuration which is different from the other cells. The cell-map, i.e. the function which converts the measured time into a position, does not include this difference. Tracks which have a segment in such a side cell are excluded. These requirements cause a loss of about 35% in both data and Monte Carlo.

Master-slave crossing: Each logical octant consist of two physical octants (`MASTER` and `SLAVE`). For 45 GeV muons originating from the vertex it is geometrically impossible to cross both these octants. Thus there was no need for L3 to install an alignment system between the `MASTER` and `SLAVE` side of an octant. For cosmic muons this geometrical constraint is gone, and there is nothing in the trigger to prevent recording this type of tracks. Without an alignment system a precise momentum measurement is impossible, thus these tracks must be removed from this analysis. In fact this cut removes only very few tracks. The majority of these tracks are already removed by the intrinsic quality criteria of the reconstruction program. This requirements cause a loss of about 9% in both data and Monte Carlo.

Two sub-tracks: A track is required to have been measured in both the upper and lower octants. The resolution of the combined track is up to a factor $\sqrt{2}$ better than the best resolution of the sub-tracks. This cut also reduces the chance of assigning the wrong Z-track to a P-track. A very large fraction of events is removed by this cut, but it is needed to obtain a good momentum resolution. The difference in the loss between data and Monte Carlo could in part be explained by the geometrical constraint imposed by the trigger requirement.
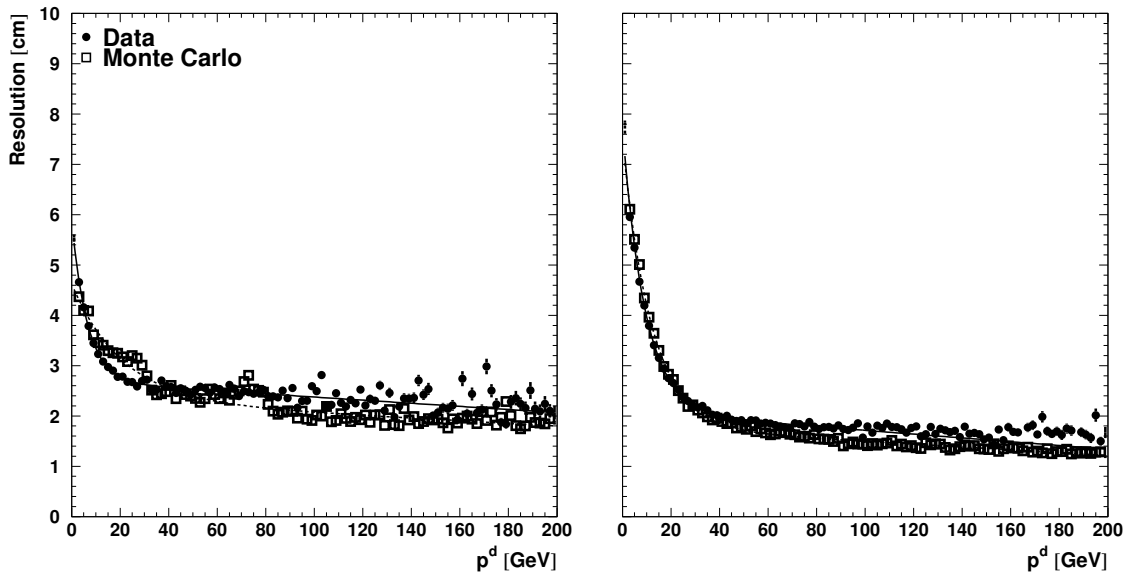
(a) Resolution in the *x* direction.   (b) Resolution in the *z* direction.

Figure 4.4: *The scintillator matching resolution as a function of the measured and generated momentum at* `MBAR` *for data and Monte Carlo respectively. The Monte Carlo resolution is slightly better than the one for data. The distributions are fitted with an exponential plus a first order polynomial, these curves are also shown.*

Coincidence gate: The two time measurements per scintillator module must be less than 7 ns apart (see figure 5.2). This cut reduces the probability of using noise hits, and thus improves the momentum resolution. This cut is only applied to data.

Triplet: Each sub-track must have been reconstructed as a triplet, i.e. the track must have crossed all three P-layers of the same physical octant. With the optical alignment system (see section 2.2.4) connecting these chambers, this category of tracks provide the best momentum resolution. This cut also removes a very large fraction of events in both data and Monte Carlo, but it is essential for a good momentum resolution. A possible explanation for the larger loss of Monte Carlo events is that the data trigger already has imposed a single triplet requirement.

Z-layers: Each track must have hits in at least three out of the four layers. This cut ensures good Z-tracks, thus a good conversion of the momentum transverse to the axis of the detector to the full momentum. The difference between the losses in data and Monte Carlo is indicative of an overestimate of the Z-chamber efficiency in Monte Carlo.

Scintillator matching: The two sub-tracks must be matched with the same scintillator module. This module must be the same as the one the combined track goes trough while back-tracked to the surface. A scintillator hit is said to match a track when either the track passes through the module or it passes within 2σ of the edge (see figure 4.4) of the nearest cassette. The discrepancy between the losses in data and Monte Carlo can

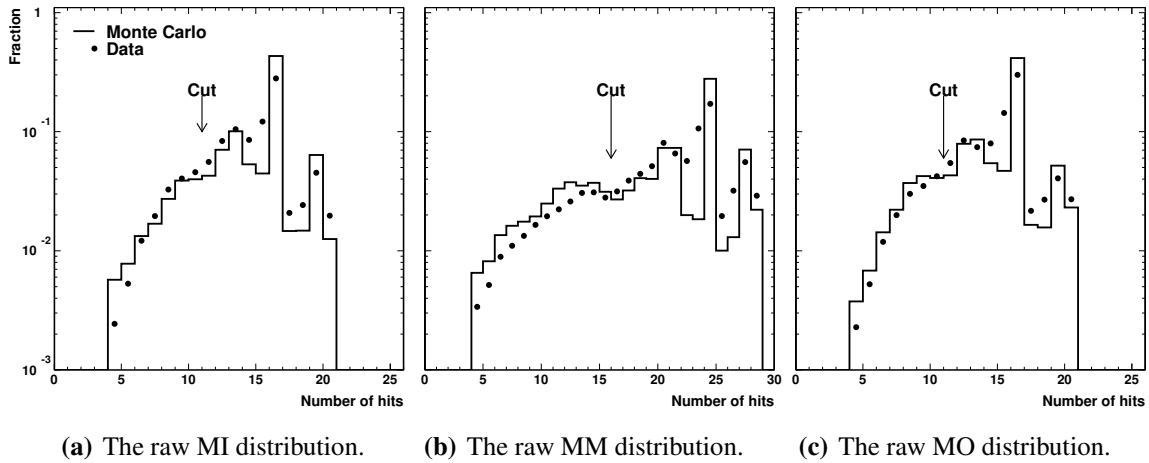**(a)** The raw MI distribution.   **(b)** The raw MM distribution.   **(c)** The raw MO distribution.

Figure 4.5: *The distribution of the number of hits per segment for the three P-chamber types.*

be explained by the superior track quality in Monte Carlo, thus a better backtracking. Furthermore, the scintillator noise may not be adequately simulated.

P-hits: Each P segment must contain more than about 70% of the typical number of hits. A MI or MO segment must have more than 10 hits, for MM it is more than 15 hits (see figure 4.5). Apart from improving the resolution this cut also reduces the effects of the trigger efficiency (see section 5.3 on page 73), since the requirement per segment is stronger than the minimum of 9 hits per layer which is imposed by the trigger. The difference between the losses in data and Monte Carlo is indicative of an overestimate of the P-chamber efficiency in Monte Carlo.

Local ϕ: The angle between a track segment and the wire plane is called ϕ_{local}. As was seen in section 3.1.1 on page 46, the cell-map function gives a poor single wire resolution for large angles. Each segment on a track must thus satisfy $|\phi_{local}| < 25°$. On figure 4.6 the raw distribution of the ϕ_{local} can be seen.

Circle fit: In the reconstruction program a circle is fitted (Karimäki 1991) to all the hits on a sub-track, this fit results in a χ^2/dof. Figure 4.6b shows the distribution of the largest value of χ^2/dof for the two sub-tracks. Removing part of the tail improves the momentum resolution, which inspires a cut whereby about 10% of the events are removed. One of the reasons for a poor reduced χ^2 is that in some cases one of the segments of the reconstructed track in reality is created by a different charged particle (e.g. a δ-electron). These tracks in general have a very poor momentum resolution and are thus not useful for this analysis.

The shape of the χ^2/dof distribution is broader for low energy tracks than for high energy tracks. Thus a momentum dependent cut is necessary to avoid a large momentum dependence in the loss of events due to this cut. The distribution of the χ^2/dof value which removes 10% of the events as a function of the momentum at MBAR is fitted with a constant plus an exponential (see figure 4.7a). The zenith angle dependence of
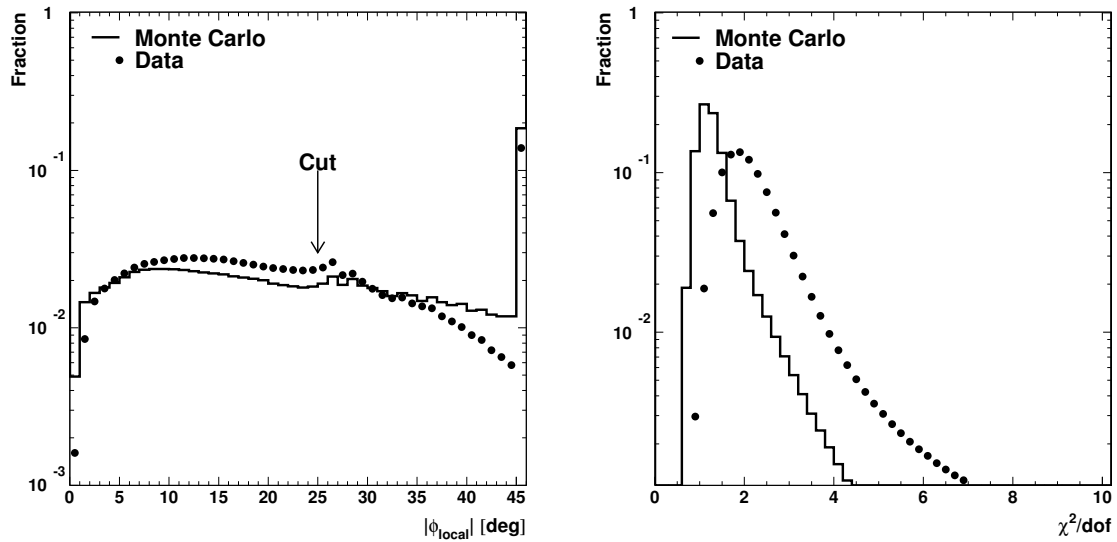
(a) The raw distribution of the maximum of the $|\phi_{local}|$ of the three P-segments. The bin at $45°$is an overflow bin. The large fraction of events in this bin is due to a well understood bug in the reconstruction program.

(b) The distribution of the largest circle-fit χ^2/dof of the two sub-tracks per track.

Figure 4.6: *The distribution of raw maximum $|\phi_{local}|$ and circle-fit χ^2/dof distributions.*

the χ^2/dof distribution can not be neglected. Figure 4.7b shows the variation of the cut at 100 GeV as a function of $\cos\theta$. The exponential part of the fitted function does not vary significantly, thus only the constant part varies with the zenith angle.

For most of the distributions, which are subject to either explicit or implicit cuts, the agreement between data and Monte Carlo is far from being satisfactory. Section 6.1.3 describes the correction necessary due to this disagreement.

The loss of events is drastic, but necessary to achieve a good momentum resolution. In total 15310046 events passed the selection.
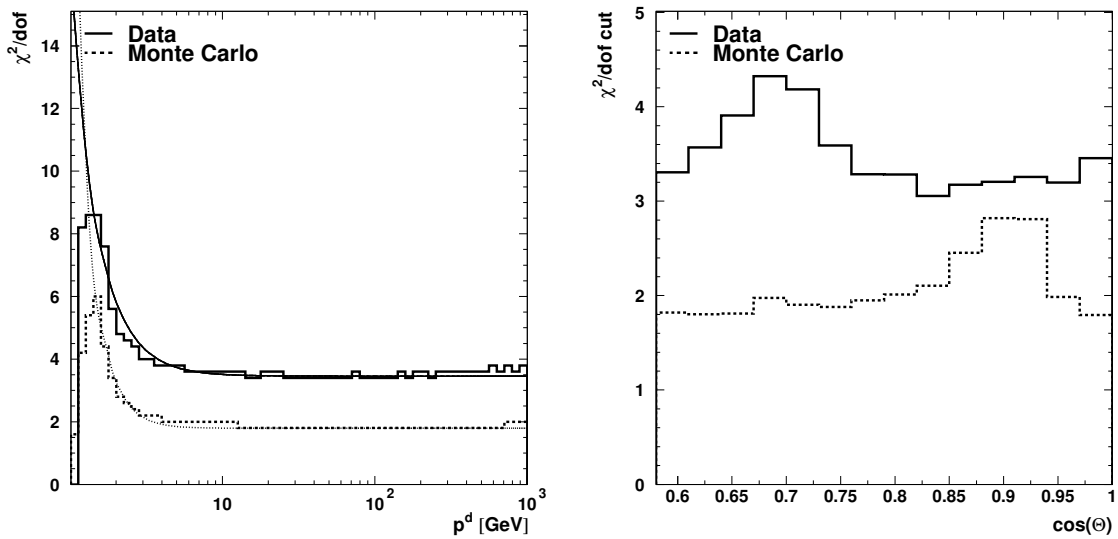
(a) The χ^2/dof cut which removes 10% of the events as a function of the MBAR momentum for the most vertical zenith bin. The fitted constant plus an exponential is also shown.

(b) The cut on the circle-fit χ^2/dof at 100 GeV as a function of cosine to zenith angle.

Figure 4.7: *The momentum and zenith angle dependence of the reduced χ^2 cut for both data and Monte Carlo . The wider χ^2/dof distribution for Monte Carlo around $\cos(\theta)$ of 0.9 is caused by a problem in the inverse cell-map. The data shows a wider distribution around $45°$, the origin of which is not clear.*

Chapter 5

Performance studies

To ensure the integrity of the data set many checks were performed. Some of these showed problems in the hardware, which were solved during data taking. Other required larger modifications, which were carried out in the winter break before the 2000 data taking[*]. The large data set enabled a very thorough check on the performance of the reconstruction program.

In this chapter some of the studies most relevant for the flux measurement are presented, which includes the measurement of the detector efficiencies.

5.1 Scintillator efficiency

For the measurement of the absolute flux of cosmic ray muons it is crucial to know the efficiencies of the detector components, which includes the scintillator efficiencies.

In total 34 scintillator modules (see section 2.3.1) are installed on top of the L_3 magnet. The efficiency of each of these modules must be known accurately. During the production, the efficiency of each cassette is measured in the laboratory using a small scintillator coincidence counter. While installing on the L_3 magnet the efficiencies of the cassettes are measured again. For some of the modules the measurement is repeated in the nominal condition with the magnet turned on. The stray field of the L_3 magnet has a potential effect on the path of the electrons inside the PMT, thus influences the gain and the efficiency as well as the effective area of the PMT face. With proper shielding of the PMTs this effect can be reduced substantially.

The best way to ensure a correct measurement of the muon detection efficiency of the scintillator system, is to use the muon chambers to define an unbiased sample of muons. The yoke and coil of the L_3 magnet serve as a very effective electron shield. The normal DAQ system is used to record the events. Any inefficiency in the electronics or DAQ will thus be correctly included in the measurement. The logical OR of trigger class 1 and 3 (see table 2.1) provide a sample of events without scintillator requirement. The efficiency is given by the fraction of tracks which has passed a given module, and has an associated scintillator hit.

---

[*]This period is not used in the analysis presented here. In 2000 the LEP beam energy was increased to its maximum, this resulted in a high noise level in the scintillator on top of the magnet.
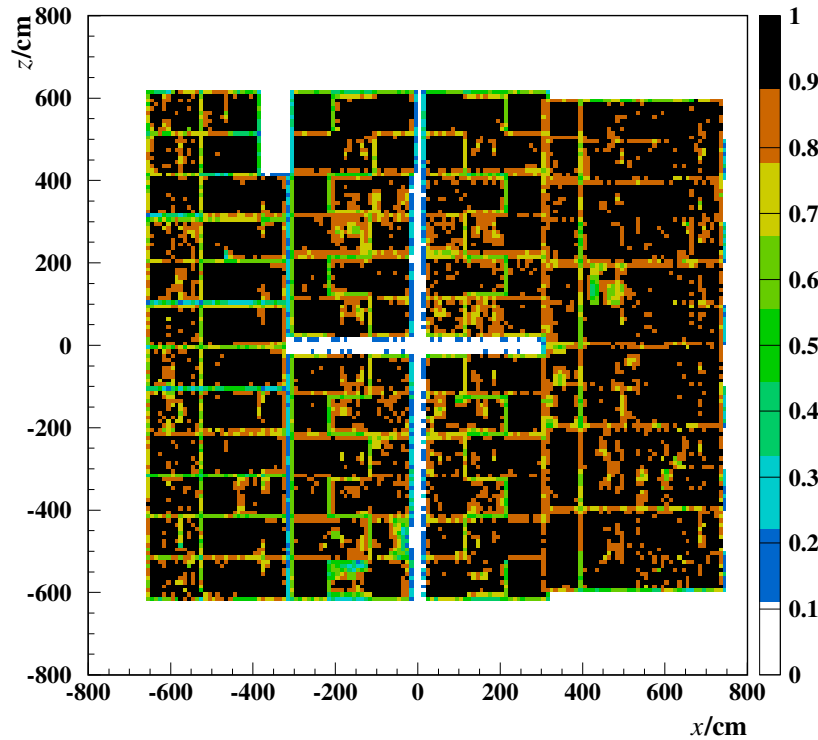
Figure 5.1: *The detection efficiency vs x and z. The gaps between the modules are clearly visible, which indicates a good pointing ability. The beam-pipe runs along the z-axis. The walk way on top of octant 2 as well as the two missing cassettes of module 10 on side 3 (-350,500) can easily be seen.*

5.1.1 Reconstruction method

In order to estimate the scintillator efficiency, events with and without a scintillator hit must be treated equally during the reconstruction. With the standard reconstruction program it is impossible to reconstruct events without a starting time, i.e. a scintillator hit. However, it is possible to obtain a rough starting time for events where the track passed a sense plane in one of the P chambers (see section 2.2.1). A dedicated reconstruction mode was written to implement this idea, see (Unger 1998) for the details of the algorithm.

The first step in this process is the search for a wire-plane crossing. When a track passes a sense-wire plane the raw time measurement from the wires has a minimum at the wire closest to where the muon crossed. A kink finding algorithm is used to identify these events. In total 48.5% of the events are found to have a sense-wire plane crossing, the remaining events are useless for this purpose.

The minimum drift-time at the crossing gives a time estimate which is good enough to be able to perform the normal pattern recognition, segment matching etc.. It is, however, not the best one can obtain. Therefore at the end of the normal refits, a series of different starting times are tried around the initial guess. The one which results in the best χ^2/dof

Module	Side					
	1	**2**	**3**	**1**	**2**	**3**
1	95.46±0.43	96.68±0.43	98.37±0.25	87.05±0.12	89.29±0.10	90.83±0.08
2	92.13±0.51	94.12±0.55	99.05±0.20	81.77±0.15	83.19±0.16	94.37±0.05
3	98.70±0.44	95.67±0.37	97.38±0.64	93.45±0.11	85.03±0.11	90.62±0.16
4	97.56±0.56	96.54±0.33	97.44±0.60	91.18±0.13	88.12±0.09	90.95±0.16
5	96.76±0.38	96.31±0.45	96.15±0.38	88.24±0.11	89.55±0.10	87.01±0.11
6	97.71±0.30	95.74±0.49	97.77±0.30	89.91±0.10	86.33±0.14	90.27±0.09
7	95.71±0.86	95.38±0.40	97.80±0.62	86.97±0.23	86.43±0.11	91.30±0.16
8	96.34±0.78	93.51±0.42	97.33±0.67	89.42±0.18	85.08±0.10	89.36±0.21
9	97.97±0.36	96.51±0.51	98.57±0.27	90.93±0.10	89.25±0.12	90.57±0.09
10	97.31±0.37	97.81±0.37	96.77±0.45	89.19±0.12	91.99±0.08	90.35±0.11
11	96.50±0.94	91.35±0.59		88.22±0.25	82.70±0.15	
12	97.44±0.75	97.93±0.25		88.46±0.22	91.49±0.06	
	|ΔT| < 25 ns			**|ΔT| < 7 ns**		

Table 5.1: *The scintillator efficiency in %. The values are given for a coincidence gate of both 25 and 7 ns.*

from a straight line fit to the segment with the sense-wire plane is used to reconstruct the final track. This track is then propagated back to the scintillator plane. Now one can check if that scintillator, where the track passed through, gave a hit. A set of cuts is applied to the muon tracks. This is done to improve the backtracking ability. Using these events with a scintillator hit, the time resolution of the method can be determined to be about 5 ns. This should be compared to the single wire resolution of 250 μm (see section 5.5.1), which in time corresponds to a resolution of 5.2 ns. It would thus seem, that the expected $1/\sqrt{n}$ improvement, due to the n measured points on a segment, is not achieved.

5.1.2 Results

In figure 5.1 the measured efficiency can be seen as a function of x and z. From the figure it is clear that the measured efficiency is artificially lower at the edges of the modules. This is due to the misidentified tracks which in reality went through the gaps between the modules. To overcome this problem the efficiency per module is determined from the inner part of the module. Notice that this also includes the small gaps between the tiles of the cassettes.

The light from each scintillator module is measured with two independent readout channels. Only when a coincidence occurs, the hits are accepted. This is done in order to reduce the sensitivity to the thermal noise in the PMTs. In the hardware the coincidence gate is rather wide, since the relative timing of the two channels is unknown. In the reconstruction program the measured times are corrected for the relative timing, whereby the true time difference can be obtained. A hit is only accepted if the difference is less than 15 ns. If one removes this restriction the measured efficiency is in good agreement with the simple efficiency measurement with the coincidence counter.
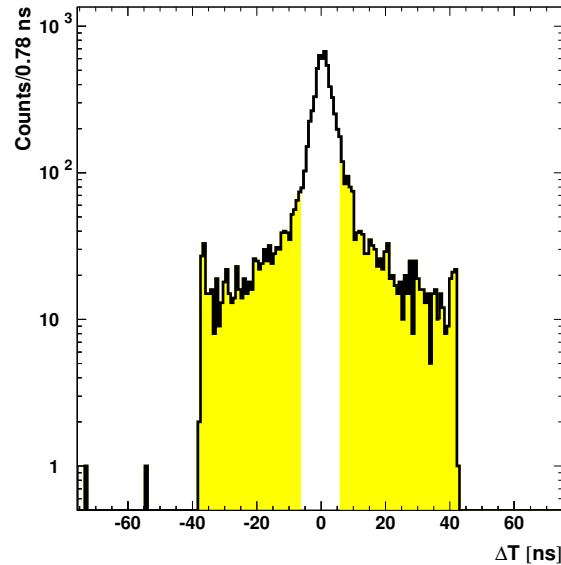
Figure 5.2: *The distribution of the difference between the two time measurements for one of the scintillator modules. The shaded area indicates the events removed by the 7 ns cut. The wide tails of the distribution are due to thermal noise in the PMTs.*

The measured efficiencies per module can be seen in table 5.1. The large drop in efficiency when imposing the 7 ns coincidence gate is cause by the large non-Gaussian tails in the ΔT distribution (see figure 5.2). The inefficiency of each module is applied in Monte Carlo by removing a fraction of the hits. For historical reasons the efficiencies with a 25 ns coincidence gate are used, whereas for data the applied coincidence gate is 15 ns. As was discussed in section 4.2, the analysis presented here imposes an even stronger cut of 7 ns. The Monte Carlo events are thus weighed with the ratio of the two efficiencies in table 5.1.

5.2   Muon chamber efficiency

The large data set enables a thorough investigation of the efficiency of the muon chambers. Operating a complicated system of this size and age means that one has to sacrifice individual elements in order to keep the full system running. In practice several cells are, for one reason or an other, unable to hold full voltage. These are either kept at a lower voltage or are completely disconnected. A list of these cells is maintained by the L3 muon group in their database.

The measurement of this inefficiency (Unger 2002) is done in much the same way as the scintillator efficiency measurement. Tracks with segments in at least two of the three layers of an octant are used to measure the efficiency of the third layer. In figure 5.3 on the next page the result of the measurement of the P-chamber efficiency can be seen. It is the case for this measurement, as well as for the time calibration (Ma 2002), that the amount of data in the horizontal octants is insufficient for a proper measurement. The average P-segment
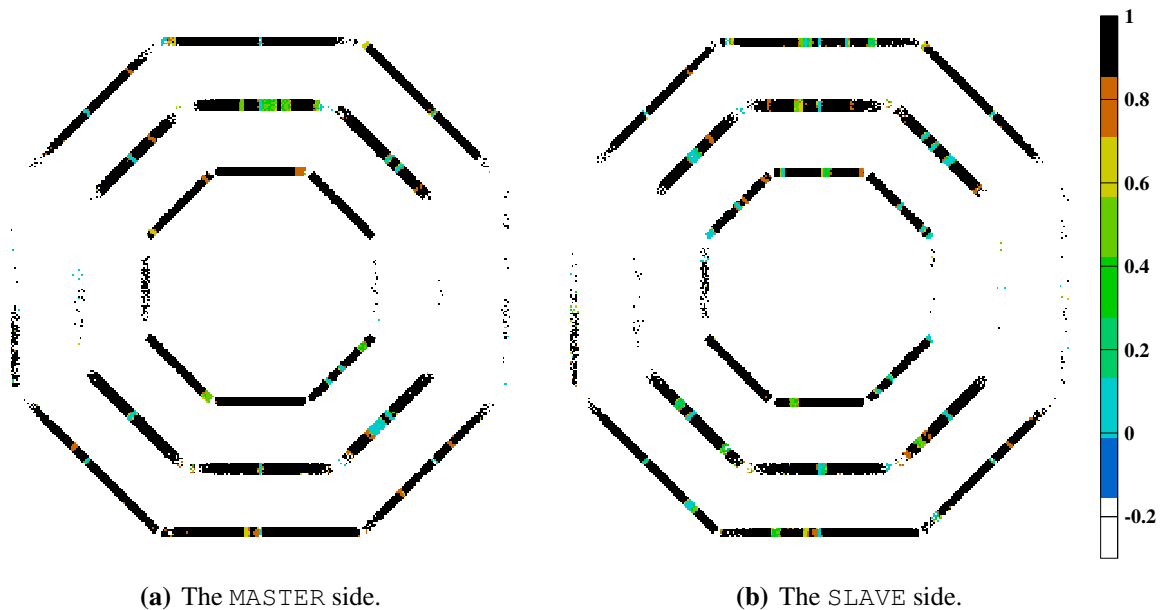
(a) The MASTER side.

(b) The SLAVE side.

Figure 5.3: *The efficiency of the P-chambers plotted vs x and y.*

efficiency is about 98% (excluding the dead cells).

The efficiency of the Z-chambers is determined in much the same way. This study revealed an unknown mis-cabling of 32 wires in octant 3 MIO, possibly due to a interchange of two connectors. The average Z-cell efficiency is about 95% (excluding the dead cells).

For the P-chambers the measurement is performed in units of cells, i.e. individual wires can be dead without harming the full cell. For the Z-chambers the natural unit is a single wire. For both the P and Z-chambers bad cells and wires were found which were not in the L3 database. For cases where the measured efficiency is lower than 80% the cell is killed in both the real detector simulation and the data reconstruction. The collaboration chose not to implement a time dependent chamber efficiency, but instead used the situation at the end of the year, which is assumed to be the worst case, for the killing. This was estimated to cause a loss of about 10% of the statistics.

5.3 Trigger efficiency

The importance of knowing the trigger efficiency encouraged the development of three independent methods. In this section the three methods will be briefly discussed and compared.

5.3.1 Unbiased trigger class

When designing the CTT (see section 2.3.5) class 9 was added to enable the determination of the efficiency of class 1. In practice it turned out to be simpler to use a slightly different approach (Timmermans 2002), whereby overcoming the problem of pre-scaling. Class 1 triplets are used, which has the advantage that the events contain a scintillator hit. The hits

in the octant which caused the trigger are excluded, whereby the remaining hits are unbiased. For each layer the number of hits are counted and compared to a variable threshold (n). The efficiencies of the three layers per octant are multiplied to give the triplet efficiency. To prevent measuring the efficiency of triggering on noise, a cut on the absolute time difference between a chamber hit and the scintillator hit was imposed, whereby selecting the central 600 ns of the drift-time distribution. Below, the obtained chamber part of the class 1 efficiency, averaged over the 6 relevant[*] octants, is presented for two values of the threshold:

$$\varepsilon_{ch,1} = 95.8 \pm 1.7\% \qquad (n > 5) \tag{5.1}$$

$$\varepsilon_{ch,1} = 99.9 \pm 0.2\% \qquad (n > 10) \tag{5.2}$$

The measurement has a negligible statistical error, but a significant systematic uncertainty due to the 600 ns time window. A threshold of 5 is what is used in the reconstruction program. Since it is lower than what is used by the majority logic, the efficiency is low. The threshold of 10 is chosen since it comes close to the cut on the number of P-hits used in the spectrum analysis (see section 4.2).

The scintillator part of the class 1 efficiency is determined by using classes 1 through 4, i.e. the triplet class with and the triplet classes without a scintillator hit. The problem is complicated by the pre-scaling of the classes without a scintillator hit. For the 1999 data set the measured efficiency is (Timmermans 2002):

$$\varepsilon_{sc} = 99.96 \pm 0.01(\text{stat}) \pm 0.02(\text{syst})\% \tag{5.3}$$

5.3.2   Trigger simulation

A trigger simulation was written (Li 2001), which works with the raw data itself. The program simulates the majority logic of the CPC cards and the response of the CTT. From the raw hits one is thus able to predict the trigger decision, which is compared to the actual output from the CTT. The algorithm revealed an efficiency of:

$$\varepsilon_2 = 99.2 \pm 0.3\% \tag{5.4}$$

For this measurement the statistical error is negligible. Only losses in the trigger logic are measured by the simulation. This means, that the losses which occur at the boundary between two CPC cards are neglected since they do not correspond to a loss in the hardware, but rather to a weakness in the trigger scheme. This efficiency also includes the efficiency of the scintillator coincidence requirement. The discrepancy with the efficiency determined with the unbiased trigger class, was shown (Li 2001) to come from losses at the boundary between two CPC cards.

5.3.3   Double tracks

The last method works on the reconstructed data rather than the raw data. This has the advantage that the efficiency can be measured for the actual event selection. The simplest selection

---

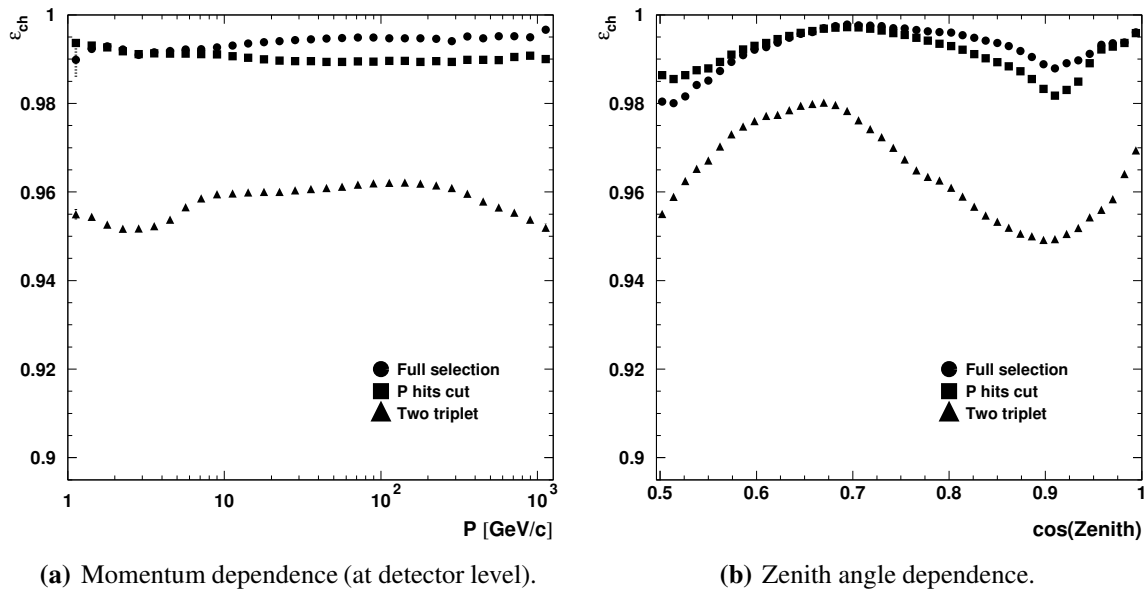[*]Excluding the two horizontal octants.

(a) Momentum dependence (at detector level). **(b)** Zenith angle dependence.

Figure 5.4: *The trigger efficiency measured by the double track method. The method is applied to three data sets:* ▲ *no cuts apart from the basic requirement of two triplets found by the reconstruction program.* ■ *additional requirement of 70% of the hits per layer.* ● *the full event selection.*

consists of events with two sub-tracks in different octants, each matched to a scintillator hit. The sample with one reconstructed triplet and the correct trigger response in the same octant provides an unbiased sampling of the other octant where the reconstruction also found a triplet. The chamber part of the trigger efficiency is thus given by the fraction of events where the trigger fired. Without any additional cuts this gives:

$$\varepsilon_{ch,3} = 95.890 \pm 0.002(\text{stat}) \pm 1.329(\text{syst})\% \qquad \text{(Two triplets)} \qquad (5.5)$$

$$\varepsilon_{ch,3} = 99.208 \pm 0.002(\text{stat}) \pm 1.076(\text{syst})\% \qquad \text{(Full selection)} \qquad (5.6)$$

The full data-set is used for this measurement which means that the statistical error is negligible. The systematic error is determined from the variance of the efficiency vs $\cos\theta$ as shown in figure 5.4. Here the momentum dependence is also shown. The dip in efficiency at $\cos\theta$ of 0.9 and 0.5, which are the regions with the largest ϕ_{local} angle, is caused by a problem at the boundary of two CPC cards. The larger the ϕ_{local} angle, the larger the chance of crossing a mesh-plane which defines the boundary between two CPC cards. It is important to notice the good agreement between this measurement and the one in section 5.3.1.

As was already hinted to in section 4.2 the number of hits per segment is important for the trigger efficiency. Figure 5.4 also shows the result of imposing the 70% cut on the number of hits per segment as well as the full selection. In the reconstruction program segments are allowed with as little as 6 hits. This means that the program will find segments which are below the threshold of the trigger, thus resulting in a lower trigger efficiency. It is interesting to note that the stronger selection removes part of the zenith angle dependence. The problem with the boundary between two CPC cards is, however, not completely removed. Equation 5.6

shows the result for the selected events.

5.3.4   Discussion

The selection which was described in section 4.2 requires two good triplets, which means that the trigger for these events has two independent chances to fire. When using the average efficiency of the full selection from equation 5.6 the trigger efficiency is:

$$
\begin{aligned}
\varepsilon_{ch} &= \left(1 - \left(1 - \overline{\varepsilon_{ch,3}}\right)^2\right) \\
&= 99.990 \pm 0.021\%
\end{aligned}
\tag{5.7}
$$

where the error is determined from the variance of the efficiency vs $\cos\theta$. Within even the most optimistic prediction of the accuracy of the L3+Cosmics flux measurement (Bähr *et al.* 1996) the trigger efficiency ($\varepsilon_{ch} \cdot \varepsilon_{sc}$) is thus compatible with 100%, and can be neglected. The third method, with the full event selection, is chosen for the chamber part, since it measures the trigger efficiency for the events which are used in this analysis. More importantly, it includes the losses at the boundary between two CPC cards.

5.4   The live-time

The determination of the absolute flux of muons relies heavily on the knowledge of the live-time of the experiment. In the L3+Cosmics experiment this responsibility is carried by the GPSTIM module (see section 2.3.6). Great care was taken in its design, to ensure that any temporary disabling of the triggers causes the live-time counter to stop. A simple mechanism was envisioned to provide a cross check of this crucial value. The 1 Hz signal from the GPS module is used as an external trigger source. This means that every second an empty event is written if, and only if, the triggers are enabled. The number of this type of events is thus a measure of the live-time. The integrated live-time of the selected runs is 4057152.4 s, these runs contain 4056018 1 Hz triggers. This means that the integrated live-time is determined with an accuracy of 0.03%. This should be compared to the expected uncertainty of the recorded live-time per run:

$$
\frac{2^{23}}{\sqrt{12}} \, 0.1 \, \mu s = 0.24 \, s
\tag{5.8}
$$

which is caused by the 23 bit truncation of the 10 MHz internal live-time counter in the GPSTIM (see section 2.3.6). For the 8217 selected runs this results in a 0.05% uncertainty on the total live-time. This uncertainty is negligible compared to the other uncertainties on the spectrum (see table 6.2).

5.5   Momentum resolution

The aim of L3+Cosmics is to measure the steeply falling muon momentum spectrum over two orders of magnitude. The measured flux is folded with the detector resolution function.

Section 6.1.2 describes the unfolding. To be able to unfold the measured spectrum, the resolution function has to be known accurately. This section describes the measurement of the resolution function as well as a short account of its different components.

5.5.1   Components of the resolution function

As was discussed in section 2.2 on page 23, the L$_3$ muon chambers are performing a distance measurement. More precisely, they measure the sagitta of a muon trajectory in the magnetic field. The error on the sagitta measurement can be written as (Fabre 1992):

$$\Delta_s = \sqrt{\Delta_{ch}^2 + \Delta_{ms}^2 + \Delta_{al}^2 + \Delta_{\vec{B}}^2 + \Delta_{t0}^2} \tag{5.9}$$

Here a brief description of these components will be given. The intention is not to derive the resolution function, but rather to obtain the expected variance with which the measured one can be compared. It is important to notice that this calculation assumes that all the measured quantities, which enter in the sagitta measurement, follow a Gaussian distribution. In general this assumption is correct, but it does neglect the well-known exponential tails, which almost all measured distributions have.

Δ_{ch} is the intrinsic resolution of the chambers. From equation (2.2) it can be seen that:

$$
\begin{aligned}
\Delta_{ch} &= \sqrt{\varepsilon_{\mathtt{MM}}^2 + \left(\frac{\varepsilon_{\mathtt{MI}}}{2}\right)^2 + \left(\frac{\varepsilon_{\mathtt{MO}}}{2}\right)^2} \\
&= \sqrt{\left(\frac{250\mu\mathrm{m}}{\sqrt{0.95 \cdot 24}}\right)^2 + \frac{1}{2}\left(\frac{250\mu\mathrm{m}}{\sqrt{0.95 \cdot 16}}\right)^2} \\
&= 69 \ \mu\mathrm{m}
\end{aligned}
\tag{5.10}
$$

Where $250\,\mu$m is a conservative estimate of the single wire resolution (see section 3.1.1). In addition, the `MI` and `MO` segments are assumed to have 16 hits and the `MM` segments 24 hits. 95% of the wires are assumed to participate in the segments, which is a conservative estimate (see figure 4.5).

Δ_{ms} is the multiple scattering on the `MM` chamber, the air between the chambers, and the gas inside them. It can be written as (Fabre 1992):

$$\Delta_{ms} = 43 \ \mu\mathrm{m} \cdot \frac{45 GeV}{p} \tag{5.11}$$

where p is the muon momentum in GeV measured at the detector.

Δ_{al} is the error caused by the misalignment of the chambers and the wires inside the chambers (see section 2.2.4). This error was measured (Fabre 1992) to be 21 μm, but here the more conservative design value is used:

$$\Delta_{al} = 30 \ \mu\mathrm{m} \tag{5.12}$$

$\Delta_{\vec{B}}$ is the error caused by the uncertainty on the size of the magnetic field. This uncertainty was measured to be 20 Gauss (Brouwer *et al.* 1992), which using equation (2.1) can be converted into an error on the sagitta:

$$\Delta_{\vec{B}} = 14 \text{ μm} \tag{5.13}$$

Δ_{t0} is the error caused by the reference[*] time needed by the drift chambers. This error is where L$_3$+Cosmics deviates from L$_3$. For L$_3$+Cosmics this can, to first order, be written as:

$$
\begin{aligned}
\Delta_{t0} &= |\omega| \cdot v_{dr} \sqrt{\Delta T_{sc}^2 + \Delta T_{TDC}^2} \\
&= |\omega| \cdot 48.5 \, \frac{\text{μm}}{\text{ns}} \sqrt{(1.8 \text{ ns})^2 + \left(\frac{25/32 \text{ ns}}{\sqrt{12}} \right)^2} \\
&= |\omega| \cdot 88 \text{ μm}
\end{aligned}
\tag{5.14}
$$

where ΔT_{sc} is the intrinsic time resolution of the scintillator system and ΔT_{TDC} is the time resolution of the TDCs. The TDC time resolution of course also affects the measurement of the chamber times, but that is already included in the single wire resolution. v_{dr} is the drift velocity of the P-chambers. An error on the reference time will move all hits either closer or further away from the sense plane. The effect on the sagitta measurement thus depends on the topology of the event as can be seen from equation (2.2). ω parameterises this dependence as:

$$
\begin{aligned}
\omega &= \omega_{\text{MM}} - \left(\frac{\omega_{\text{MI}} + \omega_{\text{MO}}}{2} \right) \\
\omega_i &= \frac{1}{N_i} \sum_{j=1}^{N_i} \begin{cases} -1 & \text{if hit } j \text{ is left}^\dagger \text{of the wire plane,} \\ +1 & \text{if hit } j \text{ is right of the wire plane.} \end{cases}
\end{aligned}
\tag{5.15}
$$

where N_i is the number of hits on segment i, e.g. the segment in MM . If all hits of the three layers are on the same side of the sense wire plane, they will move in the same direction, and the sagitta will thus not be affected ($\omega = 0$). If on the other hand the MM hits are on the opposite side of the sense plane compared to the MI and MO hits, the sagitta will get twice the contribution (see figure 2.3) of the time error, i.e. $\omega = \pm 2$. For comparison L$_3$ obtains (Fabre 1992):

$$\Delta_{t0} = |\omega| \cdot 13 \text{ μ}m \qquad (\text{L}_3) \tag{5.16}$$

In figure 5.5 both the sagitta and the momentum resolution are shown. It is interesting to note that above 20 GeV the scintillator timing becomes the dominant error (for $\omega = 1$).

---

[*]In L$_3$ this is normally denoted the *common stop* time.

[†]Left and right is defined in the "local octant" coordinate system, which corresponds to a rotation of the octant to the position of octant 2.
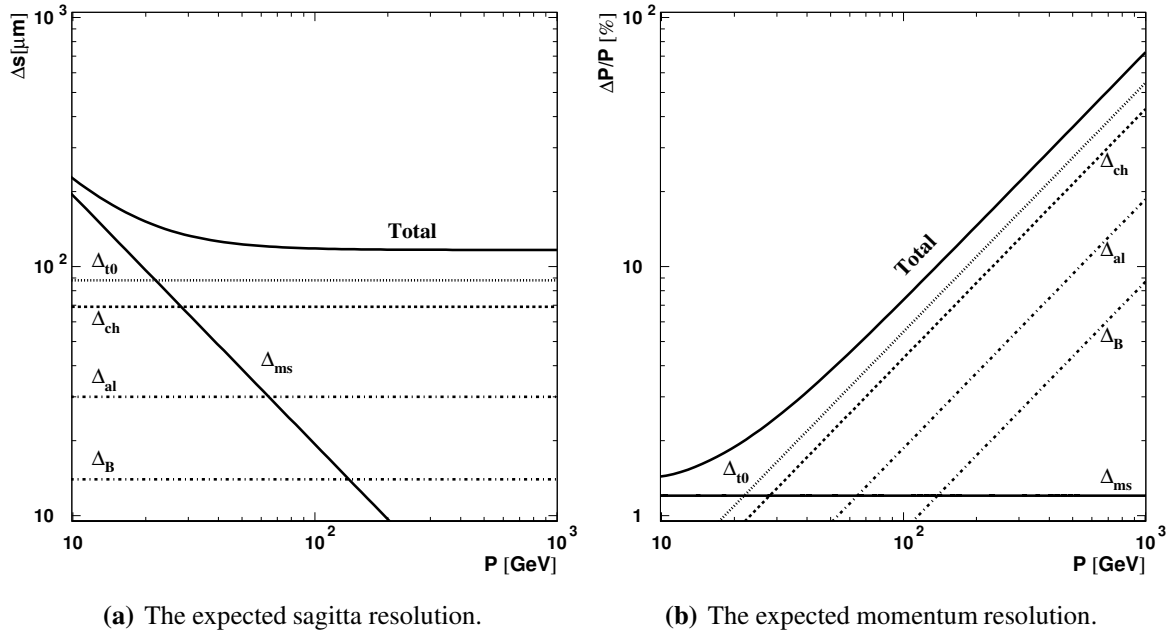
(a) The expected sagitta resolution. **(b)** The expected momentum resolution.

Figure 5.5: *The individual components as well as the total width of the expected Gaussian resolution function ($\omega = 1$).*

5.5.2 Measurement of the resolution function

The ability to measure the same muon twice, once in an upper octant and once in a lower octant, enables L$_3$+Cosmics to measure the resolution function. The inverse of the combined momentum of a track (qp) and its variance ($V(q/p)$) are given by:

$$\frac{1}{qp} = \frac{1}{w_1 + w_2}\left(\frac{w_1}{q_1 p_1} + \frac{w_2}{q_2 p_2}\right), \quad w_i = 1/V_i \quad V_i = V(q_i/p_i)$$

$$= k\frac{1}{q_1 p_1} + (k-1)\frac{1}{q_2 p_2}, \qquad\qquad k = \frac{V_2}{V_1 + V_2} \qquad (5.17)$$

$$V(q/p) = \frac{V_1 V_2}{V_1 + V_2} = kV_1 \qquad\qquad\qquad (5.18)$$

where p_i and q_i are the momentum and charge of sub-track i respectively, and V_i is the variance of q_i/p_i. At higher energies the weighed average differs little from the simple average. At lower energies, however, the effect of HCAL gives rise to a significant increase in the variance of the lower sub-track. The variance of the difference between the two sagitta measurements[*] is related to the variance of q/p by:

$$V(\Delta(q/p)) = V_1 + V_2 = \frac{V_1}{1-k}$$

$$= \frac{V(q/p)}{(1-k)k} \qquad\qquad (5.19)$$

---

[*]The difference is always taken as "top minus bottom".
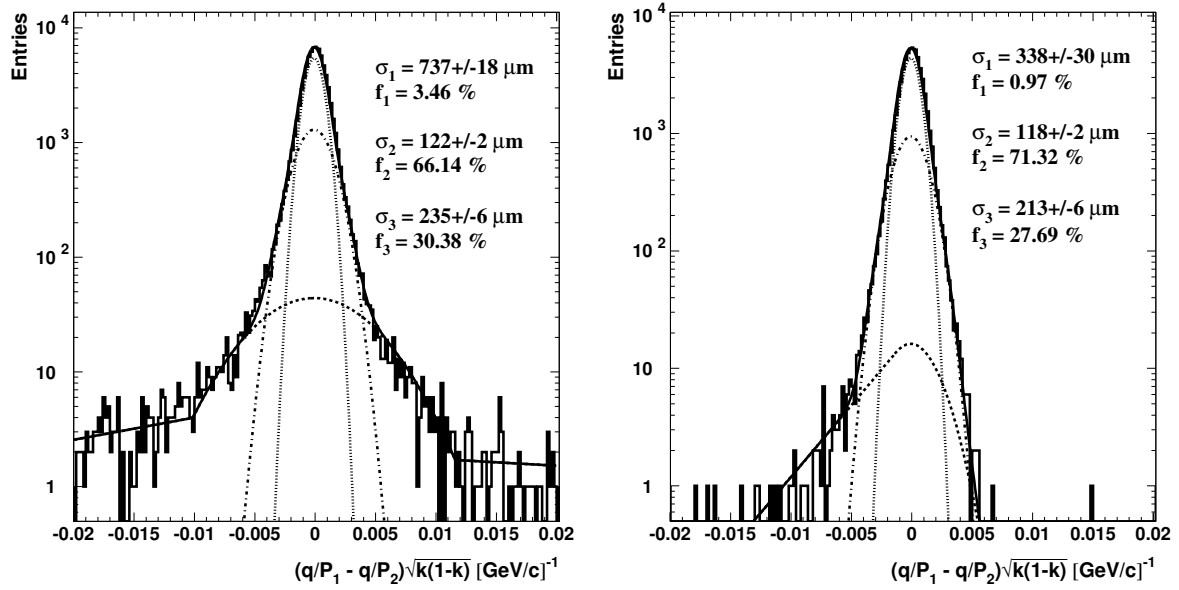
(a) The selection without the cut on the number P hits, Z layers and circle fit χ^2/dof.

(b) The full selection.

Figure 5.6: *The resolution function at 100 GeV of events with a zenith angle less than $10°$ fitted with the function in equation (5.20). The width (σ_i) of the three Gaussians are shown along with the fraction (f_i) of the area below each of the three components of the function.*

The measured resolution distribution is fitted with the sum of three concentric Gaussians, the first of which has exponential tails, starting at variable points.

$$f(x) = \frac{A_1}{2\sqrt{\pi}\sigma_1} \cdot \begin{cases} \exp\left(\frac{-(x_{low}-\mu)^2}{2\sigma_1^2}\right)\exp\left((x-x_{low})\alpha\right) & \text{if } x < x_{low}, \\ \exp\left(\frac{-(x-\mu)^2}{2\sigma_1^2}\right) & \text{if } x_{low} < x < x_{high}, \\ \exp\left(\frac{-(x_{high}-\mu)^2}{2\sigma_1^2}\right)\exp\left((x-x_{high})\beta\right) & \text{if } x > x_{high}. \end{cases}$$
$$+ \frac{A_2}{2\sqrt{\pi}\sigma_2} \cdot \exp\left(\frac{-(x-\mu)^2}{2\sigma_2^2}\right) + \frac{A_3}{2\sqrt{\pi}\sigma_3} \cdot \exp\left(\frac{-(x-\mu)^2}{2\sigma_3^2}\right)$$

(5.20)

The continuity requirement fix the scale factor of each of the two exponential tails. In total eleven parameters ($\mu, A_1, A_2, A_3, \sigma_1, \sigma_2, \sigma_3, \alpha, \beta, x_{low}, x_{high}$) are used to describe the distributions. The tails of the resolution distribution are mainly caused by the large tail in the Landau distribution, which causes large energy losses in between the two measurements (e.g. in HCAL). With the convention of the difference used here these events cause a tail on the negative side. In figure 5.6 the measured resolution at 100 GeV can be seen along with the fitted function. It is worth noting the significant improvement in the resolution obtained by the cuts on the number P hits, Z layers and circle fit χ^2/dof. These cuts remove the tails, which are dominated by poorly measured tracks.

Figure 5.7 shows the momentum dependence of the measured resolution. The width of the narrow Gaussian and the RMS of the fitted function is compared to the expected resolution
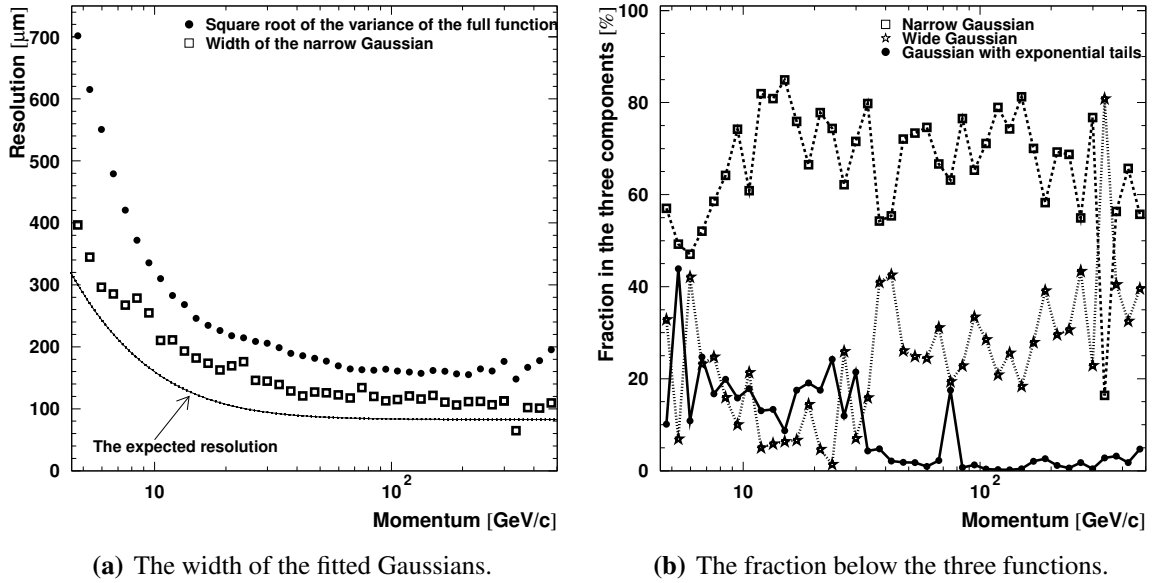
(a) The width of the fitted Gaussians.

(b) The fraction below the three functions.

Figure 5.7: *The measured resolution vs. the measured momentum in the detector. The expected resolution plotted in figure* **(a)** *as* ($\omega = 1$), *i.e. the function plotted in figure 5.5 divided by* $\sqrt{2}$.

from section 5.5.1. In spite of the great attention given to the resolution, it is clear that L3+Cosmics does not obtain the expected value. The narrow Gaussian is about 40% wider than was expected. The tails of the distribution cause the square root of the variance of the full function to be almost a factor two larger than expected, even though above 10 GeV they contain less than 30% of the data. Below 50 GeV, the exponential tails become increasingly important, whereas they play only a marginal role at high momenta. Above 100 GeV the resolution is constant. Low statistics cause the result of the fit to be unstable above about 300 GeV. The resolution function used to deconvolute the measured momentum spectrum is thus taken to be constant above about 200 GeV.

As is shown in equation (5.14), the reference time component Δ_{t0} of the resolution function has a geometrical dependence, parameterized by ω. This feature enables the measurement of the two components of the resolution function; the part that does and the part that does not depend on ω. Again the difference between the two sagitta measurements is used for the measurement:

$$V\left(\Delta\left(q/p\right)\right) = 2\Delta_1^2 + \left(\left|\omega_T + \omega_B\right|\Delta_2\right)^2 \tag{5.21}$$

where ω_T and ω_B are the topological parameters from equation (5.15) of the measured sub-track in the top and bottom octant respectively. The factor 2 in front of Δ_1 comes from the fact that the constant component $(\Delta_{ch}^2 + \Delta_{ms}^2 + \Delta_{al}^2 + \Delta_{B}^2)$ is common in the sub-track of both the top and bottom octant. The ω of the two sub-tracks must be added, and not subtracted as one might think. This comes from the definition of left and right in equation (5.15). The measurement of the resolution is performed for tracks above 100 GeV, where the multiple scattering can be neglected. The difference distribution is fitted with two concentric Gaussians. The results of the fits as a function of ω are shown in figure 5.8. The cases where one of the two sub-tracks
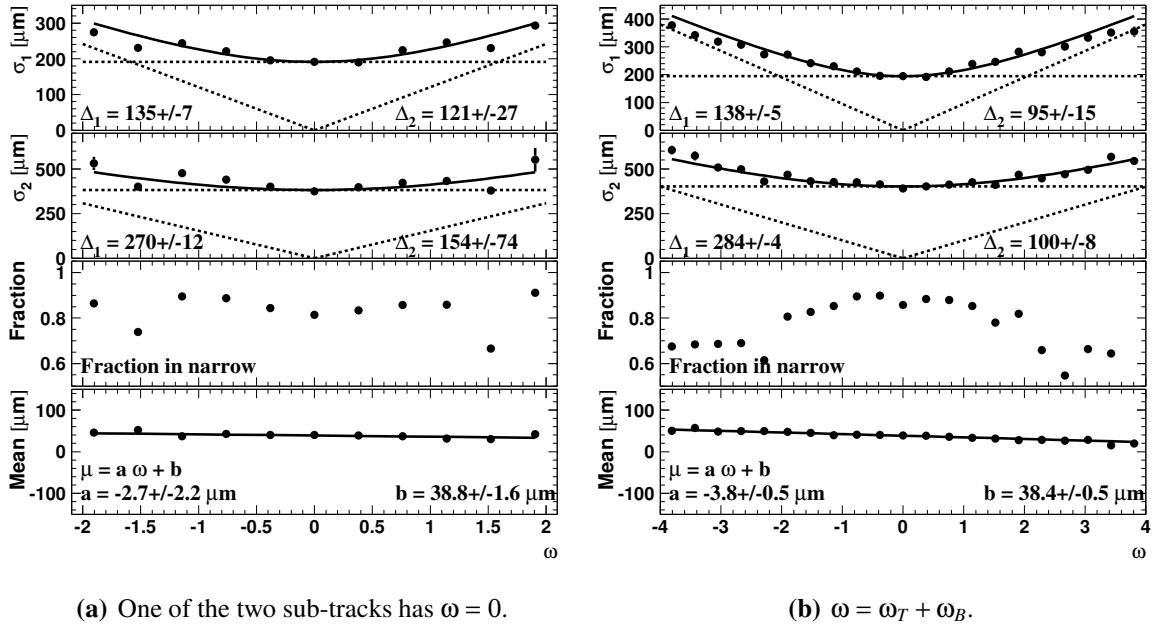
(a) One of the two sub-tracks has $\omega = 0$.

(b) $\omega = \omega_T + \omega_B$.

Figure 5.8: *The resolution above 100 GeV vs ω using the full selection. The two top plots show the fit of equation (5.21) to the width of the two Gaussians separately. The fraction of the area in the narrow Gaussian is shown below that. At the bottom a straight line is fitted to the distribution of the mean.*

has $\omega = 0$ is shown separately, since this case is the easiest to interpret. The lower statistics cause a less precise measurement of the relevant parameters, but it is important to note that the two measurements are consistent. The fit of equation (5.15) to the distribution of the width of the narrow Gaussian yield a Δ_1 value of 138 ± 5 µm. The discrepancy between the measured value of Δ_1 and the expected value of 80 µm, can be interpreted as the existence of an unknown additional component of the resolution function:

$$\Delta_? = \sqrt{\Delta_1^2 - \left(\Delta_{ch}^2 + \Delta_{ms}^2 + \Delta_{al}^2 + \Delta_{\vec{B}}^2 \right)} \qquad (5.22)$$

$$= 112 \pm 6 \text{ µm}$$

This is the single largest component of the resolution function, nevertheless its origin is unknown. The existence of a second Gaussian indicates that the event sample still contains 20-30% of events with a worse resolution.

The measurement of Δ_2 is not only consistent between figure 5.8a and 5.8b, but also between the wide and narrow Gaussian. In the following the weighed average of the two measurements in figure 5.8b will be used as the estimator of Δ_2. Equation (5.14) enables the interpretation of this measurement in terms of the time resolution of the scintillator system. This yields a resolution of:

$$\Delta T_{sc} = 2.0 \pm 0.1 \text{ ns} \qquad (5.23)$$

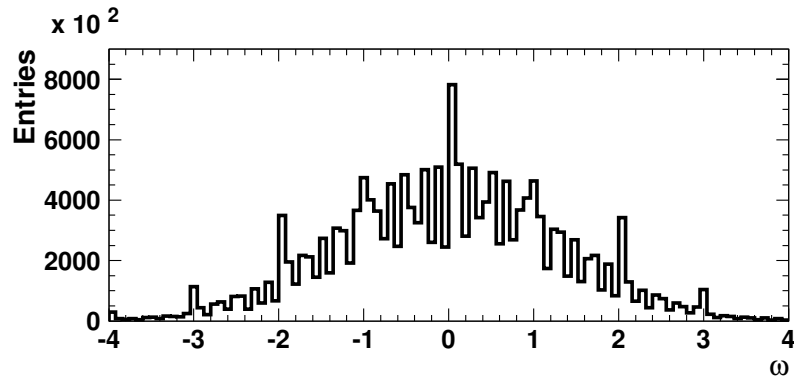which is in good agreement with the expected values of 1.8 ns.

Figure 5.9: *The distribution of $\omega_T + \omega_B$ of the selected tracks. The mean value of $|\omega|$ is 1.06.*

When compared to the width of the narrow Gaussian of the selected events at 100 GeV, shown in figure 5.6, an effective Δ_{t0} is obtained:

$$\Delta_{t0}^{\text{eff}} = \sqrt{2\sigma_2^2 - \Delta_1^2} \tag{5.24}$$
$$= 94 \pm 9 \ \mu\text{m}$$

When compared to equation (5.14) the mean values of $|\omega|$ would have to be about one, which indeed is what is observed (see figure 5.9).

5.6 Z/γ → μ⁺μ⁻ **events**

During each of the LEP2 years, LEP took data close to the Z resonance to provide typically about 500 nb⁻¹ for calibration purposes. In L₃ the relative alignment of the SMD needed to be re-measured each year along with the calibration of the TEC drift-time/distance relation. The L₃ muon group also used this data to optimise the value of the drift velocity, the Lorentz angle[*] and the global time offset (Fabre 1992).

For L₃+Cosmics this data serves a different but very important purpose. It provides a unique check of the momentum measurement. It is important here to stress that L₃+Cosmics in contrast to L₃ does **not** use this data for any calibration purposes.

One of the more important features of the L₃ muon trigger is the rejection of cosmic muons. In the analysis phase the two time measurements from the scintillator barrel serve as a second strong rejection. For L₃+Cosmics these tools are not available, therefore the biggest problem in this analysis is to find the Z-decay muons among all the cosmic muons. The trigger setting has been changed during these periods, whereby only class 1 events were accepted. In the hardware we measure two signals from L₃: the common stop[†] and the beam

---

[*]In fact the drift velocity is being optimised twice, once as the real drift velocity and once as a scale factor for the Lorentz angle.

[†]The common stop signal was only added for the 2000 running.

crossing. The common stop signal stops the L$_3$ muon chamber TDCs. It is derived from the beam crossing by delaying the beam pickup signal. The beam crossing signal also originates from the pickup signal, but this one is obtained from the L$_3$ trigger box. During the first period of 1999 the obtained signal had too large a delay, and fell outside the TDC window. During the 2000 data taking this signal carried a reflection, which was only removed in the second half of 2000.

The data obtained during these periods is also used for the normal analysis, therefore these runs are first processed with the normal reconstruction mode, i.e. assuming that the muons originate from above the detector. On this output the following pre-selection is performed:

- A very loose cut of 20 cm is applied to the distance of closest approach (DCA) to the vertex in the *xy*-plane. This cut cannot be made much stronger since the time-of-flight correction is wrong for the *Z* events, resulting in a non-perfect tracking. To check that no candidates were lost, all the data from the second half of 1999 were reconstructed with the correct time-of-flight correction.

- The difference between the scintillator time and beam crossing or common stop time is calculated. These distributions show two peaks, which originate from the bunchlet structure of the beam. The beam crossing signal only fires on the first bunchlet, 320 ns later the second bunchlet arrives. Two 100 ns gates centered at each of the peaks are imposed.

- The L$_3$+Cosmics DAQ is also running while LEP is filling etc., therefore a deselection of these events is needed. The exact starting and stopping times of the LEP physics mode are obtained from the L$_3$ database and the L$_3$ on-line logbook.

This pre-selection reduces the data set to about 0.2%.

The pre-selected events are then processed with the special *Z* mode of the reconstruction program. The most important difference to the standard reconstruction is the time-of-flight correction, which assumes that the tracks originate from the vertex. In addition, the tracks are propagated to the vertex region where a modified ambiguity resolving takes place. On the output of this reconstruction a more conventional event selection is imposed:

- The events must have two tracks, each with 3 P-segments.

- The upper track must loosely point in the direction of the scintillators. The lower track must point away.

- In the *xy*-plane each track must come within 2 cm (5σ) of the vertex. In the *z* direction the cut is 5 cm, which also corresponds to a 5σ cut.

In figure 5.10 the result of the *Z*-runs from both years can be seen. The 2σ cut on the low energy side (right) is imposed to remove events with large energy loss in HCAL. It is important to notice that the mean is determined with a precision of about 100 MeV.
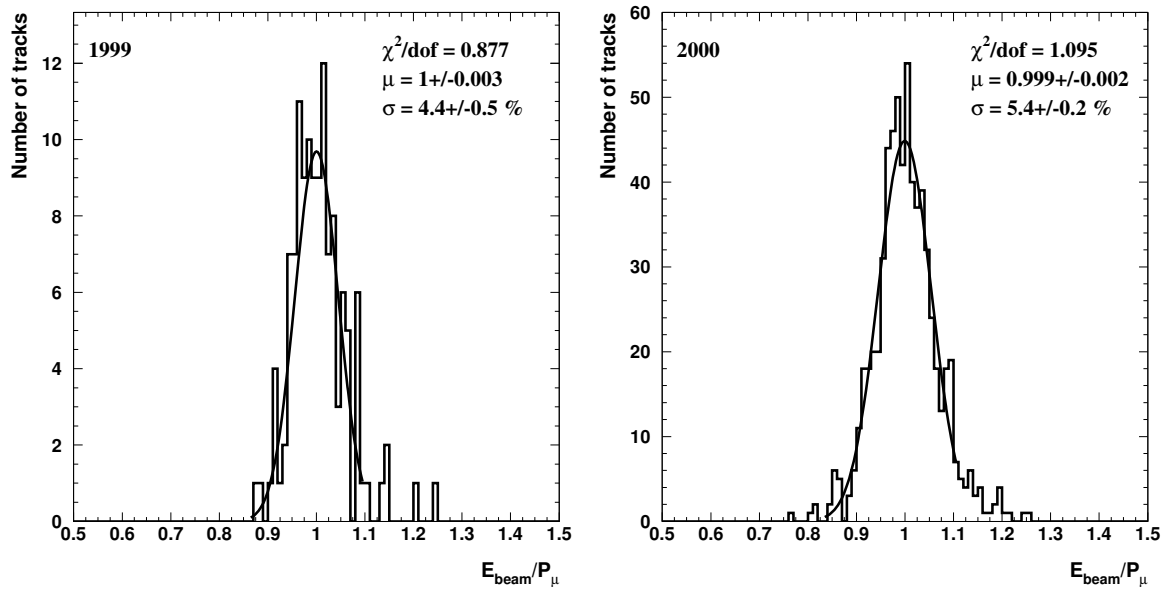
Figure 5.10: *The muon momentum distribution of the Z/γ → μ⁺μ⁻ events from the last calibration periods of 1999 and all periods of 2000. The data are fitted with a single Gaussian; mean, width and reduced χ^2 are quoted. In both cases a 2σ and 3σ cut is imposed on the high and low energy side, respectively.*

The width of the Gaussian is significantly larger than the 3.5% one would expect from the theoretical curve shown on figure 5.5 on page 79. The measured width* of the narrow Gaussian in figure 5.7 on page 81, however, corresponds to a resolution of 5.4%. Therefore, a good agreement is obtained between the resolution measured with *Z*-decay muons, and the resolution measured with cosmic ray induced muons.

---

*Notice that the width must be multiplied by $\sqrt{2}$, to get the single track resolution.

Chapter 6

The flux measurement

In this chapter the measurement of the cosmic ray induced muon spectrum is presented. First the analysis of the vertical flux is described in detail, thus explaining the method. Subsequently the study of the systematic errors is described, followed by an extension of the measurement to larger zenith angles. A description of the key variables used in this analysis can be found in table 6.1.

6.1 The method

The measurement of the muon flux is in principle a straightforward measurement. The measured number of selected muons $n\left(p_i^s, \theta_j\right)$ in a surface momentum[*] bin p_i^s and zenith angle bin θ_j is related to the perpendicular differential flux $\Phi\left(p^s, \theta\right)$ via:

$$n\left(p_i^s, \theta_j\right) = \int\limits_{S_\perp} \int\limits_0^{2\pi} \int\limits_{\cos(\theta_j)} \int\limits_{p_i^s} \int\limits_T \Phi\left(p^s, \theta, \phi\right) \chi\left(p^s, \theta, \phi, S_\perp'\right) \, \mathrm{d}t \, \mathrm{d}p^s \, \mathrm{d}\cos\theta \, \mathrm{d}\phi \, \mathrm{d}S_\perp' \qquad (6.1)$$

where T is the live-time of the data taking (see section 2.3.6), and (θ, ϕ) define the direction of the muons. The integration in p^s and $\cos\theta$ is over the bin p_i^s and θ_j, respectively. $S_\perp$ is a plane larger than the detector, which is perpendicular to the direction of the muons. χ is the probability of detecting a muon. At low energy the flux also depends on the azimuth angle ϕ, due to the geomagnetic cut-off. For the energies relevant for this measurement this effect is negligible. Figure 6.1 shows the measured number of events versus the measured momentum in the detector within the $0°$-$10°$ zenith bin. Writing the flux as:

$$\Phi\left(p^s, \theta\right) = \widehat{\Phi}\left(p_i^s, \theta_j\right) \rho_{i,j}\left(p^s, \theta\right) \qquad (6.2)$$

---

[*]Clearly L3+Cosmics can not measure the momentum of the muons at the surface, but the measured momentum at the detector is corrected for the energy loss in the molasse (see section 6.1.4).

$p^{d,obs,raw}$:	The observed momentum at MBAR.
$p^{d,obs}$:	The observed momentum at MBAR plus the momentum offset $C(\theta_i)$.
$C(\theta_i)$:	The most likely energy loss in the molasse for events in zenith bin θ_i (see figure 6.2).
$p^{d,true}$:	The true momentum at MBAR (incl. offset), i.e. $p^{d,obs}$ corrected for the effect of the momentum resolution.
p^s :	The true momentum at the surface, i.e. $p^{d,true}$ corrected for the energy loss in the molasse.
p_i :	The momentum binned in units of 0.05 in $\log_{10}(p)$ starting at 1 GeV and ending at 10 TeV. All momenta are binned in the same way.
θ_i :	The zenith angle binned in units of 0.03 in $\cos\theta$ starting $0°$ and ending $\cos\theta = 0.4$, which is about $66.4°$. θ_i is also used for the special $0°$-$10°$ bin.
ϕ_i :	The azimuth angle binned in units of $\frac{2\pi}{20}$ over the full 2π. $\phi = 0$ is defined to be the geographical north and $\phi = \frac{\pi}{2}$ is the geographical east.
$n(p_i, \theta_j)$:	The number of observed events in the momentum bin p_i and zenith bin θ_j.

Table 6.1: *The description of the key variable used in this analysis.*
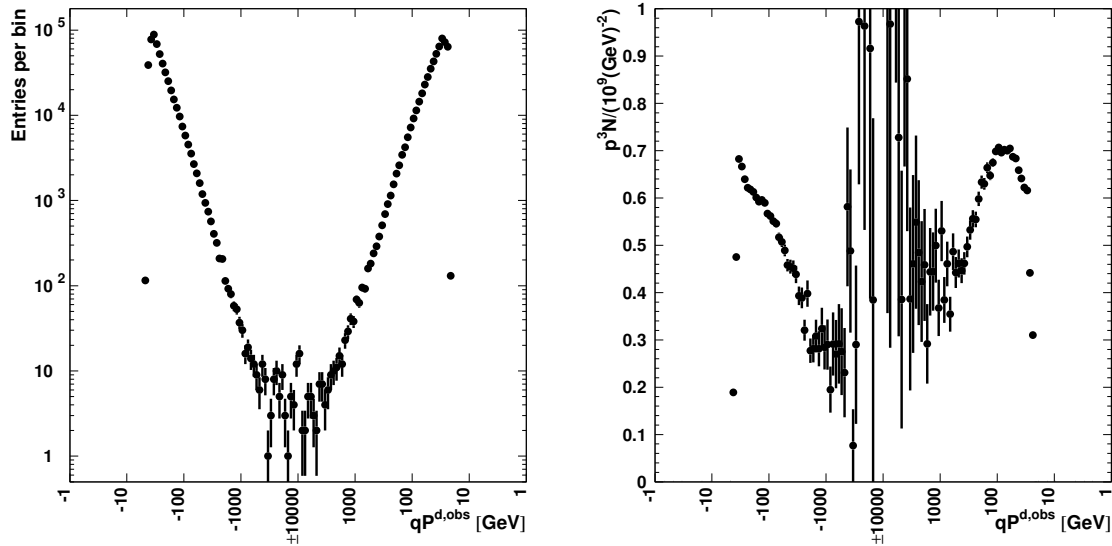
(a) The raw number of selected events per bin. The momenta are binned in units of 0.05 in $\log_{10}(p)$ starting at 1 GeV and ending at 10 TeV.

(b) The raw number of selected events per GeV multiplied by p^3.

Figure 6.1: *The selected events with a zenith angle of less than $10°$, plotted versus the electric charge times the measured momentum at MBAR times. The applied momentum offset (see figure 6.2) ensures that there are no events below about 21 GeV.*

where $\widehat{\Phi}\left(p_i^s, \theta_j\right)$ is the mean flux within the bin, and $\rho_{i,j}(p^s, \theta)$ is the probability distribution within bin $\left(p_i^s, \theta_j\right)$. The mean flux can then be written as:

$$\widehat{\Phi}\left(p_i^s, \theta_j\right) = \frac{n\left(p_i^s, \theta_j\right)}{A_{MC}\left(p_i^s, \theta_j\right) \cdot T \cdot \Delta\left(p_i^s\right)} \cdot \frac{\varepsilon_{MC}\left(p_i^s, \theta_j\right)}{\varepsilon_{Data}\left(p_i^s, \theta_j\right)} \tag{6.3}$$

where $A_{MC}\left(p_i^s, \theta_j\right)$ is the Monte Carlo estimator of the detector acceptance, which in turn is the integral over $\rho \cdot \chi$:

$$A\left(p_i^s, \theta_j\right) = \frac{1}{\Delta\left(p_i^s\right)} \int_{S_\perp} \int_0^{2\pi} \int_{\cos\theta_j} \int_{p_i^s} \rho\left(p^s, \theta\right) \chi\left(p^s, \theta, \phi, S'_\perp\right) \; \mathrm{d}p^s \, \mathrm{d}\cos\theta \, \mathrm{d}\phi \, \mathrm{d}S'_\perp \qquad (6.4)$$

The complexity of the experimental set-up requires a Monte Carlo simulation of the detector in order to be able to estimate the acceptance. At first glance it may seem counterintuitive that the acceptance would depend on the momentum, but the absorption of muons in the molasse and in HCAL does in fact cause a momentum dependence. Additionally, the disconnected cells break the symmetry of the detector resulting in a charge dependence as well. If the Monte Carlo simulation would provide a perfect description to the detector response there would be no need for the last term in equation (6.3). However, as will be shown below, this is not the case, hence the need for a ratio of the efficiencies for data, $\varepsilon_{\mathrm{Data}}\left(p_i^s, \theta_j\right)$ and Monte Carlo, $\varepsilon_{\mathrm{MC}}\left(p_i^s, \theta_j\right)$.

At energies above 500 GeV the resolution of the sagitta measurement starts to seriously affect the measurement. The steeply falling spectrum has the effect that at increasing energies a larger fraction of the measured events in fact are lower

Figure 6.2: *The most probable energy loss per Zenith angle bin $C\left(\theta_j\right)$. It is applied as a constant offset to the measured momentum. $\frac{21}{\cos\theta}$ is shown for comparison.*

energy muons. These are moved up in energy by the width of the resolution function (see section 5.5). To overcome this problem one must deconvolute the measured spectrum, using the knowledge of the resolution function, in order to obtain the real flux. The same is of course true for the efficiencies, which are measured versus the observed momentum.

In order to obtain the flux at the surface, instead of in the $\mathsf{L_3}$ pit, the energy loss in the about 30 m of molasse above the detector must be corrected for. As will be discussed below, (see section 6.1.4) this correction is applied by deconvoluting the binned data. To stabilize this procedure the majority of the correction is applied on an event by event basis. This in practice means that the most probable energy loss is added to the momentum measured in the detector. Due to the geometry of the cavern, the energy loss depends rather strongly on the zenith angle. Therefore, the most probable energy loss is determined separately for each zenith bin with Monte Carlo (see figure 6.2). The zenith angles dependence is stronger than the simple geometrical $\cos^{-1}(\theta)$ dependence, this is due to the curved roof of the cavern. In order to deconvolute the effect of the momentum resolution, it is important that this correction is constant within a zenith bin. This ensures that all the events in the histograms used in this analysis have the same offset.
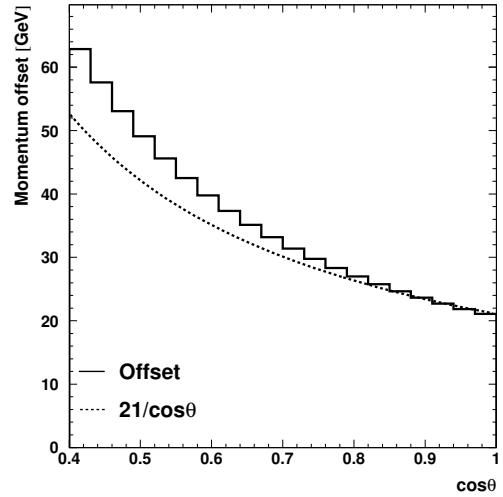
The momentum is binned in units of 0.05 in $\log_{10}(p)$ starting at 1 GeV and ending at 10 TeV. This binning is used for all types of momenta: the surface momenta p^s, the observed momenta in the detector $p^{d,obs,raw}$, the true momenta in the detector $p^{d,true,raw}$ and the energy offset corrected momenta $p^{d,obs}$ and $p^{d,true}$ respectively. Joining the spectra of the two charges at the highest momentum bin, as shown in figure 6.1, is inspired by the fact that at infinite momentum a muon follows a straight line through the detector, and it is therefore not possible to assign a charge. When deconvoluting the spectrum (see section 6.1.2), it turns out that this is the most natural way of representing the data.

In figure 6.3 an overview of the analysis can be found. The order in which the different steps are applied is indicated by the large arrows. This order is of vital importance, since the different elements are determined versus different types of momenta (see table 6.1). The raw spectrum is measured versus $p^{d,obs}$ and so are the matching efficiencies for data. The deconvolution transforms the corrected spectrum from being a function of $p^{d,obs}$ to be a function of $p^{d,true}$, the true momentum at MBAR. At this point the matching efficiencies for Monte Carlo as well as the up-down correction are applied. A second deconvolution step is needed to transform[*] this distribution from being a function of $p^{d,true}$ to be a function of p^s, the true momentum at the surface. Finally, the acceptance as well as the constant corrections are applied. The acceptance can only be determined as a function of the p^s, since it contains the probability of a muon reaching the detector. For muons not reaching the detector, one can clearly not define a momentum at MBAR. In the following each step of the analysis will be described in detail.

6.1.1 Matching efficiencies

When measuring an absolute flux it is important to know the fraction of events removed by the applied cuts. In this analysis the cuts will be split in two groups: the ones which act on a single sub-track and those using a full track. The cuts which act on a sub-track only are treated collectively with the so-called up-down method (see section 6.1.3). The two cuts which act on a combined track will be discussed individually in this section. In both cases the measured efficiency as a function of momentum is fitted with a polynomial, thus removing statistical fluctuations. The uncertainty in the fit is used as an estimator of the systematic error of the measured efficiency. The measured spectrum is corrected by the ratio $\frac{\varepsilon_{MC}}{\varepsilon_{Data}}$, but as explained above is the correction for ε_{MC} only applied after the deconvolution.

Track matching efficiency

When requiring two sub-tracks to be matched together to one full track, there will be cases where the algorithm (described in section 3.1.2) fails. The efficiency of the matching algorithm is measured with single muon events. For this purpose a sample of events is defined containing events with one and only one selected sub-track in an upper octant and one selected sub-track in a lower octant. The efficiency is then given by the fraction of matched

---

[*]The majority of this transformation is in fact applied by, on an event by event basis, adding the most likely energy loss (see figure 6.2) to the momentum used in all distributions used till this point in the analysis.
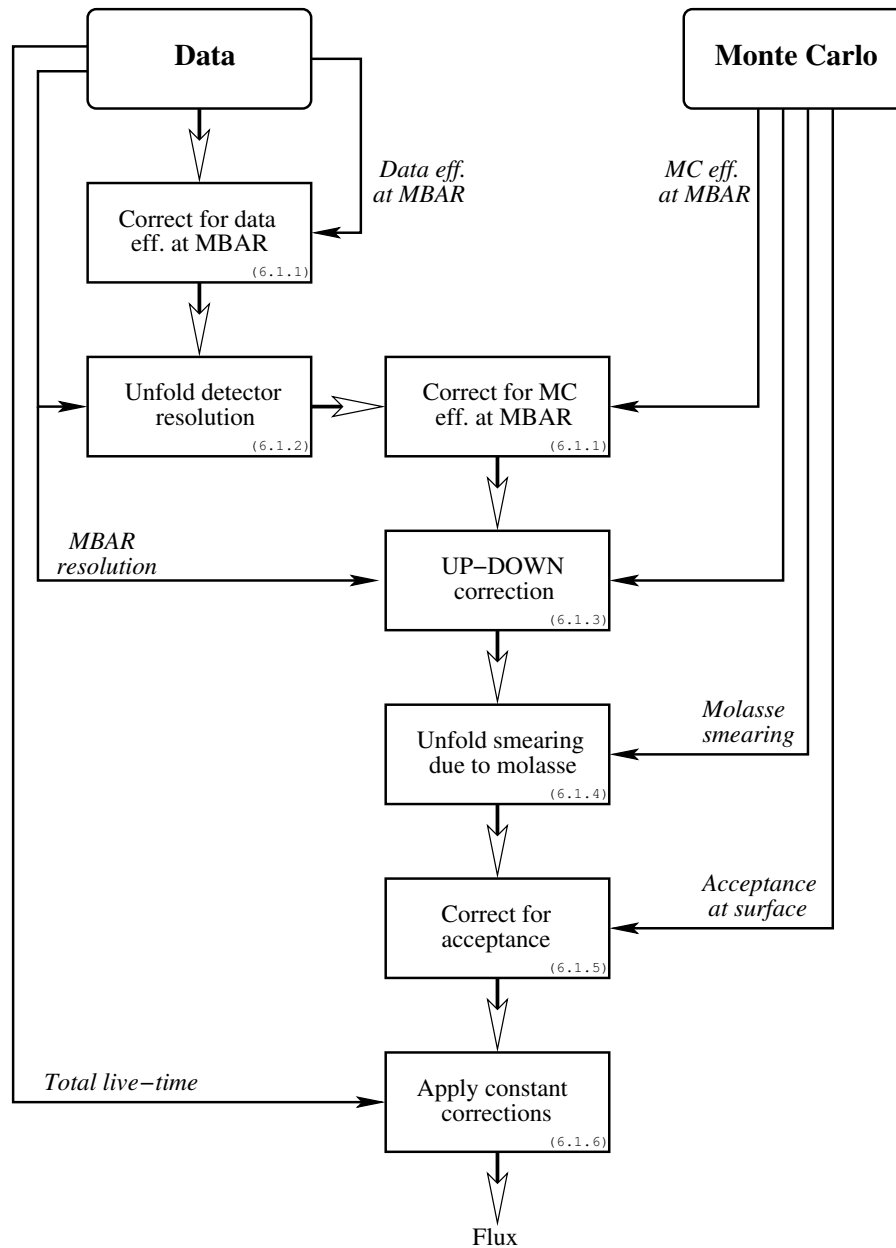
Figure 6.3: *The flow chart of the muon flux analysis. The section number describing the different elements of the analysis is given in the lower right corner of the boxes.*

events in this sample. It is thus assumed that every event in the sample is caused by a single muon passing the detector. A two muon event could, however, cause a similar situation, where the decision not to match the two sub-tracks was indeed correct. To estimate the size of the multi-muon contamination of the unmatched sample, 100 events from the unmatched sample were scanned. The scanning yielded two multi-muon events, both unambiguous multi-muons. To account for this intrinsic problem of the measurement, 2% of the inefficiency is assigned as a systematic error. The measured efficiency can be seen in fig-

(a) Data.   **(b)** Monte Carlo.

Figure 6.4: *The scintillator and track matching efficiencies for the 10° zenith angle bin. The data efficiencies are measured versus the measured momentum in the detector (*MBAR*), whereas the Mon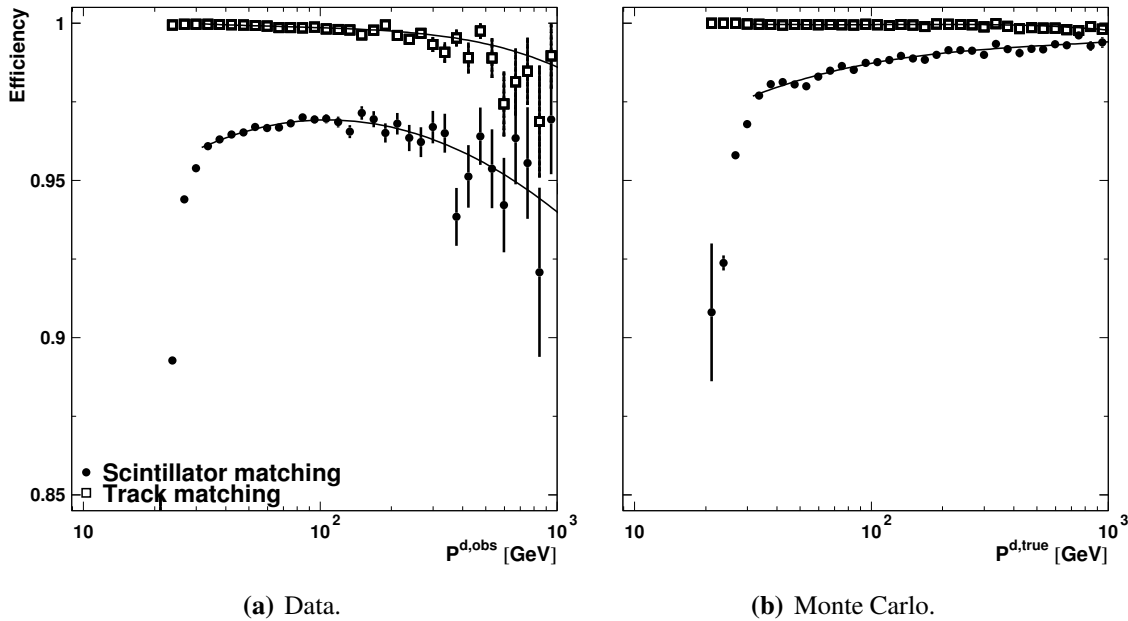te Carlo efficiencies are measured versus the true momentum at* MBAR *. Only the statistical error is shown. The fitted polynomials are also shown.*

ure 6.4. For the data the efficiency slowly starts to drop above 50 GeV resulting in about 2% inefficiency at 1 TeV. The Monte Carlo shows the same trend above 50 GeV, but the amplitude is much smaller. This inefficiency is caused by problems with the GEANE covariance matrix, which was discussed in section 3.1.2.

Scintillator matching efficiency

The scintillator matching efficiency is measured by comparing the number of events with and without the scintillator matching requirement. So as to not confuse this with the scintillator efficiency, both samples must have scintillator hits which satisfy the 7 ns coincidence requirement. The result can be seen in figure 6.4. At low energies, the precision of the back-tracking of a muon from the chamber to the scintillator modules is very sensitive to the accuracy of the estimated momentum. Both the estimated bending and the multiple scattering in the iron yoke increase at lower momentum. This effect results in a lower matching efficiency at low energies, which is clearly visible in figure 6.4. Above 50 GeV the Monte Carlo efficiency approaches 100%, whereas the data only reaches 97%. Above 100 GeV the data efficiency slowly drops to about 94% at 1 TeV. This drop could be caused by the increasing number of secondaries created in the molasse and concrete above the detector, causing additional scintillator hits, which make the matching harder. That this effect is only barely visible in the Monte Carlo would seem to suggest that the threshold of creating secondaries in GEANT is put too high.

6.1.2 The deconvolution

In this experiment as in any other, the measured distribution is different from the true distribution, due to the finite resolution of the detector. The main distortion in this analysis is due to the momentum resolution. The angular resolution in the detector is measured to be better than 0.5° (Wilkens 2001) for matched tracks, which is much smaller than the smallest bin width used in this analysis. Furthermore the variation of the flux versus the zenith angle is much gentler than the steeply falling momentum spectrum. Thus, no unfolding of the angular resolution is necessary.

The true spectrum $n(p_i^{d,true})$ can be obtained from the observed spectrum $n(p_j^{d,obs})$ by

$$n\left(p_i^{d,true}\right) = \sum_j \mathcal{P}\left(p_i^{d,true} \mid p_j^{d,obs}\right) \cdot n\left(p_j^{d,obs}\right) \tag{6.5}$$

when knowing the conditional probability $\mathcal{P}(p_i^{d,true} \mid p_j^{d,obs})$ which, as always, is unknown. The opposite conditional probability $\mathcal{P}(p_i^{d,obs} \mid p_j^{d,true})$ can, however, be obtained when knowing the resolution function.

When looking at it as a matrix, one can as a first approximation try to invert it. The matrix can, however, not always be inverted. Inverting this matrix may also yield non-physical results, such as a negative number of events (Zech 1995). One is left with two options:

- Fitting the contents of each bin $n(p_i^{d,true})$ to the measured distribution using the known conditional probability $\mathcal{P}(p_i^{d,obs} | p_j^{d,true})$. To avoid getting unstable results it is common practice to enter a so-called regularization term. This serves to dampen oscillations, but may bias the result (Zech 1995). Notice that if both histograms have the same number of bins, the only degrees of freedom of the "fit" are the one(s) introduced by the regularization term!

- Using Bayes' theorem in an iterative procedure (as proposed e.g. in (D'Agostini 1995)). Using the completeness of $\mathcal{P}(p_i^{d,true})$ Bayes' theorem can be written as:

$$\mathcal{P}\left(p_i^{d,true} \mid p_j^{d,obs}\right) = \frac{\mathcal{P}\left(p_j^{d,obs} \mid p_i^{d,true}\right) \cdot \mathcal{P}\left(p_i^{d,true}\right)}{\sum_l \mathcal{P}\left(p_j^{d,obs} \mid p_l^{d,true}\right) \cdot \mathcal{P}\left(p_l^{d,true}\right)} \tag{6.6}$$

hereby removing the measured probability distribution from the equation. At first glance, this looks like a sterile set of equations, since equation (6.6) requires the knowledge of $\mathcal{P}(p_i^{d,true})$. It was exactly what was missing in (6.5), since $n(p_i^{d,true}) = \mathcal{P}(p_i^{d,true}) \cdot N$, where N is the total number of events. However, this circular set of equations can be solved by bootstrapping, but one must provide an initial guess about the probability distribution of the true values.

In this analysis the Bayesian approach is chosen. The algorithm provided by D'Agostini is used in a slightly modified version to remove the assumption of Poissonian errors on the measured distribution.

As was suggested by D'Agostini, the $\mathcal{P}(p^{d,true})$ distribution is fitted with the function from (Hebbeker & Timmermans 2002) before each iteration. This is done to avoid amplifying the statistical fluctuations, and thus serves to regularize the result.

As prior both the probability distributions from (Hebbeker & Timmermans 2002) and from (Bugaev *et al.* 1998) were tried, without any significant difference on the result. However it turns out that the fastest convergence and highest stability is achieved by first performing a few iterations without regularization, using the (Bugaev *et al.* 1998) function as prior. The result of these iterations is fitted with the (Hebbeker & Timmermans 2002) function, and then used as prior.
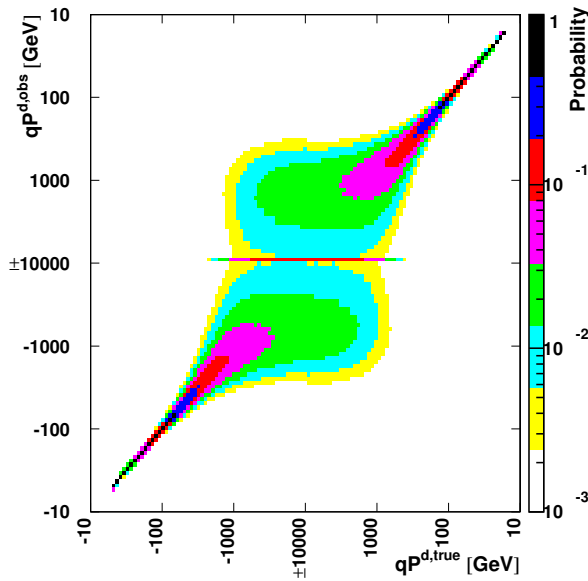

Figure 6.5: *The conditional probability* $\mathcal{P}(p_i^{d,obs} \mid p_j^{d,true})$.

The convolution matrix $\mathcal{P}(p_i^{d,obs}|p_j^{d,true})$ is determined from the measured resolution function (see section 5.5.2). In each $p_j^{d,true}$ bin 10^6 $p^{d,obs}$ momenta are generated with Monte Carlo according to:

$$ p^{d,obs} = \left(\frac{1}{\hat{p}^{d,true} - C(\theta_k)} + X \right)^{-1} + C(\theta_k) \tag{6.7} $$

where $\hat{p}^{d,true}$ is the true momentum generated as $\frac{\partial n}{\partial p} = p^{-3}$ within the $p_j^{d,true}$ bin. $C(\theta_k)$ is the momentum offset and X is a stochastic variable generated according to the resolution function (see equation 5.20). The resolution function is measured for each $p_i^{d,obs}$ bin, but it is here used as if it was measured in bins of $p^{d,true}$. This is justified by the fact that for momenta below about 200 GeV the momentum resolution and the binning are such that only very little migration between the bins occur (see figure 6.6d). Above about 200 GeV this is no longer the case, but the resolution function is constant above 100 GeV (see figure 5.7), thus enabling the use of the measured function at 100 GeV for all higher momentum bins. The resulting convolution matrix can be seen in figure 6.5.
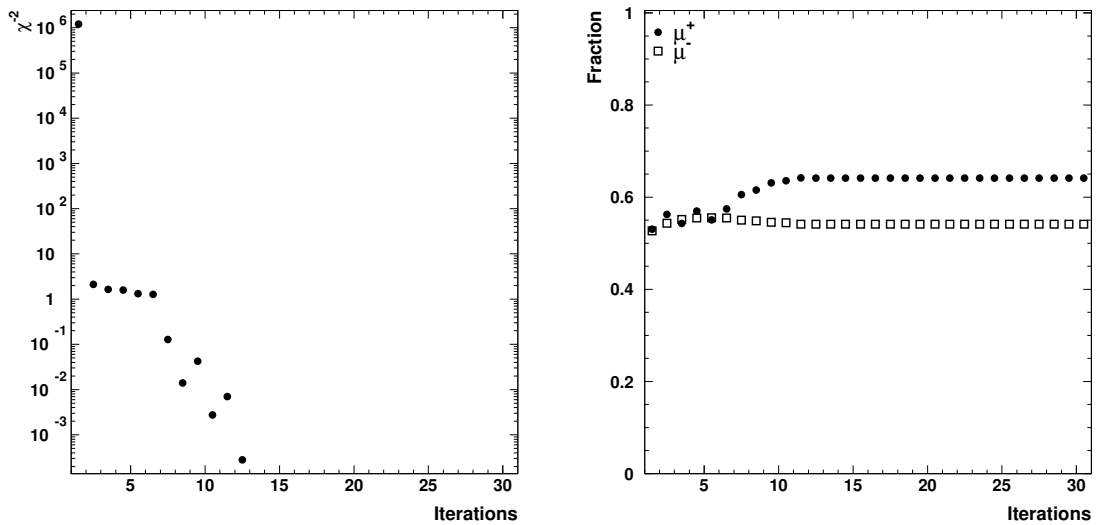
With any iterative procedure, the main question is to determine the optimum number of iterations. After each iteration the algorithm returns an estimator of the true spectrum $\hat{n}(p^{d,true})$. To assess the need for further iterations D'Agostini proposes a χ^2 comparison between two consecutive $\hat{n}(p^{d,true})$ distributions[*]. Notice that this χ^2 does not judge the quality of $\hat{n}(p^{d,true})$, since they should be the same. It only serves to judge the convergence. In figure 6.6 this χ^2 can be seen for each iteration. It is clear that the initial guess is inaccurate, but it is interesting to note how fast the χ^2 becomes O(1). A different method of looking at the stability of the method is by looking at the behaviour of the bin which is most affected by the deconvolution, i.e. the highest relevant momentum bin. Figure 6.6 also shows the contents of

---

[*]The χ^2 comparison is truncated at 1 TeV, to avoid the influence of the uninteresting bins beyond.

(a) The χ^2 of the comparison between the result of two consecutive iterations.

(b) The contents of the 1 TeV bin after each iteration over the initial contents.
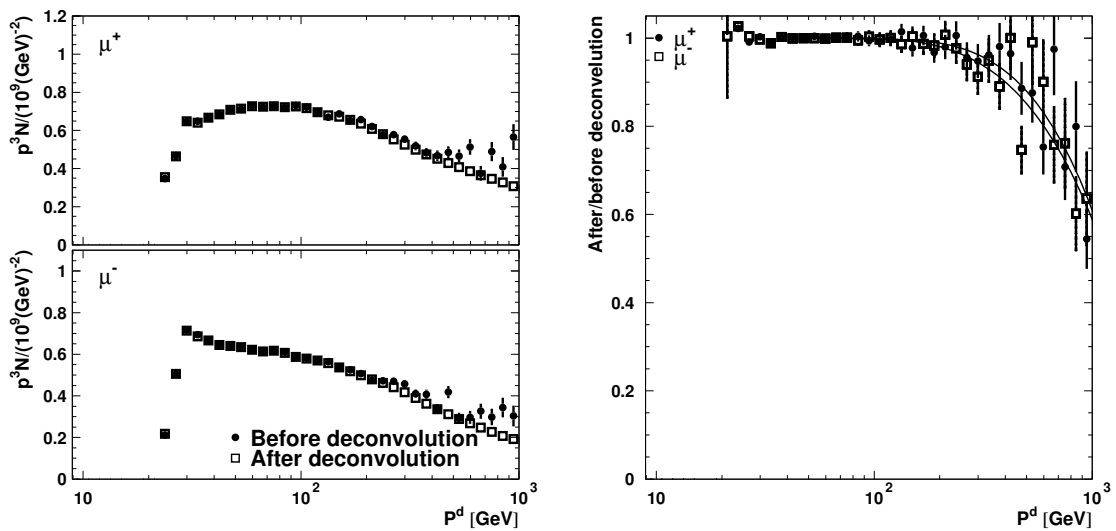
(c) The momentum distribution before and after the deconvolution. Both are multiplied by the momentum to the third power.

(d) The momentum distribution after divided by the one before the deconvolution. A third order polynomial is fitted to guide the eye.

Figure 6.6: *The two variables used to assess the need for a further iteration, and below the effect of the deconvolution.*

the 1 TeV bin after each iteration divided by the initial contents. A plateau is reached after 10 iterations. For this analysis the following stop conditions are used:

- the χ^2 comparison yields a value below 0.01; or

- the number of iterations has reached 30.

The last condition is there to ensure a finite number of iterations. These criteria are clearly
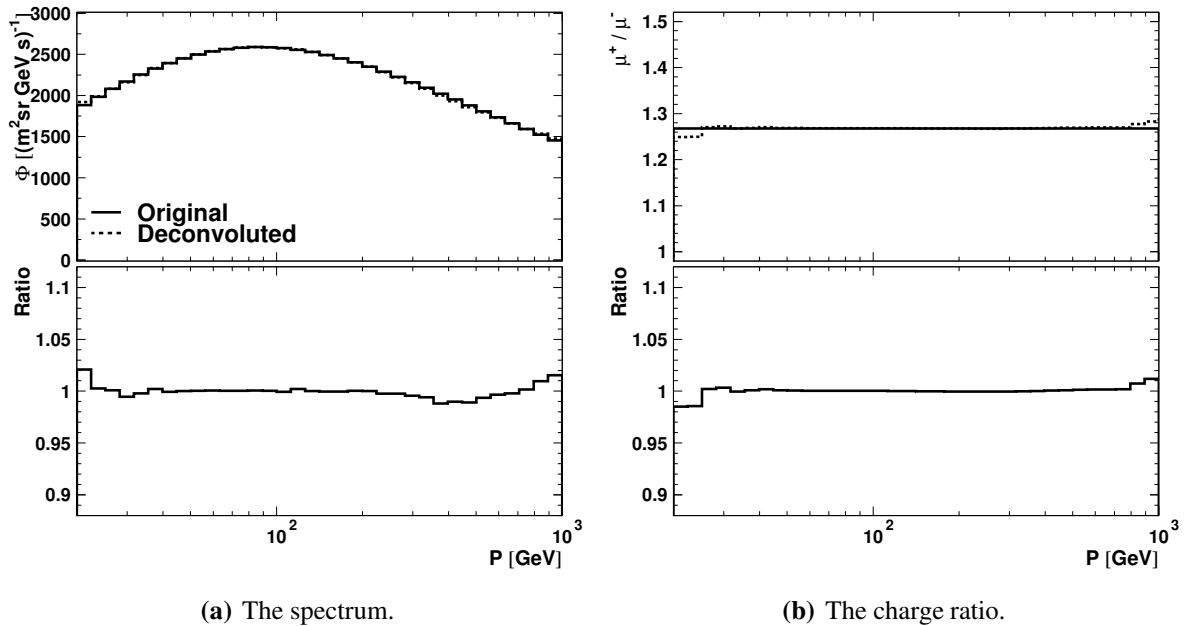
(a) The spectrum.   **(b)** The charge ratio.

Figure 6.7: *The comparison between the (Hebbeker & Timmermans 2002) spectrum and the result of first convoluting and then deconvoluting it.*

not unique, so the change of the result when varying them will be assigned as a systematic error.

In figure 6.6c the result of the deconvolution of the vertical spectrum can be seen. It shows that about 40% of both the μ^- and μ^+ measured at 1 TeV are reassigned to lower energy bins. Due to the steeply falling spectrum the gain of these events at lower energies is hardly visible. The fraction shown in figure 6.6d is at higher energies a bit lower for μ^- than for μ^+, although the resolution function is the same for the two charges. This is caused by the fact that the charge ratio $\frac{n(\mu^+)}{n(\mu^-)}$ is larger than one. On an absolute scale there are therefore more μ^+'s which can be misidentified as μ^-'s, than the other way around. By arranging the two spectra "back to back", as was discussed on page 90, the deconvolution automatically takes this effect into account. This simply follows from the fact that the primary measured quantity is the signed sagitta of a muon trajectory in a magnetic field (see section 2.2.1).

The functionality of the D'Agostini algorithm is checked by folding the flux from (Hebbeker & Timmermans 2002) with the measured resolution function and unfolding it afterwards. To make the check more realistic, the spectrum is first convoluted with the smearing by the molasse (see section 6.1.4) and corrected for the acceptance (see section 6.1.5). This folded spectrum is deconvoluted in the same way as the measured flux, both for the resolution and molasse effect. Figure 6.7 shows the comparison between the input flux and resulting flux. The difference which can be seen is in fact related to the prior. When using the correct prior, i.e. the known result, the algorithm converges almost immediately and the discrepancies are less than 0.5%. The discrepancy can then be seen as a systematic uncertainty when choosing the prior. In section 6.2.4 a slightly different approach is used to estimate this uncertainty, which results in a somewhat smaller uncertainty.
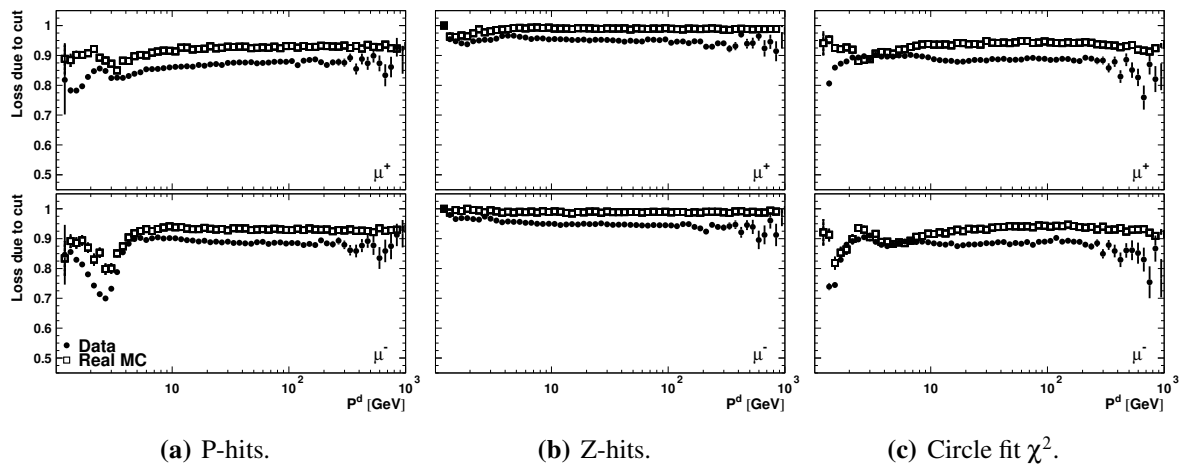
(a) P-hits. **(b)** Z-hits. **(c)** Circle fit χ^2.

Figure 6.8: *The marginal losses introduced by the three most important cuts at the octant level. The data loss is plotted vs. the measured* MBAR *momentum, whereas the Monte Carlo loss is plotted vs. the true* MBAR *momentum. The momentum offset is not applied.*

6.1.3 The up-down method

The biggest difficulty in measuring an absolute flux lies in acquiring accurate knowledge of the efficiencies. In spite of the many difficulties in using a detector designed for accelerator based physics for the measurement of the cosmic ray induced muons, it turns out that L3 has one very favorable feature: the ability to measure the same muon trajectory twice. Section 5.5 showed how this feature improved the momentum resolution, and more importantly it enabled the measurement of the resolution function. In this section this same feature will be used to measure the detector efficiencies.

To assess the agreement between data and Monte Carlo it is common to look at the effect of removing a single cut while maintaining the other cuts, i.e. to assess the marginal loss of each cut. This is shown in figure 6.8 as a function of momentum for the three most prominent cuts at the octant level. The agreement between data and Monte Carlo is clearly not satisfactory. Not only are the losses predicted by the Monte Carlo too small, the discrepancy is also momentum dependent. Furthermore, the losses due to the cut on the number of P hits are charge dependent. This can be understood by the fact that the inefficient cells[*] (see figure 5.3) break the symmetry of the detector. The curvature of the trajectories in the magnetic field is different for the two charges, causing them to sample different parts of the detector. To convert this into an efficiency the correlation between the losses must be taken into account. Moreover one needs to measure the reconstruction efficiency for data and Monte Carlo, while keeping in mind that the data is subject to the hardware trigger, while the Monte Carlo is untriggered. It is the aim of the up-down method to combine all these efficiencies into one single correction using data rather than simulation.

The essence of the up-down method is to measure the efficiency of detecting a sub-track

---

[*]The hits from these cells are killed in the initial phase of the reconstruction, thus leaving these cells as dead regions.

in a upper and lower octant, respectively. The product of these two efficiencies is thus the efficiency for detecting a full track, apart from the matching efficiencies which are treated separately (see section 6.1.1). Ideally the inefficiencies of the Monte Carlo would be identical to the ones for the data. If this was the case, the acceptance (see section 6.1.5) would be accordingly lower, and thus resulting in a correct estimate of the flux. Since this is not the case the ratio of the data and Monte Carlo efficiency must be applied in equation (6.3).

Using a set of sub-tracks measured in the lower/upper octants to "look with", it is possible to measure the efficiency of a selected sub-track in the upper/lower octant (i.e. what is being "looked at"). Per octant the set is split in three classes n^{sele}, $n^{\overline{sele}}$ and $n^{nothing}$, which are the number of selected sub-tracks, the number of not selected sub-tracks and the number of cases without a sub-track, respectively. When determining the efficiency this way, the cracks between the octants, known hardware problems etc. are included as inefficiencies. Formally the efficiency can be written as:

$$\varepsilon_{up} = \frac{n_{up}^{sele}}{n_{up}^{sele} + n_{up}^{\overline{sele}} + n_{up}^{nothing}} \tag{6.8}$$

and similar for the ε_{down}. The efficiency of measuring a full track ε_{ud} is then given by the product of the two individual efficiencies. Hereby the possible correlated losses are neglected. This potential problem is studied by comparing real and ideal Monte Carlo, and the discrepancy is used as a conservative estimate of the systematic error of the up-down method (see section 6.2.6).

The momentum dependence observed in figure 6.8 suggests that a good momentum resolution is needed. This is achieved by only using sub-tracks to "look with", which on their own pass the selection criteria. To avoid the complication of having several sets of tracks, each with their own resolution function, the efficiency is measured versus the momentum of the tracks used to "look with". A few exceptions and extensions to the normal selection are made:

- For data, the trigger must have fired in the same octant as the sub-track used to "look with". This is done to exclude the trigger efficiency, which is corrected for separately.

- As was done for the track matching efficiency, only single muon events are used. If two unmatched sub-tracks are found in opposite halves of the detector, they are manually matched. This is done to exclude the matching efficiency.

- The sub-track which is being "looked at" does **not** have to be matched with a scintillator hit. This is done to exclude the scintillator matching efficiency, which is corrected for separately.

- The reconstructed intercept with the $y = 0$ plane must satisfy $|x| < 3.5$ m and $|z| < 6$ m. This requirement only affects the single sub-track events. It is applied to ensure that no data events are included outside the Monte Carlo generator surface.

Figure 6.9 shows the fraction of events in each of the three classes for both the upper and lower octants. It is important to notice, that the case where no sub-track was found is well
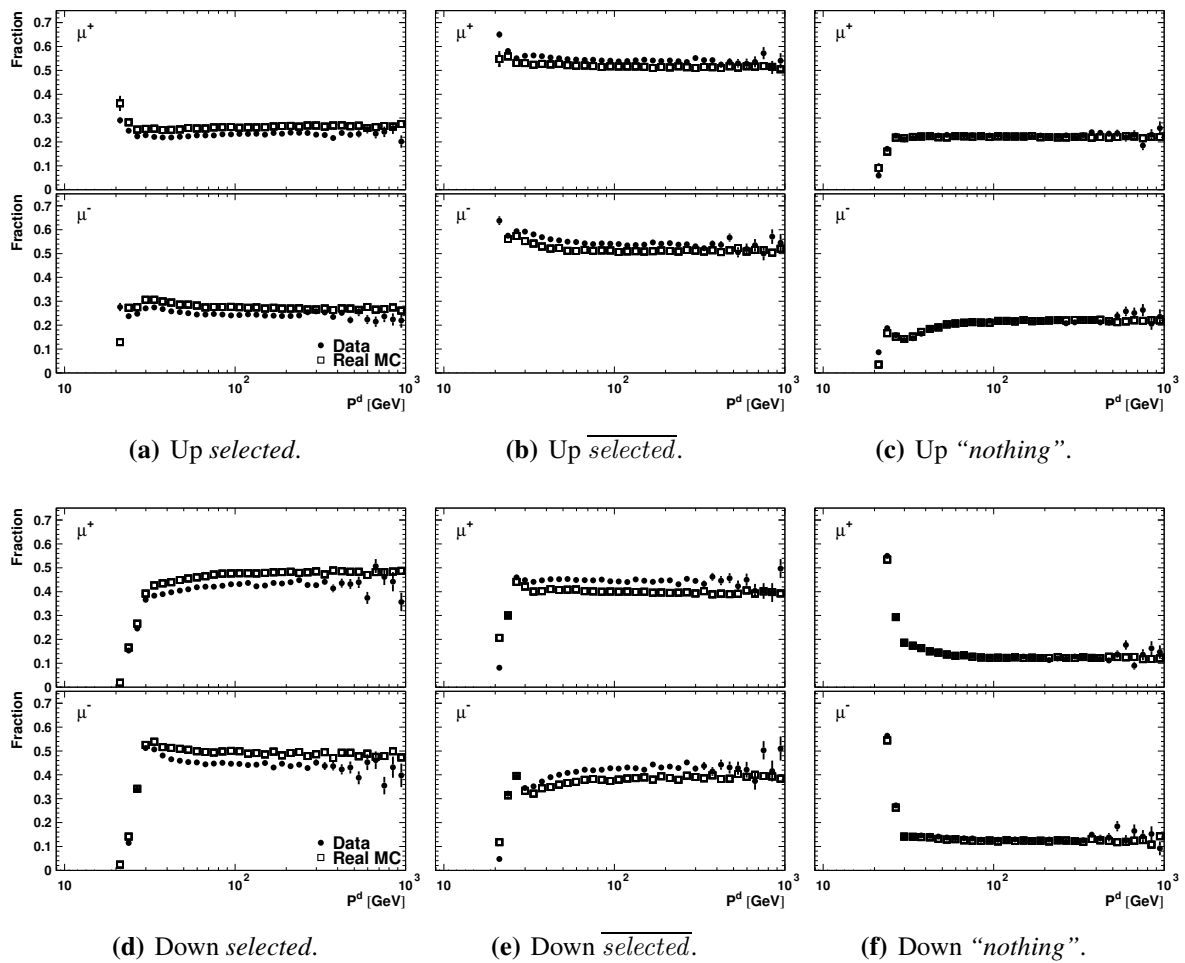
Figure 6.9: *The fraction of selected sub-tracks (selected), the fraction of sub-tracks which were not selected (selected) and the fraction where no track was found ("nothing") is shown separately for the upper and lower octant. The data fractions are plotted versus the measured* MBAR *momentum, and the Monte Carlo fractions are plotted versus the generated momentum at* MBAR.

described by the Monte Carlo . This indicates that the cracks and dead cells etc. are well described in the Monte Carlo . The discrepancy between data and Monte Carlo in the fraction of selected sub-tracks, on the other hand is a clear indication that the Monte Carlo fails to describe the detailed properties of a track. This fact was already visible when looking at the marginal losses (see figure 6.8).

The product of the up- and down-fractions of selected events (see figure 6.9a,d) are multiplied to give the up-down efficiency, i.e. the efficiency of detecting a full selected track (see figure 6.10). The data efficiency is determined versus the measured momentum at MBAR without deconvolution, since deconvoluting the up-down distributions turned out to be unstable. To overcome the problem of the momentum resolution the efficiency is assumed to be constant above 300 GeV. To prevent adding additional fluctuations to the spectrum the
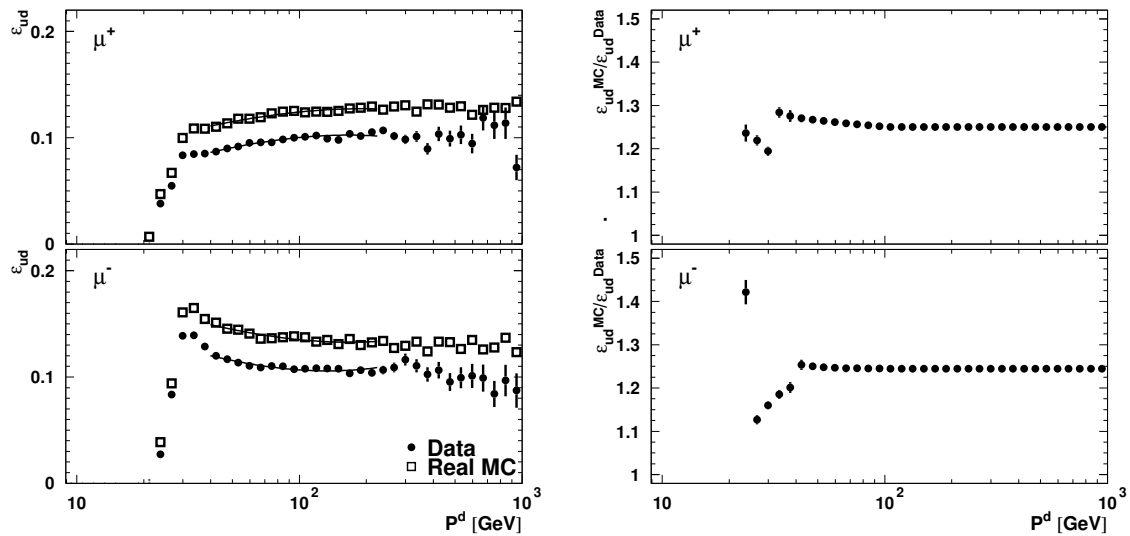
(a) The up-down efficiency for data and Monte Carlo plotted versus the momentum at MBAR . The fitted polynomials are also shown.

(b) The up-down efficiency for Monte Carlo divided by the one for data, i.e. the correction factor which the spectrum at MBAR gets multiplied by.

Figure 6.10: *The result of the up-down method for the $10°$ zenith bin.*

efficiencies are fitted with a third order polynomial from 30 to 300 GeV, as shown on figure 6.10a. The bins below 30 GeV are left unchanged by the fit. The uncertainty in the fit is used as an estimator of the systematic error. Figure 6.10b shows the up-down efficiency for Monte Carlo divided by the one for data. This correction is applied bin by bin according to figure 6.10b. For high momenta it results in an about 25% increase of the spectrum.

6.1.4 Propagation to the surface

The propagation to the surface of the observed spectrum at MBAR is done by the D'Agostini deconvolution method (see section 6.1.2). The change in momentum can be seen as an offset plus a smearing, where the offset is the most likely energy loss and the smearing is due to the stochastic part of the energy loss. As was discussed earlier, the most likely energy loss $C(\theta_j)$ is applied on an event by event basis in order to obtain an almost diagonal convolution matrix. Similar to what was done for the momentum convolution (see equation (6.5)), the molasse convolution can thus be written as:

$$n\left(p_i^{d,true}, \theta_j\right) = \sum_k \mathcal{P}\left(p_i^{d,true}, \theta_j \mid p_k^s, \theta_j\right) \cdot n\left(p_k^s, \theta_j\right) \tag{6.9}$$

where the convolution matrix $\mathcal{P}$ can be determined directly by Monte Carlo . It is very unfortunate that the Monte Carlo program used in the production, which is used for this analysis[*], contains an error in the GEANT description of the overburden. A 4 m thick cylindrical volume above the detector was simulated as if it was filled with air, whereas it should have been

---

[*]The version number is 404 and the production is known by the letter "h".

filled with molasse. For muons passing through this volume the estimated energy loss is on average about 2 GeV too small which, for the steeply falling spectrum, causes serious shifts at low energies. The complexity of the set-up does not allow for a simple correction, so an additional Monte Carlo production was initiated to overcome this problem. Apart from correcting the GEANT description, a few changes to the program were made to speed up the process:

- Only muons are tracked.

- Muons are only tracked until they reach `MBAR`, i.e. neither detector simulation nor reconstruction are performed.

- The 48 surface momentum bins between 5 and 1.2 TeV are equally filled. For momenta above 1.2 TeV the energy loss is assumed to be constant. Within each bin the events are generated as: $\frac{\partial n}{\partial p} = p^{-3}$.

- The events are generated homogeneously vs $\cos\theta$ and ϕ.

- The events are generated uniformly over a horizontal surface at the detector, and then linearly transported to the surface where the tracking starts. The generator surface is only 6.5×12.5 m^2, since only reconstructed double tracks pass the selection (see section 4.2)[*].

In total more than $3 \cdot 10^9$ events were generated. The conditional probability from equation (6.9) is obtained by:

$$\mathcal{P}\left(p_j^{d,true} \mid p_i^s, \theta_k\right) = \sum_{l,x_\perp,z_\perp} \mathcal{P}_1\left(p_j^{d,true} \mid p_i^s, \theta_k, \phi_l, x_\perp, z_\perp\right) \cdot \mathcal{P}_2\left(x_\perp, z_\perp \mid p_i^s, \theta_k, \phi_l\right) \qquad (6.10)$$

where $(x_\perp, z_\perp)$ is the projection of the intercept of the track with the `LEP3` volume down on $y = 0$. The first probability $\mathcal{P}_1$ is determined with this new Monte Carlo and the second probability $\mathcal{P}_2$ with the official Monte Carlo. $\mathcal{P}_2$ includes the selection requirement, in order to obtain the correct sampling.

Notice that the conditional probability does not include the absorption of muons in the molasse, which will be treated as part of the acceptance (see section 6.1.5). Figure 6.11 shows the convolution matrix for the 10° bin with and without the momentum offset. It is clear that a more diagonal matrix is obtained, which means that the majority of the effect of the molasse is removed. This stabilizes the deconvolution procedure.

6.1.5 The detector acceptance

The detector acceptance, including known hardware problems, the losses due to the molasse etc., is calculated using Monte Carlo . From equation (6.4) it follows that the acceptance can

---

[*]The official Monte Carlo production was used to check that less than 0.2% of the selected events are caused by events generated outside of the 6.5×12.5 m^2 surface.
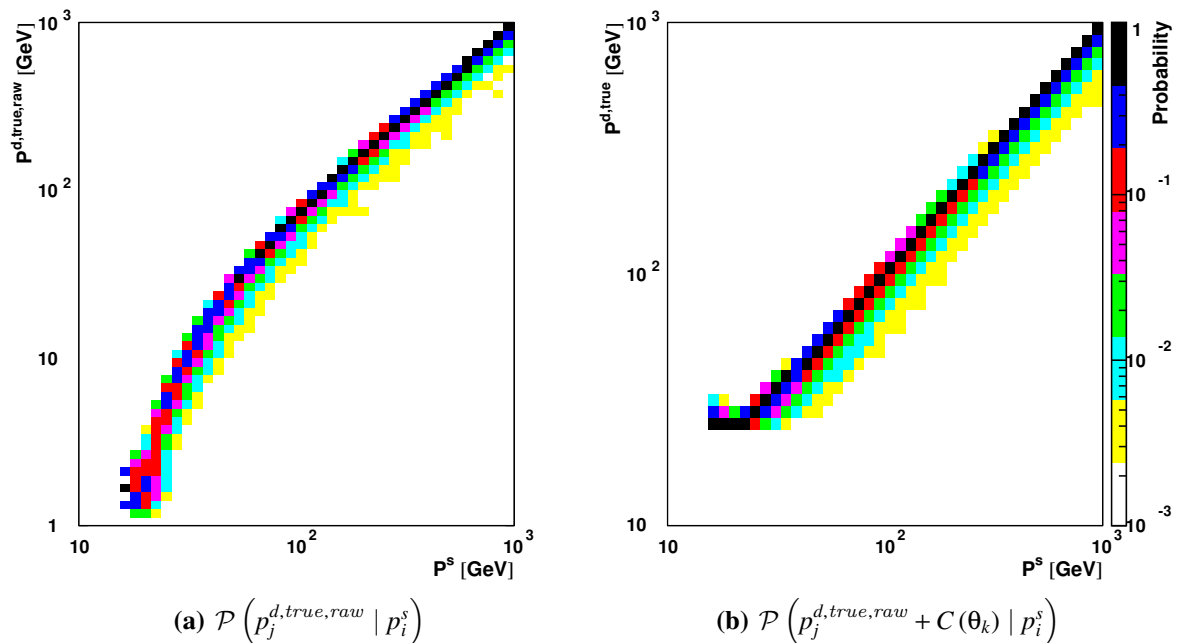
(a) $\mathcal{P}\left(p_j^{d,true,raw} \mid p_i^s\right)$ **(b)** $\mathcal{P}\left(p_j^{d,true,raw} + C\left(\theta_k\right) \mid p_i^s\right)$

Figure 6.11: *The conditional probability with and without the momentum offset $C\left(\theta_k\right)$ for the $10°$ bin. The momentum offset succeeds in creating a much more diagonal matrix.*

be estimated by:

$$A_{MC}\left(p_i^s, \theta_j\right) \quad = \quad 2\pi \frac{N_{acc}\left(p_i^s, \theta_j, \phi\right)}{N_{gen}\left(p_i^s, \theta_j, \phi\right)} \int\limits_{\cos(\theta_j)} S_\perp\left(\theta\right) d\left(\cos\left(\theta\right)\right) \tag{6.11}$$

Assuming that the Monte Carlo program correctly samples the phase space, the number of accepted Monte Carlo events, N_{acc}, over the number of generated events, N_{gen}, could directly be used as an estimator of the probability of accepting an event. The Monte Carlo generator L₃Cgen (Hebbeker & Korn 1998) is generating events according to a parametrization of CORSIKA (Heck & Knapp 2001, Heck *et al.* 1998), thus providing the best a priory estimate of ρ from equation (6.4). But with the bug in the molasse description used by the Monte Carlo program (see page 100) this approach must be modified. The probability of detecting a muon (χ) is split in two, and the integral over ϕ is made explicit:

$$A_{MC}\left(p_i^s, \theta_j\right) = \frac{2\pi}{N} \sum_{l=1}^{N} \mathcal{P}_1\left(p_i^s, \theta_j, \phi_l\right) \cdot \mathcal{P}_2\left(p_i^s, \theta_j, \phi_l\right) \cdot \rho\left(p_i^s, \theta_j\right) \int\limits_{\cos(\theta_j)} S_\perp^\dagger\left(\theta\right) d\cos\theta \tag{6.12}$$

where $\mathcal{P}_1$ is the probability of a muon reaching the MBAR volume, and $\mathcal{P}_2$ is the probability of detecting a muon knowing that it has reached the MBAR volume. Figure A.1 on page 131 shows the ϕ binning with respect to the shafts. $\mathcal{P}_1$ is estimated with the additional Monte Carlo by:

$$\mathcal{P}_1\left(p_i^s, \theta_j, \phi_l\right) = \left.\frac{N_{\text{MBAR}}\left(p_i^s, \theta_j, \phi_l\right)}{N_{gen}\left(p_i^s, \theta_j, \phi_l\right)}\right|_{S_\perp^\dagger} \tag{6.13}$$

(a) $\mathcal{P}_1$.
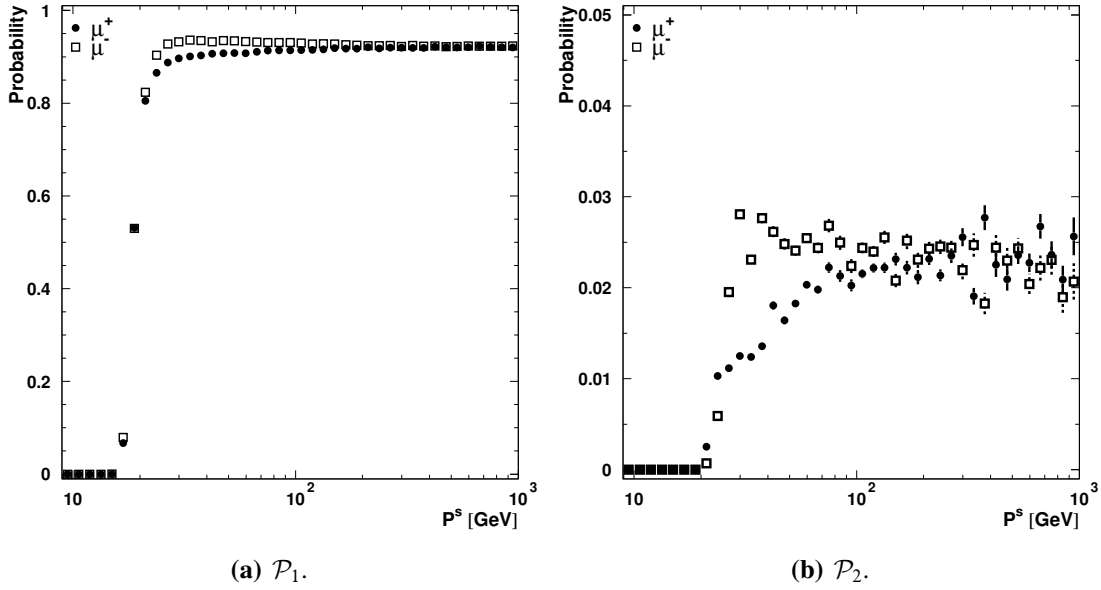
(b) $\mathcal{P}_2$.

Figure 6.12: *The probality of reaching* MBAR *($\mathcal{P}_1$) and the probability ($\mathcal{P}_2$) of accepting an event knowing that it hit* MBAR *as a function of the surface momentum. Both probabilities are shown for the 10° zenith bin and azimuth bin 15 (see figure A.1).*

where N_{MBAR} is the number of muons which reached MBAR out of the N_{gen} muons, which were generated. By using the additional Monte Carlo to estimate this probability, the perpendicular generator surface becomes equal to the one of the additional Monte Carlo ($S_\perp^\dagger$), which in turn is given by the 6.5×12.5 m^2 surface multiplied by $\cos \theta$.

$\mathcal{P}_2$ is estimated from the official Monte Carlo production, since the additional Monte Carlo did not include detector simulation. To join the two different Monte Carlo generators it is necessary to constrain the official one to the smaller generator surface of the additional Monte Carlo production:

$$\mathcal{P}_2 \left(p_i^{d,true}, \theta_j, \phi_l \right) = \frac{N_{acc} \left(p_i^{d,true}, \theta_j, \phi_l \right)}{N_{gen} \left(p_i^{d,true}, \theta_j, \phi_l \right)} \Bigg|_{\text{MBAR}, S^\dagger} \tag{6.14}$$

where N_{acc} is the number of events which passed the selection criteria out of the N_{gen}, which were generated on the 6.5×12.5 m^2 surface $S^\dagger$ and had a MBAR hit. Due to the molasse bug the ratio of accepted over generated events can only be measured as function of $p^{d,true}$, and is thus deconvoluted with the correct molasse response to obtain the probability as a function of p^s.

Figure 6.12 shows the two constituent probabilities $\mathcal{P}_1$ and $\mathcal{P}_2$ for one particular azimuth bin. As expected* the probability of reaching MBAR is about 92% for high energy muons. Below about 20 GeV the energy loss in the molasse prevents the muons from penetrating. The probability of detecting a muon, knowing that it reached MBAR, also decreases rapidly at lower energies. This can be understood by the fact that the selection requires, that the angle

---

*Muons are generated to a distance of 6.5 m in z, whereas the chambers only are 6 m long.

(a) 30 GeV.   **(b)** 100 GeV.
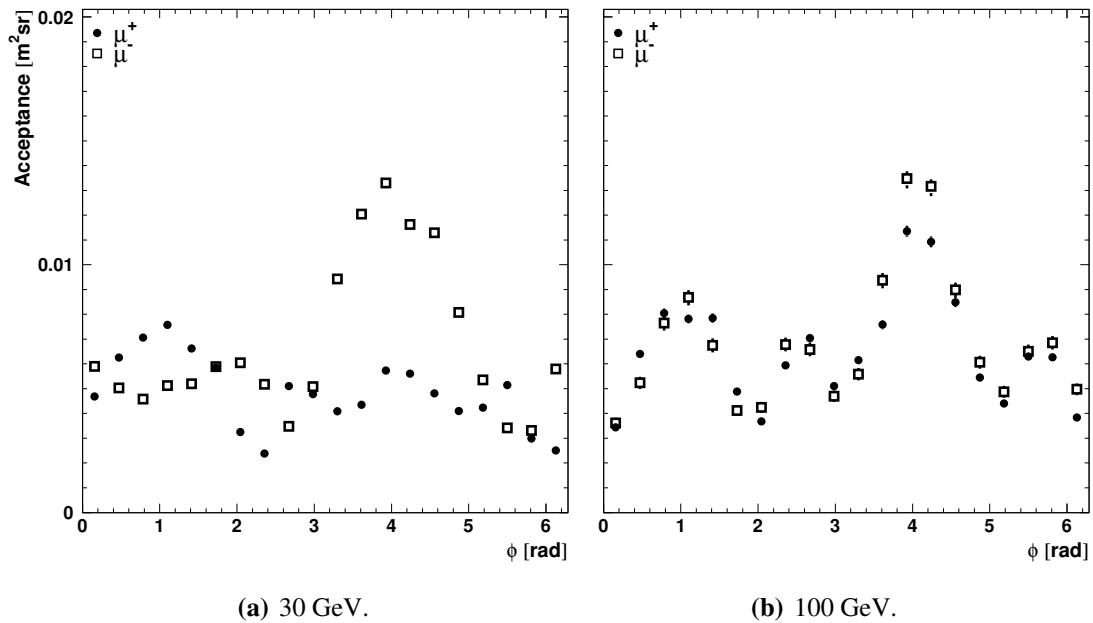
Figure 6.13: *The acceptance for the 10° zenith bin versus azimuth for the 30 GeV and 100 GeV surface momentum bins seperately.*

with respect to the wire plane of all six segments must be less than 25°. At lower energies the bending power of the magnet is too strong for this requirement to be satisfied in all six segments. At higher energies one would expect this probability to be constant, but in fact a small decrease is seen. The origin of this decrease is not well understood. Overall $\mathcal{P}_2$ is low (only about 2%), this is a result of the strong event selection (see section 4.2 and table 4.2). In addition it is interesting to notice the difference in the acceptance between μ^+ and μ^-. This has the same origin as the difference which was seen in figure 6.8, i.e. the different sampling of the detector by the two charges. The symmetry of the detector is broken by the dead cells (see figure 5.3). The acceptance determined from the "ideal" Monte Carlo is the same for two charges. The ideal Monte Carlo (see section 3.2.3) does not kill the dead cells and thus uses a symmetric detector. Some insight into the origin of the large difference between the acceptance of μ^+ and μ^-, is provided when studying its azimuth dependence (see the discussion of figure 6.13 below).

In section 5.1.2 the measurement of the scintillator efficiencies was described. Two sets of efficiencies were presented. One which is used in the Monte Carlo, and one which is applicable within this analysis. The ratio of these two is applied as an event weight to the accepted events which enter in $\mathcal{P}_2$.

In figure 6.13 the acceptance is shown versus azimuth for a low and medium energy bin. It is remarkable how different the acceptance is for the different azimuth bins. It clearly shows one of the difficulties of using a detector designed for accelerator physics, for the measurement of cosmic rays. Furthermore, a large difference in acceptance between the two charges is observed at low energy, whereas at 100 GeV this difference is substantially reduced. The two peaks in the acceptance (at 1 and at 4 radians) correspond to the barrel part
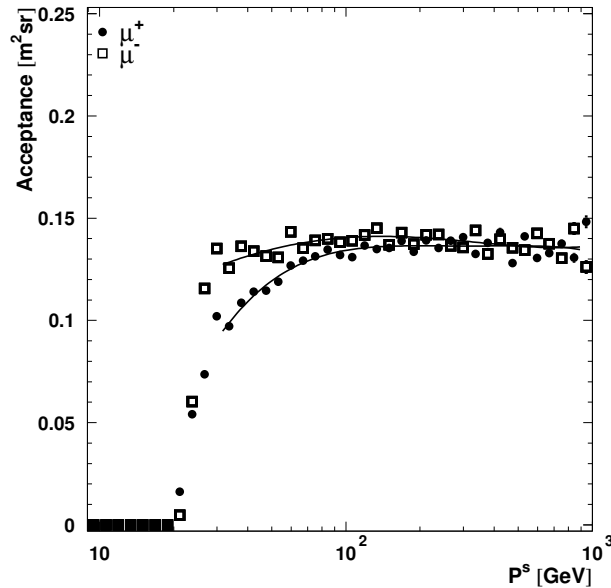
Figure 6.14: *The acceptance for the 10° zenith bin versus the surface momentum. The fitted fourth order polynomial is also shown.*

of the detector and the valleys in between are due to the doors, which are insensitive since the forward-backward chambers are not used. The difference between the height of the two peaks can be understood when looking at figure 5.3. The bad cells in `MM` of octant 2 `MASTER` essentially prohibits the measurement of a triplet when the muon originate from the right, but has only little effect on the measurement of muons originating from the left. The difference of the height of the peaks for the two charges at low energy is caused by the bending of the trajectories in the magnetic field. The main access shaft is located between 2 and 3 radians, which means that the majority of that effect is hidden by the doors.

Figure 6.14 shows the resulting acceptance for the 10°zenith bin. To avoid introducing fluctuations in the spectrum, the acceptance is fitted with a fourth order polynomial. The rapid decrease in acceptance at lower energies can not be described by the chosen function, so the distribution is only fitted from 30 GeV onward. The uncertainty in the fit is used as an estimator of the systematic error of the acceptance. It is interesting to note that only above 200 GeV the acceptance becomes the same for the two charges. Once again it is the dead cells which break the symmetry of the detector, which for low energy muons result in a different acceptance for the two charges.

6.1.6   Constant corrections

After the acceptance has been applied the spectrum is corrected for the momentum bin width and the total live-time. Table A.1 in appendix A shows the momentum range of the relevant momentum bins. The measured cosmic ray induced muon spectrum and charge ratio is shown in section 6.3 after the discussion of the systematic uncertainties.

6.2 Systematic errors

The uncertainties associated with a measurement are conventionally separated in the statistical and the systematic errors. Before starting the detailed description of the systematic error analysis, a short description of the error propagation will be given.

In a counting experiment like this, the covariance matrix of the statistical error on the measured distribution $n(p_i^{d,obs}, \theta_j)$ is a diagonal matrix containing the Poisson variance. Figure 6.3 shows schematically how the measured spectrum is transformed into the flux at the surface. For each correction, apart from the two deconvolutions, the distribution after the correction (Y) is given by the one before (X) scaled by the correction (C). In these cases the covariance matrix transforms as follows:

$$
\begin{aligned}
Y_i &= C_i \cdot X_i \\
V(Y)_{i,j} &= C_i \cdot C_j \cdot V(X)_{i,j}
\end{aligned}
\tag{6.15}
$$

The uncertainty on the correction is considered as a systematic error and is added to the diagonal of the covariance matrix containing the systematic errors. It thus transforms as:

$$
V(Y)_{i,j} = C_i \cdot C_j \cdot V(X)_{i,j} + \delta_{ij} V(C)_i \cdot X_i^2
\tag{6.16}
$$

The transformation due to a deconvolution is the same for both covariance matrices. To first order it is given by:

$$
V(Y) = M \cdot V(X) \cdot M^T,
\tag{6.17}
$$

where M is the convolution matrix, e.g. $\mathcal{P}(p_i^{d,obs} \mid p_j^{d,true})$. The two deconvolution steps thus give rise to correlations between the bins. Table A.2 in appendix A contains the covariance matrix for the statistical uncertainty of the flux presented in figure 6.23a. At the end of the discussion of the systematic errors the full covariance matrix will be presented along with the correlation coefficients.

The effects causing potential systematic errors to the measurement are grouped in the following three categories:

- the ones which only affect the normalisation of the flux;

- the ones which affect the measured points differently, and thus may affect the shape;

- finally the uncertainty on the momentum scale.

The first two categories will be quoted as uncertainties on the flux. Below the different ingredients of the analysis will be discussed separately, followed by a summary. For each error the effect on the spectrum and charge ratio will be discussed.

6.2.1 Event selection

To estimate how accurate the selection efficiencies are known, the cut positions are varied wherever possible. It is, for instance, not possible to change the P-triplet requirement. The

momentum resolution of a P-doublet is so poor compared to that of a P-triplet, that a meaningful comparison is impossible. The four cut variations described below are all used to estimate a normalization error:

Local ϕ cut: The local ϕ cut is changed from $25°$ to $24°$ and $26°$. The RMS of these three spectra is used as an estimator of the systematic uncertainty of this cut. It yields a negligible effect on both the spectrum and charge ratio. At first glance it would seem that the local ϕ cut would have the same effect on the two charges. But the symmetry of the detector is broken both by the Lorentz angle of the drift lines in the cells and by the dead cells. Thus it is not a priori possible to exclude the effect of the local ϕ cut on the charge ratio. But as the result shows the effect is indeed small.

Coincidence gate: The scintillator coincidence gate is changed from 7ns to 15ns. This results in an uncertainty of 0.1% on the normalization of the spectrum. The response of the scintillators is assumed to be the same for the two charges, thus this cut variation does not yield an uncertainty in the charge ratio.

Scintillator matching: The matching requirement of the scintillator matching is changed from 2σ to 0σ, i.e. the track must have an intercept within the boundaries of the cassette. This results in an uncertainty of 0.4% on the normalization of the spectrum, and results in an uncertainty of 1.0% on the average charge ratio. In spite of the name, this cut is mainly sensitive to the track quality rather than the scintillator response. It is thus not possible to a priori exclude the effect on the charge ratio.

Track quality: The cut on the number of Z-layers, P hits and circle fit χ^2/dof are all removed simultaneously. This results in an uncertainty of 0.5% in the normalization of the spectrum, and an uncertainty of 0.5% in the charge ratio.

For energies below 20 GeV the change of the coincidence gate and the scintillator matching requirement causes a momentum dependent increase in the uncertainty, but above 20 GeV the uncertainty is constant.

6.2.2 Scintillator efficiency

The systematic error from the measurement of the scintillator efficiencies (Unger 2002) are propagated as a normalisation uncertainty on the flux measurement. This amounts to 0.5%. The scintillator efficiency does not have any effect on the charge ratio.

6.2.3 Matching efficiencies

The systematic error on the measured matching efficiencies (see section 6.1.1) is estimated by the uncertainty on the fit, which is used to describe the efficiencies (see figure 6.4). In addition 2% of the inefficiency of the track matching is added as a systematic uncertainty (see page 91). Figure 6.15 shows the estimated uncertainty. The matching efficiencies are measured independently of the charge, and thus do not directly affect the charge ratio.
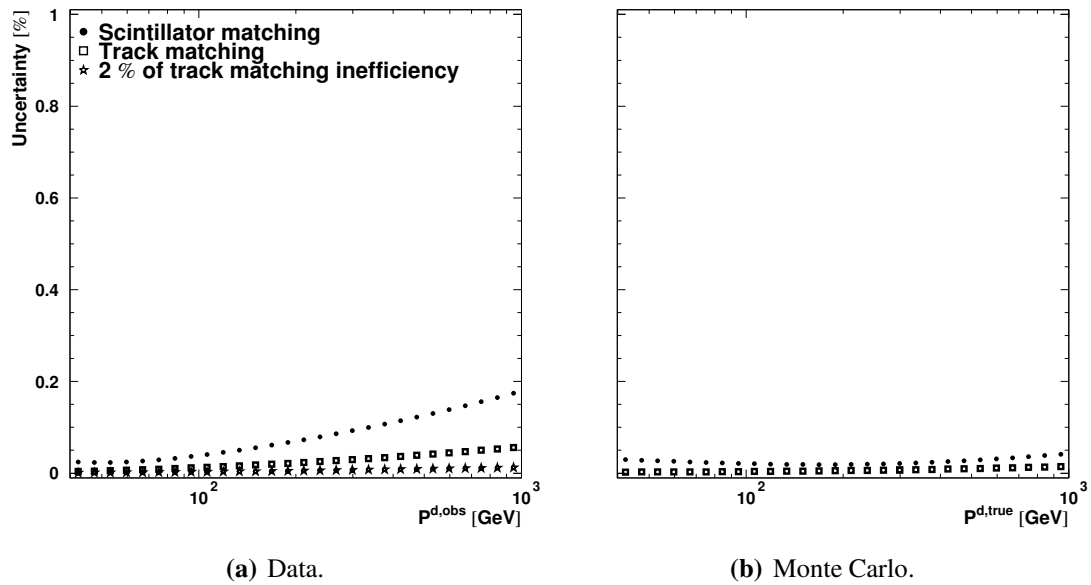
(a) Data.   (b) Monte Carlo.

Figure 6.15: *The estimated systematic error on the matching efficiencies. The data uncertainty is plotted versus the measured momentum at* MBAR *and the Monte Carlo is plotted versus the true momentum at* MBAR.

6.2.4 Deconvolution

The complexity of the deconvolution algorithm requires special care when estimating the systematic uncertainties. This importance of the deconvolution in this analysis is emphasized by the requirement to measure the flux to the highest possible energies. Below the most important ingredients of the algorithm are studied individually.

Convolution matrix

The effect of the uncertainty in the measurement of the momentum resolution function (see section 5.5.2), and thus on the conditional probability $\mathcal{P}(p_i^{d,obs}|p_j^{d,true})$, is estimated by moving the fitted parameters by $\pm$ 1σ along the axis of the error ellipsoid. This in practice means finding the eigenvalues and eigenvectors of the covariance matrix*. For each of the 11 eigenvalues the parameters of the function are moved by plus and minus the square root of the eigenvalue along the direction given by the eigenvector. In cases where an eigenvalue is negative, the parameter with the largest component of the eigenvector is moved by the square root of the diagonal element of the covariance matrix, the other parameters are left unchanged. In total 22 different convolution matrices are determined, giving rise to 22 different spectra. The uncertainty is estimated as the RMS of these spectra with respect to the spectrum using the nominal convolution matrix. The result can be seen in figure 6.16. As expected from the shape of the convolution matrix (see figure 6.5), the effect of varying the fit parameter only really affects the spectrum above 500 GeV.

---

*This was done with the NAGlib routine `F02FAF`.

(a) Flux. **(b)** Charge ratio.
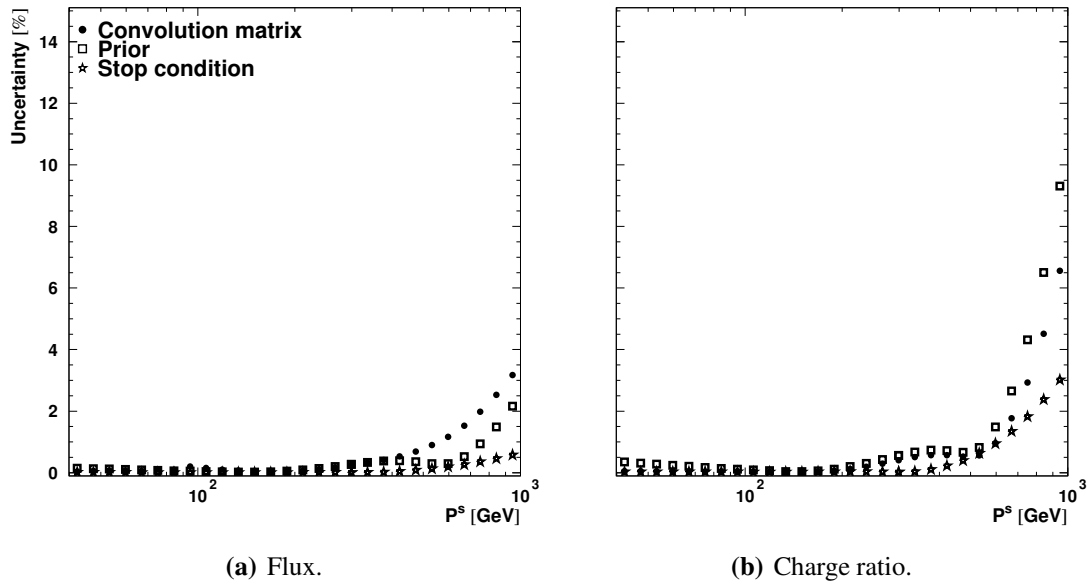
Figure 6.16: *The estimated uncertainty due to the convolution matrix and the prior used in the D'Agostini algorithm. The uncertainties are plotted versus the surface momentum.*

A dip in the uncertainty for both the spectrum and charge ratio is observed at about 500 GeV. Above 500 GeV the deconvolution algorithm must move a large fraction of the events to lower bins (see figure 6.6d) primarily the bins above 100 GeV. When elements of the algorithm are altered the fraction of high energy events, which are moved down changes, resulting in a change in the number of events added to the bins above 100 GeV. 500 GeV turns out to represent the boundary between these two effects, resulting in a stable point and thus a dip in the estimated uncertainty.

Prior

The potential bias introduced by the initial guess of the probability distribution $\mathcal{P}(p_i^{d,true})$, is studied by altering the spectral index of the prior. The prior is normally obtained by fitting the function from (Hebbeker & Timmermans 2002) to the measured distribution. The result of this fit is substituted by a power law beyond 100 GeV. 11 such priors are tried with spectral indices varying from -4 to -2. A spectral index of -4 clearly is too steep at 100 GeV and an index of -2 is not steep enough. The RMS of these 11 spectra is used as an estimator of the systematic uncertainty introduced by the prior. The result can be seen in figure 6.16. At 1 TeV the uncertainty amount to about 2%, which clearly shows the robustness of the algorithm.

Stop condition

The effect of the stop condition is studied by moving the χ^2 cut up and down by a factor 10. As expected from figure 6.6 the stop condition only has a marginal effect on the resulting spectrum and charge ratio.

(a) Flux.   **(b)** Charge ratio.   **(c)** Estimated uncertainty.

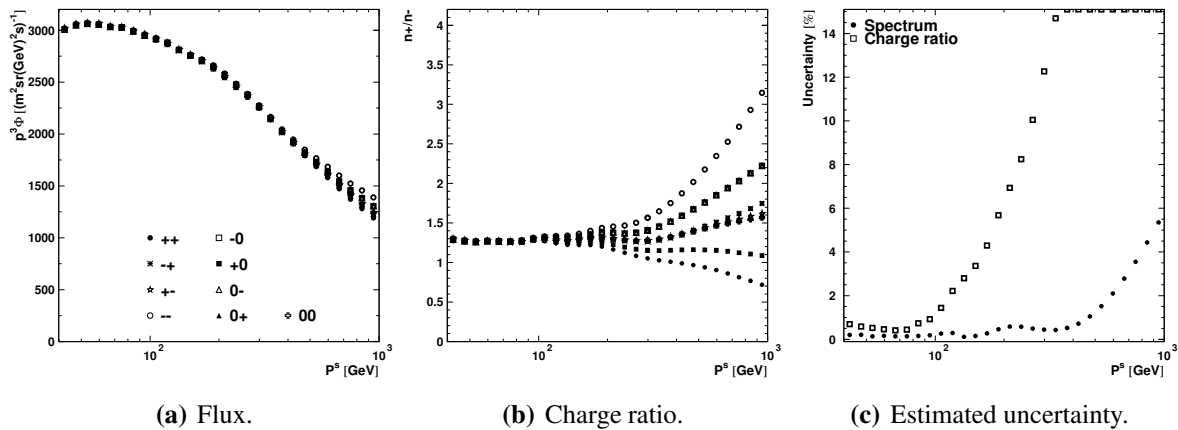**Figure 6.17:** *The measured flux and charge ratio for all nine combinations of misalignment. The RMS of all nine sign combinations is used as an estimator of the systematic uncertainty.*

6.2.5   The alignment

In section 5.5.1 the uncertainty in the alignment perpendicular to the wire plane of MM with respect to MI and MO was assumed to be 30 μm. A recent measurement (Unger 2002) indicates that this uncertainty could be as large as 50 μm. A misalignment can take place in both the upper and lower octant of a track. To study the influence of such a misalignment on the flux and charge ratio measurement the analysis is performed on 8 raw spectra where the measured sagitta has been altered by ±50 μm. The combinations with opposite signs in the two octants are only marginally influenced due to the weighed average. Figure 6.17a,b show the measured flux and charge ratio for all nine misalignment combinations. The devastating effect on the charge ratio at high energies is clearly visible, this uncertainty ultimately limits the momentum range within which the charge ratio can be measured. The RMS, with respect to the default, is used as the estimator of the systematic uncertainty in the flux and charge ratio due to the potential alignment error (see figure 6.17c). The effect on the flux is less dramatic, but it nevertheless is a significant contribution to the uncertainty at high energies.

6.2.6   The up-down method

The up-down method can be seen as a way of correcting the Monte Carlo acceptance in order to obtain the acceptance of the detector. The accuracy of the method can be estimated by comparing the acceptance of two different detector simulations, one with and one without the killing of bad cells, known as real and ideal Monte Carlo simulation respectively. The equality which will be tested is thus:

$$\frac{A_{real}}{A_{ideal}} = \frac{\varepsilon_{real}}{\varepsilon_{ideal}} \tag{6.18}$$

The implicit correction of the scintillator efficiency in the real Monte Carlo is removed to enable a comparison of the difference in chamber efficiency. Figure 6.18 shows the compar-
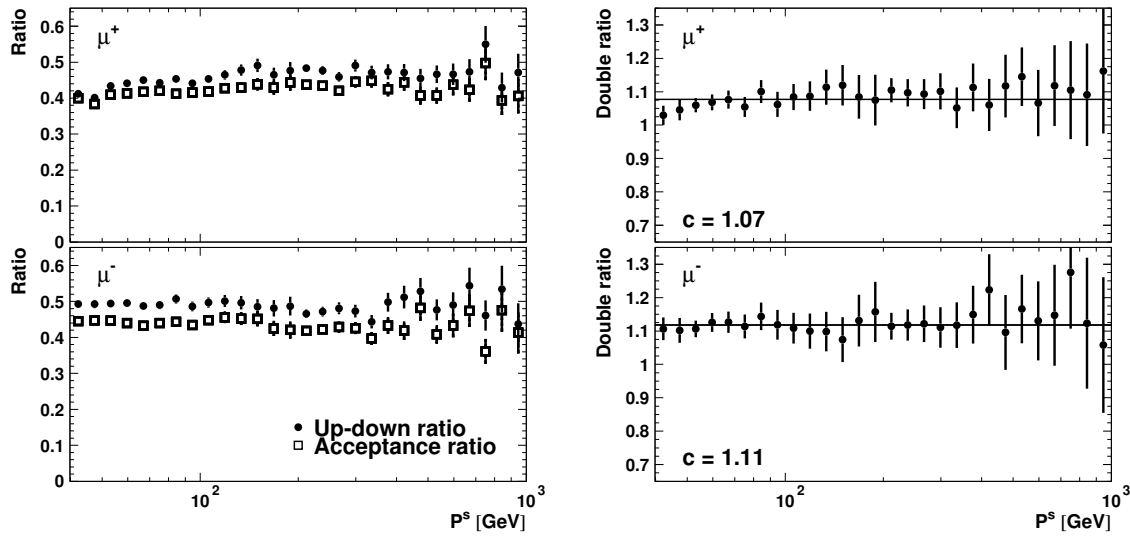
(a) The up-down efficiency for the real Monte Carlo divided by the one for the ideal Monte Carlo, compared to the same ratio of the acceptances.

(b) The up-down ratio divided by the acceptance ratio. The fitted constant is also shown.

Figure 6.18: *The comparison between up-down efficiency for real and ideal Monte Carlo and the acceptances for the two Monte Carlo types.*

ison between the two ratios from equation (6.18). The comparison shows that the up-down correction ($\frac{\varepsilon_{real}}{\varepsilon_{ideal}}$) is about 10% too large. Correlated looses in the real Monte Carlo could be a cause of this difference. This is used as an estimator of the uncertainty on the correction used in the analysis (see figure 6.10), which results in a 2.5% normalization error on the flux. The about 3% difference in the discrepancy between the two charges corresponds to a 0.8% uncertainty in the charge ratio.

The uncertainty in the fit of the polynomial to the up-down efficiencies (see figure 6.10b) is used as an additional momentum dependent uncertainty, which is added to the covariance matrix containing the systematic errors before it is propagated to the surface. This corresponds to an about 2% uncertainty on the flux.

6.2.7   The molasse

The uncertainty due to the molasse can be separated in two parts, one caused by the uncertainty of the variation of overburden, and one due to the uncertainty of the total overburden. The latter is estimated by assuming a 1m uncertainty in the overburden, for vertical muons this corresponds to about 500 MeV uncertainty in the momentum. The molasse was thoroughly studied during the geophysical survey before the building of LEP, so the 1m uncertainty is a conservative estimate. Variations are studied by comparing the flux in 20 different azimuth bins. For each momentum bin a χ^2 comparison between the 20 independent mea-

Type	Uncertainty [%]	
	Flux	**Charge ratio**
Atmospheric stability	2.5	–
Scintillator eff.	0.5	–
Scint. matching	0.4	1.0
Coincidence gate	0.1	–
Local ϕ	0.0	0.0
Track quality	0.5	0.5
Up-down method	2.5	0.8
Total	**3.7**	**1.4**

Table 6.2: *The individual and total uncertainty on the normalization of the flux and the average charge ratio.*

surements is made, which yield an estimate of the systematic error $\sqrt{V_{syst}\left(p_i^s, \theta_j\right)}$:

$$\chi^2 = \sum_{k=1}^{N} \frac{\left(\widehat{\overline{\Phi}\left(p_i^s, \theta_j\right)} - \widehat{\Phi}\left(p_i^s, \theta_j\, \phi_k\right)\right)^2}{V\left(p_i^s, \theta_j\, \phi_k\right) + V_{syst}\left(p_i^s, \theta_j\right)} \equiv N - 1 \tag{6.19}$$

Figure 6.19 shows the azimuth dependence of the flux for four low energy bins. The estimated uncertainty is indicated by the grey band. Figure 6.20a shows the momentum dependence of this systematic error. As expected, this uncertainty mainly affects low momentum muons. Above about 100 GeV the χ^2 from equation (6.19) is less than $N-1$, which means that no additional systematic uncertainty is needed. It is assumed that the imperfect description of the overburden has the same influence for the two charges and thus has no effect on the charge ratio.

6.2.8   The acceptance

The uncertainty from the fit to the measured acceptance (see figure 6.14) is used as the estimator of the systematic uncertainty of the acceptance. It is added to the diagonal of the covariance matrix. The estimated uncertainty can be seen in figure 6.20b.

6.2.9   The total systematic error

The uncertainties described in the sections above are added in quadrature. Table 6.2 shows the compilation of the uncertainties contributing to the normalization error. For the flux measurement the systematic uncertainty on the up-down correction dominates together with the uncertainty due the atmospheric variation during the data taking (see equation 4.1). This means that the normalization of the flux measurement is limited by the disagreement between data and Monte Carlo and by the variation in the atmospheric conditions. The uncertainty
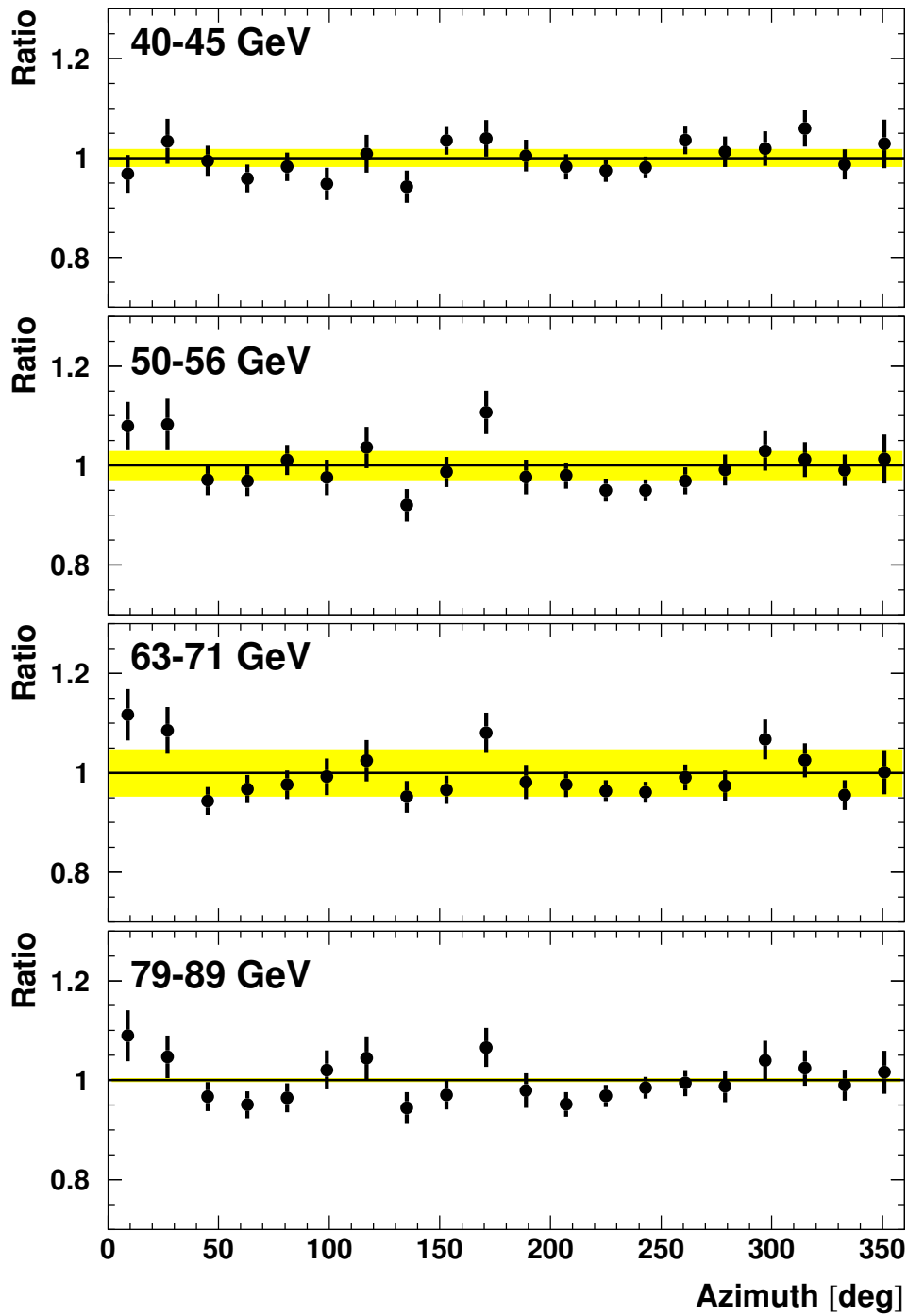
Figure 6.19: *The azimuth dependent flux is shown for four momentum bins. The flux is plotted relative to the weighed average of the 20 azimuth bins. The grey band indicates the estimated systematic uncertainty due to the variation of the overburden. The χ^2 for the last shown momentum bin is less than 19, so no additional uncertainty can be assigned.*
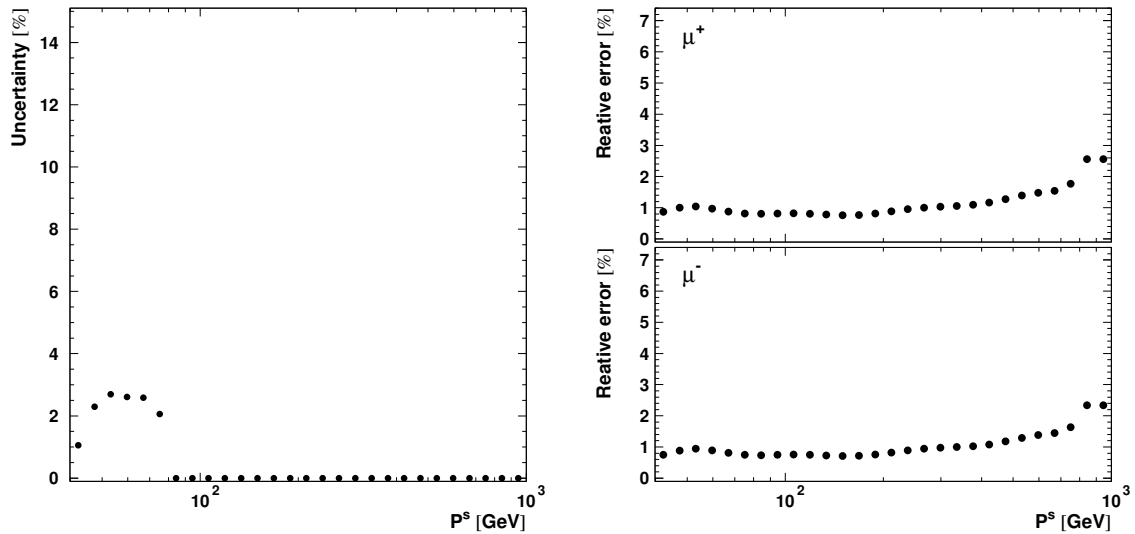
(a) The systematic uncertainty caused by the varia-
tion of the overburden.

(b) The relative error on the fit of the measured ac-
ceptance.

Figure 6.20: *The systematic uncertainty due to the last two steps of the analysis.*
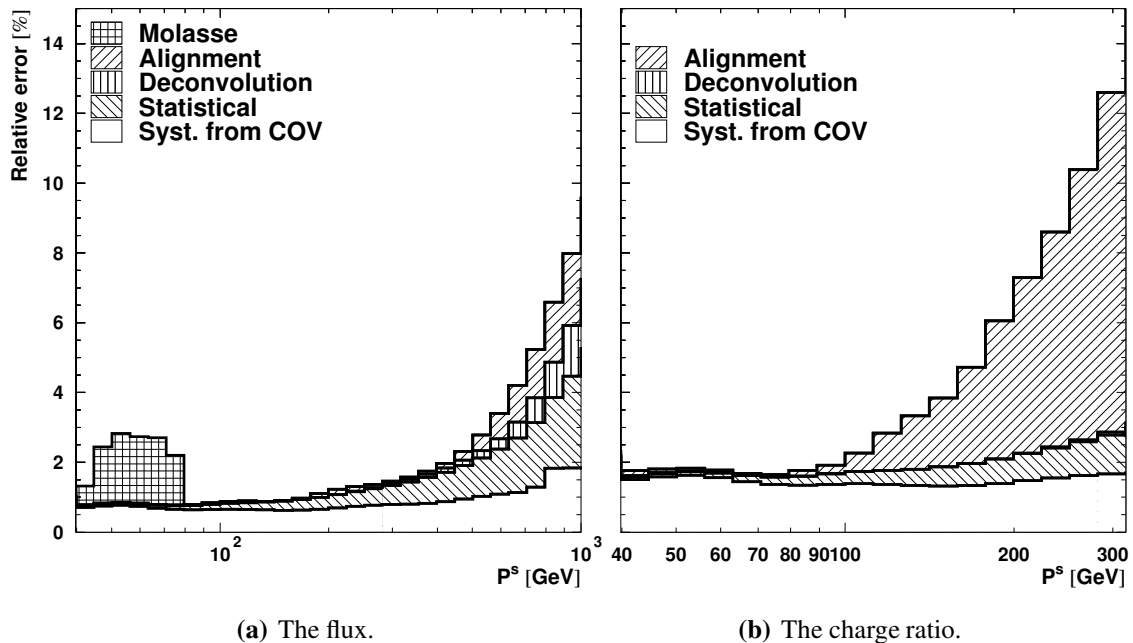
(a) The flux.

(b) The charge ratio.

Figure 6.21: *The total uncertainty in the shape of the spectrum and charge ratio shown along
with the individual components. The components are added in quadrature one by one.*

on the average charge ratio is all together smaller, and it is also dominated by two sources,
namely the uncertainty on the up-down correction, and the scintillator matching.

Figure 6.21 shows the total uncertainty on the shape of the spectrum and charge ratio. The
diagonal of the covariance matrix containing the statistical error is also shown. To enable the

(a) The flux. (b) The charge ratio.
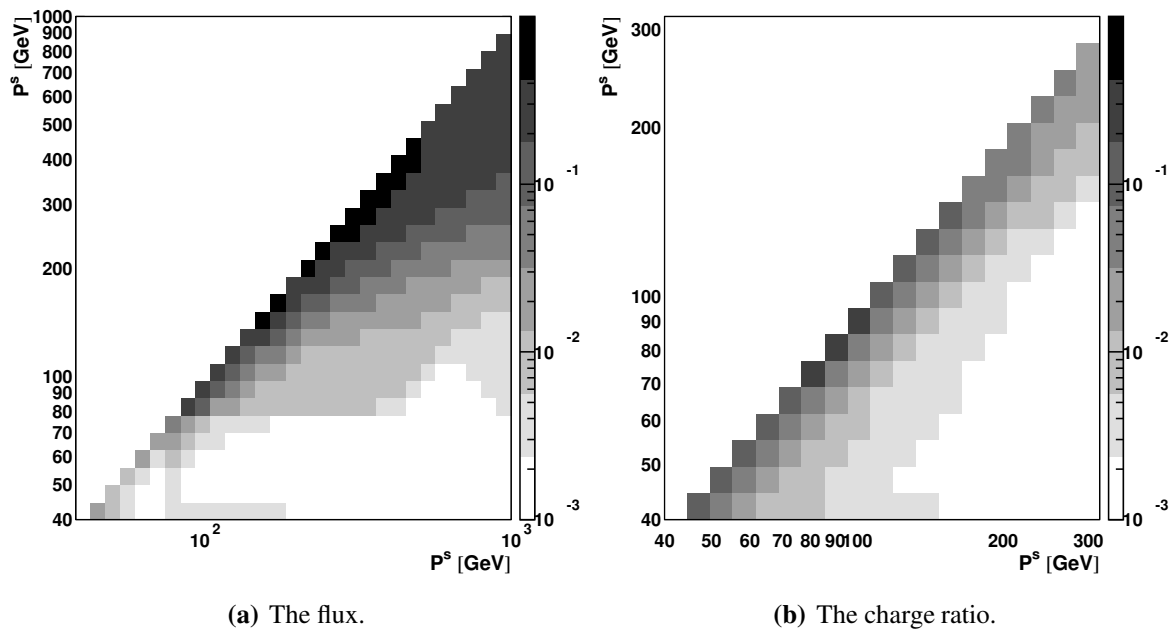
Figure 6.22: *The correlation coefficients for the measured spectrum and charge ratio. To simplify the plots both the diagonal and upper half of the matrices are suppressed.*

judgment of the importance of the individual components, they have been added in quadrature one by one. The plots show the incremental error as they have been added together, starting with the diagonal of the propagated covariance matrix and ending with the uncertainty due to the variation of the overburden and the chamber alignment for the flux and charge ratio, respectively.

In appendix A the full covariance matrix for the flux measurement can be found in table A.3 and for the charge ratio in table A.4. Figure 6.22 shows the correlation coefficients for the flux and charge ratio measurement. It is clear to see that the deconvolution of the momentum smearing introduces significant correlations between the bins at high energy. This effect is somewhat reduced by the addition of the systematic uncertainties to the diagonal of the propagated covariance matrix. For the charge ratio the large uncertainty due to the chamber alignment largely reduces the correlation coefficients.

6.3 The vertical flux

Figure 6.23 shows the measured flux of cosmic ray induced muons and the comparison with the world average from (Hebbeker & Timmermans 2002). Their quoted uncertainty in the shape is shown as a band around the function, while the uncertainty in the normalization is shown by a box at 100 GeV. The theoretical prediction from (Bugaev *et al.* 1998) is also shown along with the new calculation with the CORT code[*] (Fiorentini *et al.* 2001). It is a

---

[*]The CORT spectrum comes from a dedicated calculation, where the atmospheric pressure has been set to the average pressure of the runs used in this measurement.
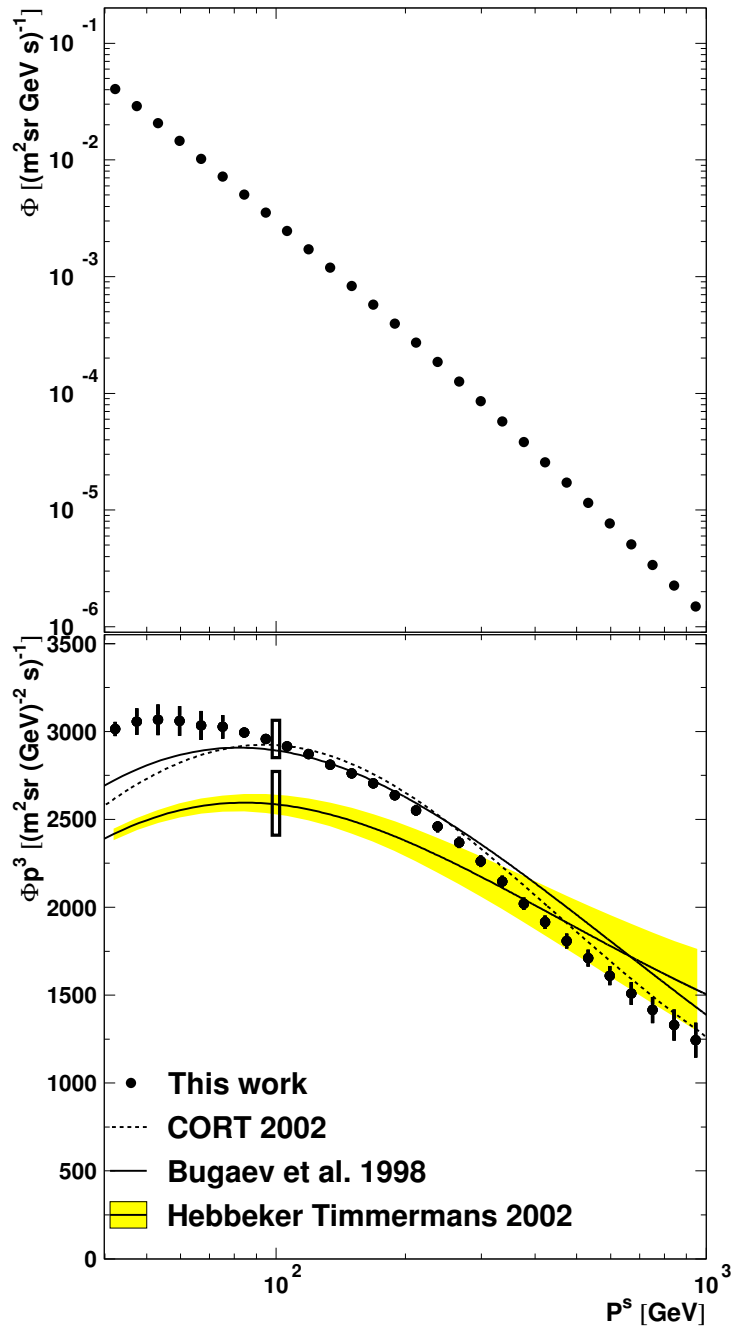
Figure 6.23: *The measured vertical flux in the 10° zenith bin along with the total uncertainty (top). To enable seeing the details of the measured spectrum it is conventionally multiplied by p^3 (bottom). The error bars indicate the uncertainty on the shape of the spectrum. The world average from (Hebbeker & Timmermans 2002) is shown for comparison along with the theoretical prediction from (Bugaev et al. 1998) and the CORT code (Fiorentini et al. 2001). At 100 GeV the normalization error is shown for this work and for (Hebbeker & Timmermans 2002).*

one-dimensional* model of the atmospheric shower, which uses the measured primary spectrum and composition as input (see section 1.4). The measured spectrum is multiplied by p^3 to enable one to see the structure of the spectrum (lower part of figure 6.23). The two deconvolution steps in the analysis prohibits applying p^3 as an event weight, thus the average momentum per bin must be determined. The spectrum from (Hebbeker & Timmermans 2002) is integrated numerically to obtain the average momentum per bin. When looking at the flux multiplied by p^3 it seems like a nice and slowly varying distribution, but when looking at the flux itself one realizes that a distribution has been measured over four orders of magnitude.

The normalization of the measured flux deviates by about 1.5σ from that of the world average from (Hebbeker & Timmermans 2002) and at higher energies the measured spectrum is significantly steeper. Since the world average at higher energies is dominated by a single measurement (Rastin 1984), this disagreement is caused by the disagreement between this measurement and the measurement by the Nottingham group. The prediction by the CORT code on the other hand follows the measured distribution very well above 100 GeV. Below 100 GeV the shape of the measured distribution disagrees with both the world average and the prediction by the CORT code. This trend is also present when the measurement is extended to larger zenith angles. This fact is troublesome, the world average from (Hebbeker & Timmermans 2002) contains many good measurements at low energies. A possible explanation could be that the L3+Cosmics surface momentum is too high. To explain this discrepancy a difference of 1 GeV is needed. This is twice the 500 MeV uncertainty estimated for the momentum scale. The momentum measurement in the detector was verified with the $Z/\gamma \rightarrow \mu^+\mu^-$ events (see section 5.6) to a precision of 0.1 GeV. This leaves the total overburden, which thus would have to be overestimated by 2 m (equivalently its density would have to be overestimated by 7%).

Figure 6.24 shows the measured charge ratio in the $10°$ zenith angle bin, along with the world average from (Hebbeker & Timmermans 2002) and the prediction from the CORT code (Fiorentini *et al.* 2001). The measured charge ratio is in good agreement with the world average, whereas the prediction from CORT is significantly higher. The increase in the charge ratio as a function of momentum predicted by CORT, can not be excluded.

6.4   Zenith angle dependence

The measurement of both the flux and charge ratio is extended to larger zenith angles. The distribution of the number of selected events for both data and Monte Carlo is shown in figure 6.25a for the 100 GeV bin along with the normalized ratio of the two. The distribution shows several peaks of which only the one at $\cos\theta = 0.92$ has a simple explanation. It is caused by the overlap in acceptance between the vertical octant and the side octants. The ϕ_{local} cut of $25°$ compared to the $22.5°$ zenith angle of the edge of the vertical octant allows for this small overlap. The slow drop of events below $\cos\theta = 0.6$ can be understood when looking at the geometry of the scintillator plane on top of the magnet. The drop is not sharp

---

*One-dimensional in the sense that all secondaries are assumed to follow the direction of the primary particle.
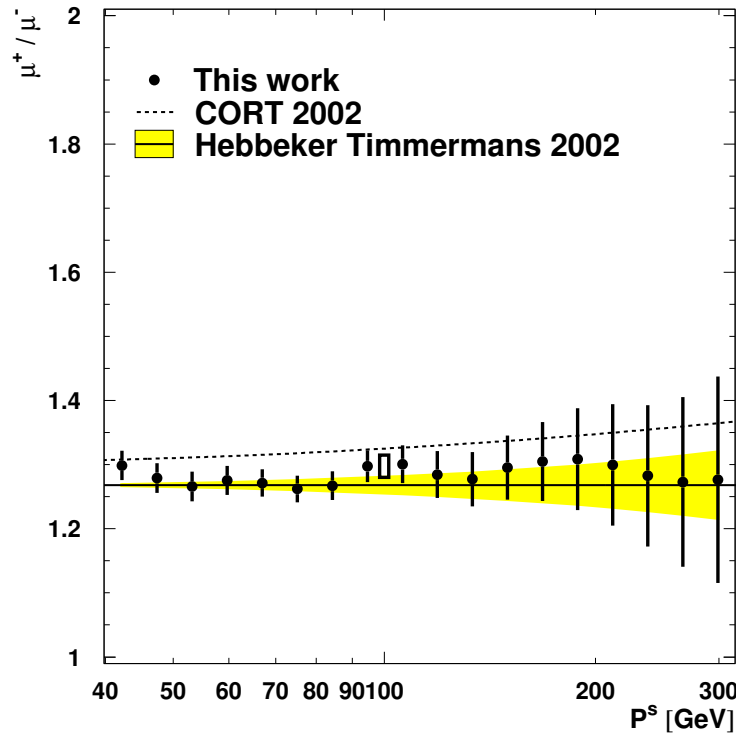
Figure 6.24: *The charge ratio for the 10° zenith bin. The error bars indicate the uncertainty on the shape of the charge ratio, while the box at 100 GeV indicate the uncertainty on the average. The charge ratio obtained by (Hebbeker & Timmermans 2002) is shown for comparison along with the prediction by the CORT code (Fiorentini et al. 2001).*

since the cosmic muons do not have to pass through the center of the detector. The analysis is only performed for the bins above $\cos\theta = 0.59$. At the top of the upper plot the large ticks indicate the boundaries between the 20 bins in $\cos\theta$, see table A.1 on page 132 for the exact boundaries.

In general the Monte Carlo describes the data distribution rather well, which leads one to believe that the shape of the distribution is due to complicated geometry of the set-up[*]. However, discrepancies from 10% to 20% can be seen when looking at the normalized ratio of the two. This seems like a reasonable agreement, but it is important to keep in mind that the disagreement is largely reduced by the very large difference in the tightness of the circle fit χ^2/dof cut applied for data and Monte Carlo (see figure 4.7).

The analysis is performed for each zenith bin individually, identically to the previously described analysis of the vertical flux and charge ratio (see section 6.1). Most of the efficiencies etc. vary only little between the 10° bin and the zenith bins, so they will not be shown. However, both the acceptance and the up-down correction have large variations. Figure 6.25b shows the zenith angle dependence of the acceptance and the up-down correction for both charges. The shape of the acceptance distribution follows the distribution of the

---

[*]This clearly shows the main disadvantage of using a detector to measure cosmic muons, which was designed to measure muons origination from its center.
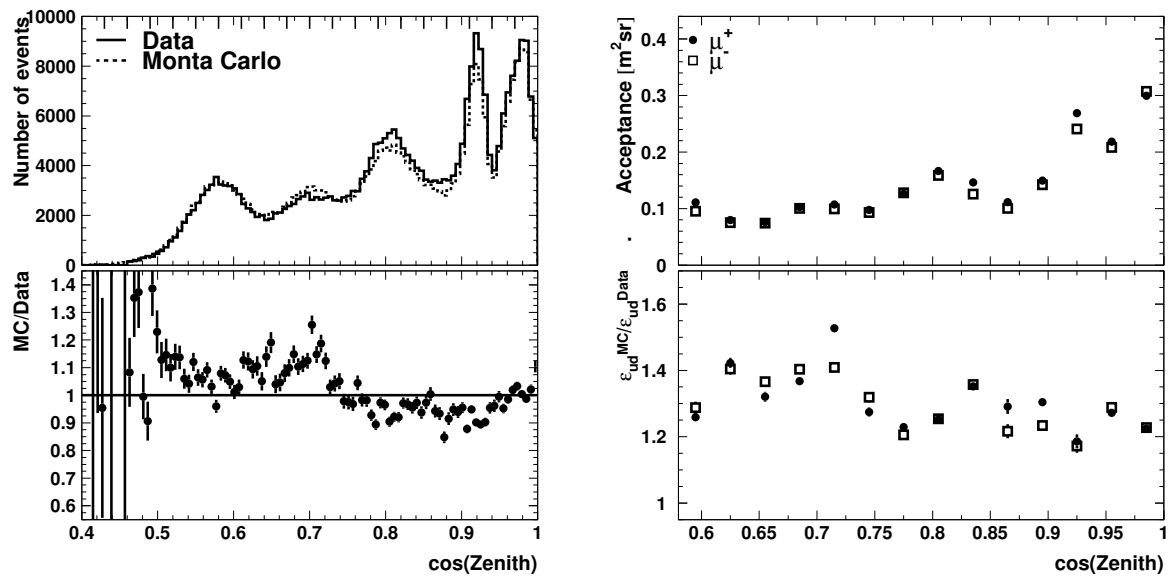
(a) Number of selected events for data and Monte Carlo along with the normalized ratio.

(b) Up-down correction and acceptance.

Figure 6.25: *The zenith angle dependence of the number of selected events at 100 GeV for data and Monte Carlo . The big ticks at the top of the upper plot of (**a**) show the bin boundaries of the zenith bins. The zenith dependence of the up-down correction and acceptance are also shown for the 100 GeV bin.*

Type	Zenith bin													
	7	**8**	**9**	**10**	**11**	**12**	**13**	**14**	**15**	**16**	**17**	**18**	**19**	**20**
Atmos. stability	2.5	2.5	2.5	2.5	2.5	2.5	2.5	2.5	2.5	2.5	2.5	2.5	2.5	2.5
Scintillator eff.	0.5	0.5	0.5	0.5	0.5	0.5	0.5	0.5	0.5	0.5	0.5	0.5	0.5	0.5
Scint. matching	0.0	0.1	0.0	0.0	0.3	0.4	0.1	0.4	0.1	0.1	0.2	0.2	0.2	0.3
Coincidence gate	0.3	0.4	0.3	0.4	0.9	1.2	2.0	1.1	1.6	1.4	1.7	1.4	0.9	0.3
Local ϕ	0.2	0.3	0.2	0.2	0.4	0.7	1.6	0.4	0.8	1.1	0.9	3.2	0.6	0.3
Track quality	0.6	0.4	0.2	0.5	0.5	0.8	1.1	0.7	1.1	0.8	1.3	0.5	1.1	0.8
Up-down method	2.8	1.8	3.3	10.1	11.6	7.1	7.5	8.7	6.9	1.1	1.9	2.2	9.4	3.8
Total	**3.9**	**3.2**	**4.2**	**10.5**	**12.0**	**7.7**	**8.4**	**9.2**	**7.7**	**3.5**	**3.9**	**5.0**	**9.9**	**4.7**

Table 6.3: *The relative systematic uncertainty on the normalisation of the spectrum as a function of the zenith angle, quoted in %.*

number of selected Monte Carlo events, as expected. The shape of the up-down correction nicely follows the normalized ratio of the number of selected Monte Carlo and data events. Here again the problem around $\cos\theta = 0.7$ is clearly visible (see figure 4.7).

The systematic error analysis is also performed in the same manner as for the vertical flux and charge ratio (see section 6.2). In table 6.3 the individual components of the uncertainty on the normalization of the flux is shown along with the total. Table 6.4 shows the zenith dependence of the uncertainty on the average charge ratio. The variation of the uncertainty due to the scintillator system varies only little for the different zenith bins, it is explicitly assumed to be identical for all bins. The uncertainty due to the ϕ_{local} is negligible except for

Type	Zenith bin													
	7	8	9	10	11	12	13	14	15	16	17	18	19	20
Scint. matching	0.0	0.1	0.0	0.0	0.4	0.2	0.0	0.6	0.0	0.1	0.1	0.3	0.7	0.2
Local ϕ	0.2	0.5	0.1	0.1	0.2	0.8	2.4	1.1	0.8	0.8	1.1	2.9	1.0	0.3
Track quality	0.2	0.3	0.3	0.2	0.4	0.6	0.5	0.2	0.4	0.7	0.7	0.7	0.7	0.6
Up-down method	0.6	0.8	0.6	2.1	1.9	0.3	0.4	0.3	1.3	0.1	0.2	0.1	1.3	0.1
Total	**0.7**	**1.0**	**0.8**	**2.2**	**2.0**	**1.1**	**2.6**	**1.3**	**1.6**	**1.1**	**1.4**	**3.1**	**1.9**	**0.7**

Table 6.4: *The systematic uncertainty on the average charge ratio as a function of the zenith angle, quoted in %.*

bin 18, which exactly corresponds to the bin with the overlap between the vertical and side octants, and thus a bin which primarily contains events with very large ϕ_{local} angles[*]. For this bin the ϕ_{local} cut constitutes the dominant uncertainty for both the flux and the charge ratio. For the uncertainty on the charge ratio the ϕ_{local} cut constitutes a significant but still low contribution for almost all zenith bins. The estimated uncertainty on the total overburden is as for the vertical spectrum $\frac{1\,\mathrm{m}}{\cos\theta}$. Thus about 500 MeV for the vertical bin and about 830 MeV for the lowest zenith bin, bin 7 (see table A.1).

The uncertainty due to the cut on the track quality varies only little with the zenith angle. It contributes modestly to the uncertainty on the flux, but contributes significantly to the uncertainty on the average charge ratio for almost all zenith bins. The uncertainty due to the up-down method dominates the uncertainty on the flux especially in the region around $\cos\theta = 0.7$. As was the case for the vertical flux, this indirectly means that the measurement is limited by the disagreement between data and Monte Carlo . The uncertainty due to the atmospheric conditions play a secondary role for almost all zenith bins, since the uncertainty on the up-down correction is so large. When comparing the zenith angle dependence of the flux it is important to keep in mind that this error is completely correlated for all bins.

The plots on the following pages show the result of the analysis of the flux and charge ratio for the 14 zenith bins. Figures 6.27 and 6.28 show the measured spectrum multiplied by p^3 along with the prediction of the CORT code. The minimal momentum for which the flux and charge ratio are presented is defined as the most likely energy loss in the molasse (see figure 6.2) with an addition of 25 GeV. This is to make sure that edge effects do not play an important role. Figures 6.29 and 6.30 show the momentum dependence of the measured charge ratio along with the prediction of the CORT code. The zenith angle dependence of the flux and charge ratio for four momentum bins can be seen in figure 6.31 and figure 6.32, respectively. The normalization uncertainty is, apart from the atmospheric conditions, uncorrelated between the different zenith bins. It must thus be included when comparing the measured and predicted zenith angle dependences.

In general a reasonable agreement between the measurement and the CORT prediction is observed. For the low energy bins the uncertainty on the flux can be seen to be significantly larger for zenith bin 12 to 17, which is due to the main shaft. Figure 6.26 shows the azimuth dependence of the flux for zenith bin 15, as an example of this problem.

---

[*]Since cell-map as well as the inverse cell map have a problem for segments with a large ϕ_{local} angle it was to be expected that the flux measurement would be less accurate for the bin.
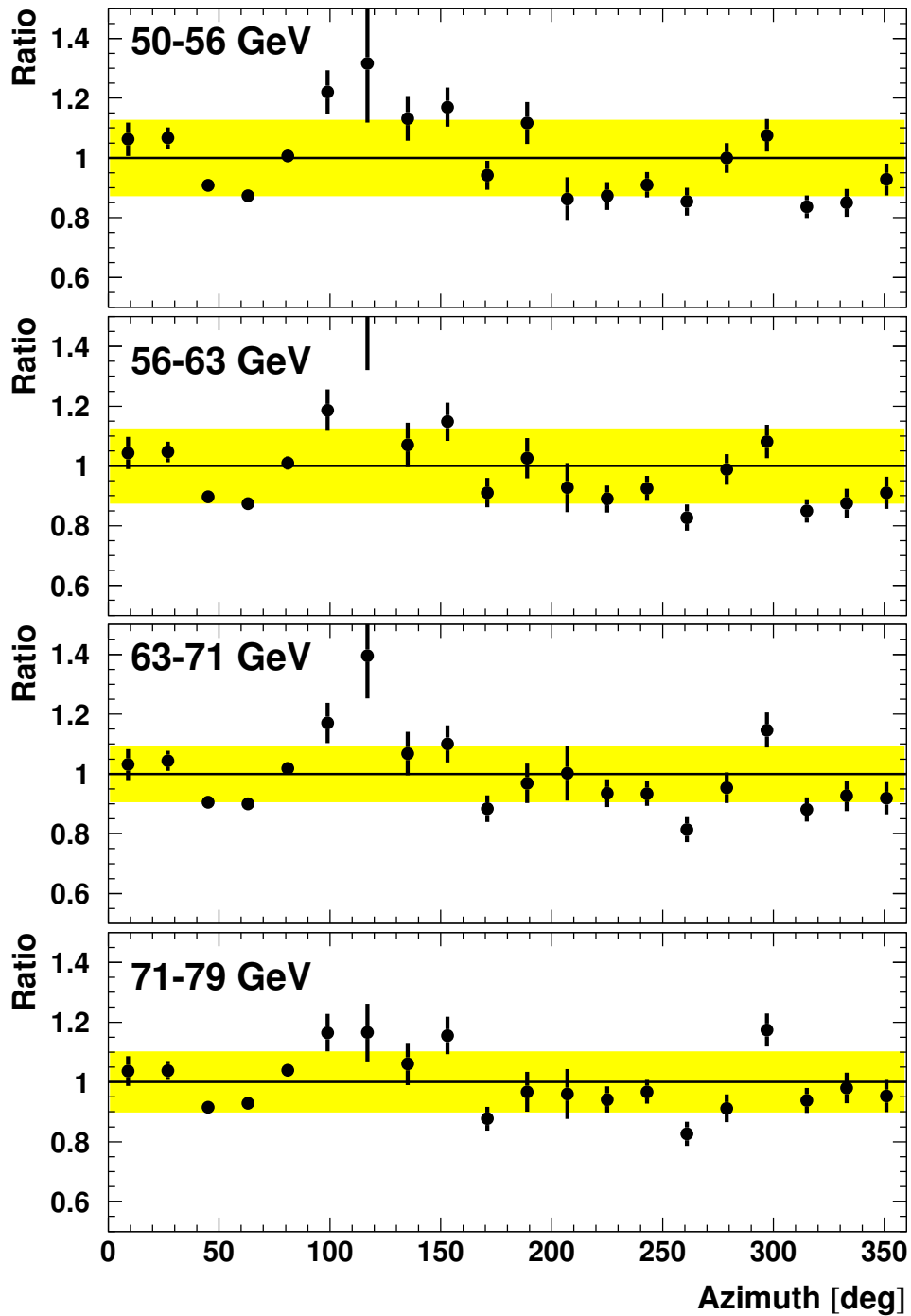
Figure 6.26: *The azimuth dependent flux of zenith bin 15 is shown for four momentum bins. The flux is plotted relative to the weighed average of the 20 azimuth bins. The grey band indicates the estimated systematic uncertainty due to the variation of the overburden.*
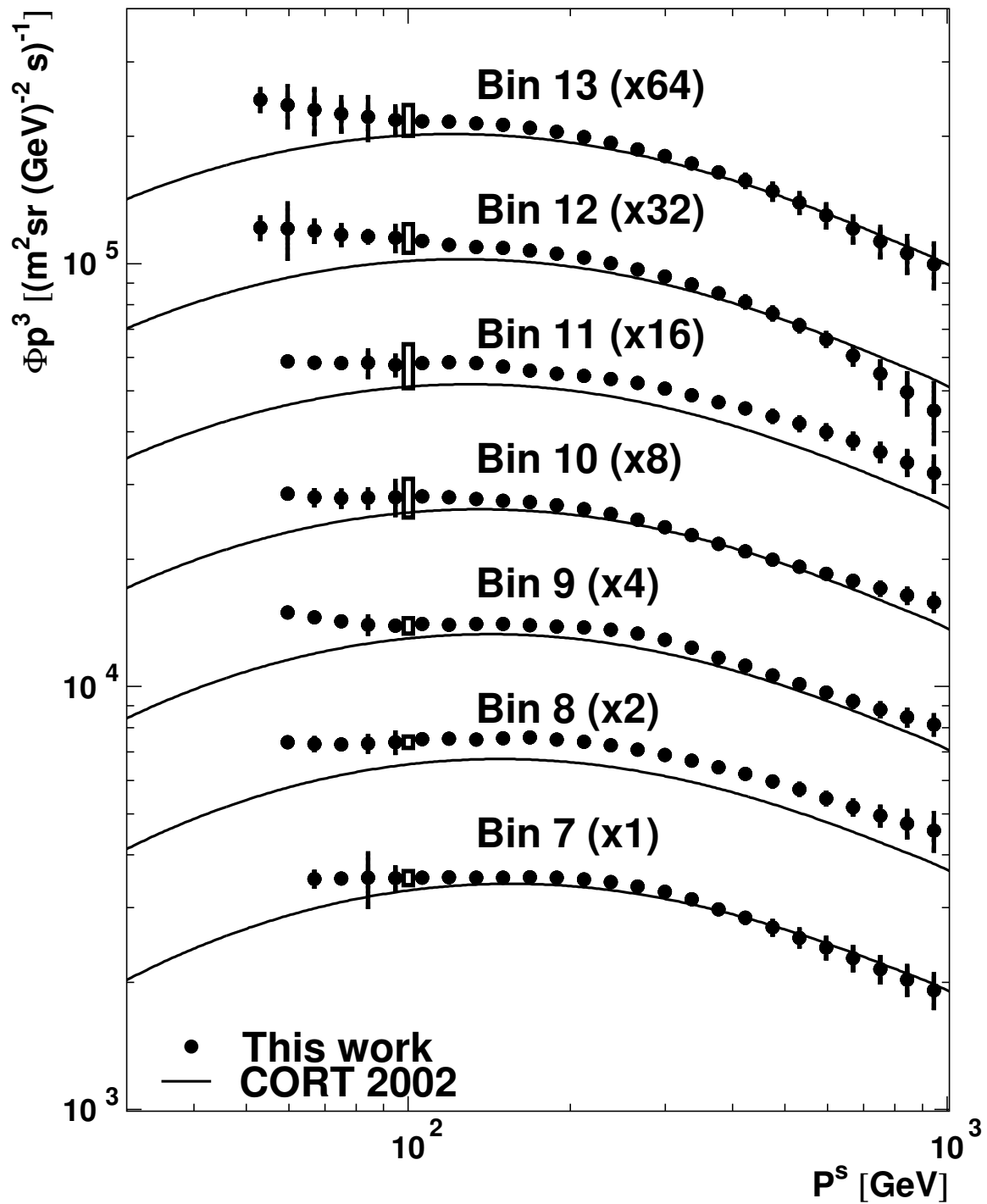
Figure 6.27: *The momentum spectrum for the lowest 7 zenith bins (see table A.1). The normalization uncertainty is indicated by a rectangle at 100 GeV. The result of the dedicated calculation by the CORT code (Fiorentini et al. 2001) is also shown.*
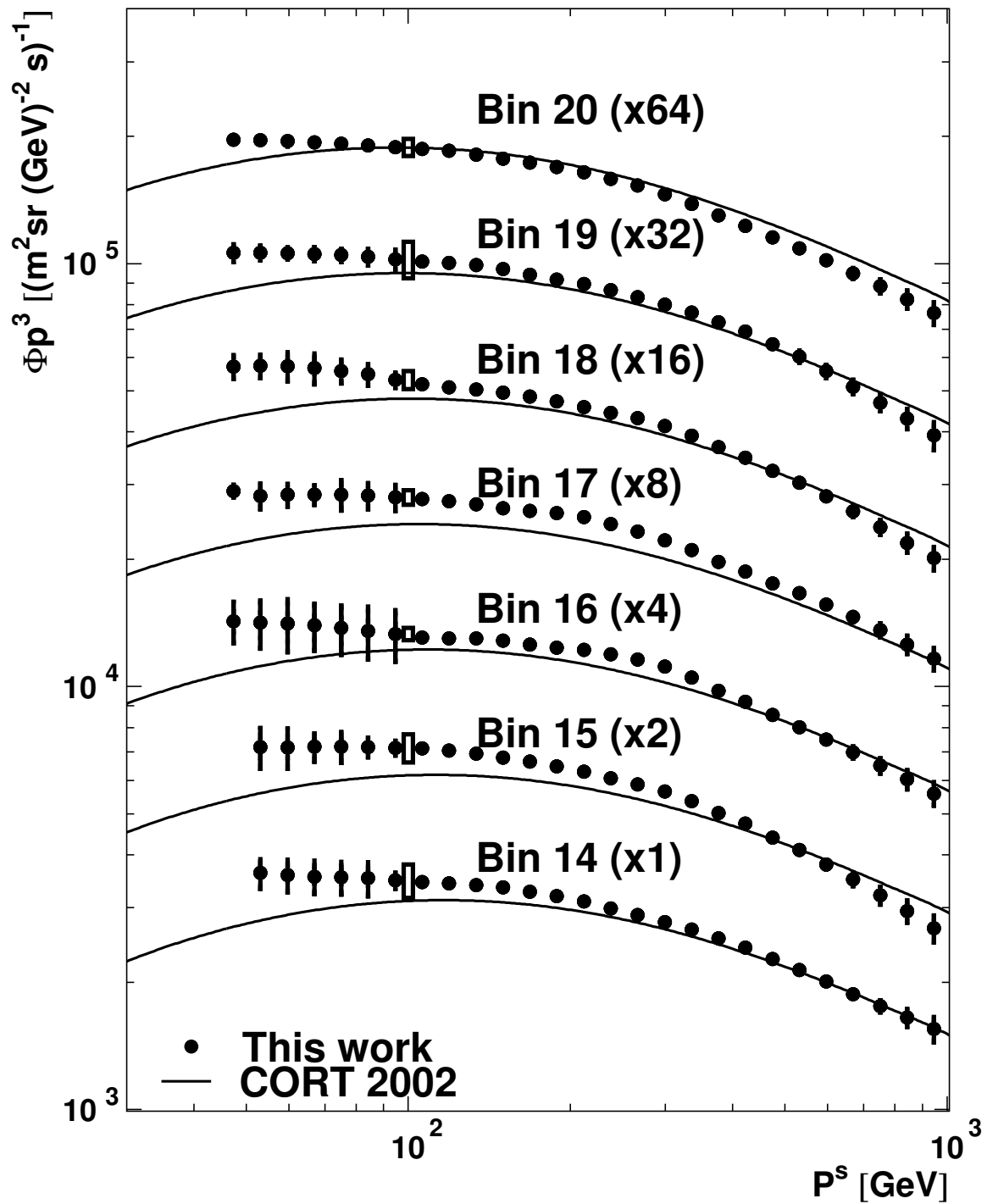
Figure 6.28: *The momentum spectrum for the highest 7 zenith bins (see table A.1). The normalization uncertainty is indicated by a rectangle at 100 GeV. The result of the dedicated calculation by the CORT code (Fiorentini et al. 2001) is also shown.*
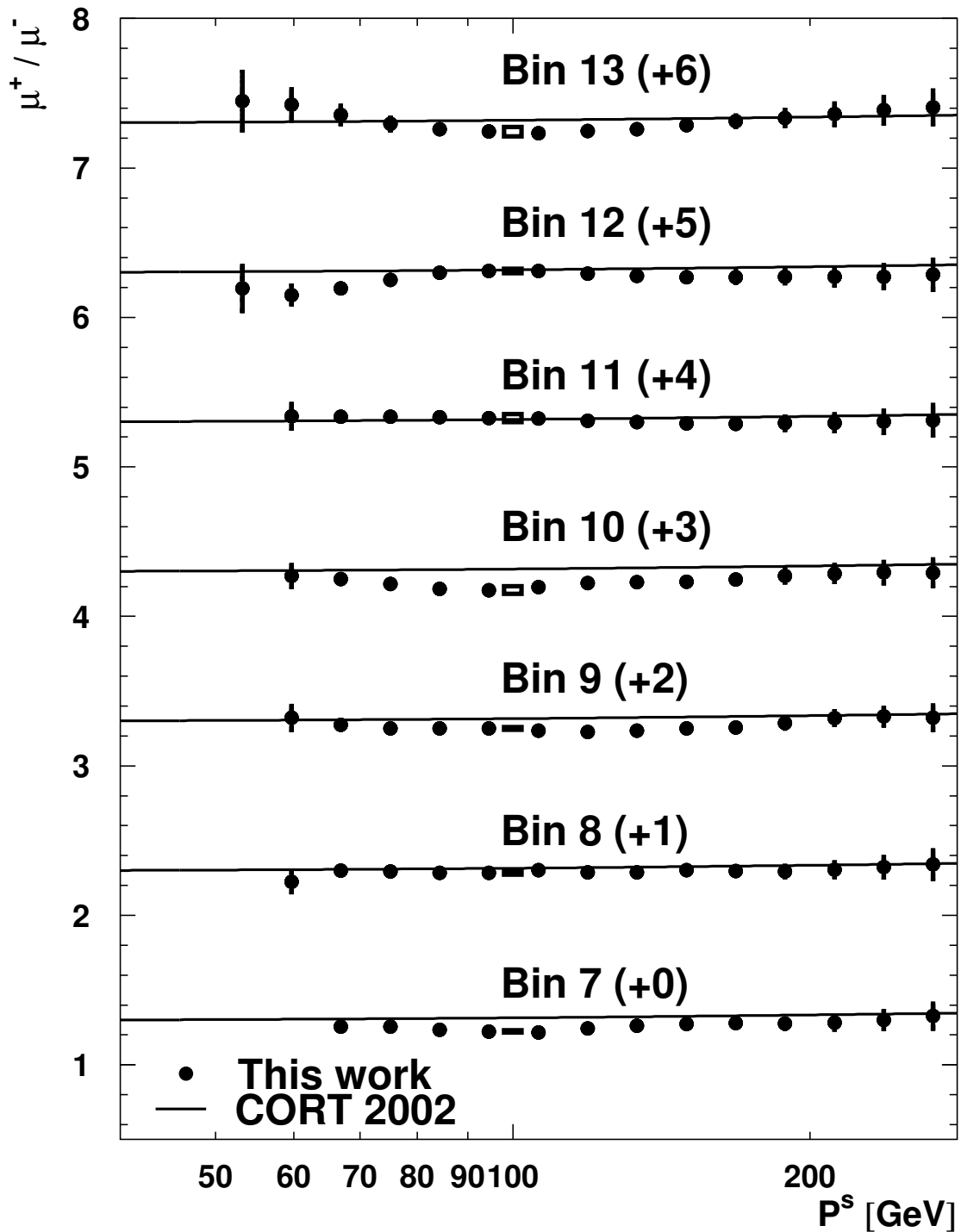
Figure 6.29: *The muon charge ratio for the lowest 7 zenith bins (see table A.1). The uncertainty on the average charge ratio is indicated by a rectangle at 100 GeV. The result of the dedicated calculation by the CORT code (Fiorentini et al. 2001) is also shown.*
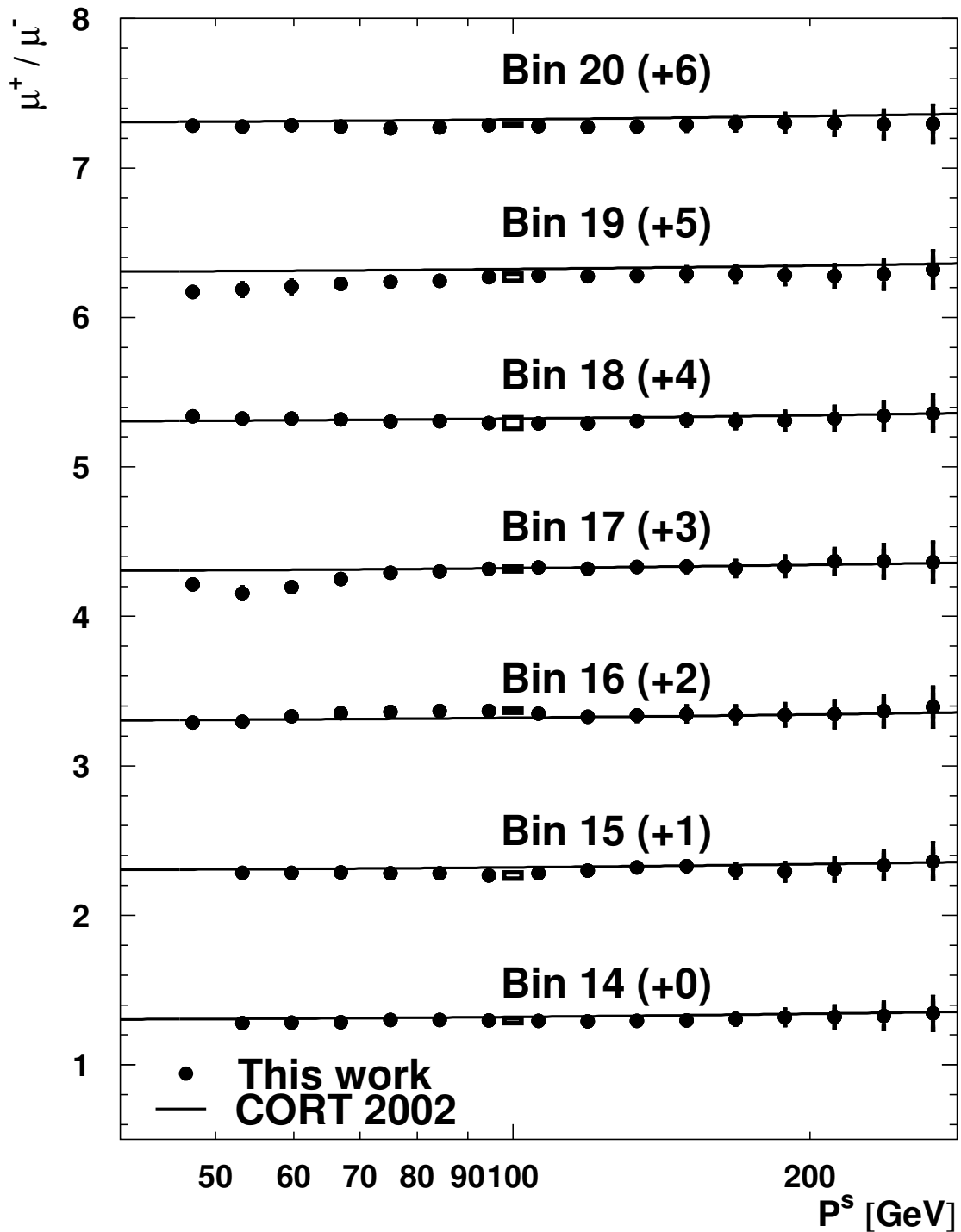
Figure 6.30: *The muon charge ratio for the highest 7 zenith bins (see table A.1). The uncertainty on the average charge ratio is indicated by a rectangle at 100 GeV. The result of the dedicated calculation by the CORT code (Fiorentini* et al. *2001)is also shown.*
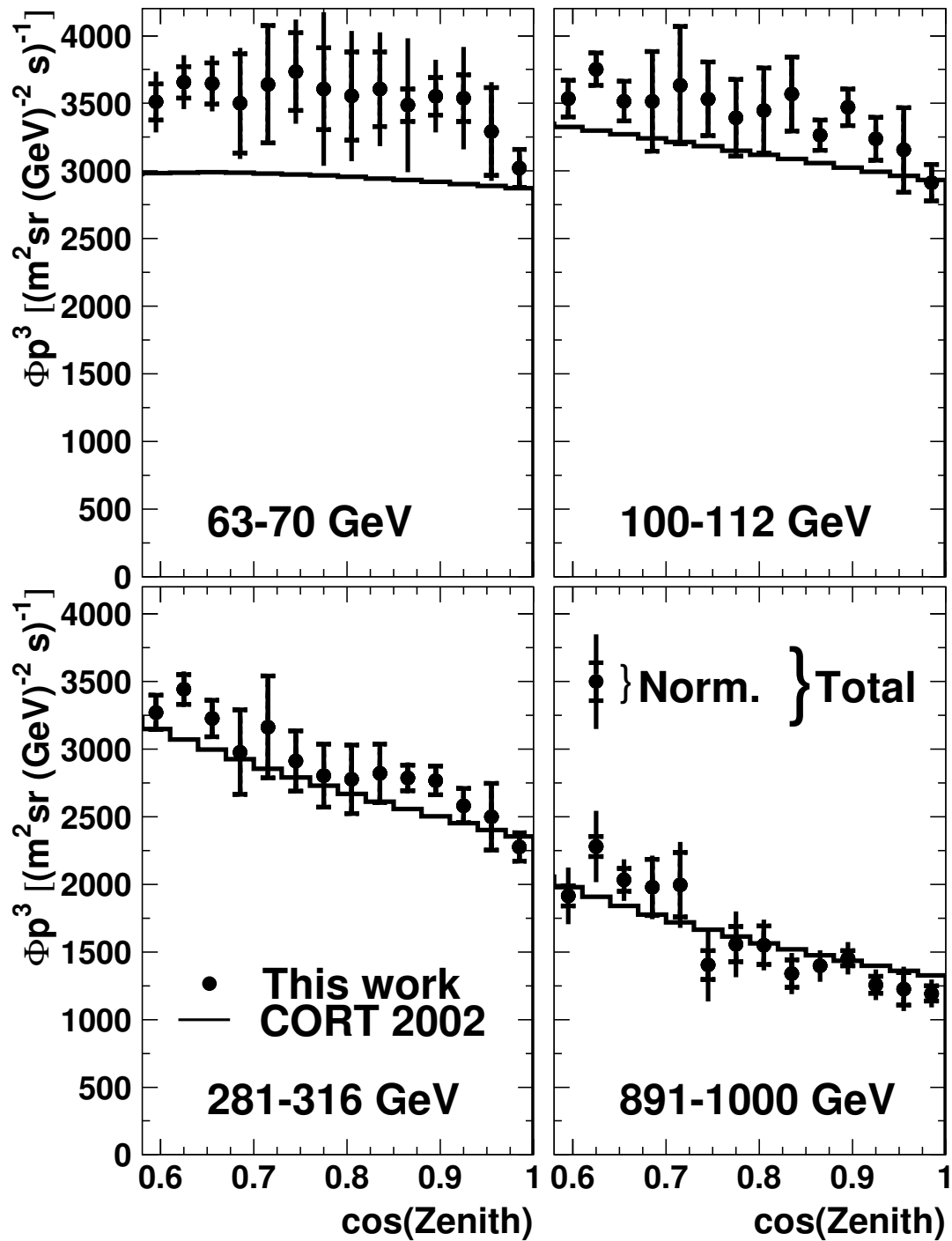
Figure 6.31: *The zenith dependence of the muon flux for four momentum bins. The uncertainty on the normalization as well as the total uncertainty is indicated. The normalization error is indicated here for each point since the points are uncorrelated, however, it is important to notice that the uncertainty on the normalization is the same across the four plots. The result of the dedicated calculation by the CORT code (Fiorentini et al. 2001) is also shown.*
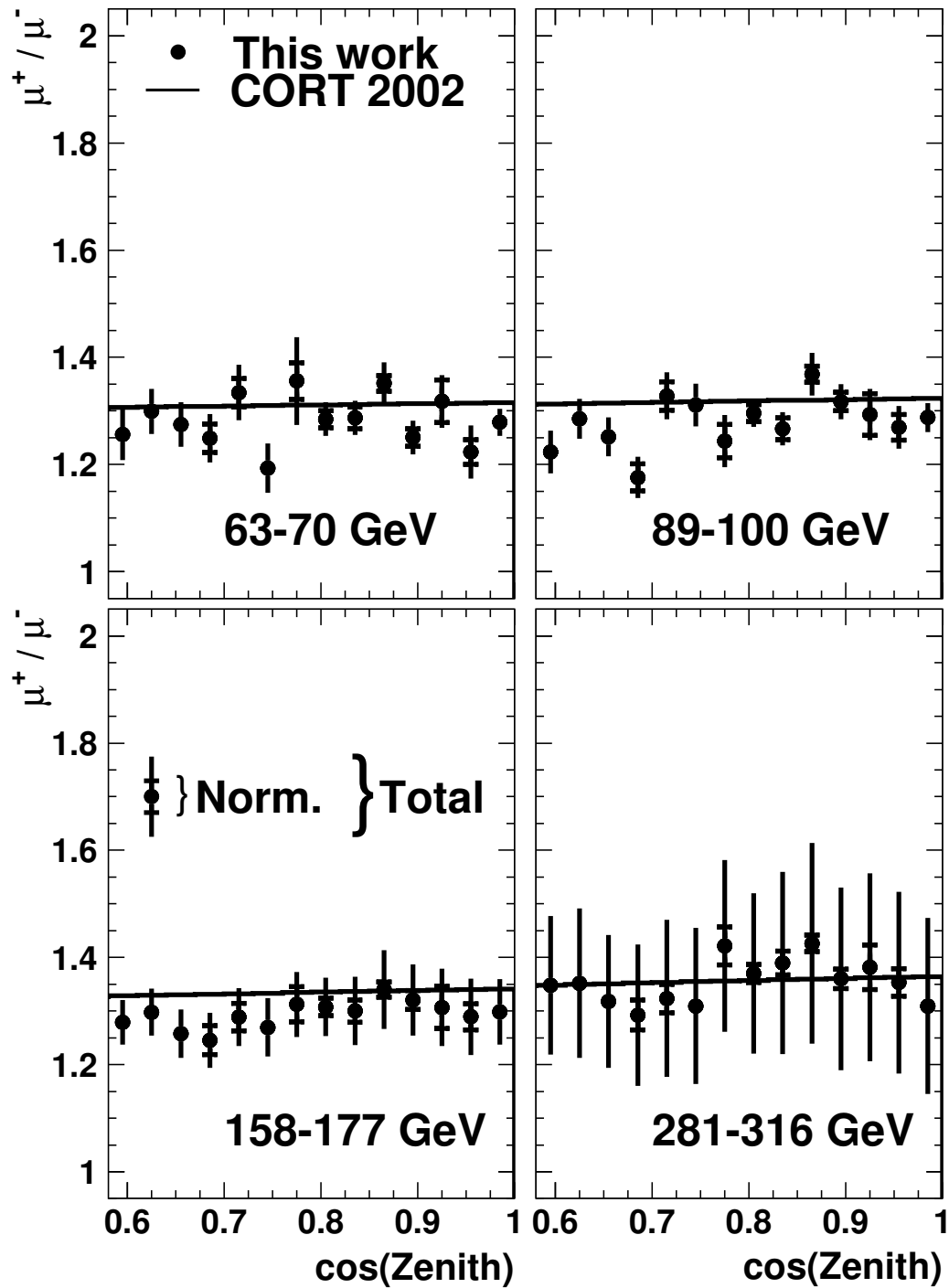
Figure 6.32: *The zenith dependence of the muon charge ratio for four momentum bins. The uncertainty on the normalization as well as the total uncertainty is indicated. The normalization error is indicated here for each point since the points are uncorrelated, however, it is important to notice that the uncertainty on the normalization is the same across the four plots. The result of the dedicated calculation by the CORT code (Fiorentini et al. 2001) is also shown.*

Conclusions

The thesis presents a new measurement of the muon flux at sea level, as a function of momentum and zenith angle, in the range $40 < p < 1000$ GeV and $0.6 < \cos\theta < 1.0$. It improves on previous studies both by increased statistics and as far as studies of potential sources of systematic uncertainties are concerned. The result improves on the current world average by about a factor of two in absolute normalization accuracy; knowledge of the spectrum shape is improved a great deal between 100 GeV and 1000 GeV. In this range, the spectrum and angular distribution agree rather well with recent predictions based on high accuracy primary spectra and elaborate models of the atmospheric cascade they cause. This agreement concerns both the normalization and the shape of the distributions. With the improvement in accuracy, a systematic disagreement with previous measurements, especially at high energies, is observed.

At low energies, uncertainties in the amount and density of the experiments overburden preclude a firm conclusion on the observed differences to both the world average and cascade calculations.

The good agreement with theory at high energies is reassuring since it shows that current models of cosmic ray interactions with the atmosphere, in an energy range not too far above the range of reliable accelerator data and in the unexplored kinematical region of the far-forward direction, can describe air showers with an accuracy of a few percent. Future measurements of high energy hadronic processes at the LHC as well as future measurements of the primary flux in the multi-TeV region will allow to further sharpen these conclusions.

Appendix A

Covariance matrices
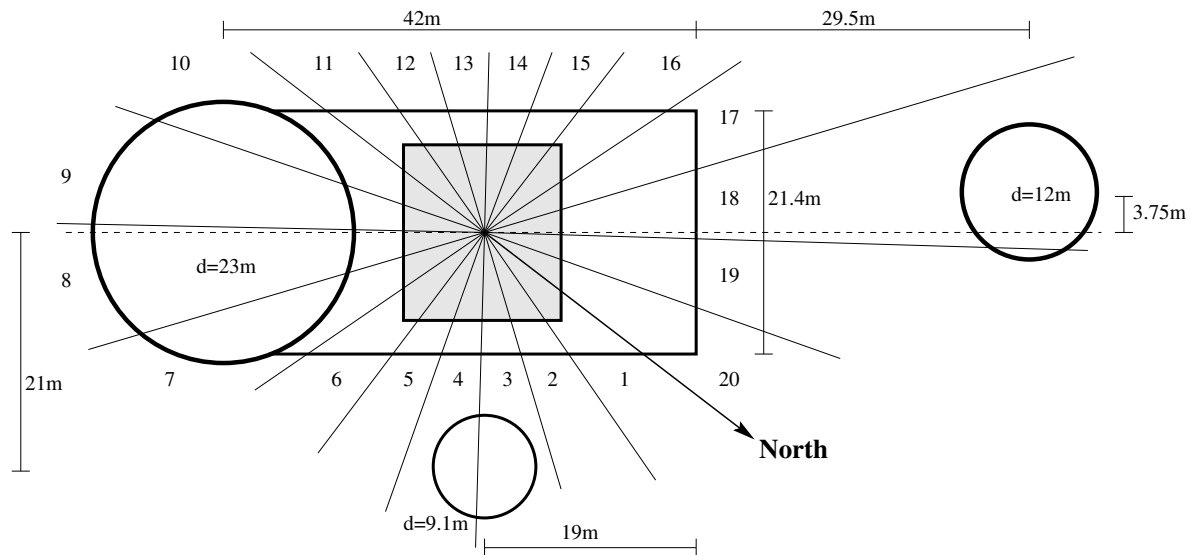
Figure A.1: *Schematic view of the detector (the shaded area in the middle) in the cavern surrounded by the three access shafts. The LEP tunnel runs along the dashed line. Both the LEP tunnel and the by-pass tunnel is omitted from this drawing, since they are of no relevance to the experiment. The direction of north is indicated along the lines showing the boundaries of the azimuth bins. The bin numbering is also indicated.*

Bin number	Momentum range [GeV]
30	31.6– 35.5
31	35.5– 39.8
32	39.8– 44.7
33	44.7– 50.1
34	50.1– 56.2
35	56.2– 63.1
36	63.1– 70.8
37	70.8– 79.4
38	79.4– 89.1
39	89.1– 100.0
40	100.0– 112.2
41	112.2– 125.9
42	125.9– 141.3
43	141.3– 158.5
44	158.5– 177.8
45	177.8– 199.5
46	199.5– 223.9
47	223.9– 251.2
48	251.2– 281.8
49	281.8– 316.2
50	316.2– 354.8
51	354.8– 398.1
52	398.1– 446.7
53	446.7– 501.2
54	501.2– 562.3
55	562.3– 631.0
56	631.0– 707.9
57	707.9– 794.3
58	794.3– 891.3
59	891.3–1000.0

Bin number	Zenith angle range [degree]
1	66.4–64.5
2	64.5–62.6
3	62.6–60.7
4	60.7–58.7
5	58.7–56.6
6	56.6–54.5
7	54.5–52.4
8	52.4–50.2
9	50.2–47.9
10	47.9–45.6
11	45.6–43.1
12	43.1–40.5
13	40.5–37.8
14	37.8–34.9
15	34.9–31.8
16	31.8–28.4
17	28.4–24.5
18	24.5–19.9
19	19.9–14.1
20	14.1– 0.0

(a) *Momentum bins*   **(b)** *Zenith angle bins*

Table A.1: *The range of the relevant momentum and zenith angle bins.*

	30	31	32	33	34	35	36	37	38	39	40	41	42	43	44
30	**8.94e-09**	4.53e-09	1.06e-09	2.85e-10	1.12e-10	5.56e-11	3.02e-11	1.87e-11	1.21e-11	8.24e-12	5.56e-12	3.97e-12	2.90e-12	2.09e-12	1.33e-12
31		**4.94e-09**	2.71e-09	6.43e-10	1.67e-10	6.45e-11	3.14e-11	1.78e-11	1.11e-11	7.22e-12	4.75e-12	3.29e-12	2.32e-12	1.67e-12	1.21e-12
32			**3.50e-09**	1.71e-09	4.14e-10	1.07e-10	4.04e-11	2.02e-11	1.18e-11	7.22e-12	4.72e-12	3.09e-12	2.18e-12	1.52e-12	1.14e-12
33				**2.31e-09**	1.04e-09	2.58e-10	6.61e-11	2.49e-11	1.28e-11	7.10e-12	4.57e-12	2.89e-12	2.00e-12	1.39e-12	9.89e-13
34					**1.46e-09**	6.27e-10	1.60e-10	4.07e-11	1.53e-11	7.62e-12	4.57e-12	2.71e-12	1.87e-12	1.25e-12	8.76e-13
35						**9.00e-10**	3.81e-10	9.81e-11	2.49e-11	9.16e-12	4.66e-12	2.69e-12	1.72e-12	1.13e-12	7.82e-13
36							**5.44e-10**	2.33e-10	6.15e-11	1.55e-11	5.63e-12	2.84e-12	1.67e-12	1.07e-12	7.15e-13
37								**3.27e-10**	1.46e-10	3.92e-11	9.97e-12	3.54e-12	1.76e-12	1.03e-12	6.71e-13
38									**1.93e-10**	8.94e-11	2.53e-11	6.58e-12	2.27e-12	1.09e-12	6.60e-13
39										**1.10e-10**	5.47e-11	1.69e-11	4.55e-12	1.52e-12	7.24e-13
40											**6.34e-11**	3.37e-11	1.14e-11	3.30e-12	1.11e-12
41												**3.63e-11**	2.05e-11	7.70e-12	2.47e-12
42													**2.08e-11**	1.23e-11	5.11e-12
43														**1.17e-11**	7.22e-12
44															**6.63e-12**

	45	46	47	48	49	50	51	52	53	54	55	56	57	58	59
30	5.25e-13	3.10e-14	6.91e-16	7.17e-17	8.64e-17	6.18e-17	1.51e-17	3.69e-18	1.58e-17	1.73e-17	4.62e-18	1.96e-17	6.65e-18	8.42e-19	7.22e-18
31	8.08e-13	2.74e-13	1.94e-14	1.65e-15	1.44e-15	1.04e-15	3.18e-16	1.18e-16	3.05e-16	3.14e-16	9.79e-17	3.54e-16	1.46e-16	4.80e-17	1.39e-16
32	7.79e-13	5.27e-13	1.49e-13	1.58e-14	3.18e-15	2.08e-15	1.75e-15	1.28e-15	1.20e-15	8.94e-16	4.85e-16	8.54e-16	7.12e-16	5.96e-16	4.71e-16
33	6.88e-13	5.14e-13	3.24e-13	9.35e-14	1.21e-14	3.05e-15	3.19e-15	2.94e-15	1.95e-15	1.57e-15	1.43e-15	1.06e-15	1.29e-15	1.43e-15	8.28e-16
34	6.10e-13	4.83e-13	3.32e-13	2.15e-13	5.72e-14	1.04e-14	3.26e-15	2.86e-15	1.83e-15	2.19e-15	2.09e-15	1.07e-15	1.17e-15	1.46e-15	9.16e-16
35	5.38e-13	4.11e-13	3.01e-13	2.14e-13	1.32e-13	3.82e-14	7.95e-15	2.59e-15	2.16e-15	2.17e-15	1.82e-15	1.15e-15	1.13e-15	1.14e-15	7.80e-16
36	4.86e-13	3.58e-13	2.60e-13	1.88e-13	1.31e-13	8.65e-14	2.50e-14	4.88e-15	2.03e-15	1.64e-15	1.40e-15	1.33e-15	8.94e-16	8.72e-16	7.73e-16
37	4.45e-13	3.15e-13	2.18e-13	1.65e-13	1.18e-13	8.88e-14	5.43e-14	1.47e-14	3.54e-15	1.50e-15	9.98e-16	1.07e-15	7.81e-16	7.50e-16	6.11e-16
38	4.09e-13	2.80e-13	1.94e-13	1.40e-13	1.03e-13	7.59e-14	5.43e-14	2.99e-14	9.17e-15	2.36e-15	1.19e-15	8.41e-16	7.34e-16	5.99e-16	4.69e-16
39	4.00e-13	2.56e-13	1.74e-13	1.19e-13	8.70e-14	6.34e-14	4.47e-14	3.08e-14	1.79e-14	6.10e-15	1.83e-15	7.71e-16	6.06e-16	4.91e-16	4.25e-16
40	4.84e-13	2.62e-13	1.64e-13	1.09e-13	7.60e-14	5.39e-14	3.77e-14	2.74e-14	1.95e-14	1.11e-14	4.19e-15	1.25e-15	9.69e-16	3.80e-16	3.16e-16
41	8.51e-13	3.54e-13	1.83e-13	1.09e-13	7.08e-14	4.85e-14	3.35e-14	2.42e-14	1.74e-14	1.26e-14	7.00e-15	2.80e-15	9.69e-16	4.08e-16	2.42e-16
42	1.83e-12	6.68e-13	2.80e-13	1.38e-13	7.78e-14	4.87e-14	3.19e-14	2.23e-14	1.56e-14	1.18e-14	7.75e-15	4.45e-15	1.94e-15	7.42e-16	3.14e-16
43	3.32e-12	1.33e-12	5.29e-13	2.29e-13	1.11e-13	6.09e-14	3.60e-14	2.30e-14	1.55e-14	1.11e-14	7.50e-15	5.11e-15	2.93e-15	1.42e-15	5.95e-16
44	4.24e-12	2.11e-12	9.39e-13	4.11e-13	1.88e-13	9.39e-14	5.05e-14	2.93e-14	1.84e-14	1.22e-14	7.97e-15	5.55e-15	3.66e-15	2.22e-15	1.13e-15
45	**3.74e-12**	2.45e-12	1.32e-12	6.44e-13	3.08e-13	1.51e-13	7.84e-14	4.31e-14	2.55e-14	1.58e-14	9.98e-15	6.74e-15	4.61e-15	3.10e-15	1.87e-15
46		**2.09e-12**	1.41e-12	8.13e-13	4.32e-13	2.24e-13	1.18e-13	6.43e-14	3.69e-14	2.22e-14	1.37e-14	9.02e-15	6.13e-15	4.25e-15	2.81e-15
47			**1.17e-12**	8.13e-13	4.96e-13	2.82e-13	1.57e-13	8.79e-14	5.08e-14	3.04e-14	1.87e-14	1.21e-14	8.16e-15	5.68e-15	3.91e-15
48				**6.66e-13**	4.67e-13	2.96e-13	1.77e-13	1.05e-13	6.23e-14	3.79e-14	2.35e-14	1.52e-14	1.02e-14	7.13e-15	4.98e-15
49					**3.73e-13**	2.64e-13	1.73e-13	1.09e-13	6.74e-14	4.21e-14	2.67e-14	1.75e-14	1.18e-14	8.27e-15	5.82e-15
50						**2.06e-13**	1.47e-13	9.89e-14	6.47e-14	4.20e-14	2.74e-14	1.82e-14	1.25e-14	8.81e-15	6.24e-15
51							**1.13e-13**	8.14e-14	5.62e-14	3.80e-14	2.56e-14	1.75e-14	1.22e-14	8.68e-15	6.21e-15
52								**6.22e-14**	4.52e-14	3.19e-14	2.22e-14	1.55e-14	1.10e-14	7.99e-15	5.78e-15
53									**3.43e-14**	2.52e-14	1.81e-14	1.30e-14	9.42e-15	6.94e-15	5.08e-15
54										**1.91e-14**	1.42e-14	1.04e-14	7.71e-15	5.77e-15	4.28e-15
55											**1.08e-14**	8.13e-15	6.12e-15	4.66e-15	3.50e-15
56												**6.24e-15**	4.78e-15	3.69e-15	2.81e-15
57													**3.72e-15**	2.91e-15	2.24e-15
58														**2.30e-15**	1.79e-15
59															**1.41e-15**

Momentum bin number

Table A.2: *The covariance matrix of the statistical uncertainty of the measured flux in the 10° zenith bins (see figure 6.23).*

Momentum bin number

	30	31	32	33	34	35	36	37	38	39	40	41	42	43	44
30	**3.49e-06**	8.79e-08	1.62e-08	4.52e-09	1.84e-09	9.26e-10	5.03e-10	3.11e-10	2.02e-10	1.37e-10	9.25e-11	6.62e-11	4.78e-11	3.45e-11	2.22e-11
31		**3.40e-07**	3.25e-08	6.52e-09	1.92e-09	8.23e-10	4.14e-10	2.39e-10	1.52e-10	9.90e-11	6.50e-11	4.59e-11	3.20e-11	2.33e-11	1.65e-11
32			**2.84e-07**	1.16e-08	2.49e-09	7.38e-10	3.14e-10	1.66e-10	9.93e-11	6.23e-11	4.08e-11	2.69e-11	1.90e-11	1.32e-11	9.86e-12
33				**5.00e-07**	5.05e-09	1.11e-09	3.11e-10	1.30e-10	7.02e-11	3.98e-11	2.59e-11	1.66e-11	1.14e-11	7.98e-12	5.64e-12
34					**3.38e-07**	2.68e-09	5.99e-10	1.62e-10	6.65e-11	3.45e-11	2.11e-11	1.27e-11	8.74e-12	5.87e-12	4.08e-12
35						**1.58e-07**	1.50e-09	3.40e-10	9.16e-11	3.68e-11	1.94e-11	1.14e-11	7.34e-12	4.85e-12	3.34e-12
36							**7.64e-08**	8.30e-10	1.96e-10	5.24e-11	2.07e-11	1.09e-11	6.52e-12	4.20e-12	2.81e-12
37								**2.52e-08**	4.69e-10	1.15e-10	3.08e-11	1.19e-11	6.11e-12	3.65e-12	2.38e-12
38									**1.58e-09**	2.68e-10	6.98e-11	1.88e-11	6.96e-12	3.45e-12	2.14e-12
39										**8.78e-10**	1.58e-10	4.46e-11	1.23e-11	4.32e-12	2.16e-12
40											**4.72e-10**	9.36e-11	2.89e-11	8.51e-12	3.01e-12
41												**2.37e-10**	5.44e-11	1.89e-11	6.10e-12
42													**1.08e-10**	3.19e-11	1.24e-11
43														**5.62e-11**	1.86e-11
44															**3.11e-11**

	45	46	47	48	49	50	51	52	53	54	55	56	57	58	59
30	8.83e-12	1.06e-13	3.97e-14	3.22e-14	3.08e-14	4.01e-14	4.12e-14	3.87e-14	4.03e-14	3.51e-14	3.18e-14	3.75e-14	3.61e-14	3.51e-14	3.02e-14
31	1.13e-11	2.47e-12	8.04e-14	2.95e-14	3.14e-14	4.25e-14	3.65e-14	3.85e-14	3.87e-14	3.42e-14	2.87e-14	3.04e-14	2.92e-14	2.90e-14	2.52e-14
32	6.68e-12	4.18e-12	7.52e-13	6.25e-14	3.22e-14	3.79e-14	3.68e-14	3.43e-14	3.59e-14	3.52e-14	3.07e-14	2.92e-14	2.73e-14	2.72e-14	2.21e-14
33	3.88e-12	2.74e-12	1.64e-12	3.94e-13	5.28e-14	3.68e-14	3.98e-14	3.51e-14	3.54e-14	3.19e-14	3.15e-14	3.02e-14	2.98e-14	2.84e-14	2.03e-14
34	2.81e-12	2.18e-12	1.46e-12	9.56e-13	2.24e-13	5.21e-14	3.19e-14	3.12e-14	3.24e-14	3.27e-14	3.05e-14	2.65e-14	2.60e-14	2.59e-14	1.79e-14
35	2.27e-12	1.71e-12	1.25e-12	8.88e-13	5.72e-13	1.45e-13	3.96e-14	2.78e-14	2.81e-14	3.14e-14	2.46e-14	1.93e-14	2.01e-14	2.13e-14	1.90e-14
36	1.90e-12	1.39e-12	1.01e-12	7.25e-13	5.15e-13	3.56e-13	9.23e-14	2.39e-14	2.10e-14	1.89e-14	1.65e-14	1.73e-14	1.61e-14		
37	1.59e-12	1.12e-12	7.70e-13	5.91e-13	4.29e-13	3.27e-13	2.12e-13	5.47e-14	2.57e-14	1.99e-14	1.72e-14	1.63e-14	1.40e-14	1.52e-14	1.44e-14
38	1.33e-12	9.12e-13	6.32e-13	4.63e-13	3.45e-13	2.56e-13	1.88e-13	1.12e-13	3.76e-14	1.87e-14	1.56e-14	1.41e-14	1.23e-14	1.25e-14	1.11e-14
39	1.21e-12	7.84e-13	5.37e-13	3.68e-13	2.75e-13	2.05e-13	1.46e-13	1.04e-13	6.66e-14	2.54e-14	1.46e-14	1.15e-14	1.08e-14	1.02e-14	9.16e-15
40	1.36e-12	7.53e-13	4.80e-13	3.25e-13	2.30e-13	1.66e-13	1.18e-13	8.82e-14	6.59e-14	4.13e-14		1.08e-14	9.07e-15	8.12e-15	7.10e-15
41	2.17e-12	9.31e-13	4.95e-13	3.03e-13	2.01e-13	1.42e-13	9.97e-14	7.35e-14	5.50e-14	4.20e-14	2.64e-14	1.25e-14	8.34e-15	6.58e-15	5.55e-15
42	4.45e-12	1.65e-12	7.04e-13	3.55e-13	2.07e-13	1.33e-13	8.89e-14	6.39e-14	4.65e-14	3.66e-14	2.58e-14	1.63e-14	9.11e-15	5.89e-15	4.59e-15
43	8.02e-12	3.19e-12	1.28e-12	5.64e-13	2.79e-13	1.56e-13	9.50e-14	6.28e-14	4.39e-14	3.26e-14	2.31e-14	1.66e-14	1.10e-14	6.39e-15	4.33e-15
44	1.07e-11	5.06e-12	2.24e-12	9.84e-13	4.54e-13	2.30e-13	1.26e-13	7.50e-14	4.86e-14	3.31e-14	2.27e-14	1.64e-14	1.17e-14	7.83e-15	4.84e-15
45	**1.90e-11**	6.12e-12	3.13e-12	1.52e-12	7.27e-13	3.59e-13	1.88e-13	1.05e-13	6.33e-14	4.03e-14	2.62e-14	1.83e-14	1.30e-14	9.20e-15	6.13e-15
46		**1.11e-11**	3.45e-12	1.90e-12	1.00e-12	5.21e-13	2.75e-13	1.52e-13	8.81e-14	5.39e-14	3.39e-14	2.27e-14	1.58e-14	1.12e-14	7.82e-15
47			**5.85e-12**	1.95e-12	1.14e-12	6.48e-13	3.60e-13	2.04e-13	1.18e-13	7.15e-14	4.45e-14	2.92e-14	2.00e-14	1.41e-14	9.95e-15
48				**2.98e-12**	1.10e-12	6.77e-13	4.06e-13	2.41e-13	1.44e-13	8.80e-14	5.51e-14	3.60e-14	2.44e-14	1.71e-14	1.22e-14
49					**1.55e-12**	6.17e-13	3.94e-13	2.49e-13	1.55e-13	9.76e-14	6.23e-14	4.10e-14	2.78e-14	1.95e-14	1.40e-14
50						**8.15e-13**	3.43e-13	2.27e-13	1.49e-13	9.74e-14	6.39e-14	4.28e-14	2.94e-14	2.07e-14	1.49e-14
51							**4.44e-13**	1.91e-13	1.30e-13	8.88e-14	6.02e-14	4.13e-14	2.88e-14	2.05e-14	1.49e-14
52								**2.57e-13**	1.07e-13	7.51e-14	5.27e-14	3.71e-14	2.64e-14	1.91e-14	1.40e-14
53									**1.58e-13**	6.06e-14	4.35e-14	3.14e-14	2.28e-14	1.68e-14	1.25e-14
54										**1.02e-13**	3.47e-14	2.55e-14	1.89e-14	1.41e-14	1.07e-14
55											**6.80e-14**	2.02e-14	1.52e-14	1.15e-14	8.81e-15
56												**4.58e-14**	1.20e-14	9.24e-15	7.14e-15
57													**3.12e-14**	7.36e-15	5.74e-15
58														**2.19e-14**	4.61e-15
59															**1.41e-14**

Table A.3: *The covariance matrix of the total uncertainty of the measured flux in the 10° zenith bins (see figure 6.23).*

Momentum bin number		30	31	32	33	34	35	36	37	38	39
	30	**3.40e-04**	1.61e-04	4.00e-05	1.52e-05	8.55e-06	6.13e-06	4.72e-06	4.09e-06	3.80e-06	3.82e-06
	31		**8.25e-04**	1.08e-04	2.95e-05	1.21e-05	7.42e-06	5.29e-06	4.29e-06	3.92e-06	3.75e-06
	32			**4.22e-04**	7.05e-05	2.10e-05	8.85e-06	5.34e-06	3.95e-06	3.39e-06	3.13e-06
	33				**4.59e-04**	5.82e-05	1.83e-05	7.24e-06	4.24e-06	3.28e-06	2.73e-06
	34					**4.81e-04**	6.14e-05	1.95e-05	7.41e-06	4.34e-06	3.31e-06
	35						**4.67e-04**	6.96e-05	2.22e-05	8.58e-06	5.05e-06
	36							**4.23e-04**	7.69e-05	2.61e-05	1.03e-05
	37								**3.96e-04**	8.76e-05	3.16e-05
	38									**4.10e-04**	1.06e-04
	39										**4.69e-04**
		40	41	42	43	44	45	46	47	48	49
	30	3.70e-06	3.73e-06	3.86e-06	4.07e-06	3.81e-06	2.19e-06	2.02e-08	-1.72e-08	-2.21e-08	-3.13e-08
	31	3.54e-06	3.53e-06	3.52e-06	3.76e-06	3.86e-06	3.83e-06	1.15e-06	1.18e-08	-2.05e-08	-3.48e-08
	32	2.94e-06	2.74e-06	2.77e-06	2.81e-06	3.05e-06	2.98e-06	2.66e-06	6.60e-07	1.93e-08	-3.32e-08
	33	2.55e-06	2.31e-06	2.28e-06	2.32e-06	2.38e-06	2.35e-06	2.38e-06	2.04e-06	6.40e-07	1.34e-08
	34	2.91e-06	2.46e-06	2.43e-06	2.37e-06	2.40e-06	2.39e-06	2.65e-06	2.52e-06	2.37e-06	7.07e-07
	35	3.82e-06	3.17e-06	2.92e-06	2.80e-06	2.80e-06	2.76e-06	2.98e-06	3.10e-06	3.16e-06	2.88e-06
	36	5.81e-06	4.30e-06	3.68e-06	3.46e-06	3.34e-06	3.27e-06	3.43e-06	3.55e-06	3.63e-06	3.69e-06
	37	1.22e-05	6.60e-06	4.85e-06	4.22e-06	3.98e-06	3.83e-06	3.86e-06	3.76e-06	4.13e-06	4.29e-06
	38	3.99e-05	1.52e-05	7.98e-06	5.75e-06	5.15e-06	4.62e-06	4.53e-06	4.46e-06	4.61e-06	4.95e-06
	39	1.33e-04	5.32e-05	2.10e-05	1.07e-05	7.73e-06	6.25e-06	5.77e-06	5.61e-06	5.42e-06	5.84e-06
	40	**5.11e-04**	1.60e-04	7.09e-05	3.05e-05	1.56e-05	1.01e-05	8.03e-06	7.25e-06	6.97e-06	7.09e-06
	41		**5.15e-04**	1.88e-04	9.57e-05	4.49e-05	2.30e-05	1.42e-05	1.07e-05	9.28e-06	8.86e-06
	42			**5.29e-04**	2.31e-04	1.31e-04	6.83e-05	3.63e-05	2.21e-05	1.59e-05	1.33e-05
	43				**5.84e-04**	2.87e-04	1.80e-04	1.04e-04	5.97e-05	3.77e-05	2.72e-05
	44					**6.53e-04**	3.50e-04	2.40e-04	1.53e-04	9.68e-05	6.58e-05
	45						**7.48e-04**	4.21e-04	3.11e-04	2.19e-04	1.54e-04
	46							**8.53e-04**	4.94e-04	3.96e-04	3.09e-04
	47								**9.58e-04**	5.83e-04	5.07e-04
	48									**1.08e-03**	7.07e-04
	49										**1.26e-03**

Table A.4: *The covariance matrix of the total uncertainty of the measured charge ratio in the 10° zenith bins (see figure 6.24).*

Bibliography

Abu-Zayyad T. *et al.* (2000). "The prototype high-resolution Fly's Eye cosmic ray detector". *Nucl. Instr. and Meth.* **A450**, 253–269. HiRes.

Adam A. *et al.* (1994). "Test beam results from the prototype L$_3$ silicon microvertex detector". *Nucl. Instr. and Meth.* **A344**, 521.

Afanasiev B.N. *et al.* (1996). In Nagano M., ed., "Proceedings Int. Symposium of Extremely High Energy Cosmic Rays", p. 32. Tokyo. Yakutsk.

AGASA Collaboration (1992). "Akeno giant air shower array (AGASA) covering 100 km^2 area". *Nucl. Instr. and Meth.* **A311**, 338–349.

Aitchison I.J.R. & Hey A.J.G. (1989). *Gauge Theories in Particle Physics*. Graduate Student Series in Physics. Adam Hilger, Bristol and Philadelphia, 2nd edition.

ALEPH Collaboration (1990). "ALEPH: A detector for electron-positron annihilation at LEP". *Nucl. Instr. and Meth.* **A294**, 121–178.

AMS Collaboration (1994). "Antimatter spectrometer in space". *Nucl. Instr. and Meth.* **A350**, 351–367.

AMS Collaboration (2000a). "Cosmic protons". *Phys. Lett.* **B490**, 27–35.

AMS Collaboration (2000b). "Helium in near earth orbit". *Phys. Lett.* **B494**, 193–202.

AMS Collaboration (2000c). "Protons in near earth orbit". *Phys. Lett.* **B472**, 215–226.

Bähr J., Grabosch H.J., Kantserov V., Leich H., Leiste R. & Nahnhauer R. (1997). "An effective method to read out large scintillator areas with precise timing". In "SCIFI97: Conference on Scintillating and Fiber Detectors", pp. 385–392.

Bähr J. *et al.* (1996). *Precision measurement of the cosmic ray muon momentum spectrum between 20 and 2000* GeV/c. CERN. L$_3$ internal note 1977.

Bergman D.R. (2002). "Monocular UHECR spectra as measured by HiRes". In "31st International Conference on High Energy Physics", Amsterdam.

BESS Collaboration (2000a). "Precise measurement of cosmic-ray proton and helium spectra with the BESS spectrometer". *Astrophys. J.* **545**, 1135–1142.

BESS Collaboration (2000b). "A superconducting solenoidal spectrometer for a balloon-borne experiment". *Nucl. Instr. and Meth.* **A443**, 71–100.

BOOMERanG Collaboration (2002). "The BOOMERanG experiment and the curvature of the universe". *Prog. Part. Nucl. Phys.* **48**, 243–261.

Bottai S. & Perrone L. (2001). "Simulation of UHE muons propagation for GEANT3". *Nucl. Instr. and Meth.* **A459**, 319–325.

Brouwer C. *et al.* (1992). "The magnetic measurement system of the L3 detector". *Nucl. Instr. and Meth.* **A313**, 50–62.

Brun R., Goossens M., Schaile O., Shiers J. & Zoll J. (1995). *ZEBRA*. CERN. Q100/Q101.

Brun R. *et al.* (1994). *GEANT, Detector description and simulation tool*. CERN, Geneva.

Bugaev E.V. *et al.* (1998). "Atmospheric muon flux at sea level, underground and underwater". *Phys. Rev.* **D58**, 054001.

Butt Y.M., Torres D.F., Combi J.A., Dame T. & Romero G.E. (2001). "Is the supernova remnant RX J1713.7-3946 a hadronic cosmic-ray accelerator?" *Astrophys. J.* **562**, L167–L171.

Catalano O. (2001). "Extreme Universe Space Observatory - EUSO: An innovative project for the detection of extreme energy cosmic rays and neutrinos". *Nuovo Cim.* **C24**, 445–469.

Cerrada M., Durán I., González E., Martínes L., Olmos P., Salicio J. & Willmott C. (1988). "Results of the calibration of multicell drift chamber prototypes for the L3-LEP muon spectrometer". *Nucl. Instr. and Meth.* **A263**, 343–350.

Chen H. *et al.* (1997). "Seach for new massive particles in cosmic rays." *Phys. Rep.* **282**, 1–34.

Christiansen J. (1997). *32 Channel general purpose Time to Digital Converter*. CERN/ECP-MIC.

Costa C.G.S. (2001). "The prompt lepton cookbook". *Astropart. Phys.* **16**, 193–204.

Cronin J.W. (1981). "CP symmetry violation: The search for its origin". *Rev. Mod. Phys.* **53**, 373–383.

D'Agostini G. (1995). "A multidimentional unfolding method based on Bayes' theorem". *Nucl. Instr. and Meth.* **A362**, 487–498.

DELPHI Collaboration (1991). "The DELPHI detector at LEP". *Nucl. Instr. and Meth.* **A303**, 233–276.

DONUT Collaboration (2001). "Observation of tau-neutrino interactions". *Phys. Lett.* **B504**, 218–224.

Duinker P. *et al.* (1982). "Space resolution of a drift chamber with multiwire sampling". *Nucl. Instr. and Meth.* **201**, 351–356.

Duinker P. *et al.* (1988). "Some methods and tools for testing and optimizing proportional wire chambers". *Nucl. Instr. and Meth.* **A273**, 814–819.

Erlykin A.D., Lipski M. & Wolfendale A.W. (1998). "High energy cosmic ray spectroscopy. iv. the evidence from direct observations at lower energies and directional anisotropies". *Astropart. Phys.* **8**, 283–292.

Fabre M. (1992). "The dimuon mass resolution of the L_3 experiment at LEP". Ph.D. thesis, ETH Zürich.

Fiorentini G., Naumov V.A. & Villante F.L. (2001). "Atmospheric neutrino flux supported by recent muon experiments". *Phys. Lett.* **B510**, 173–188.

Flye's Eye Collaboration (1985). "The Utah Fly's Eye detector". *Nucl. Instr. and Meth.* **A240**, 410–428.

Flye's Eye Collaboration (1994). "The cosmic ray energy spectrum observed by the Fly's Eye". *Astrophys. J.* **424**, 491–502.

Foreman T. (1993). "Bottom quark production at the Z resonance". Ph.D. thesis, University of Amsterdam.

Fukuda Y. *et al.* (1998). "Evidence for oscillation of atmospheric neutrinos". *Phys. Rev. Lett.* **81**, 1562–1567.

Gaisser T.K. (1990). *Cosmic Rays and Particle Physics*. Cambridge University Press.

Gaisser T.K. (2002). "Semi-analytical approximations for production of atmospheric muons and neutrinos". *Astropart. Phys.* **16**, 285–294.

Gaisser T.K. & Honda M. (2002). "Flux of atmospheric neutrinos". *Ann. Revs. Nucl. Part. Sci.* **52**. (to be published, hep-ph/0203272).

Gaisser T.K., Honda M., Lipari P. & Stanev T. (2001). "Primary spectrum to 1 TeV and beyond". In "Proceedings of the 27th International Cosmic Ray Conference", pp. 1643–1646. Hamburg.

Gaspar C. & Dönszelmann M. (1993). "DIM - a Distribution Information Management system for the DELPHI experiment at CERN". In "Proceedings of the IEEE Eight Conference REAL TIME '93 on Computer Applications in Nuclear, Particle and Plasma Physics", Vancouver, Canada.

Greisen K. (1956). "The extensive air showers". *Progress in Cosmic Ray Physics* **3**.

Greisen K. (1966). "End of the cosmic-ray spectrum?" *Phys. Rev. Lett.* **16**, 748–750.

Grigorov N.L. *et al.* (1971). "Energy spectrum of cosmic ray α-particles in 5×10^{10}-10^{12} eV/nucleon energy range". In Hobart, ed., "Proceedings 12th International Cosmic Ray Conference", volume 5, pp. 1760–1766. Proton Satellite.

Groenstege H.L. (1989). *The Muon Trigger Interface for L3:MPC, PAC, PCC-P, PCC-Z, PCS and PCT.*. NIKHEF. EA 89-01.

Groenstege H.L. & Boerkamp T. (1998). *L3 Cosmic: Inteference test*. NIKHEF. ETR 98-01.

Groenstege H.L., König A.C., Rewiersma P.A.M. & Wijnen T.A.M. (1996). *NIMROD, the ROD for the Moditored Drift Tubes in ATLAS*. NIKHEF. ETR 96-09.

Groenstege H.L., Rewiersma P.A.M., Wijnen T.A.M. & Zwart A.N.M. (1999a). *The NIM-ROD*. NIKHEF. ETR 99-06.

Groenstege H.L., Wijnen T.A.M., Rewiersma P.A.M. & Stolte J. (1999b). *Cosmic Personality Card for the L3 +Cosmics experiment*. NIKHEF. ETR 99-02.

Halzen F. *et al.* (1999). "From the first neutrino teloscope, the Anartic Muon and Neutrino Detector Array AMANDA, to the icecube observatory". In Kieda D., Salamon M. & Dingus B., eds., "Proceedings of the 26th International Cosmic Ray Conference", volume 2, pp. 428–431. Salt lake City.

Hebbeker T. & Timmermans C. (2002). "Compilation of the vertical muon flux". *Astropart. Phys.* **18**, 107–127.

Hebbeker T. (2000). *The Effectice Atmospheric Temperature*. Humboldt-University, Berlin. Internal note.

Hebbeker T. & Korn A. (1998). *Simulation Porgram for the L3+Cosmics Experiment*. Humboldt-University, Berlin. Internal note.

Heck D. & Knapp J. (2001). *Extensive air shower simulation with CORSIKA: A user's guide*. Karlsruhe.

Heck D., Knapp J., Capdevielle J., Schatz G. & Thouw T. (1998). "CORSIKA: A monte-carlo code to simulate extensive air showers". Technical report, Forschungszentrum Karlsruhe.

HEGRA Collaboration (1999). "The time structure of Čerenkov images generated by TeV γ-rays and by cosmic rays". *Astropart. Phys.* **11**, 363–377.

Hess V.F. (1912). "Über Beobachtungen der durchdringenden Strahlung bei sieben Freiballonfahrten". *Phys. Z.* **13**, 1084–1091.

IMB Collaboration (1986). "Calculation of atmospheric neutrino-induced backgrounds in a nucleon-decay search". *Phys. Rev. Lett.* **57**, 1986–1989.

Innocente V., Maire M. & Nagy E. (1991). *GEANE: Average Tracking and Error Porpagation Package*. CERN. W5013-E.

Ivanenko I.P. *et al.* (1993). "Energy spectra of cosmic rays above 2 TeV as measured by the SOKOL apparatus". In "Proceedings of the 23rd International Cosmic Ray Conference", volume 2, pp. 17–20. Calgary. SOKOL satellite.

JACEE Collaboration (1998). "Cosmic-ray proton and helium spectra: Results from the JACEE experiment". *Astrophys. J.* **502**, 278–283.

Jung C.K., McGrew C., Kajita T. & Mann T. (2001). "Oscillations of atmospheric neutrinos". *Ann. Revs. Nucl. Part. Sci.* **51**, 451–488.

Kajita T. & Totsuka Y. (2001). "Observation of atmospheric neutrinos". *Rev. Mod. Phys.* **73**, 85–119.

Karimäki V. (1991). "Effective circle fitting for particle trajectories". *Nucl. Instr. and Meth.* **A305**, 187–191.

Knoll G.F. (1989). *Radiation Detection and Measurement*. John Wiley & Son, 2nd edition.

Koffeman E.N. (1996). "A luminosity measurement at LEP using the L3 detector". Ph.D. thesis, University of Nijmegen.

Korn A. (1998). "Cosmic muons in the L3 detector". Master's thesis, Humboldt-Universität zu Berlin.

L3 Collaboration (1990). "The construction of the L3 experiment". *Nucl. Instr. and Meth.* **A289**, 35–102.

L3 Collaboration (1993). "Results from the L3 experiment at LEP". *Phys. Rep.* **236**, 1–146.

L3 Collaboration (1994). "The L3 silicon microvertex detector". *Nucl. Instr. and Meth.* **A351**, 300–312.

L3 F/B Muon Group (1996). "The forward muon detector of L3". *Nucl. Instr. and Meth.* **A383**, 342–366.

L3 Muon Group (1990). "Study of θ-inclined tracks in L3 muon chambers". *Nucl. Instr. and Meth.* **A290**, 115–121.

Ladron P.G. (2000). *The Good Bad Guys List*. CIEMAT, Madrid. Internal note.

Lavrijsen W.T.L.P. (2002). "Combined muon recosntruction for ATLAS". Ph.D. thesis, University of Nijmegen.

Lawrence M.A., Reid R.J.O. & Watson A.A. (1991). "The cosmic ray energy spectrum above 4×10^{17} eV as measured by the Haverah Park array". *J. Phys.* **G17**, 733–757.

Leich H. (1998a). *The GPSTIM: User's Guide*. DESY-Zeuthen.

Leich H. (1998b). *The L3CD: User's Guide*. DESY-Zeuthen.

Leijtens X.J.M. (1993). "Production of tau pairs at the Z resonance". Ph.D. thesis, University of Amsterdam.

Li Z. (2001). "Solar flare search with L3+Cosmics". Ph.D. thesis, IHEP, Beijing.

Longair M.S. (1992). *High Energy Astrophysics*, volume 1 and 2. Cambridge University Press, 2nd edition.

Ma X. (2002). *T0 calibration*. IHEP, Beijing. Internal note.

MACRO Collaboration (1993). "First supermodule of the MACRO detector at Gran Sasso". *Nucl. Instr. and Meth.* **A324**, 337–362.

Metzger W. (1992). "Statistical methods in data analysis". University of Nijmegen.

van Mil A. (2001). "Cosmic-ray muons in the L3 detector". Ph.D. thesis, University of Nijmegen.

Nagano M. & Watson A.A. (2000). "Observations and implications of the untrahigh-energy cosmic rays". *Rev. Mod. Phys.* **72**, 689–732.

Naumov V.A. (2001). "Atmospheric muons and neutrinos". In "Proceedings of 2nd Workshop on Methodical Aspects of Underwater/Ice Neutrino Telescopes", Hamburg. (to be published, hep-ph/0201310).

Onvlee J. (1989). "The behaviour of the L3 muon chambers in a magnetic field". Ph.D. thesis, University of Amsterdam.

OPAL Collaboration (1991). "The OPAL detector at LEP". *Nucl. Instr. and Meth.* **A305**, 275–319.

Pantzer B. *et al.* (1998). *The Central Data Recording system*. CERN.

Parker K. (1998). *The Boundry-Scan Handbook, Analog and Digital*. Kluwer Academic Publishers, 2nd edition.

Peng Y. (1988). "The muon spectrometer of the L3 detector at LEP". Ph.D. thesis, University of Amsterdam.

Ptuskin V.S., Völk H.J., Zirakashvili V.N. & Breitschwerdt D. (1997). "Transport of relativistic nucleons in a galactic wind driven by cosmic rays". *Aston. Astrophys.* **321**, 434–443.

Ramelli R.G.E. (2002). "Search for cosmic ray point sources and anisotropy measurement with the L$_3$+Cosmics experiment". Ph.D. thesis, ETH Zürich.

Rastin B.C. (1984). "An accurate measurement of the sea-level muon spectrum within the range 4 to 3000 GeV". *J. Phys.* **G10**, 1609–1628. Nottingham.

Rewiersma P.A.M. (1986). *The L$_3$ Wire Amplifier*. NIKHEF. NH19-6112.

Rewiersma P.A.M. (1987). *The L$_3$ 48 Channel High Speed Discriminator Card*. NIKHEF. NH19-6523.

Rewiersma P.A.M. (1992). *A Practical Guide to the T0Cal Electronics*. NIKHEF. 819.11.11.

Rewiersma P.A.M. (1998). *NIMROD Auxiliary cards*. NIKHEF.

Reines F. & Cowan C.L. (1953). "Detection of the free neutrino". *Phys. Rev.* **92**, 830–831.

van Rhee T. (2000). "Charmonium formation in two-photon collisions". Ph.D. thesis, University of Utrecht.

RUNJOB Collaboration (2001). "Composition and energy spectra of cosmic-ray primaries in the energy range 10^{13}-10^{15} eV/particle observed by Japanese-Russian joint balloon experiment". *Astropart. Phys.* **16**, 13–46.

Ryan M.J., Ormes J.F. & Balasubrahmanyan V.K. (1972). "Cosmic-ray proton and helium spectra above 50 GeV". *Phys. Rev. Lett.* **28**, 985–988. [E] 1497.

Sauli F. (1977). *Principles of Operation of Multiwire Proportional and Drift Chambers*. CERN 77-09.

Sea E.S., Ormes J.F., Streitmatter R.E., Stochaj S.J., Jones W.V., Stephens S.A. & Bowen T. (1991). "Measurement of cosmic-ray proton and helium spectra during the 1987 solar minimum". *Astrophys. J.* **378**, 763–772. LEAP.

Streitmatter R.E. (1998). "Orbiting wide-angle light-collectors". In Krinmanic J.F., Ormes J.F. & Streitmatter R.E., eds., "Proceedings of the Workshop on Observing Giant Cosmic Ray Air Showers from $> 10^{20}$ eV Particles from Space", p. 95. AIP Conf. Proc. No. 433, AIP, Woodbury, N.Y.

Swordy S.P. *et al.* (2002). "The composition of cosmic rays at the knee". *Astropart. Phys.* (to be published, astro-ph/0202159).

Timmermans C. (1992). "Measurement of muon pair production around the Z-resonance using the L$_3$ detector at LEP". Ph.D. thesis, University of Nijmegen.

Timmermans C. (1998). *Rate estimates for phase 2 of the L$_3$+Cosmics experiment*. University of Nijmegen.

Timmermans C. (2002). *Using the raw data to get the L_3 +C trigger efficiency*. University of Nijmegen. HEN-444.

Unger M. (1998). "Detection of cosmic muons the scintillating tiles on top of the L_3 detector". Master's thesis, Humboldt-University, Berlin.

Unger M. (2002). "Measurement of the atmospheric muon spectrum with the L_3 detector". Ph.D. thesis, Humboldt-University, Berlin.

Verkooijen H. (1999). *CTT-V2*. NIKHEF. ETR 99-01.

Wijnen T.A.M., Petersen B.G. & Timmermans C. (1999). *The L_3 Cosmics Data Format*. University of Nijmegen. HEN-425.

Wilkens H. (2001). Private communication.

Wilkens H. (2003). "Experimental study of energetic muons from extensive air showers in the energy range from 100 TeV to 10 PeV". Ph.D. thesis, University of Nijmegen.

Yao Z. (1999). Private communication.

Zatsepin G.T. & Kuzmin V.A. (1966). "Upper limit of the spectrum of cosmic rays". *JETP Lett.* **4**, 78–80.

Zech G. (1995). *Comparing Statistical Data to Monte Carlo Simulation - Parameter Fitting and Unfolding*. DESY 95-113.

Zhang D.H. (1994). "Muon pair production in e^+e^- collisions at the Z resonance". Ph.D. thesis, University of Amsterdam.

Zillig M. (1998). "L_3+Cosmics: First data analysis - recosntruction of very inclined tracks". Master's thesis, ETH Zürich.

Summary

This thesis presents a measurement of the cosmic ray induced muon spectrum and charge ratio in the energy range from about 40 GeV to 1 TeV. The measurement is performed with the L3+Cosmics detector at CERN, Geneva, on a sample of events from the 1999 data taking. This measurement makes use of the about 200 m^2 of scintillators and dedicated DAQ added to the L3 detector during 1998 and the early spring of 1999.

The accurate measurement of the muon flux and charge ratio is interesting on its own in light of the large discrepancies between previous measurements. Furthermore, the close connection between the muon and muon neutrino fluxes makes this measurement an important input for the atmospheric cascade models similar to those used in the analysis which lead to the discovery of neutrino oscillations. Precise knowledge of the muon neutrino flux is also of big importance for the planned neutrino telescopes. For these experiments the atmospheric neutrinos constitute both an important calibration source and the dominant background. The cascade models also play an important role in the interpretation of the data in the so-called knee region of the cosmic ray spectrum, the origin of which is still being debated.

The precise measurement of muons with energies up to 1 TeV requires a large experimental live-time and acceptance. To achieve this goal the muon chambers of the L3 detector were equipped with additional readout electronics, and a scintillator detector is placed on the magnet. Chapter 2 contains a thorough description of the additional hardware and software, as well as the relevant features of the muon chamber system.

Preceding the actual measurement of the muon flux and charge ratio the performance of the experimental set-up is studied. The efficiency of the scintillators is found to be about 90% for the tight selection used in the analysis presented here, and about 97% when allowing a wider coincidence gate between the measured times from the two PMTs recording the signal from the same module. The efficiency of the muon chamber system was also studied. Excluding cells with problems, the efficiency in the bending and non-bending direction are found to be about 98% and 95%, respectively. The trigger efficiency is found to be better than 99.9%. In addition to the efficiencies of the detector elements, the flux normalization also depends on an accurate determination of the experimental live-time. The integrated live-time of the data is found to have been determined with an uncertainty less than 0.05%. For the shape of the momentum spectrum, the momentum resolution is of great importance. The resolution function is studied in detail, among others to allow for the deconvolution of the measured spectrum. The asymptotic resolution of the sagitta measurement of high energy muons is found to be about 160 μm while the width of the narrow Gaussian containing about 70% of the data is found to be about 120 μm. Furthermore, this study allowed for the measurement

of the time resolution of the scintillator system, which is found to be 2.0±0.1 ns, in good agreement with the design value of 1.8 ns. The resolution is confirmed by the measurement of LEP induced $Z/\gamma \rightarrow \mu^+\mu^-$ events. More importantly these events provide a check of the absolute momentum scale of the detector. The mean momentum is found to be correct with a precision of about 100 MeV.

The analysis of the muon momentum spectrum and charge ratio is performed in bins of the zenith angle. The vertical flux is measured within a half opening angle of 10°. Potential sources of systematic uncertainties are studied in detail. The normalization of the vertical flux is determined with an uncertainty of 3.7%, while the average vertical charge ratio is determined with an uncertainty of only 1.4%. The uncertainty on the shape of the flux is dominated by the uncertainty on the variation of the overburden below 100 GeV, resulting in a uncertainty of about 3%. Above 100 GeV, where the overburden is less important, the uncertainty on the shape drops to about 1%, slowly rising to about 8% at 1 TeV. This is mainly due to the uncertainty in the chamber alignment. The shape of the charge ratio is at low energies determined up to about 2%. This uncertainty rapidly rises to about 13% at 300 GeV due to uncertainties in the chamber alignment. The uncertainty on the absolute overburden results in a 500 MeV uncertainty on the momentum scale. The measured spectrum above 100 GeV is in good agreement with the prediction from CORT, but disagrees with the world average both in normalization and shape. Below 100 GeV the measured flux is larger than both the CORT prediction and the world average. This could be due to an overestimate of the overburden. The measured charge ratio is in good agreement with the world average, while the prediction from CORT is systematically higher. The obtained accuracy is not high enough to observe the small variation of the charge ratio with momentum predicted by CORT.

The zenith angle dependence of the flux and charge ratio is presented in 14 bins in $\cos\theta$ from vertical down to about 53°. The estimated uncertainty on the flux varies substantially, due to the very different sampling of the detector in different bins. It ranges from about 3% to about 12%. The estimated uncertainty on the average charge ratio only varies between 0.7% and 3%. CORT describes well the measured zenith angle dependence of both the flux and the charge ratio.

Samenvatting

Dit proefschrift beschrijft een meting aan de door kosmische straling ontstane muonen. Het energiespectrum tussen 40 GeV en 1 TeV en de verhouding tussen positief en negatief geladen muonen wordt besproken. De analyse is gedaan op data genomen door het L3+Cosmics experiment in Genève in 1999. Er is gebruik gemaakt van de 200 m^2 scintillator en onafhankelijk DAQ systeem die toegevoegd zijn aan de L3 detector gedurende 1998 en het begin van 1999.

Gezien de grote verschillen in de resultaten van voorgaande experimenten, is een nauwkeurige meting van de muon flux en ladingsverhouding op zichzelf interessant. Deze meting is, gezien de samenhang tussen de muon- en de muon neutrinoflux, een belangrijk gegeven voor de modellen die de deeltjeslawine door de atmosfeer beschrijven. Vergelijkbare modellen zijn gebruikt bij de analyse die geleid heeft tot de ontdekking van neutrino-oscillaties. Nauwkeurige kennis van de muon neutrino flux is ook van belang voor de geplande neutrino telescopen. Voor deze experimenten vormen de atmosferische neutrino's zowel een dominante achtergrond, als een methode om de detector te kalibreren. Bovengenoemde modellen spelen ook een belangrijke rol bij de interpretatie van de data in het zogenaamde knie-gebied van het energie-spectrum van kosmische straling. Over de herkomst hiervan wordt nog steeds gedebatteerd.

De precieze meting van muonen met energieën tot 1 TeV vereist een lange experimentele levensduur, en een grote acceptantie. Om dit doel te bereiken is de muon detector van L3 uitgerust met een extra uitleessysteem, en is er een scintillator detector op de magneet geplaatst. Hoofdstuk 2 bevat een gedetailleerde beschrijving van de toegevoegde hardware en software. De relevante eigenschappen van de muon detector worden hier ook besproken.

Alvorens de meetresultaten te beschrijven, wordt eerst ingegaan op de kwaliteit van de experimentele opstelling. Uitgaande van de strenge selectie die in deze analyse is gebruikt, is de efficiëntie van de scintillatoren ongeveer 90%. Indien het vereiste coïncidentie interval tussen de tijdsmetingen van twee PMTs uitgebreid wordt, is de efficiëntie ongeveer 97%.

De efficiëntie van de muon detector is ook bestudeerd. Na uitsluiting van cellen met problemen zijn de efficiënties in de krommende en niet-krommende richting respectievelijk 98% en 95%. De efficiëntie van de trigger is beter dan 99%. De normalisatie van de flux hangt, naast van de efficiëntie van de detector, ook af van een nauwkeurige bepaling van de experimentele levensduur. Voor de periode waarin de bestudeerde data is genomen is dit bepaald met een onzekerheid van minder dan 0.05%. Voor de vorm van het energiespectrum is de resolutie van de impuls erg belangrijk. Deze resolutie is in detail bestudeerd, onder andere om het gemeten spectrum te kunnen de-convolueren. Asymptotisch is de resolutie van de sagitta

voor hoog energetische muonen 160 μm, terwijl de breedte van de smalle Gaussische verde-
ling, die ongeveer 70% van de data bevat, ongeveer 120 μm is. Deze studie maakt ook een
meting van de tijdsresolutie van het scintillator-systeem mogelijk, deze blijkt 2.0±0.1 ns te
zijn, wat goed overeenkomt met de ontwerpwaarde van 1.8 ns. De resolutie is bevestigd door
de meting van $Z/\gamma \rightarrow \mu^+\mu^-$ gebeurtenissen geproduceerd door LEP. Belangrijker is dat deze
meting het toelaat de absolute impulsschaal van de detector te controleren. De gemiddelde
impuls blijkt correct te zijn met een precisie van ongeveer 100 MeV.

De analyse van het muon energiespectrum en de ladingsverhouding is uitgevoerd als func-
tie van zenit. De verticale flux is gemeten binnen een halve openingshoek van 10°. Mogelijke
bronnen van systematische onzekerheden zijn in detail bestudeerd. De normalisatie van de
verticale flux is vastgesteld met een onzekerheid van 3.7%, de gemiddelde verticale ladings-
verhouding is bepaald met een onzekerheid van slechts 1.4%. De onnauwkeurigheid op de
vorm van de flux wordt beneden de 100 GeV bepaald door de onzekerheid op de variatie
van de dikte van de laag grond boven de detector, wat resulteert in een onzekerheid van on-
geveer 3%. Boven de 100 GeV daalt de onzekerheid op de vorm tot ongeveer 1%, waarna
dit langzaam stijgt tot 8% bij 1 TeV. Dit is voornamelijk te wijten aan de onzekerheid in de
bepaling van de exacte locaties van de muonkamers. De vorm van de ladingsverhouding is
bij lage energieën bepaald tot op 2%. Deze onzekerheid gaat snel omhoog tot ongeveer 13%
bij 300 GeV door de onzekerheid in de plaatsbepaling van de muonkamers. De onzekerheid
in de gemiddelde dikte van de laag grond boven de detector geeft een 500 MeV onzekerheid
op de impuls. Het gemeten spectrum boven de 100 GeV is in goede overeenstemming met
de voorspelling van CORT, maar komt, zowel in vorm en normalisatie, niet overeen met een
compilatie van alle gepubliceerde data. Onder de 100 GeV is de gemeten flux groter dan zo-
wel de voorspelling van CORT als de compilatie van data. Een mogelijke oorzaak hiervoor is
een overschatting van de hoeveelheid grond boven de detector. De gemeten ladingsverhou-
ding komt goed overeen met de compilatie, terwijl de voorspelling van CORT systematisch
hoger ligt. De verkregen nauwkeurigheid is niet genoeg om de kleine variatie als functie van
impuls, zoals beschreven door CORT, waar te nemen.

De zenit afhankelijkheid van de flux en ladingsverhouding is gepresenteerd in 14 delen
in $\cos\theta$, van verticaal tot een hoek van ongeveer 53°. De geschatte onzekerheid op de flux
varieert substantieel doordat verschillende gedeelten van de detector belangrijk zijn in de
verschillende zenit-delen. De onzekerheid varieert tussen 3% en 12%. De geschatte onzeker-
heid in de gemiddelde ladingsverhouding varieert tussen de 0.7 en 3%. CORT beschrijft de
gemeten zenit-afhankelijkheid van zowel de flux als de ladingsverhouding goed.

Acknowledgements

Many people have contributed to this thesis. This might sound like a cliché, but nevertheless, it is true that an experiment as large as L3+Cosmics would be impossible without the close collaboration of many people with different talents and skills. It has been an enormous opportunity for me to be part of something so much bigger than what a single human being can achieve. Therefore, I would like to thank everyone for giving me this unique experience.

Martin, I would like to thank you for the many inspiring discussions we have had over the years. Professionally, I learned tremendously from the many times you were right and I was wrong; while personally, I learned a lot from the few occasions where I managed to convince you otherwise. With remarkable speed you always separated the sense and nonsense in my ideas and plans.

Charles, I would like to thank you for your daily support and the many hours we spent at the blackboard trying to understand the peculiarities of my analysis. Most of all, I would like to thank you for your good sense of humor (appropriately sarcastic), without which I would not have survived the last two years.

Henric, I am very grateful for the close collaboration we have had ever since you joined the group. This thesis contains many parts which are a result of our combined effort. I hope you will soon find your way to "the ticket office".

Albert, Hans, Henk, Paul, and Thei, I would like to thank you for the great time we had while designing and debugging the electronics. Our many visits to l'Aviation surely increased the creativity. The on-line team, Andrei, Bert, Charles, Henric, Pedro, Rudolf, Ruud, Xiaofeng, and Yupeng, I am very thankful to you for your enthusiasm in realizing a fully automated DAQ. Special thanks goes to Clara for your readiness to help us solve our DIM problems, regardless whether the problems were due to DIM or our use of it.

The Col3 boys, Albert, Andreas, Henric, Matthias, Michael, Tomasso, Xinhua, and Zhiguo, in spite of the "dirty job" it was, I really appreciated the open and positive atmosphere in which we solved the problems. To Albert (Mr. Cosmics himself) a special thanks for showing me the ins and outs of the code (here not a word about acceptance ☺). I am particularly grateful to Andreas, Michael and Zhiguo for their work on Sil3c. I would like to thank Thomas for his tough but fair leadership of the off-line group. Special thanks to Vjeran for providing the field-map of the coil and yoke.

I have received plenty of help from the members of L3 during my stay at CERN. Bob and Ingrid, I would like to thank you for sharing your experience with me. I especially give thanks to Brian, Gerjan, Guy, Joe, Michel, Steve, and Yoshi for explaining the muon system to me, and for your help and understanding during the design and installation of our

Curriculum Vitae

The author of this thesis was born on the 2nd of February 1970, and spent the first 18 years of his life in Kolding, Denmark. In 1989 he obtained the "Studenter Eksamen" in mathematics and physics from Kolding Gymnasium.

Following a year of travelling in Canada and the US, he started the study of physics and computer science at the University of Århus. During the last year he worked in the experimental nuclear physics group at the faculty of Natural Sciences, studying nuclei along the drip-line, participating in experiments at GANIL, GSI and ISOLDE. His diploma work contained an experimental study of the decay chain of ^{31}Ar from data obtained at ISOLDE. In 1996 this resulted in a Master's Degree (Cant. Scint) in experimental physics and a Bachelor's Degree in computer science.

The author was employed as "Assistent In Opleiding" (AIO) at the University of Nijmegen from July 1996 until the end of 2000. In this period he took part in the design and realization of the L3+Cosmics experiment. During his two-year stay at CERN, he was in charge of the online software group and contributed to the conceptual design and prototype testing of the readout and trigger electronics. After his return to the University of Nijmegen, he assisted in a practical electronics course and an introductory course regarding the structure of matter. Furthermore, he participated in the modification of the existing L3 software enabling the reconstruction of the measured cosmic ray muons. This resulted in the measurement of the momentum spectrum and charge ratio.

During the same period, he participated in several international summer schools and conferences, among which: "The 4th school on Non-Accelerator Particle Astrophysics" in Trieste, Italy, "The X International Symposium on Very High Energy Cosmic Ray Interactions", in Gran Sasso, Italy, "The Chacaltaya Meeting on Cosmic Ray Physics" in La Paz, Bolivia, and "The XI International Symposium on Very High Energy Cosmic Ray Interactions", in Campinas, Brazil.

This thesis presents the results of the research mentioned above.